National Snow and Ice Data Center

Special Report - 4

ATMOSPHERIC AND SEA ICE CHARACTERISTICS OF THE ARCTIC OCEAN AND THE SHEBA FIELD REGION IN THE BEAUFORT SEA

Mark C. Serreze

James A. Maslanik

Jeffrey R. Key

National Snow and Ice Data Center
Cooperative Institute for Research in Environmental Sciences
University of Colorado, Boulder, Colorado, USA

Atmospheric and Sea Ice Characteristics of the Arctic Ocean and the SHEBA Field Region in the Beaufort Sea

Mark C. Serreze, James A. Maslanik

Division of Cryospheric and Polar Processes,
Cooperative Institute for Research in Environmental Sciences
Campus Box 449, University of Colorado, Boulder, CO 80309-0449

Jeffrey R. Key

Department of Geography, Boston University

Special Report - 4

ATMOSPHERIC AND SEA ICE CHARACTERISTICS OF THE ARCTIC OCEAN AND THE SHEBA FIELD REGION IN THE BEAUFORT SEA

Mark C. Serreze

James A. Maslanik

Jeffrey R. Key

Atmospheric and Sea Ice Characteristics of the Arctic Ocean and the SHEBA Field Region in the Beaufort Sea

Mark C. Serreze, James A. Maslanik

Division of Cryospheric and Polar Processes,
Cooperative Institute for Research in Environmental Sciences
Campus Box 449, University of Colorado, Boulder, CO 80309-0449

Jeffrey R. Key

Department of Geography, Boston University

TABLE OF CONTENTS

INTRODUCTION

The Surface Heat Budget of the Arctic Ocean (SHEBA) program is designed to improve our understanding of the thermodynamic coupling between the Arctic atmosphere, the sea ice and ocean. The program is motivated by large discrepancies among simulations by global climate models of the present and future state of the Arctic and uncertainty regarding the impact of the Arctic on climate change. SHEBA Phase I includes the analysis of existing data sets, modeling, satellite studies and experiment planning for Phase II, a field experiment in the Beaufort Sea designed to collect a suite of data sets leading to better understanding of the Arctic surface heat budget, in particular, the sea ice albedo feedback mechanism.

As a contribution to SHEBA Phase I, we have used existing data sets, data sets generated in-house and previously published results to provide characterizations of the mean state and variability of atmospheric and sea ice conditions for the Arctic Ocean. When applicable or data permit, regional analyses are also carried out for the vicinity of the SHEBA manned camp in the Beaufort Sea, slated for deployment at approximately 77°N, 145°W. This work is intended to: 1) provide an up-to-date overview of Arctic atmospheric, sea ice and surface conditions useful as a general reference; 2) assist in assessing how representative the Beaufort Sea SHEBA field area is of "central Arctic" conditions; 3) identify the probable mean states and range of conditions that may be encountered at the field camp, 4) provide a climatological framework against which conditions encountered in the field may be compared and contrasted.

Summaries are provided of the following:

* Atmospheric circulation
* Water vapor characteristics
* Cloud cover properties
* Precipitation and precipitation characteristics
* Two-meter and tropospheric temperatures
* Surface winds
* Surface radiation fluxes and albedo
* Sea ice conditions, including concentration, motion, snow on sea ice and the timing of melt onset

Results are organized in atlas form, where monthly spatial fields for the Arctic Ocean and larger domains as appropriate are followed by analyses for the SHEBA region. The latter results are primarily expressed in terms of seasonal cycles and histograms for a grid point near the planned initial deployment location of the manned camp. Each section starts with an overview of the data analysis followed by a brief discussion of results. More detailed discussions are provided for new data sets or for those not widely examined in previous studies (e.g., gridded fields of global radiation fields and precipitation characteristics). It is not our intent to provide in-depth interpretation of these data. Detailed discussions of the spatio-temporal characteristics of most of the variables examined here are available in the refereed literature.

1. ATMOSPHERE

1.1 Sea Level Pressure, 500 mb Heights and Daily Standard Deviations

Results were compiled from fields provided by the National Center for Environmental Prediction/National Center for Atmospheric Research (NCEP/NCAR) "reanalysis" project. Mean monthly fields and daily standard deviations for each month (Figure 1.1.1) were calculated from the 00Z analyses. Summaries for the SHEBA region are provided in Figures 1.1.2 and 1.1.3. The NCEP/NCAR fields are intended to represent improvements over existing analyses as a result of: 1) the elimination of discontinuities through the use of a "frozen" state-of-the-art T62 model and data assimilation system; 2) concerted efforts to use all available historical data in the assimilations with strict quality control. Details of the NCEP/NCAR system are provided by Kalnay et al. [1996]. Our results are based on the 17-year period, 1979-1995, for which analyses include Arctic Ocean sea level pressure (SLP) measurements from the International Arctic Buoy Program [Thorndike and Colony, 1981]. The NCEP/NCAR reanalysis will eventually cover a 40 year time period (1957-1996). A Cressman interpolation [Cressman, 1959] was used to interpolate the data to a 100x100 km version of the EASE-Grid centered over the pole [Armstrong and Brodzik, 1995]. This is a lower-resolution form of the 25x25 km EASE-Grid being used at the National Snow and Ice Data Center (NSIDC) in Boulder, Colorado, for producing Special Sensor Microwave Imager (SSM/I) global brightness temperature grids and geophysical products from the National Oceanic and Atmospheric Administration/National Aeronautics and Space Administration (NOAA/NASA) SSM/I, AVHRR and TOVS polar pathfinder programs.

Note that while sea level pressure (SLP) over the Central Arctic Ocean is fairly high for winter months (appearing as a saddle of relatively high pressure between the Siberian and Alaskan highs), it is only from April-July that the region exhibits a closed anticyclone, centered roughly over the Beaufort Sea. August shows a weak mean low near the Pole (1008 mb). For individual years this region is typically characterized by a strong mean low during at least one month between June and September, reflecting frequent cyclone activity (see Section 2.2). Results for the SHEBA region show a strong seasonal cycle, with minimum SLP in August and maximum 500 mb heights in July. Standard deviations are largest during winter.

Figure 1.1.1

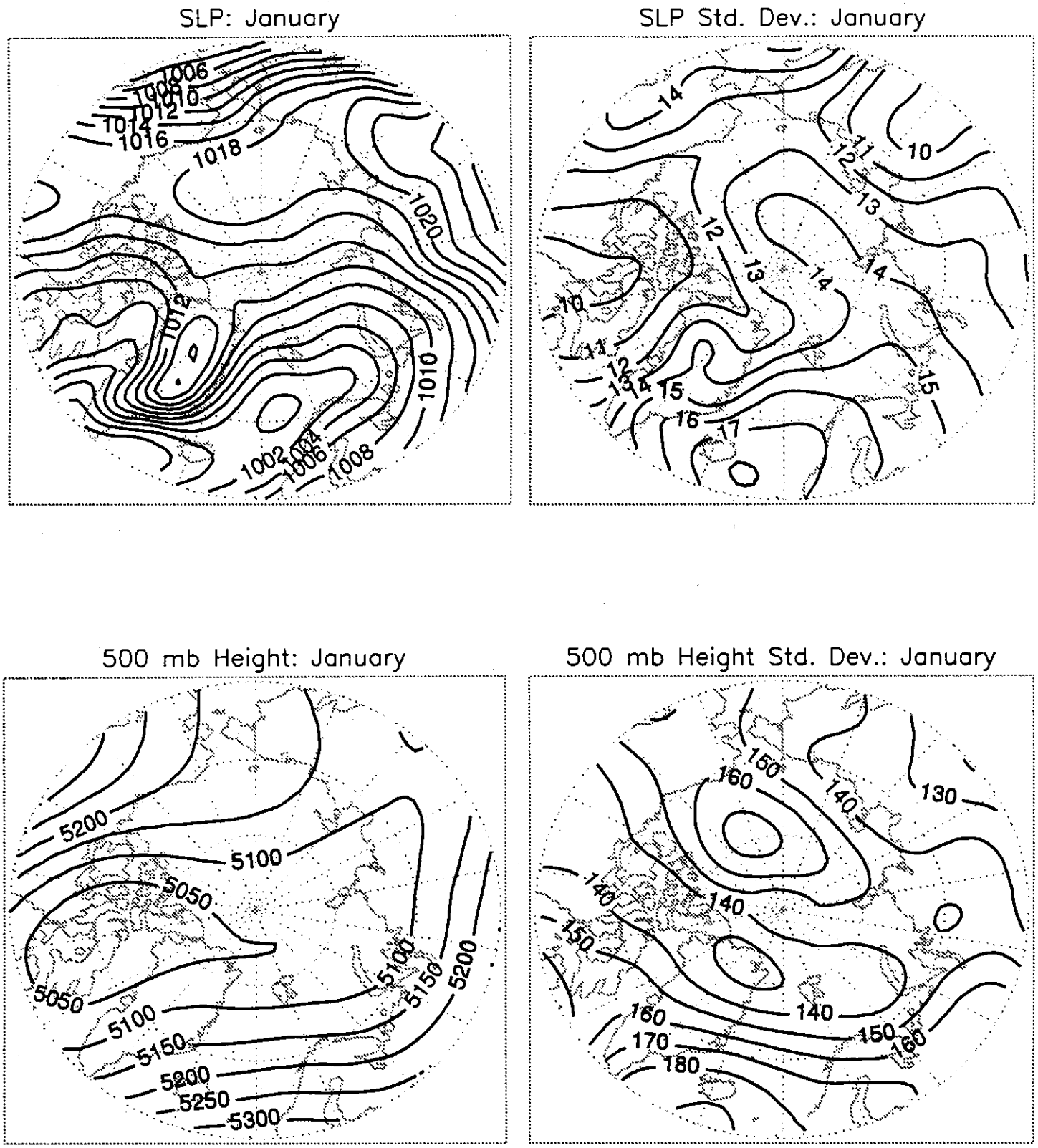

Units for Sea Level Pressure and Standard Deviation: Millibars
Units for 500 mb Height and Standard Deviation: Geopotential Meters

Figure 1.1.1 (Continued)

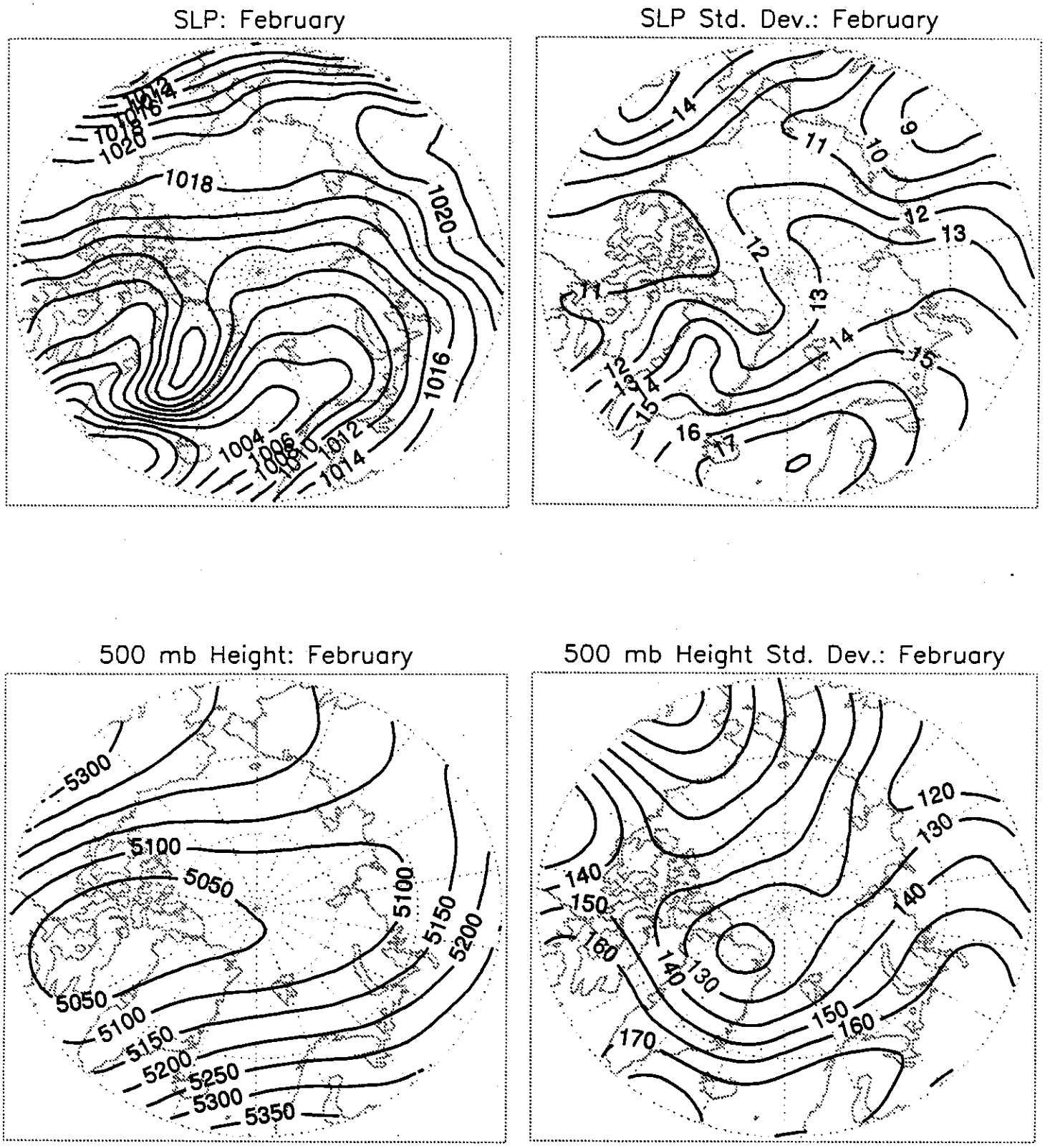

Units for Sea Level Pressure and Standard Deviation: Millibars
Units for 500 mb Height and Standard Deviation: Geopotential Meters

Figure 1.1.1 (Continued)

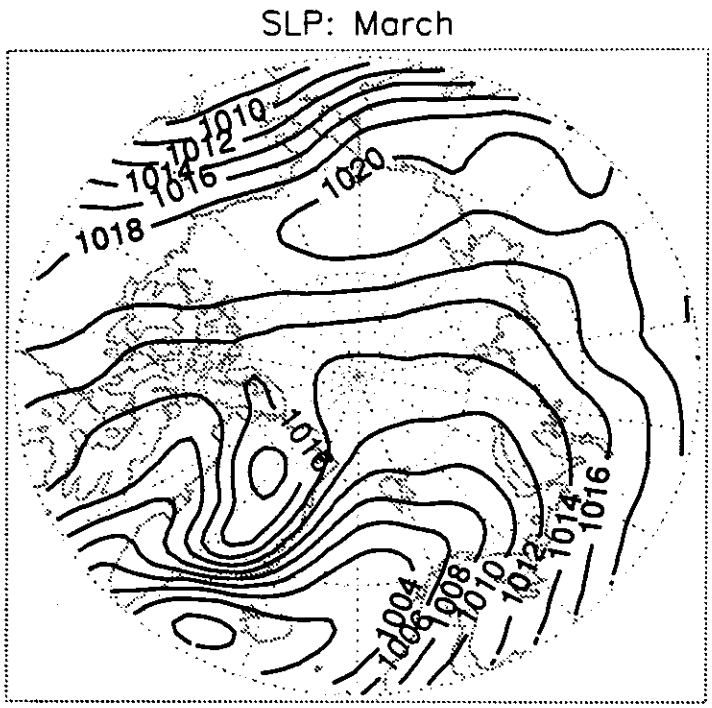

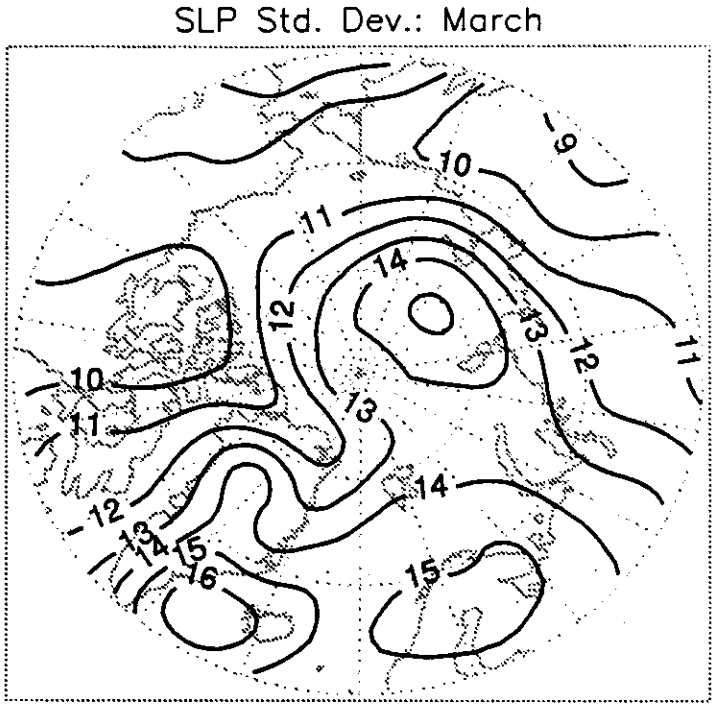

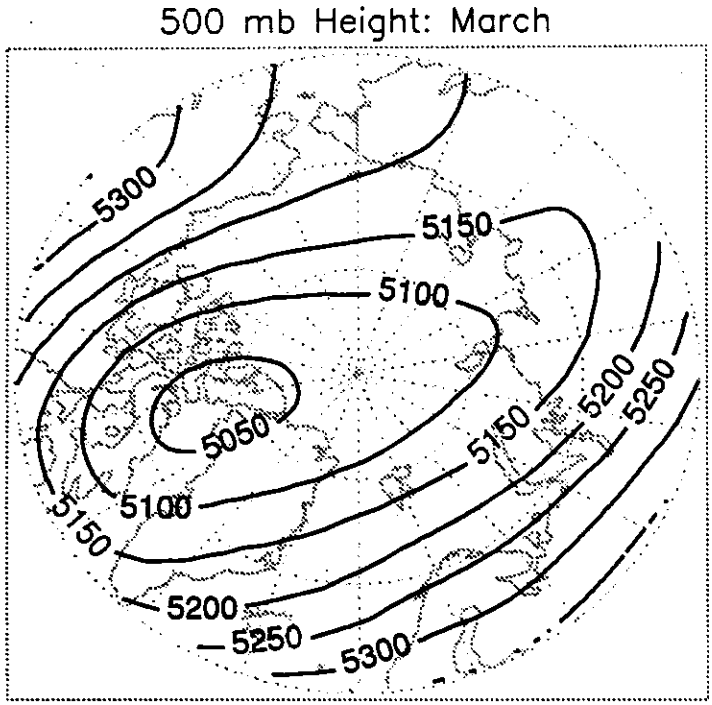

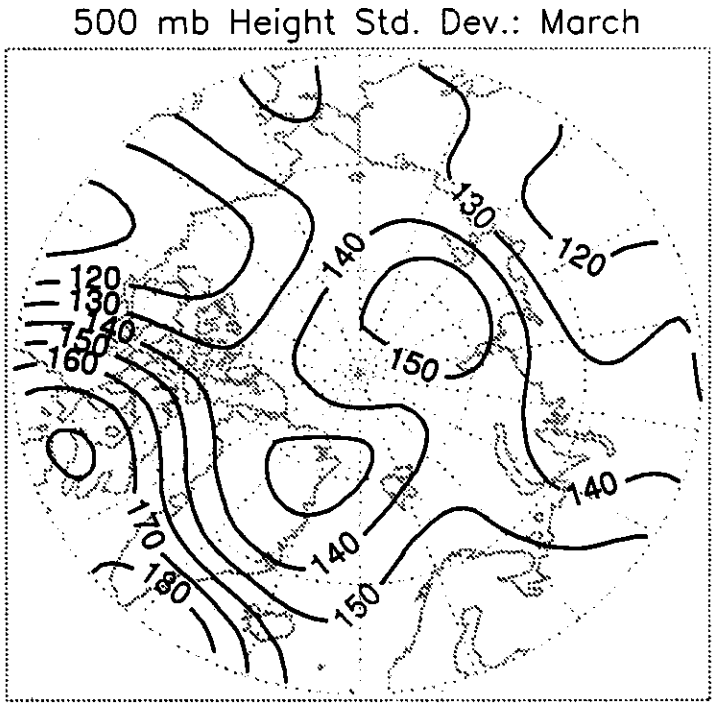

Units for Sea Level Pressure and Standard Deviation: Millibars
Units for 500 mb Height and Standard Deviation: Geopotential Meters

Figure 1.1.1 (Continued)

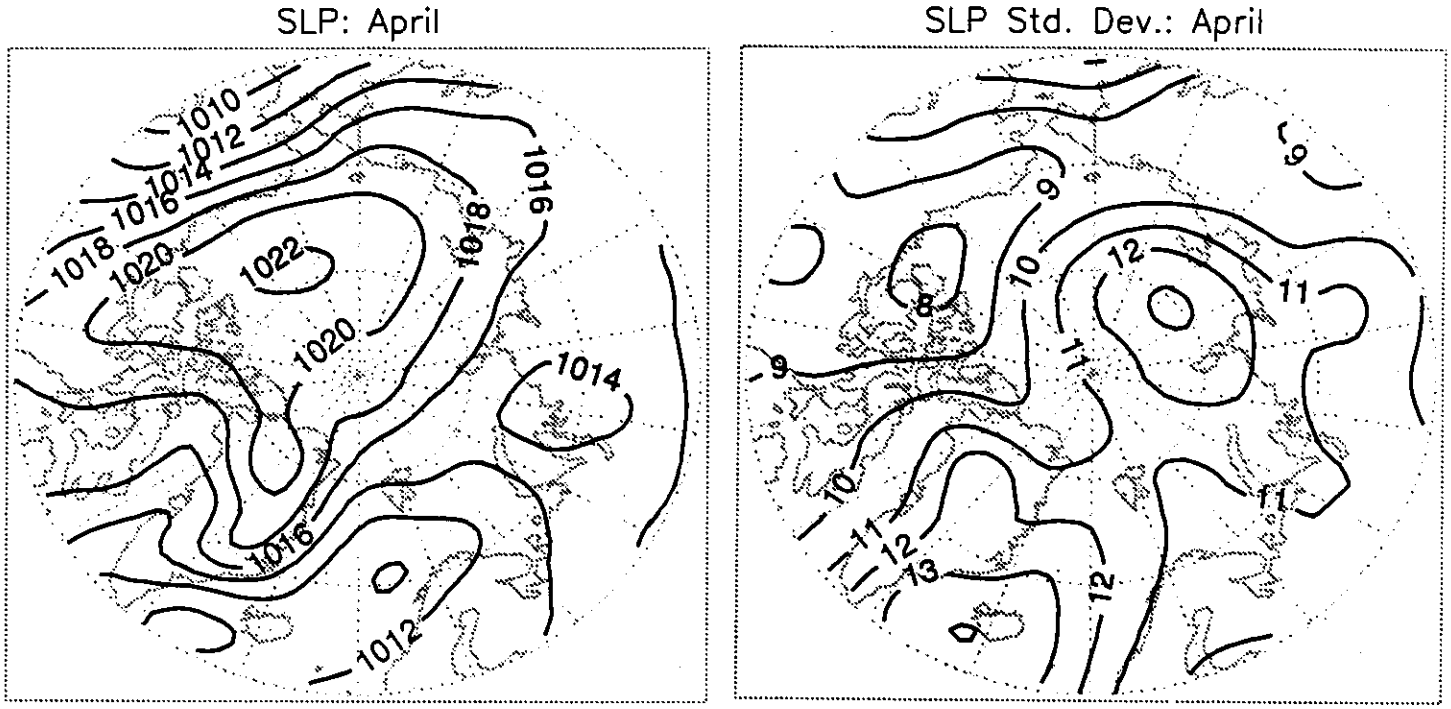

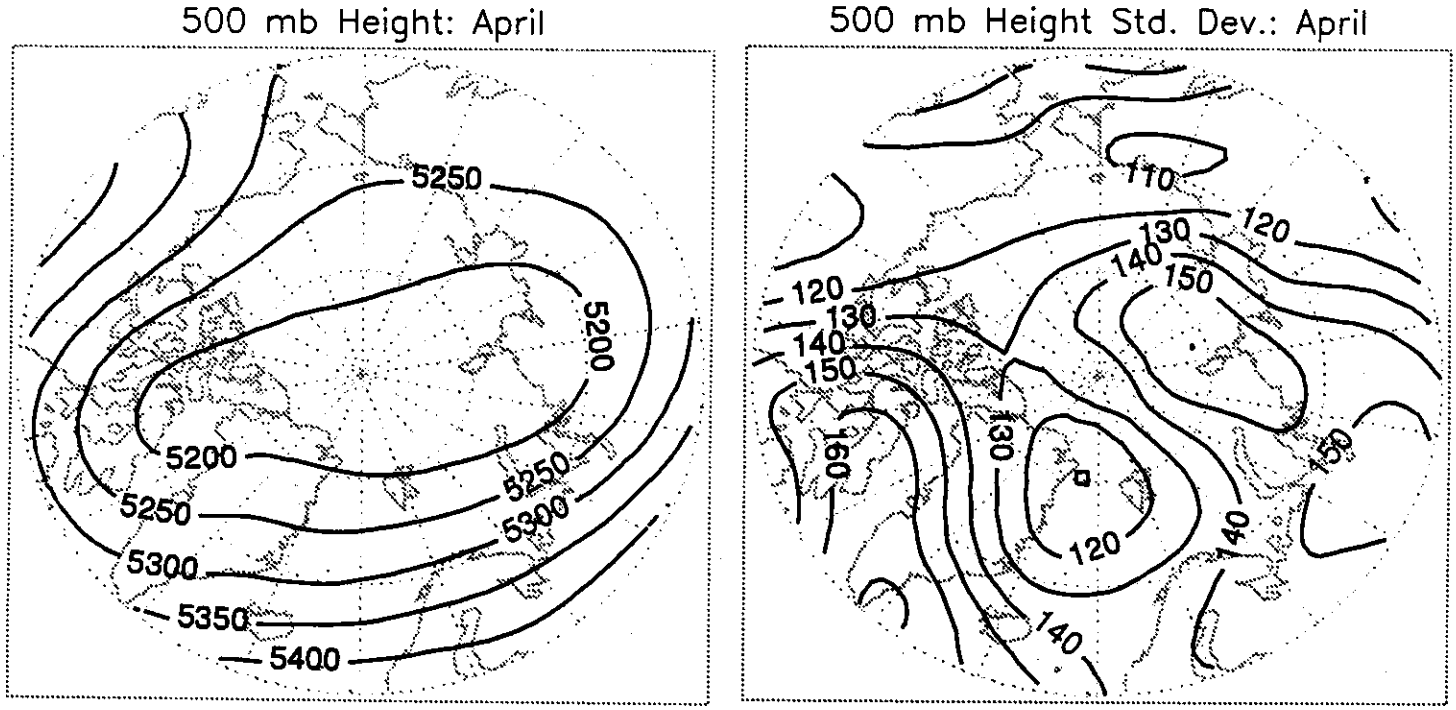

Units for Sea Level Pressure and Standard Deviation: Millibars
Units for 500 mb Height and Standard Deviation: Geopotential Meters

Figure 1.1.1 (Continued)

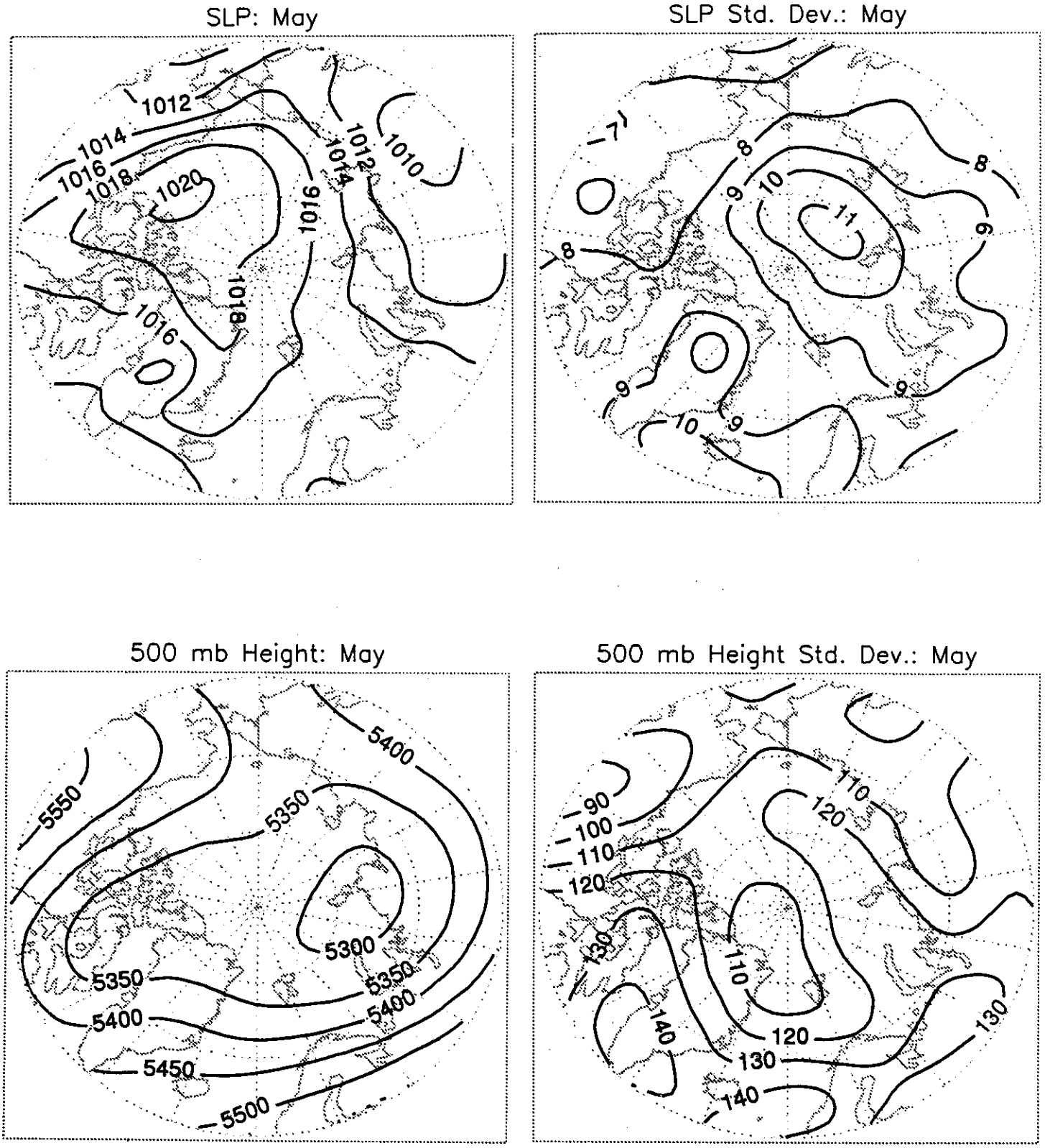

Units for Sea Level Pressure and Standard Deviation: Millibars
Units for 500 mb Height and Standard Deviation: Geopotential Meters

Figure 1.1.1 (Continued)

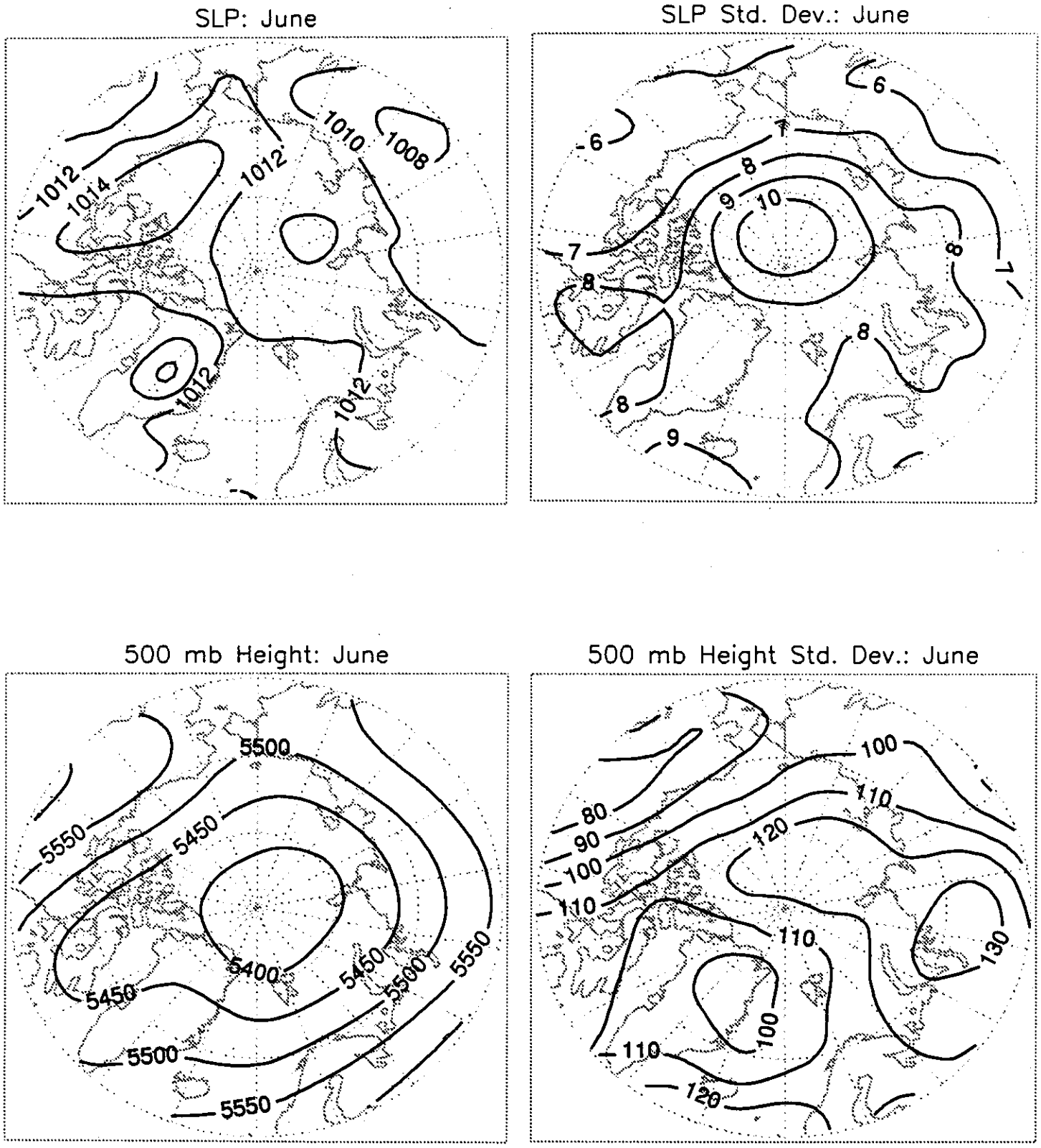

Units for Sea Level Pressure and Standard Deviation: Millibars
Units for 500 mb Height and Standard Deviation: Geopotential Meters

Figure 1.1.1 (Continued)

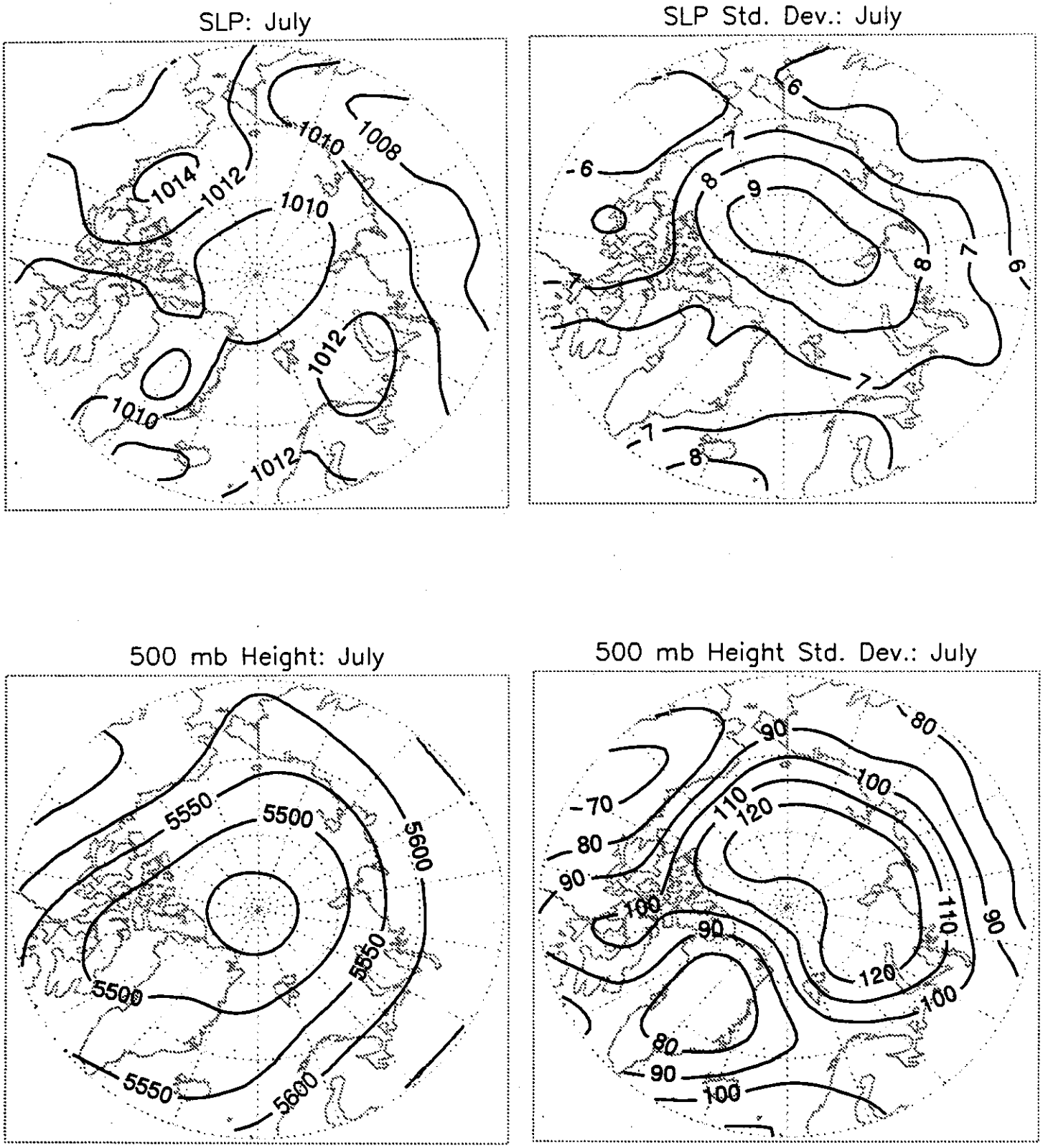

Units for Sea Level Pressure and Standard Deviation: Millibars
Units for 500 mb Height and Standard Deviation: Geopotential Meters

Figure 1.1.1 (Continued)

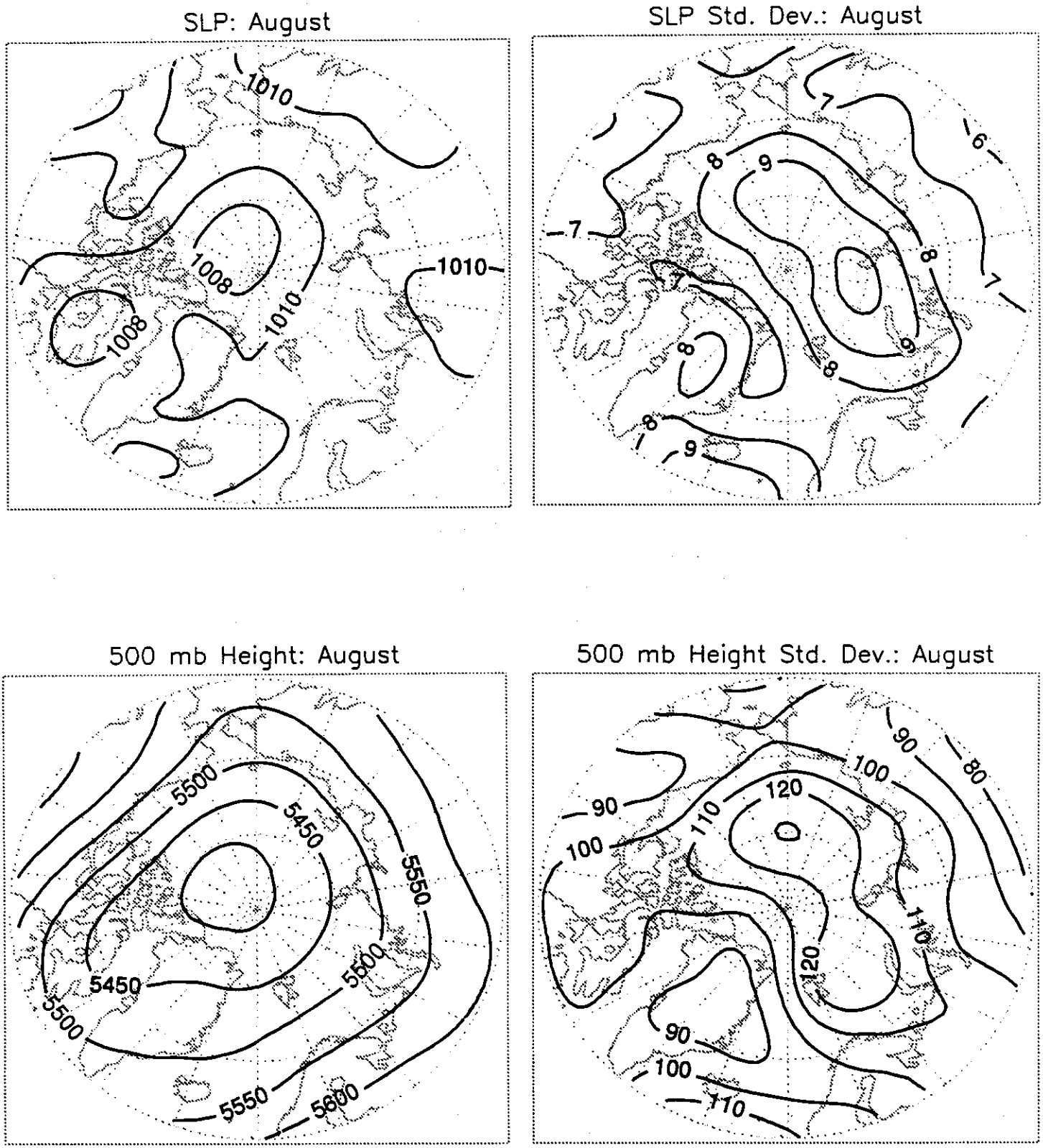

Units for Sea Level Pressure and Standard Deviation: Millibars
Units for 500 mb Height and Standard Deviation: Geopotential Meters

Figure 1.1.1 (Continued)

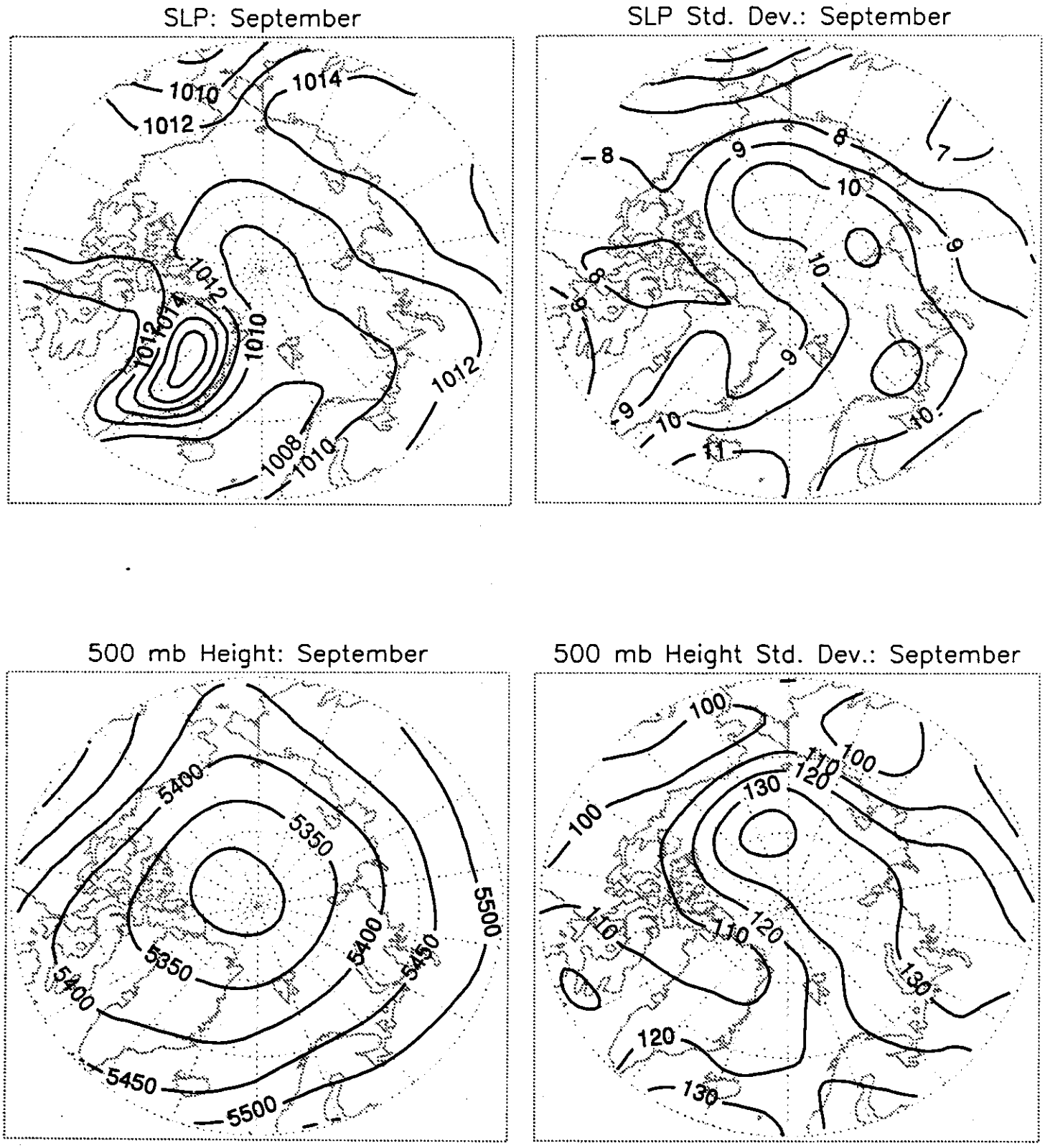

Units for Sea Level Pressure and Standard Deviation: Millibars
Units for 500 mb Height and Standard Deviation: Geopotential Meters

Figure 1.1.1 (Continued)

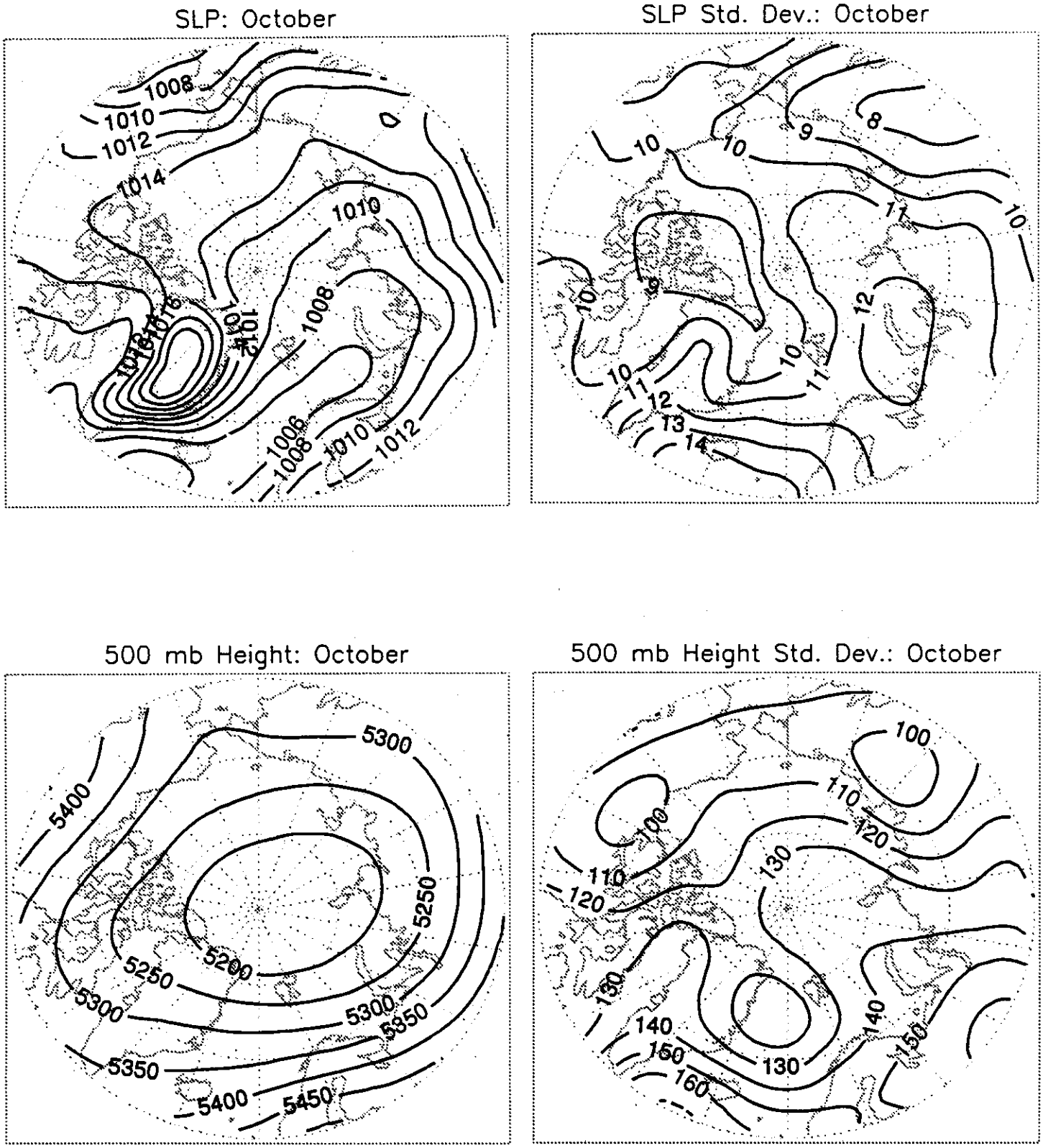

Units for Sea Level Pressure and Standard Deviation: Millibars
Units for 500 mb Height and Standard Deviation: Geopotential Meters

Figure 1.1.1 (Continued)

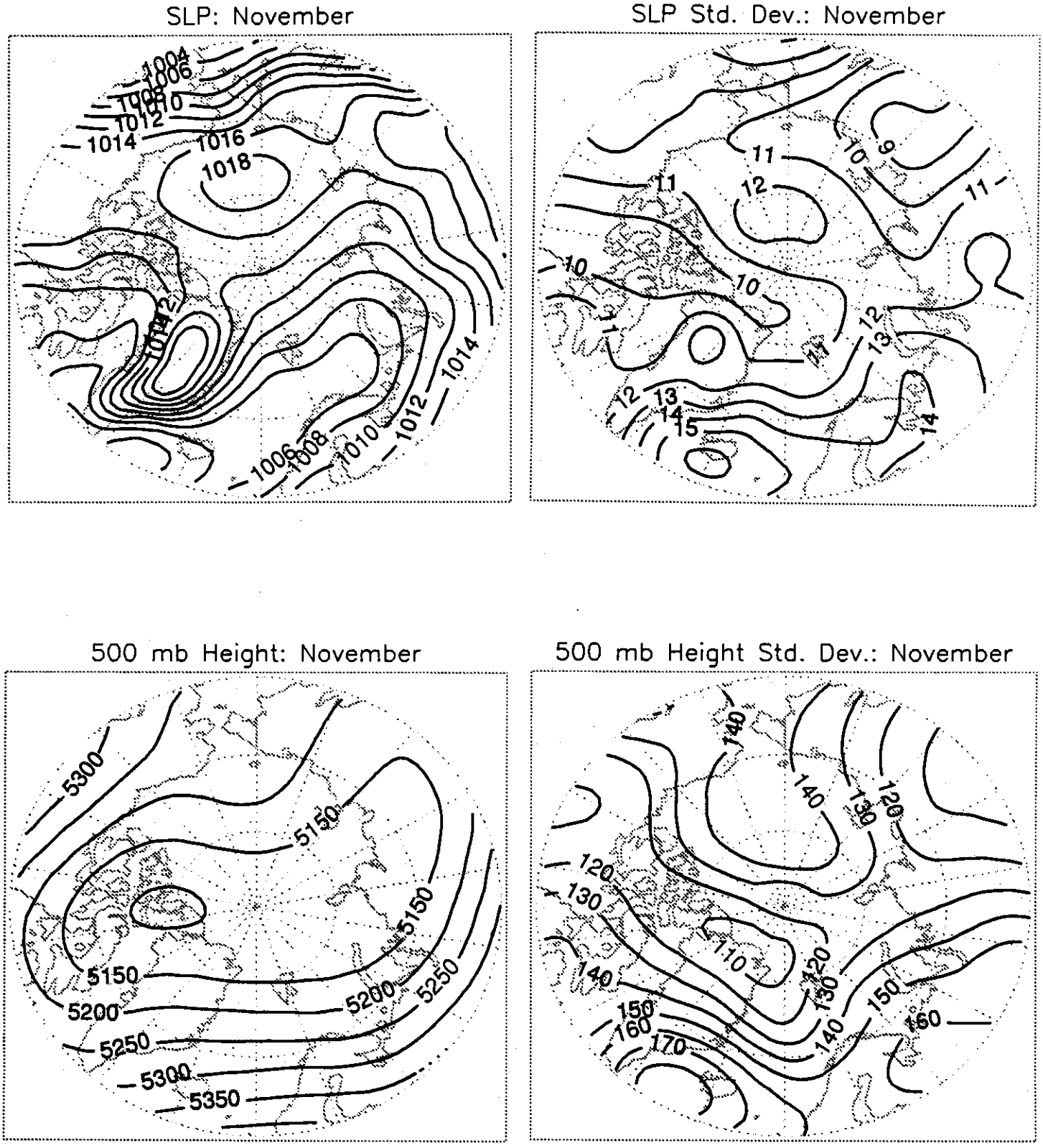

Units for Sea Level Pressure and Standard Deviation: Millibars
Units for 500 mb Height and Standard Deviation: Geopotential Meters

Figure 1.1.1 (Continued)

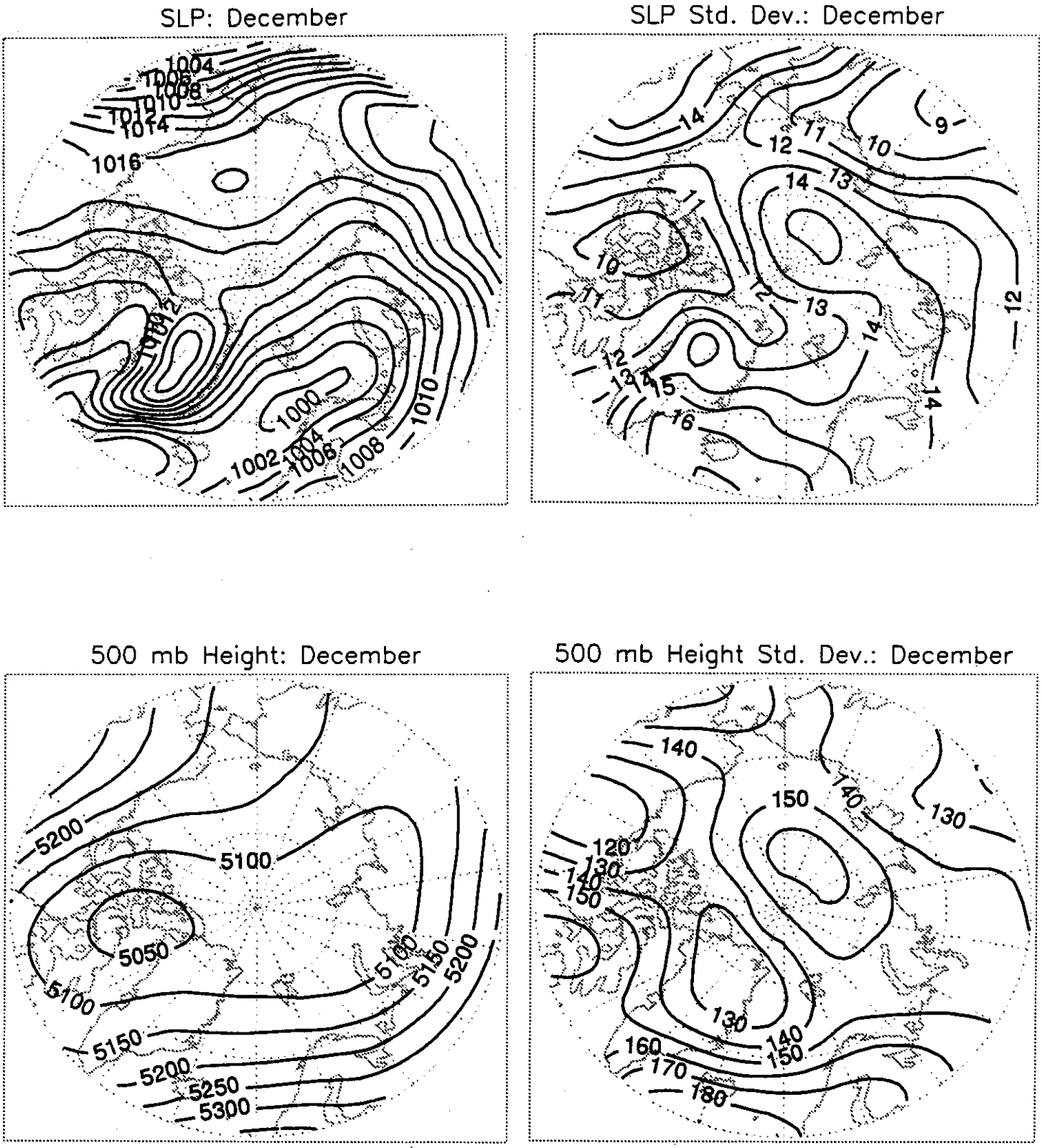

Units for Sea Level Pressure and Standard Deviation: Millibars
Units for 500 mb Height and Standard Deviation: Geopotential Meters

Figure 1.1.2

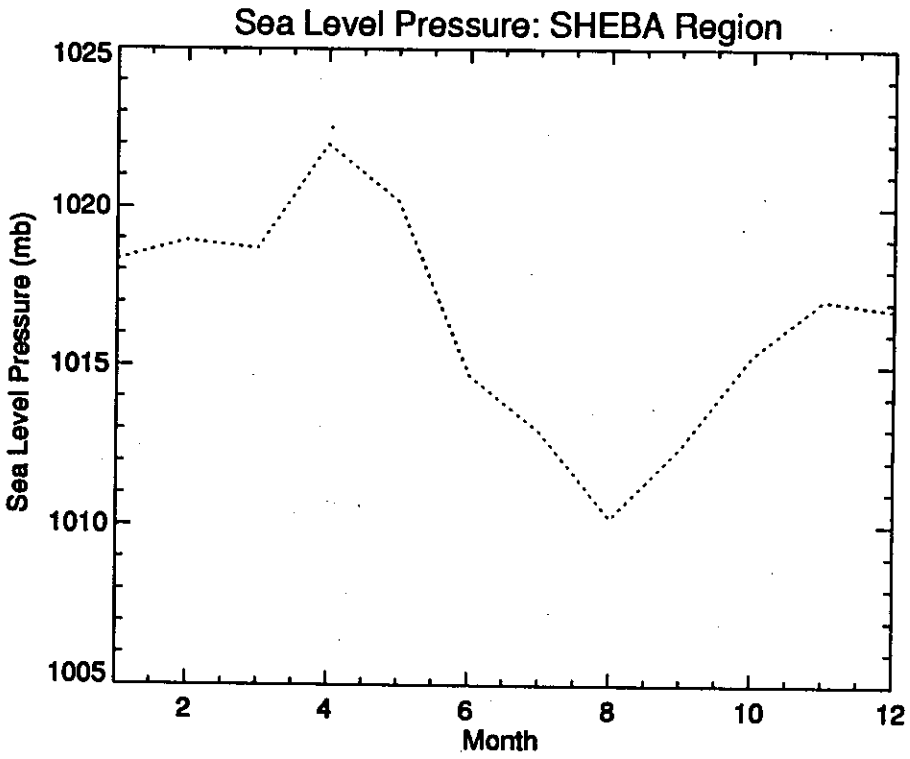
Sea Level Pressure: SHEBA Region
Sea Level Pressure (mb)
1025
1020
1015
1010
1005
2
4
6
8
10
12
Month

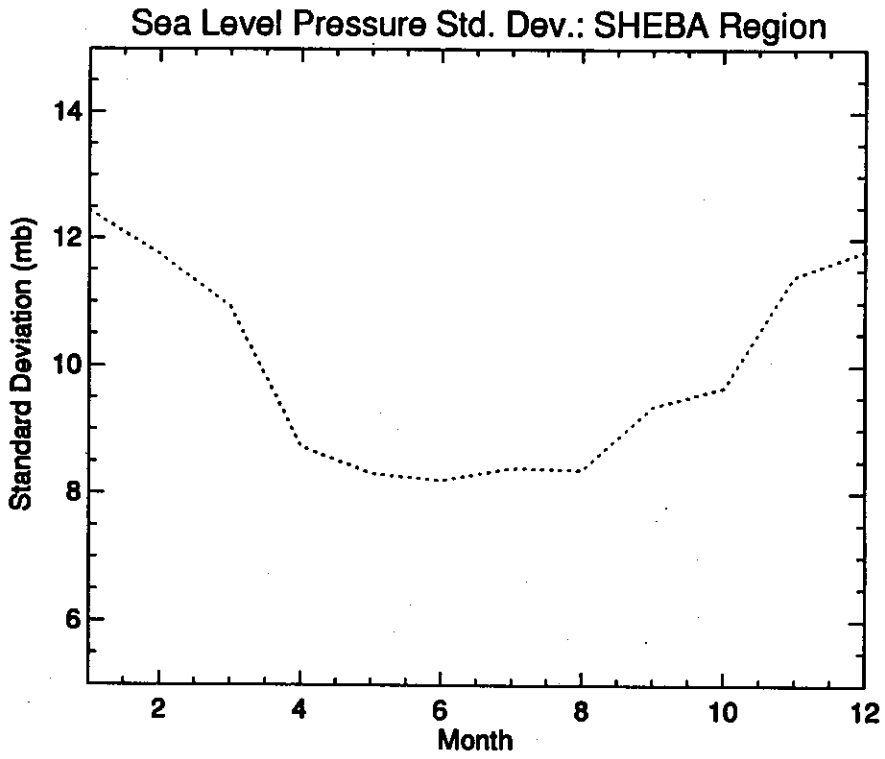
Sea Level Pressure Std. Dev.: SHEBA Region
Standard Deviation (mb)
14
12
10
8
6
2
4
6
8
10
12
Month

Figure 1.1.3

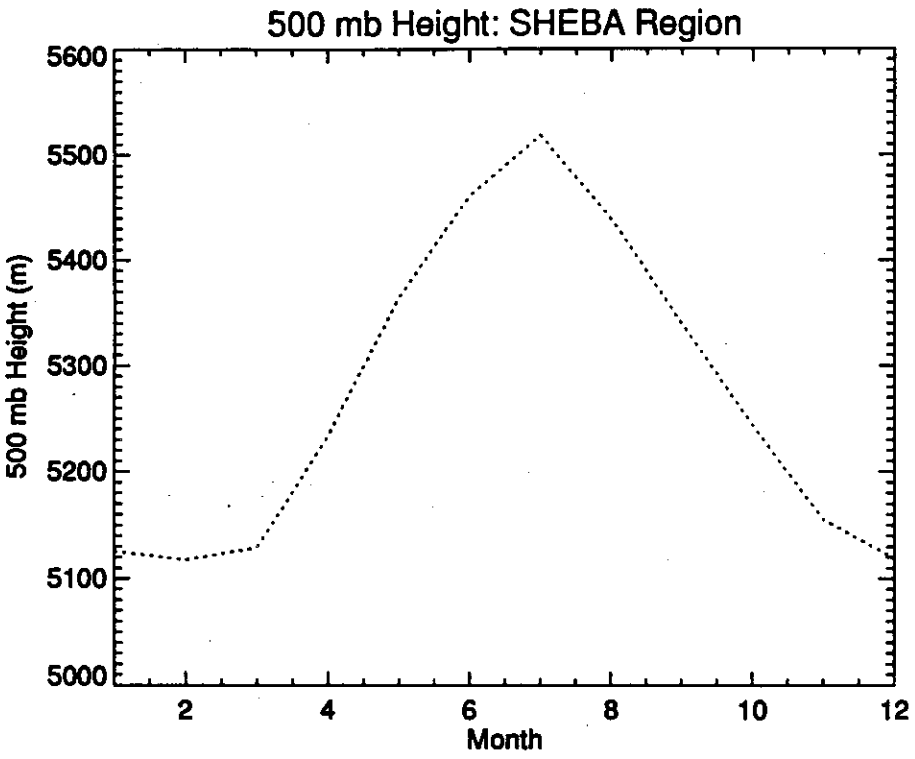
500 mb Height: SHEBA Region
500 mb Height (m)
5600
5500
5400
5300
5200
5100
5000
2
4
6
8
10
12
Month

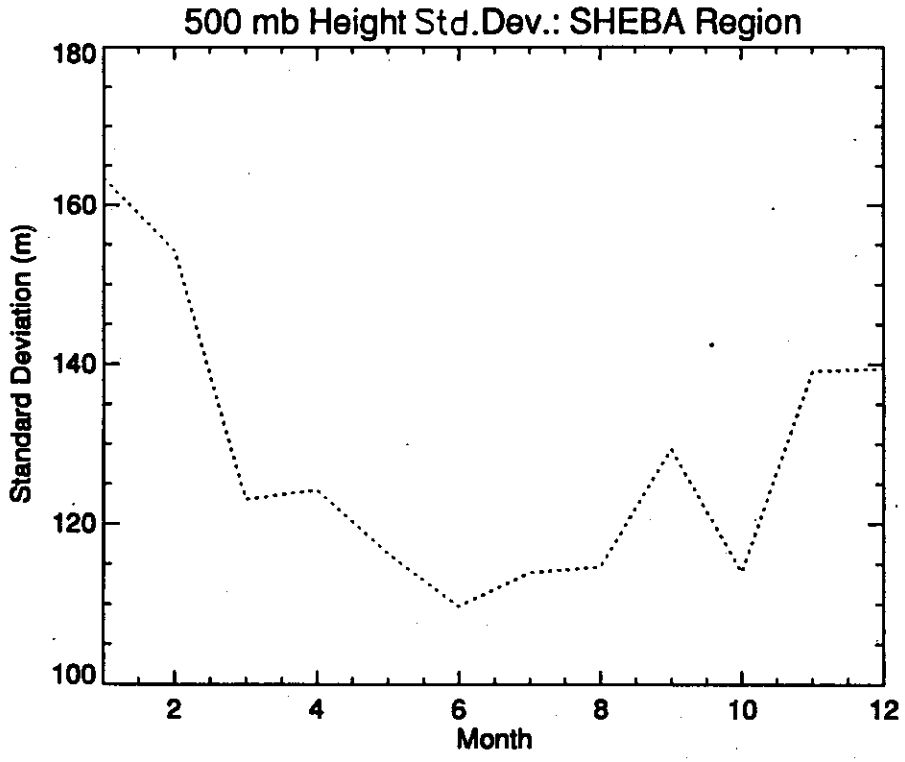
500 mb Height Std.Dev.: SHEBA Region
Standard Deviation (m)
180
160
140
120
100
2
4
6
8
10
12
Month

1.2 Cyclone and Anticyclone Distributions

Each map (Figure 1.2.1) depicts isolines of monthly total counts of the centers of cyclones and anticyclones from twice-daily SLP data for the 28-year period, 1966-1995. Results are based on NCEP pre-reanalysis fields on the NCEP Octagonal Grid. Data were subsequently transformed to the EASE-Grid discussed in Section 1.1. The algorithm used to define cyclone and anticyclone centers is identical to that of Serreze et al. [1997]. This algorithm is based on a series of search patterns that test whether a grid-point SLP value is surrounded by grid-point values at least 2 mb higher (lower) than the central point being examined. The area represented by an NCEP Octagonal Grid increases with latitude. Consequently, prior to transformation to the EASE-Grid the system counts were adjusted to a 60°N reference latitude. We consider only systems lasting at least 24 hours (two charts) and have also adjusted results for missing data (representing only about 2% of all days).

With respect to possible influences on the SHEBA field region, there is a maximum in central Arctic cyclone activity north of the Beaufort Sea from July through September. May through July show high counts over the Alaska/Yukon region, which is known to be an area of frequent cyclogenesis; central Arctic cyclones, by contrast, are typically occluded systems that migrate into the Central Arctic from Siberia and the North Atlantic. The frequency of anticyclone centers over the Beaufort Sea shows a June-July maximum. These seasonal changes are in turn reflected in the SLP distribution (Section 1.1).

Figure 1.2.1

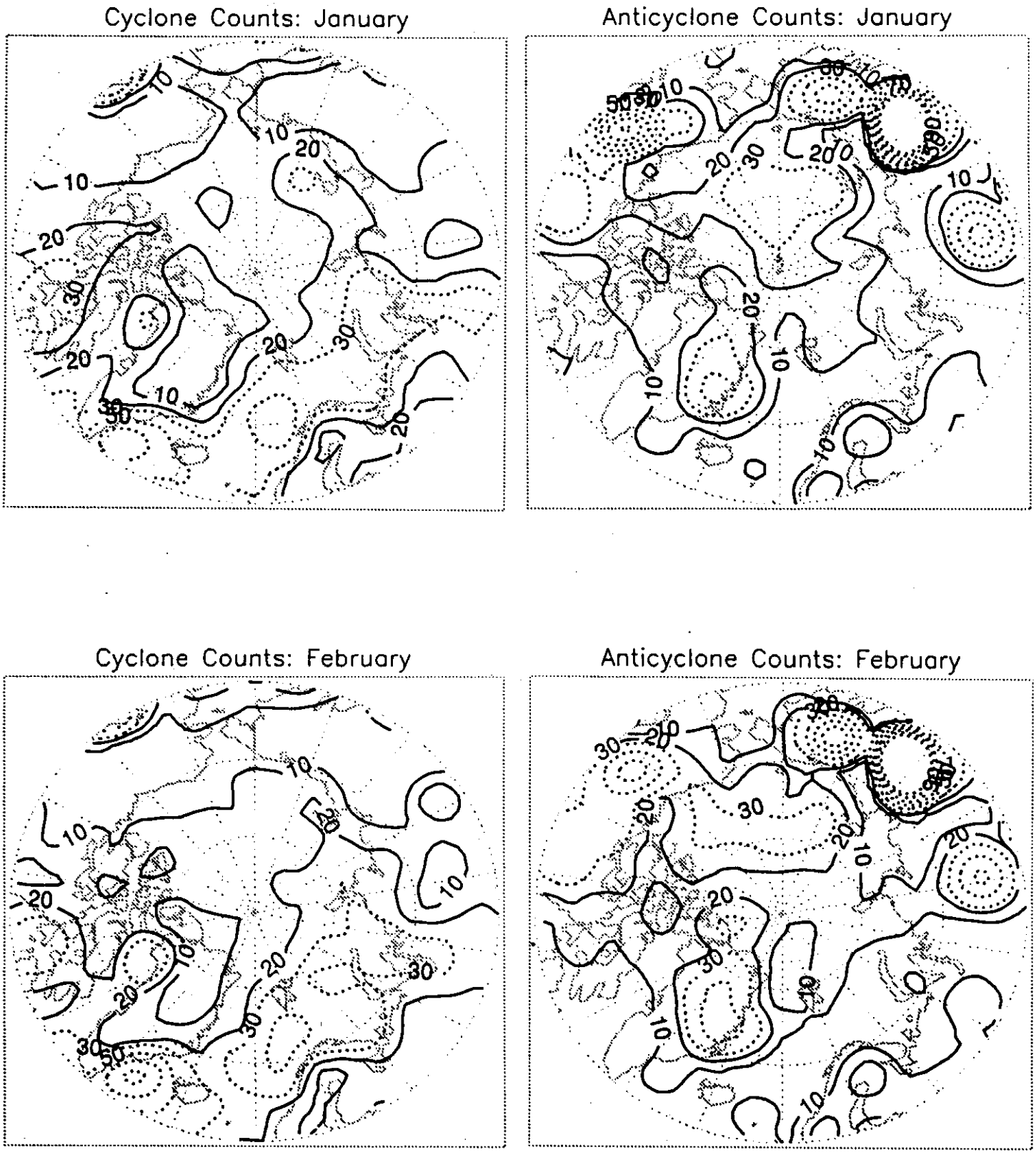

Units: Total Counts
Contours: 0-20 x 10 (solid), 30+ x 20 (dotted)

Figure 1.2.1 (Continued)

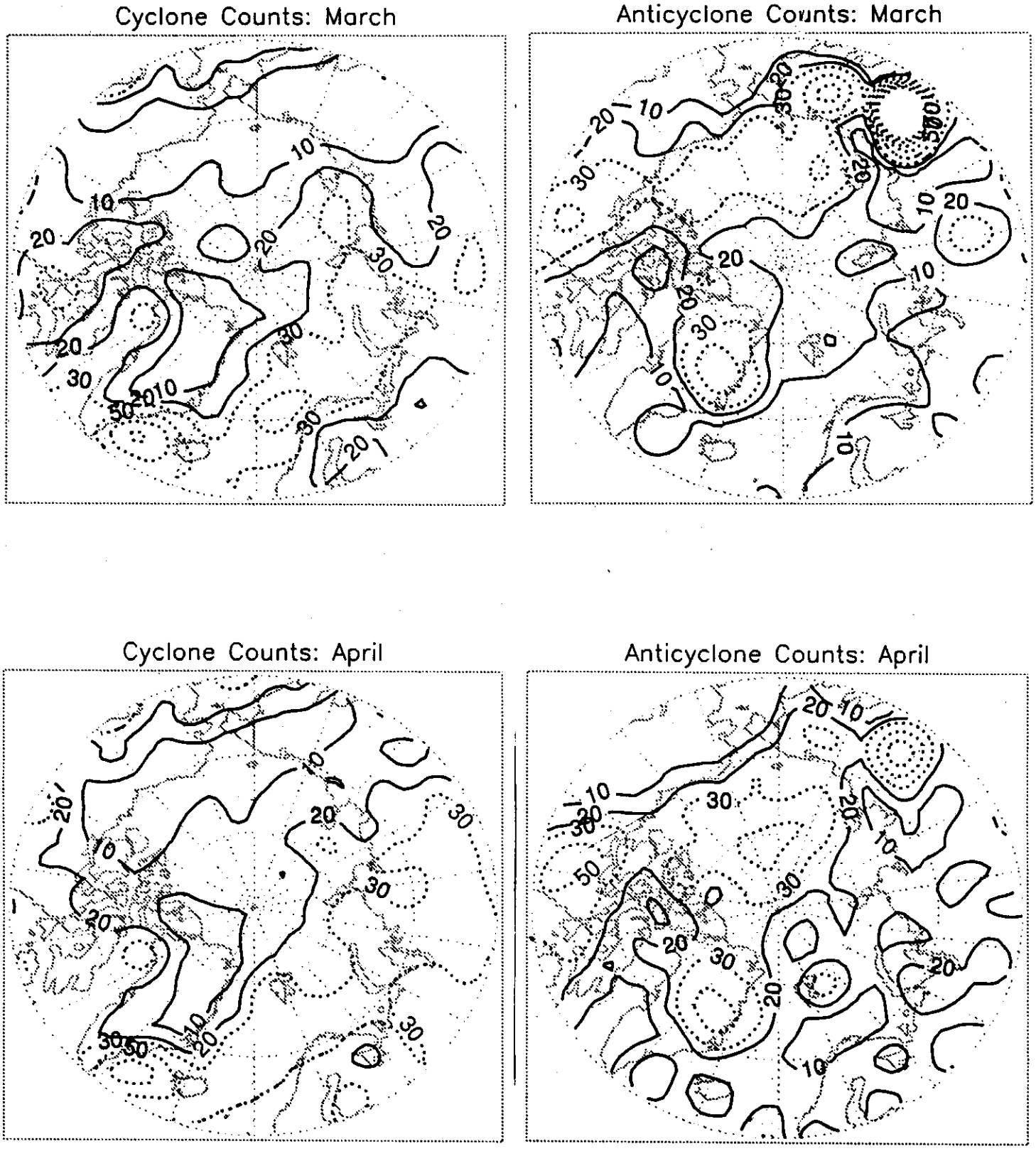

Units: Total Counts
Contours: 0-20 x 10 (solid), 30+ x 20 (dotted)

Figure 1.2.1 (Continued)

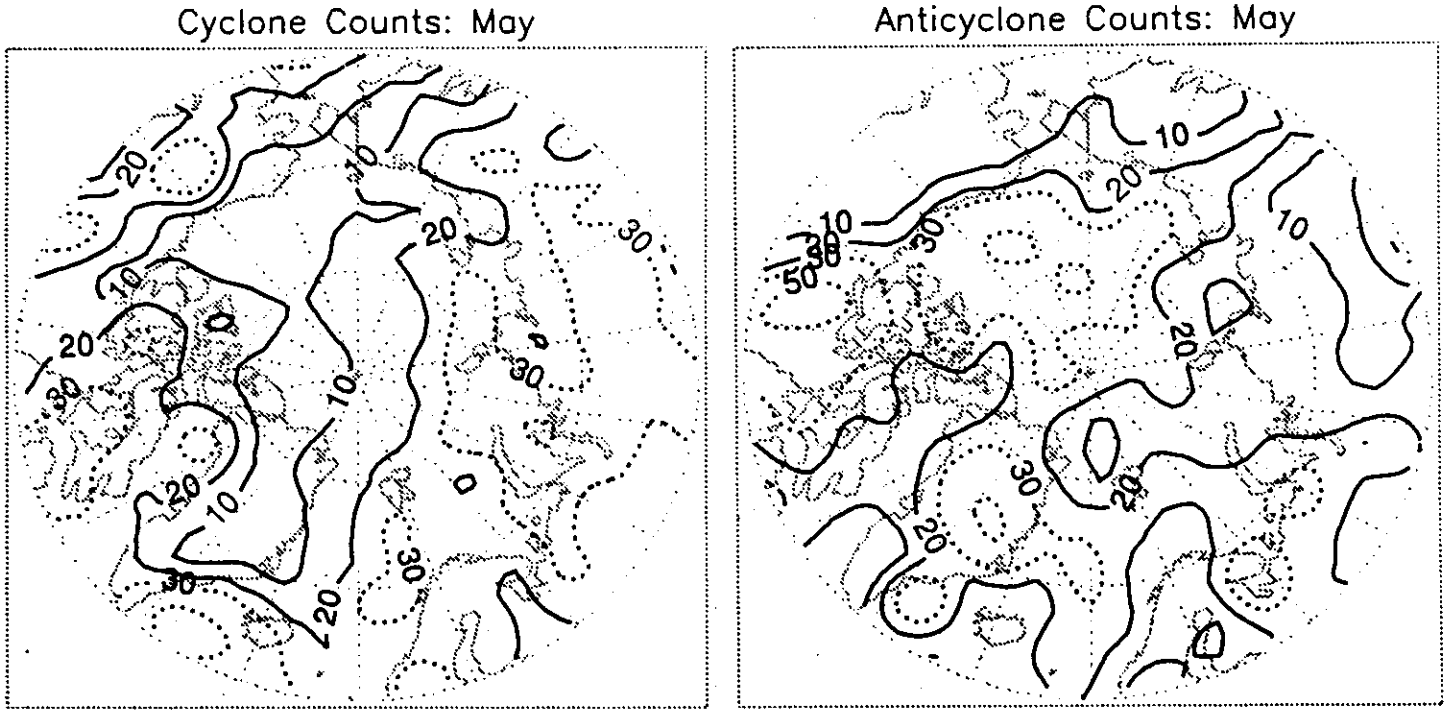

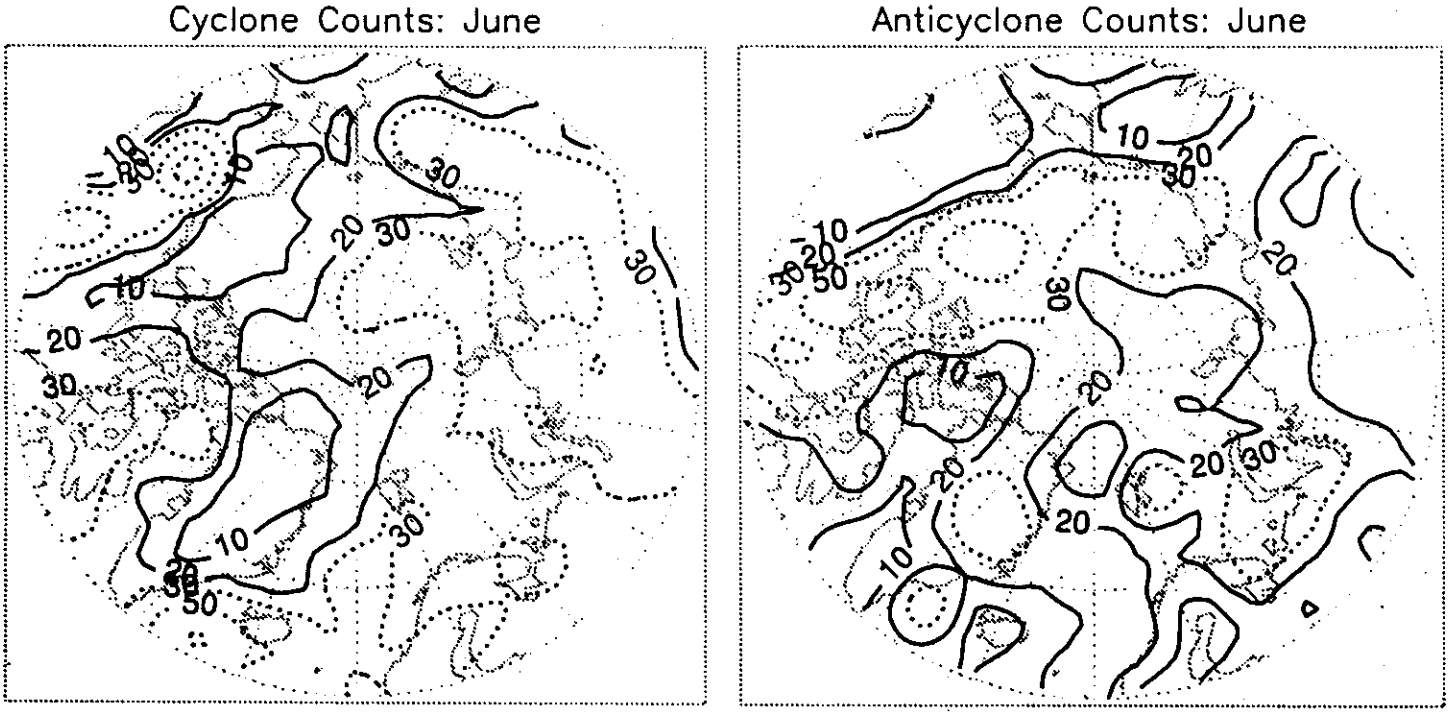

Units: Total Counts
Contours: 0-20 x 10 (solid), 30+ x 20 (dotted)

Figure 1.2.1 (Continued)

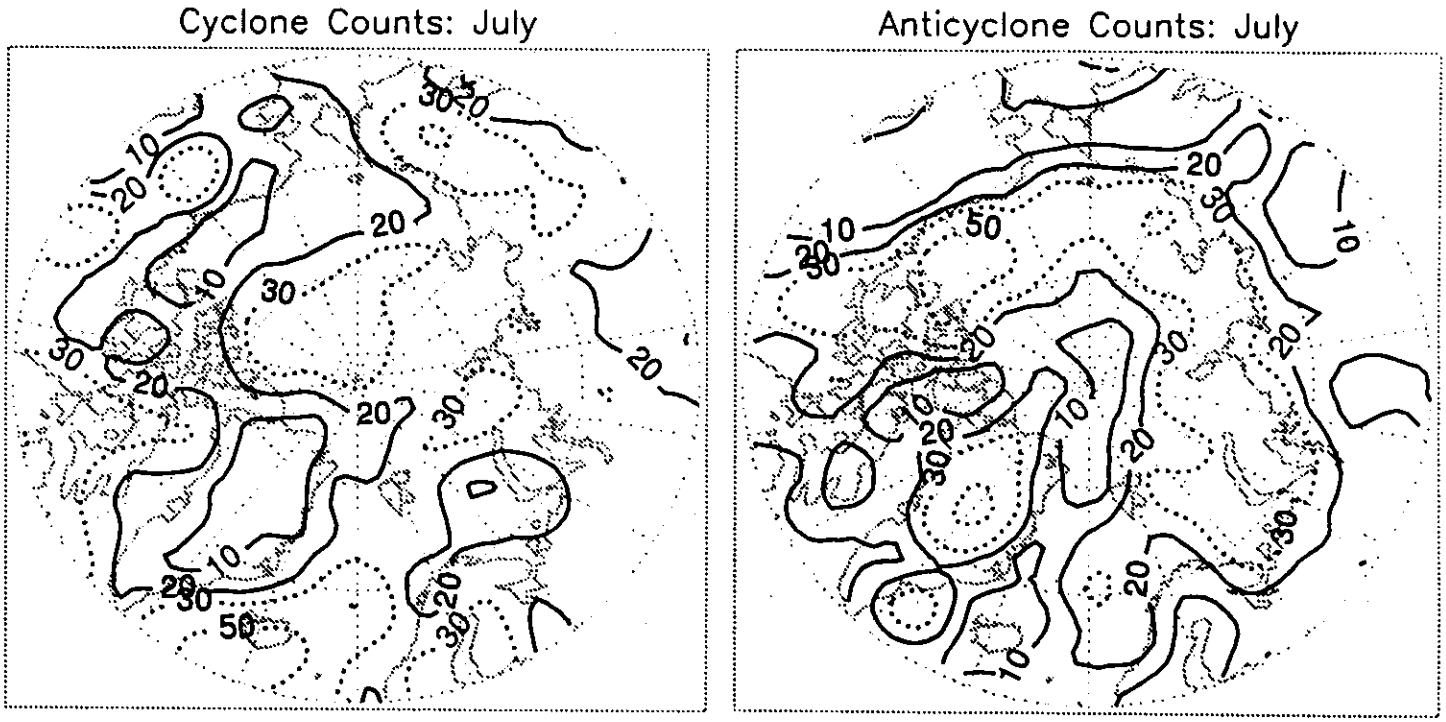

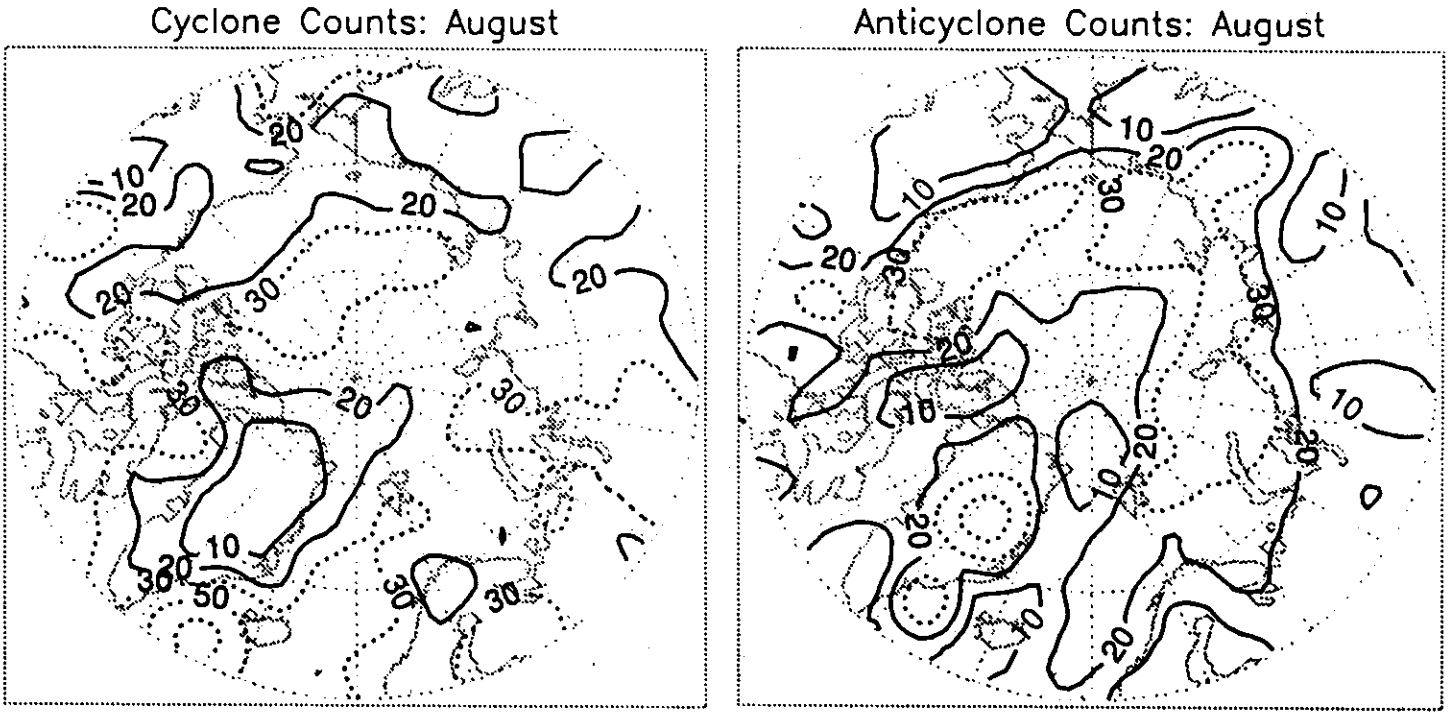

Units: Total Counts
Contours: 0-20 x 10 (solid), 30+ x 20 (dotted)

Figure 1.2.1 (Continued)

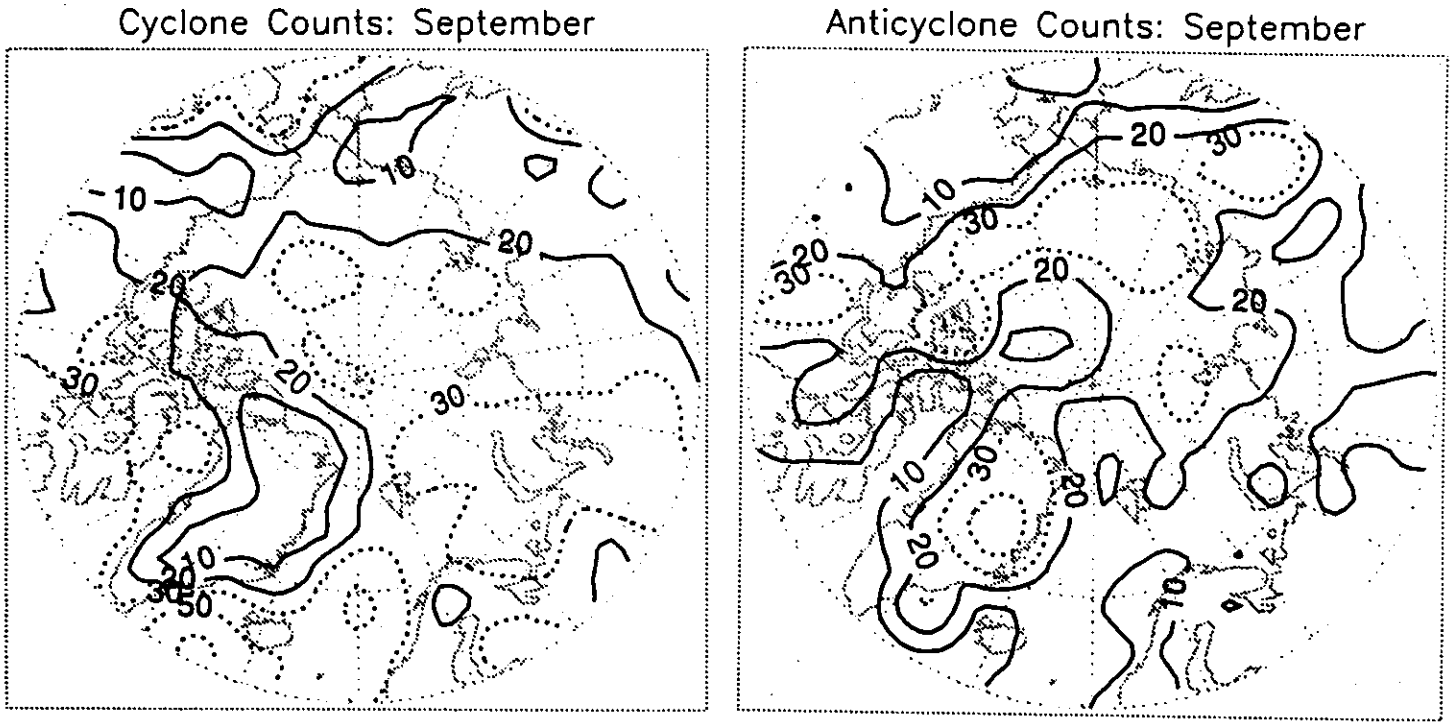

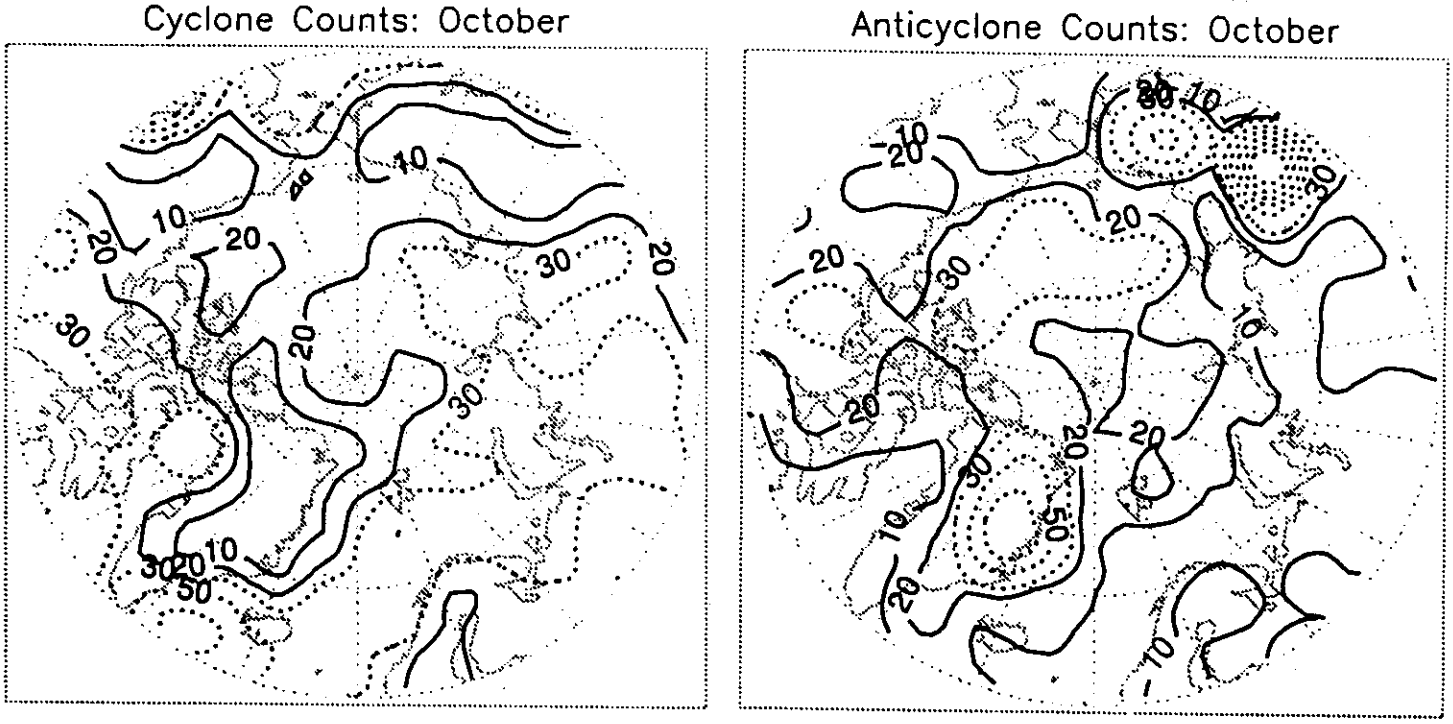

Units: Total Counts
Contours: 0-20 x 10 (solid), 30+ x 20 (dotted)

Figure 1.2.1 (Continued)

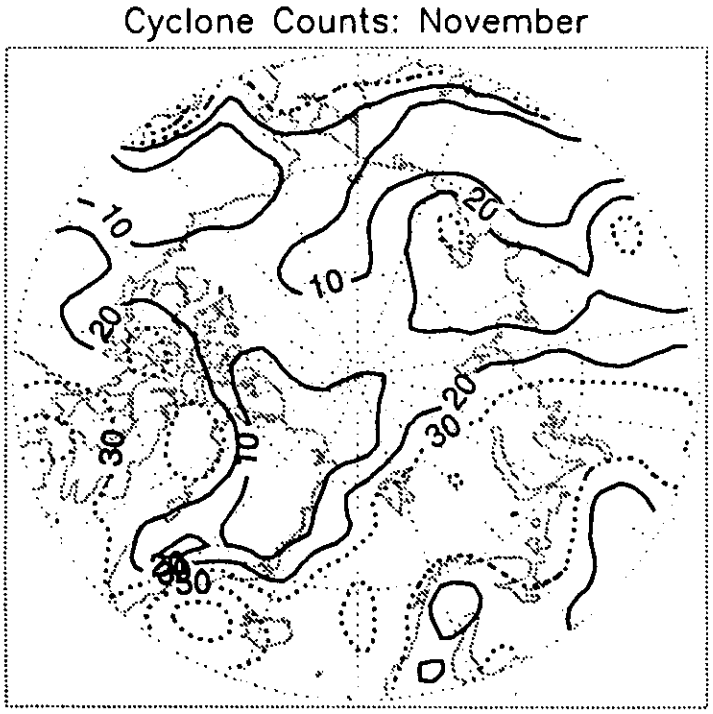

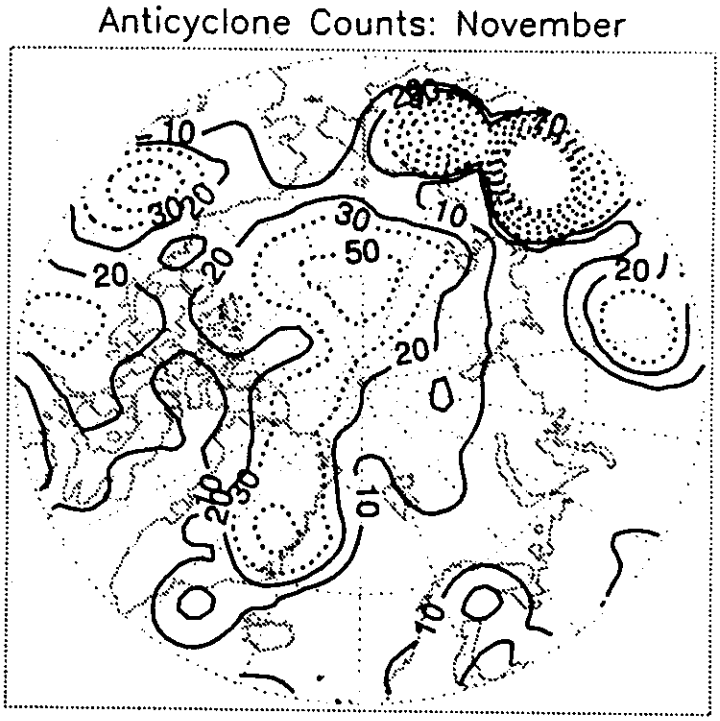

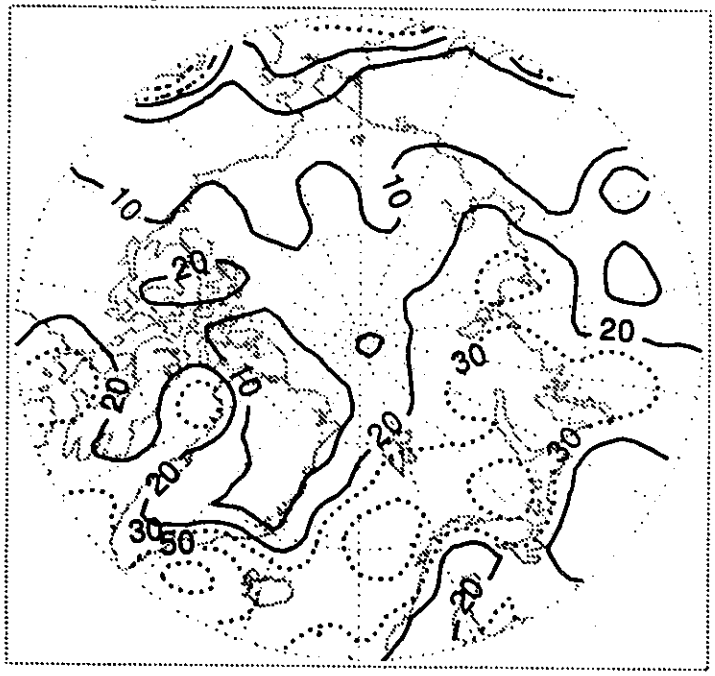

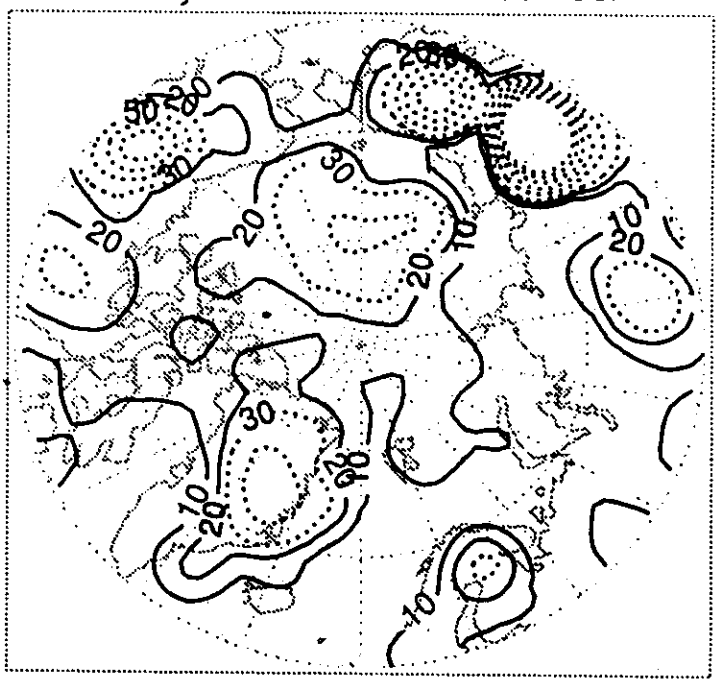

Units: Total Counts
Contours: 0-20 x 10 (solid), 30+ x 20 (dotted)

1.3 Atmospheric Water Vapor and Vertically-Integrated Vapor Fluxes

Serreze et al. [1995] used a Cressman interpolation to provide monthly-mean climatological fields of precipitable water and vertically integrated vapor fluxes for points north of 65°N corresponding to the NCEP Octagonal grid. Input data consisted of rawinsonde ascents through 1991 from land stations, the Russian "North Pole" (NP) series of drifting stations and ships. Integrals were evaluated from the surface to the 300 mb level, above which the amount of water vapor is negligible. That study also provided vertical profiles of specific humidity and temperature at each grid point by interpolating the rawinsonde data to 50 mb levels from the surface to 300 mb. The spatial fields of precipitable water and vertically-integrated fluxes (zonal, meridional and total) have been transformed to the EASE-Grid and are provided in Figure 1.3.1. The mean monthly vertical profiles of specific humidity (Figure 1.3.2) and the seasonal cycle in precipitable water (Figure 1.3.3) which follow are for the original NCEP Octagonal grid point closest to the planned deployment location of the SHEBA camp.

The atmosphere over the Arctic Ocean is extremely dry during the winter months (< 3 mm of precipitable water), with precipitable water increasing towards the North Atlantic. By contrast, precipitable water exhibits a primarily zonal distribution during summer. Winter vapor fluxes over the central Arctic Ocean are accordingly small. However, note the large positive zonal fluxes over the Beaufort Sea from June through August (and to a lesser extent, May). This seems to reflect: 1) a seasonal increase in available water vapor; and 2) transient, relatively strong moisture-bearing westerly winds at lower tropospheric levels, which relate to the summertime increase in cyclone activity north of the Beaufort Sea. Results for the SHEBA region show that water vapor (specific humidity) for the winter months peaks above the surface at the 900-850 mb level, driven by the strong low-level temperature inversion. This feature is less apparent in summer when inversions are weaker and less frequent. This seasonal change in the vertical structure is typical of the central Arctic Ocean. As for all of the Arctic, precipitable water over the Beaufort Sea peaks in July. For the SHEBA region, the mean July value is about 14 mm. This compares to a global annual average of about 24 mm.

Figure 1.3.1

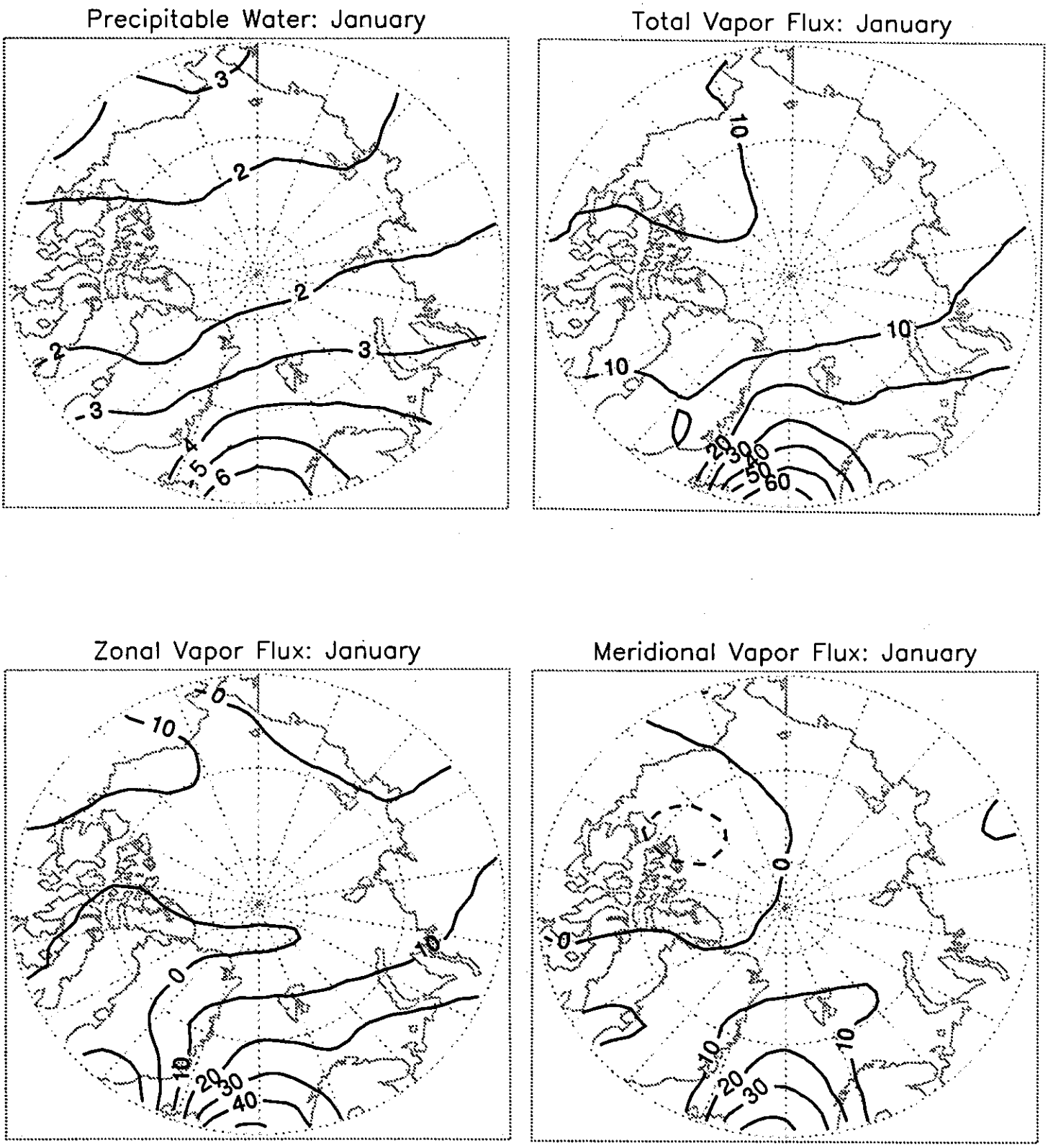

Units for Precipitable Water: Millimeters
Units for Vapor Fluxes: kg s^{-1} m^{-1} (Negative Contours Dashed)

Figure 1.3.1 (Continued)

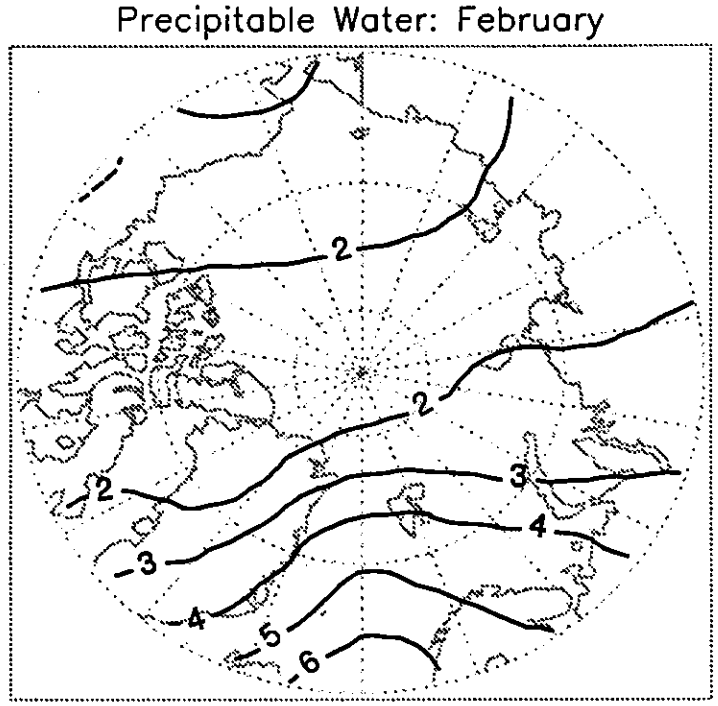

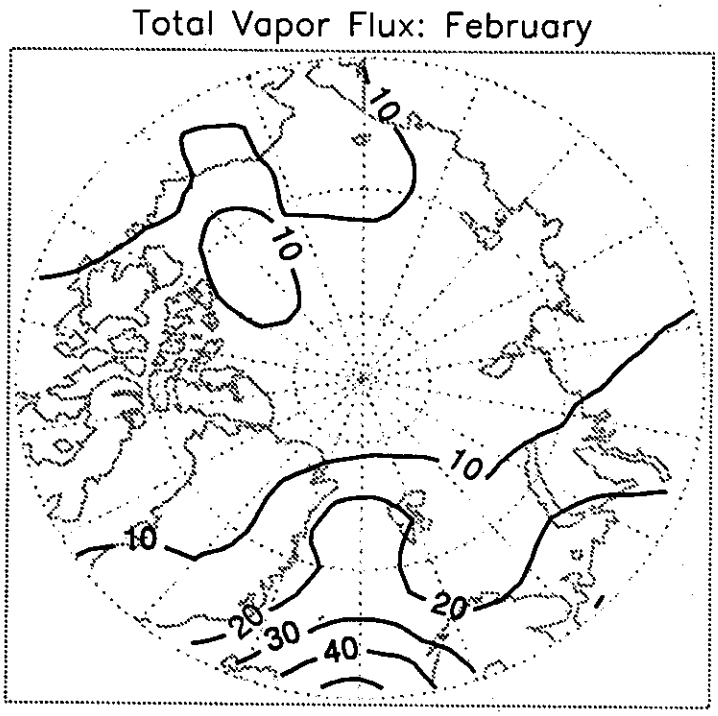

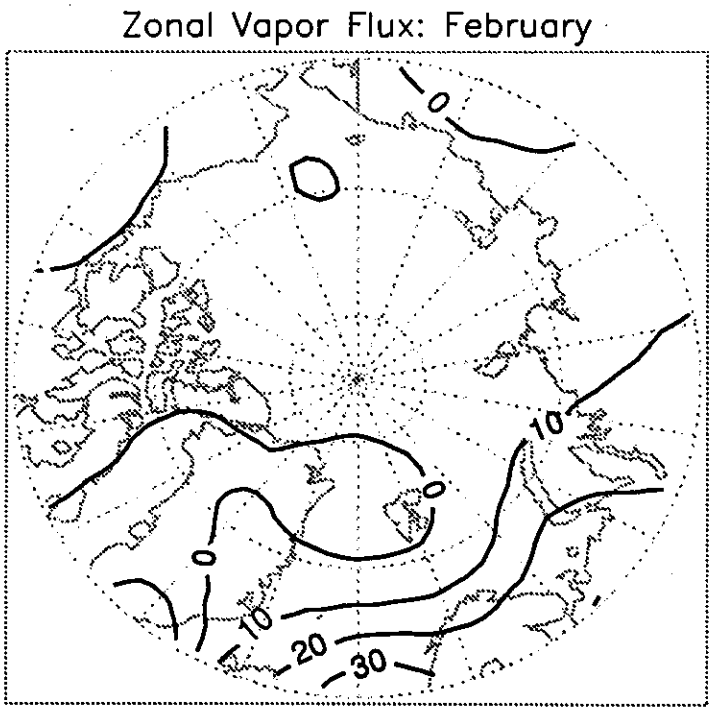

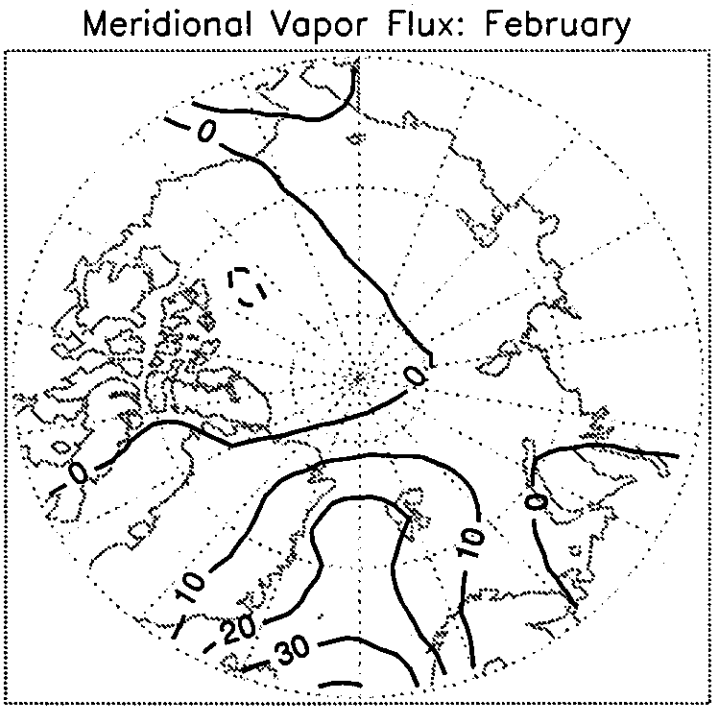

Units for Precipitable Water: Millimeters
Units for Vapor Fluxes: kg s^{-1} m^{-1} (Negative Contours Dashed)

Figure 1.3.1 (Continued)

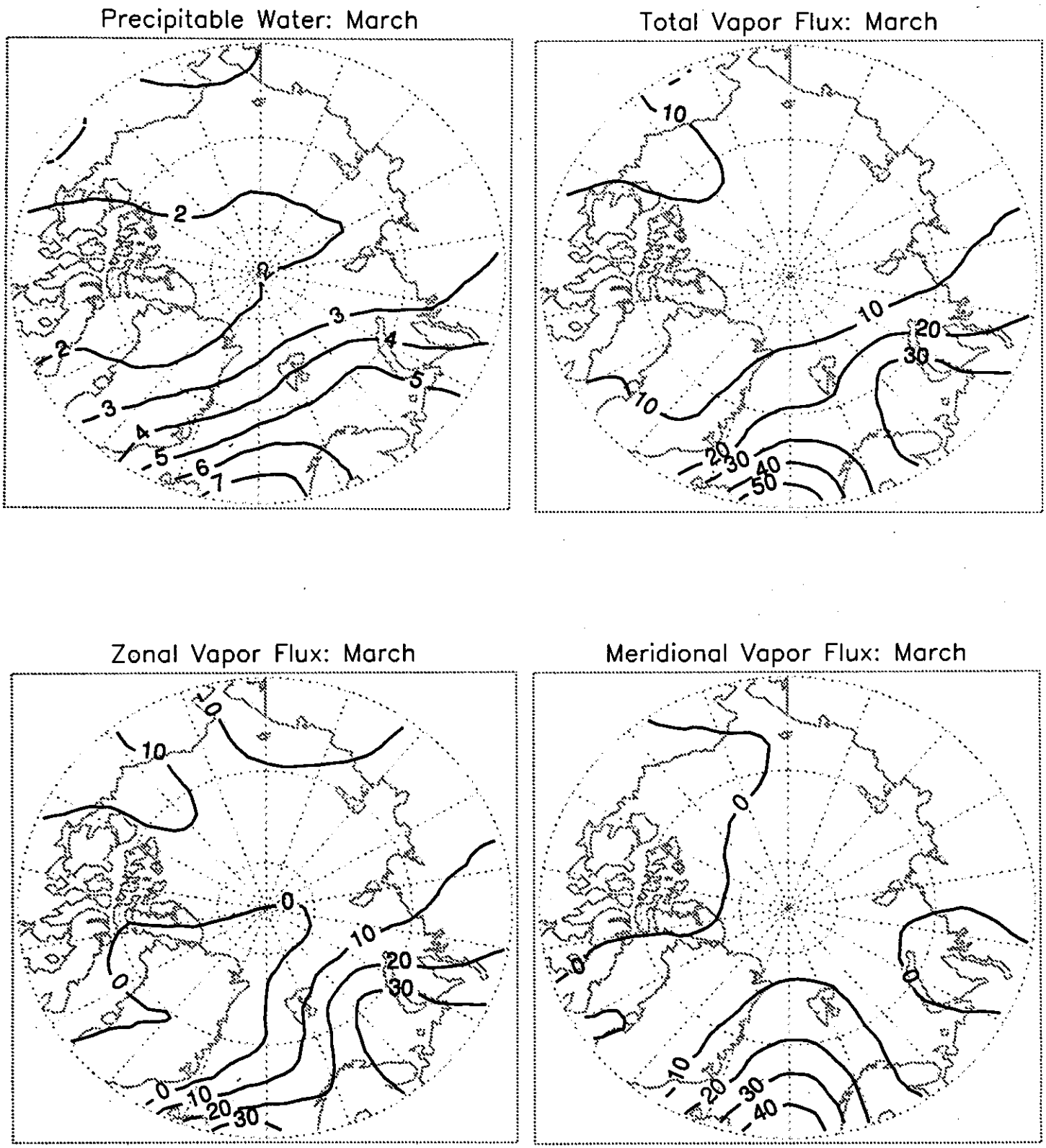

Units for Precipitable Water: Millimeters
Units for Vapor Fluxes: kg s^{-1} m^{-1} (Negative Contours Dashed)

Figure 1.3.1 (Continued)

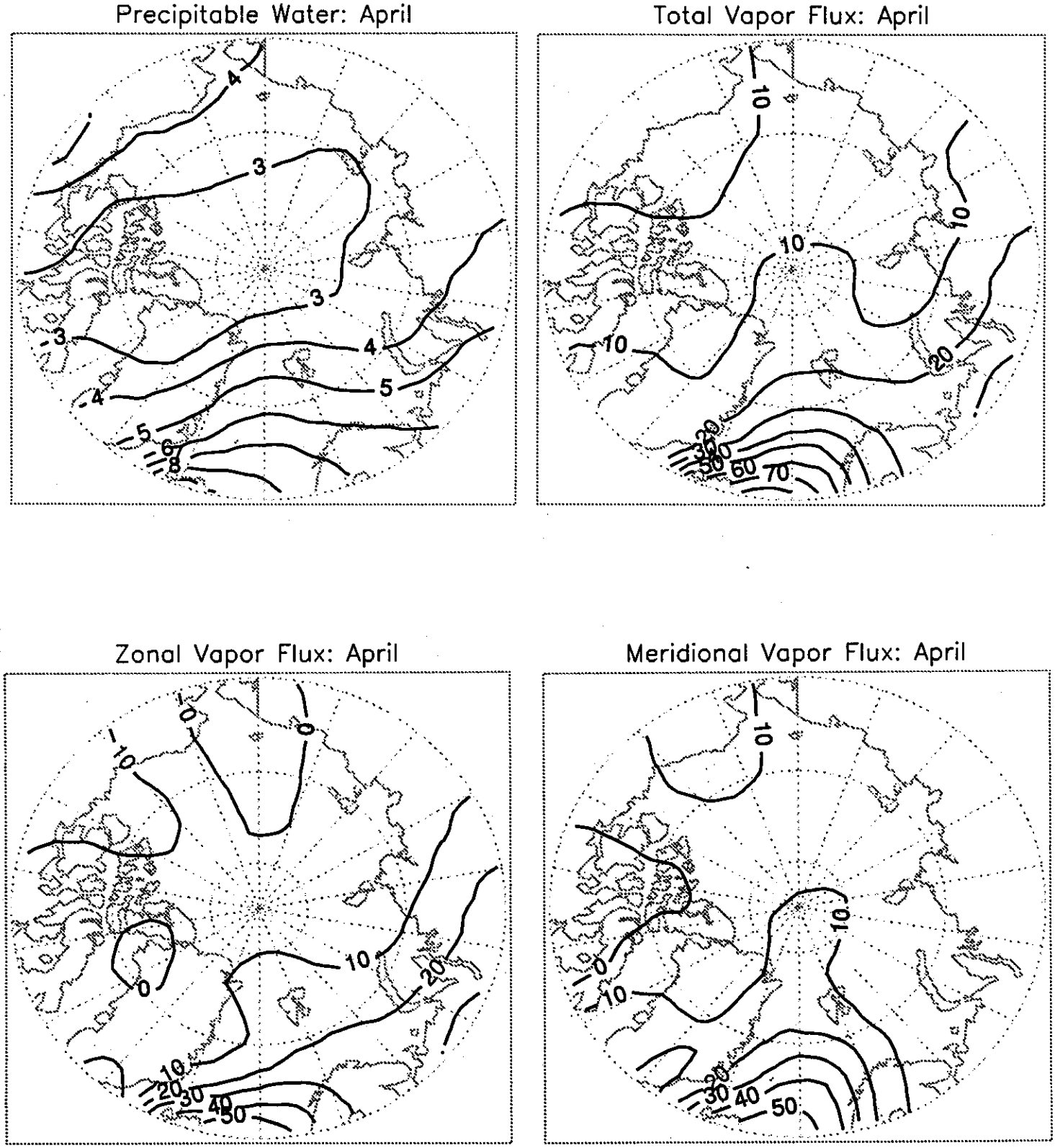

Units for Precipitable Water: Millimeters
Units for Vapor Fluxes: kg s^{-1} m^{-1} (Negative Contours Dashed)

Figure 1.3.1 (Continued)

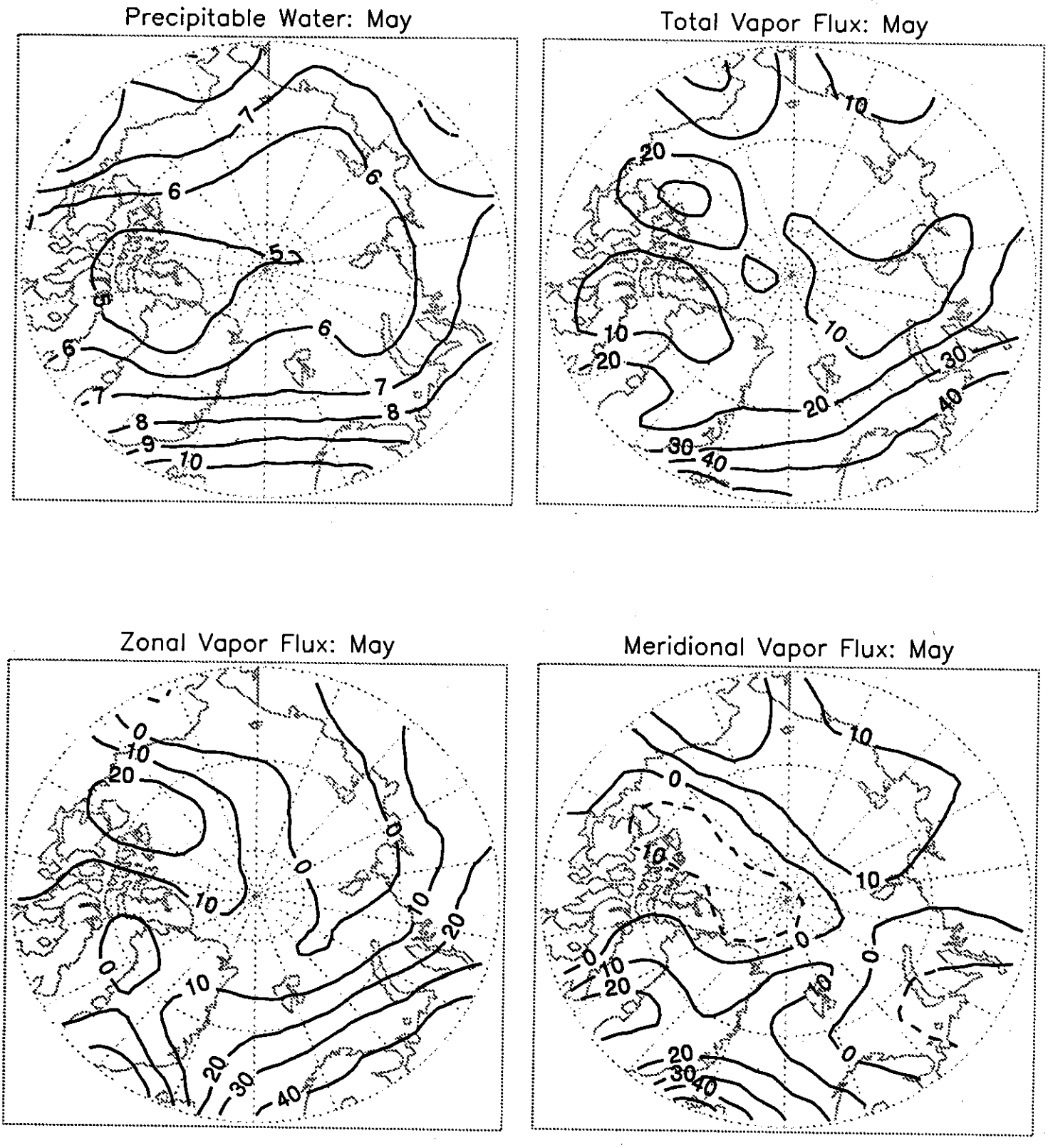

Units for Precipitable Water: Millimeters
Units for Vapor Fluxes: kg s^{-1} m^{-1} (Negative Contours Dashed)

Figure 1.3.1 (Continued)

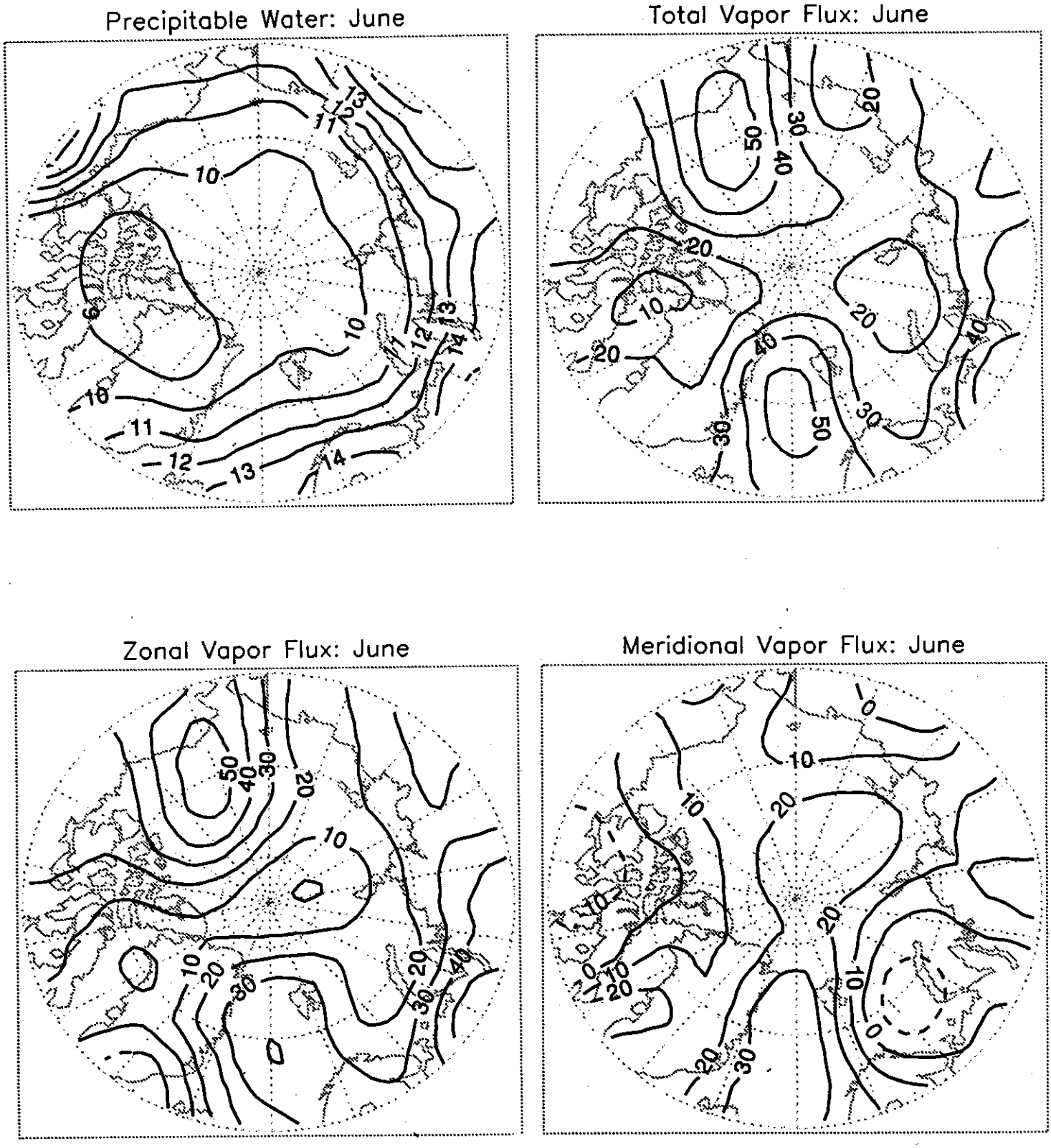

Units for Precipitable Water: Millimeters
Units for Vapor Fluxes: kg s^{-1} m^{-1} (Negative Contours Dashed)

Figure 1.3.1 (Continued)

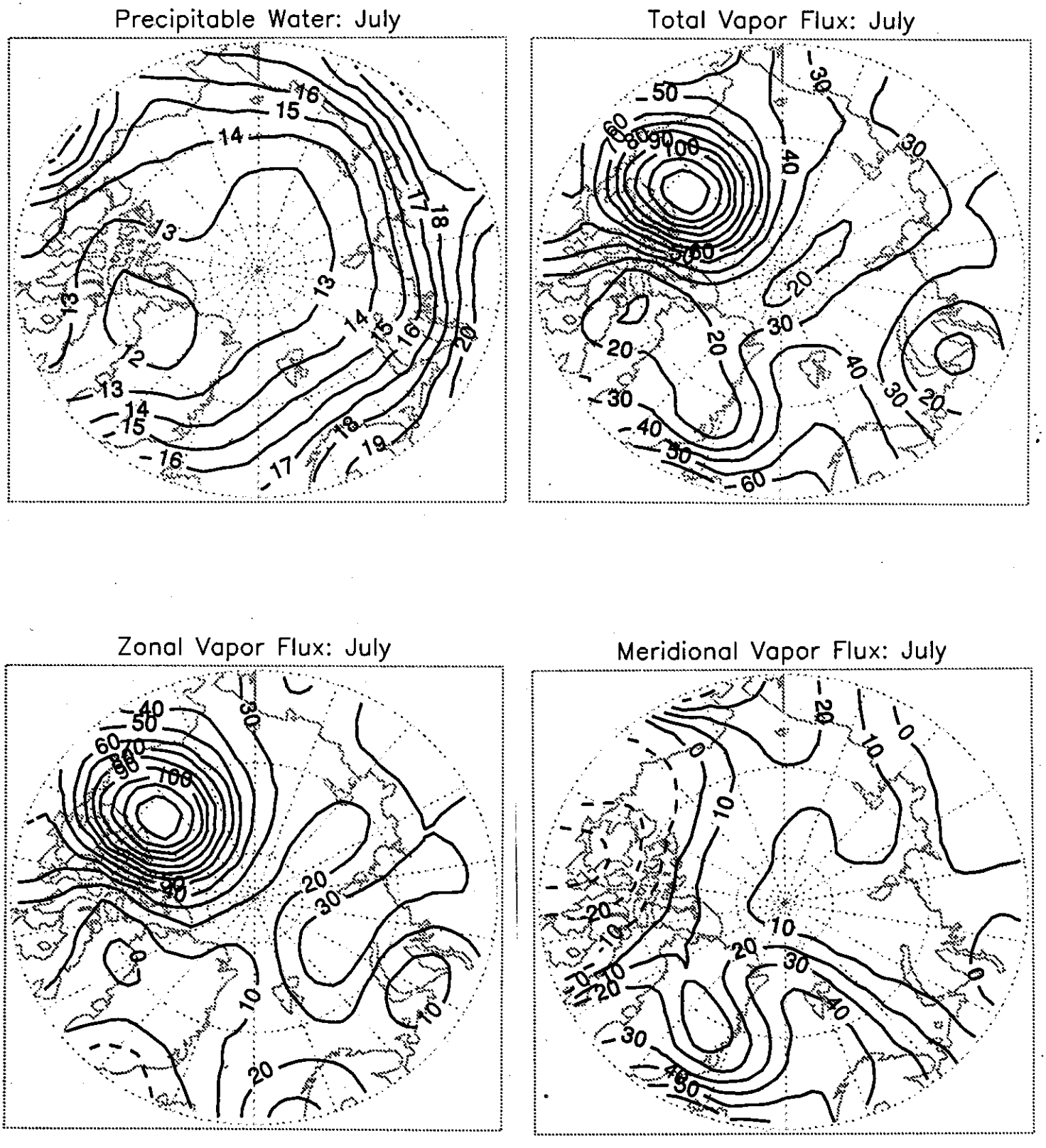

Units for Precipitable Water: Millimeters
Units for Vapor Fluxes: kg s^{-1} m^{-1} (Negative Contours Dashed)

Figure 1.3.1 (Continued)

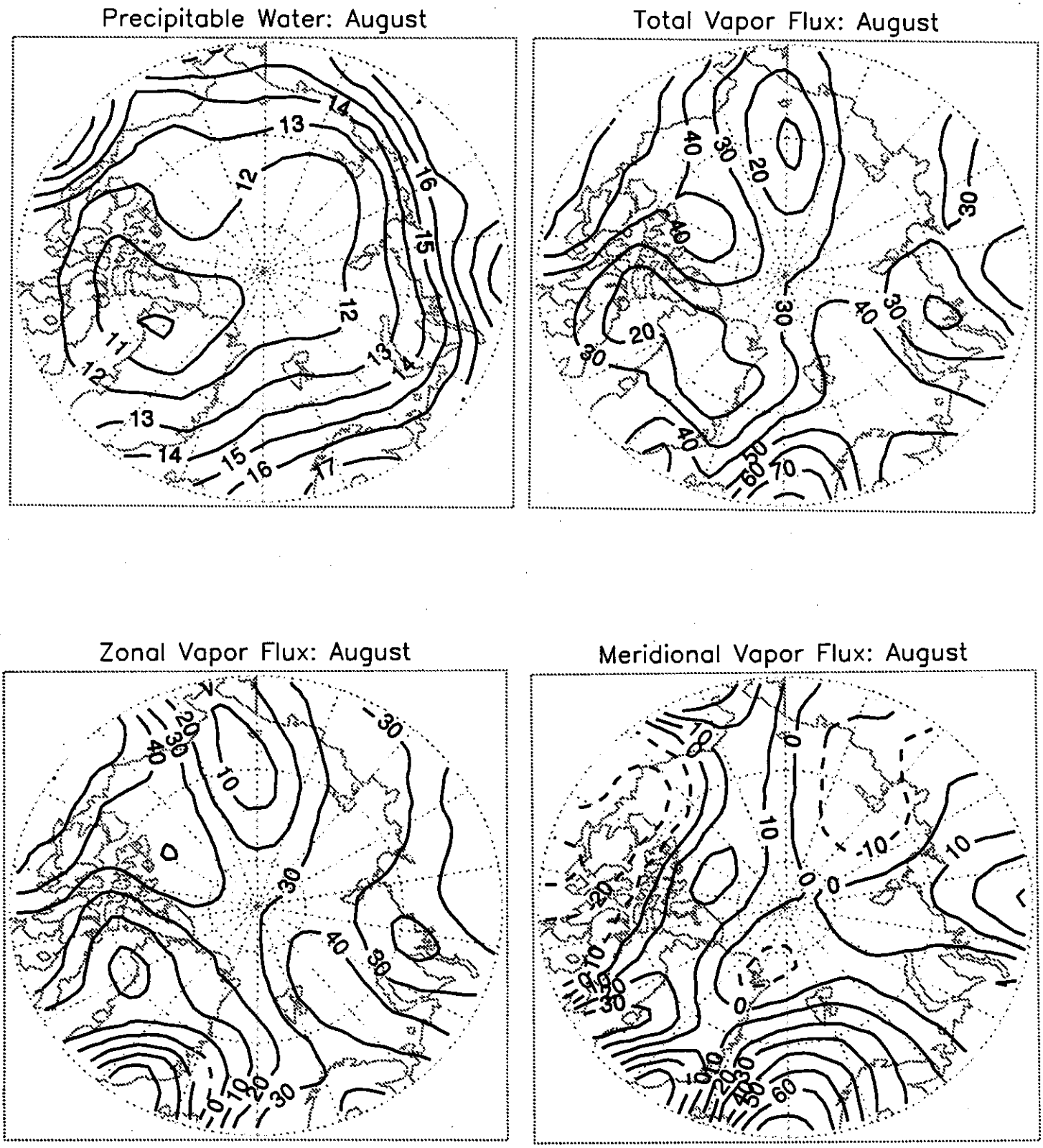

Units for Precipitable Water: Millimeters
Units for Vapor Fluxes: kg s^{-1} m^{-1} (Negative Contours Dashed)

Figure 1.3.1 (Continued)

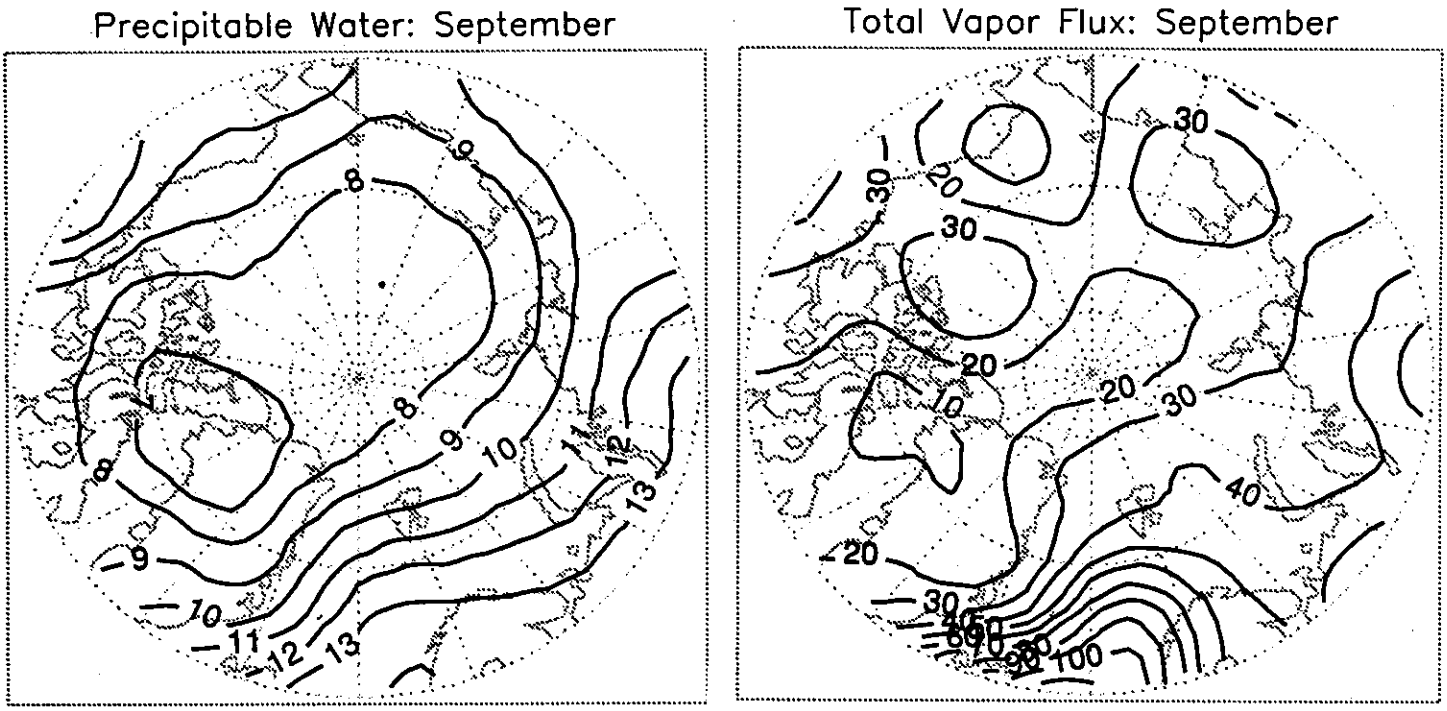

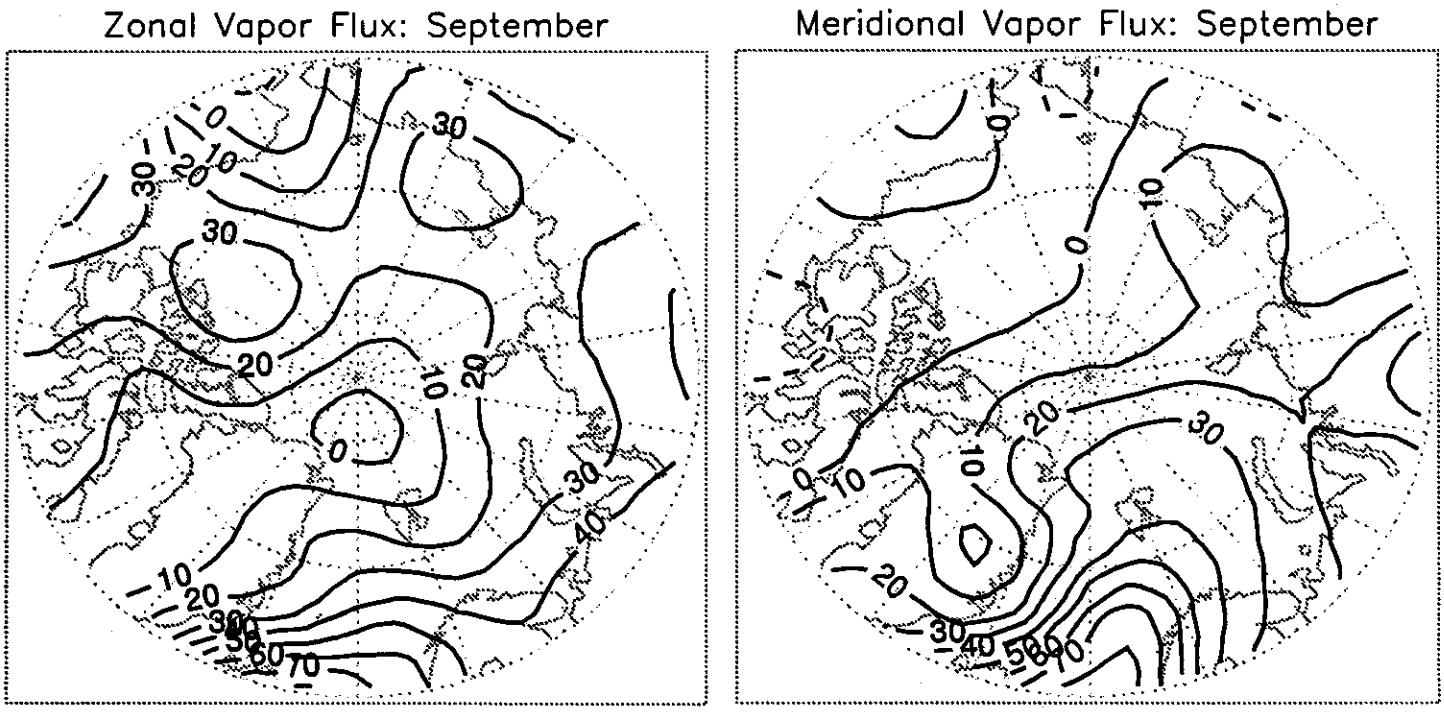

Units for Precipitable Water: Millimeters
Units for Vapor Fluxes: kg s^{-1} m^{-1} (Negative Contours Dashed)

Figure 1.3.1 (Continued)

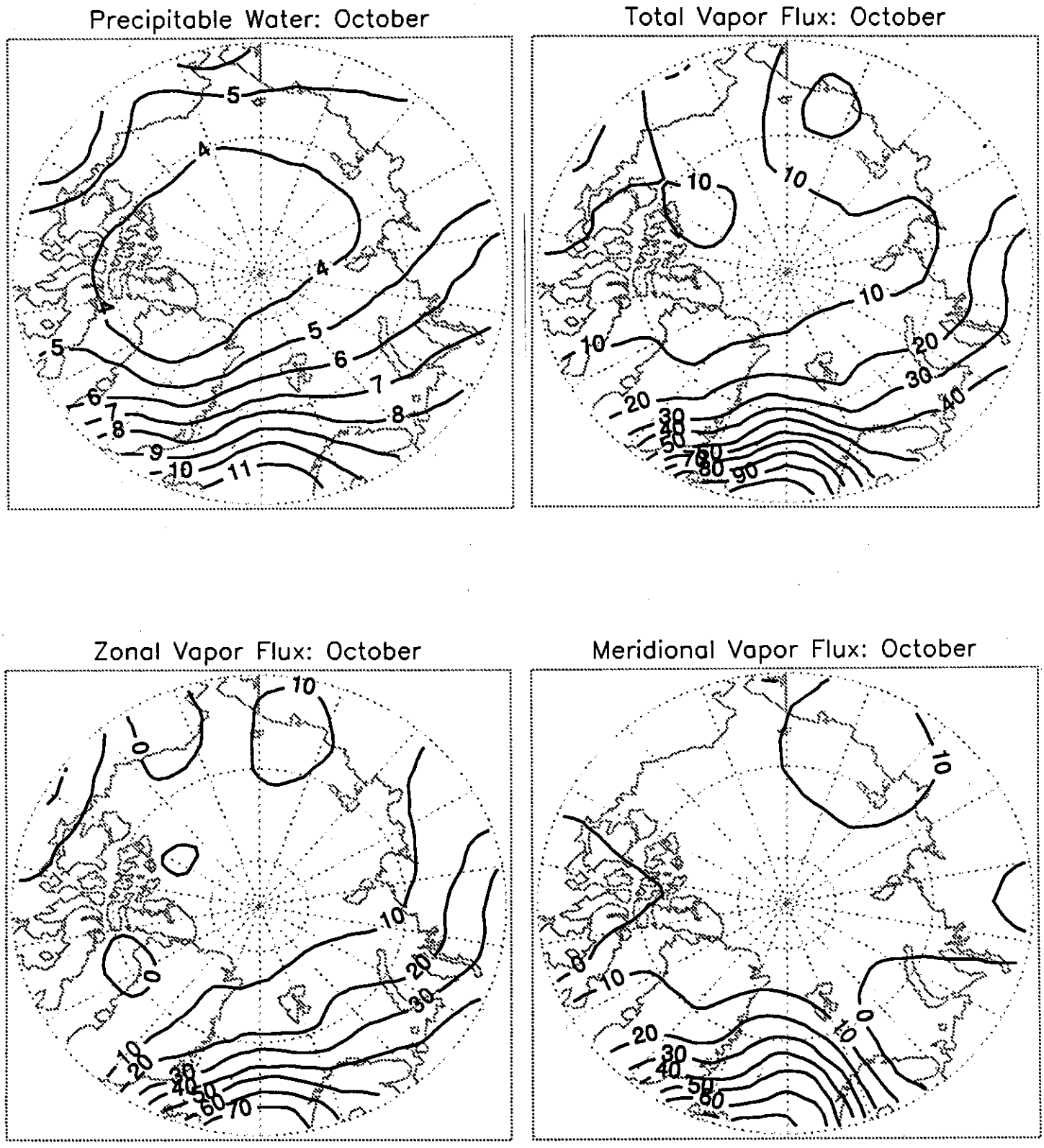

Units for Precipitable Water: Millimeters
Units for Vapor Fluxes: kg s^{-1} m^{-1} (Negative Contours Dashed)

Figure 1.3.1 (Continued)

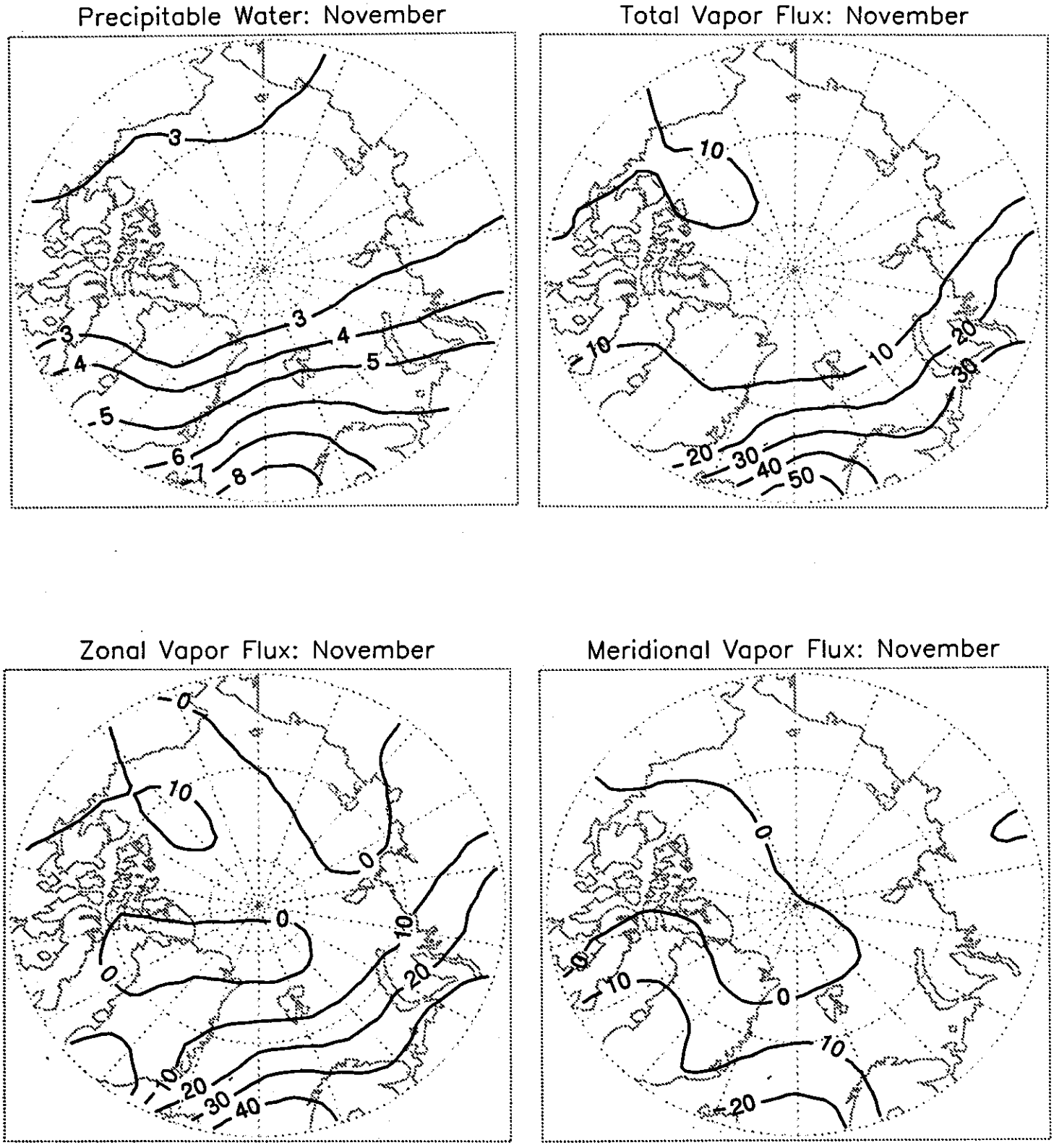

Units for Precipitable Water: Millimeters
Units for Vapor Fluxes: kg s^{-1} m^{-1} (Negative Contours Dashed)

Figure 1.3.1 (Continued)

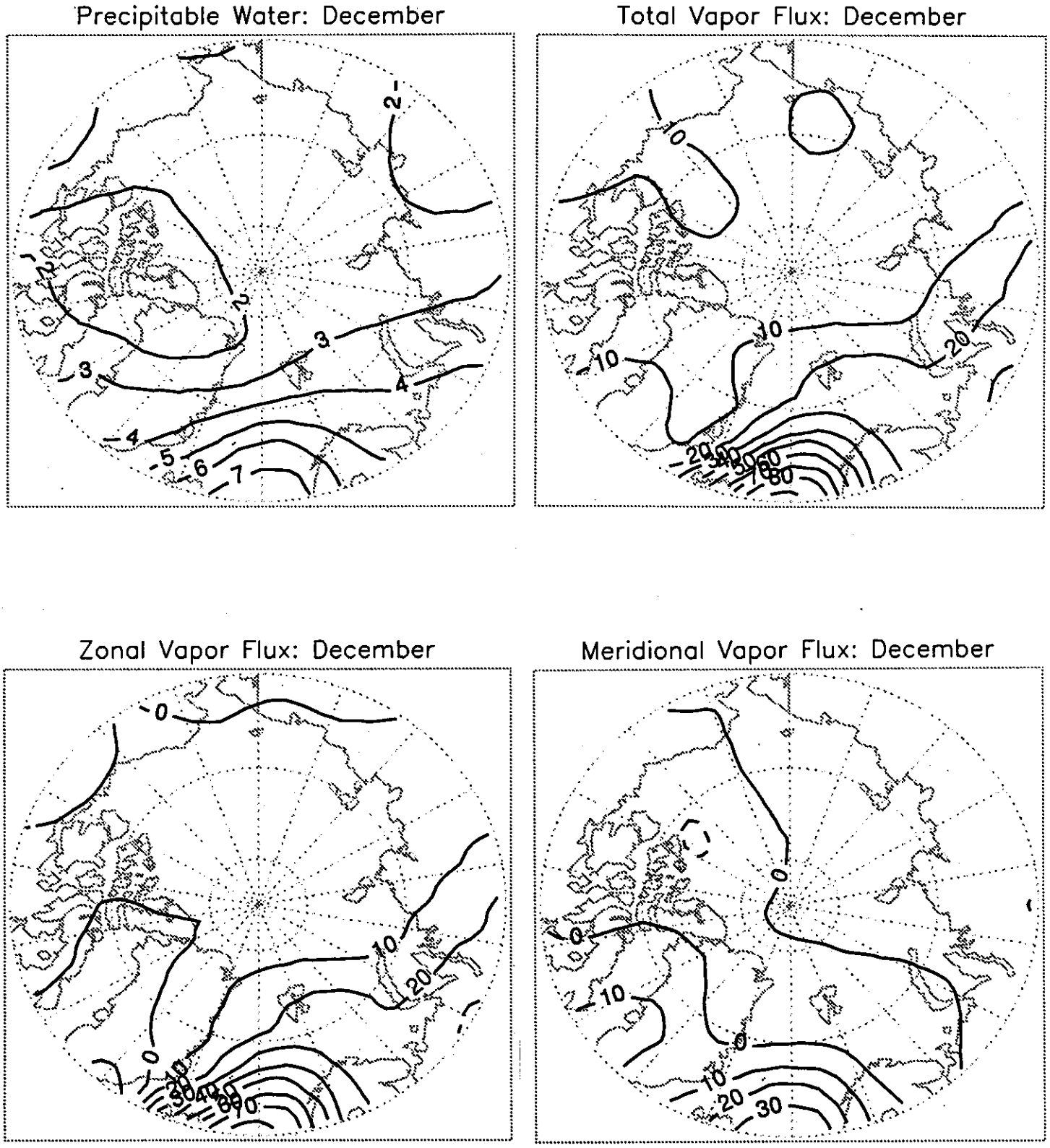

Units for Precipitable Water: Millimeters
Units for Vapor Fluxes: kg s^{-1} m-1 (Negative Contours Dashed)

Figure 1.3.2

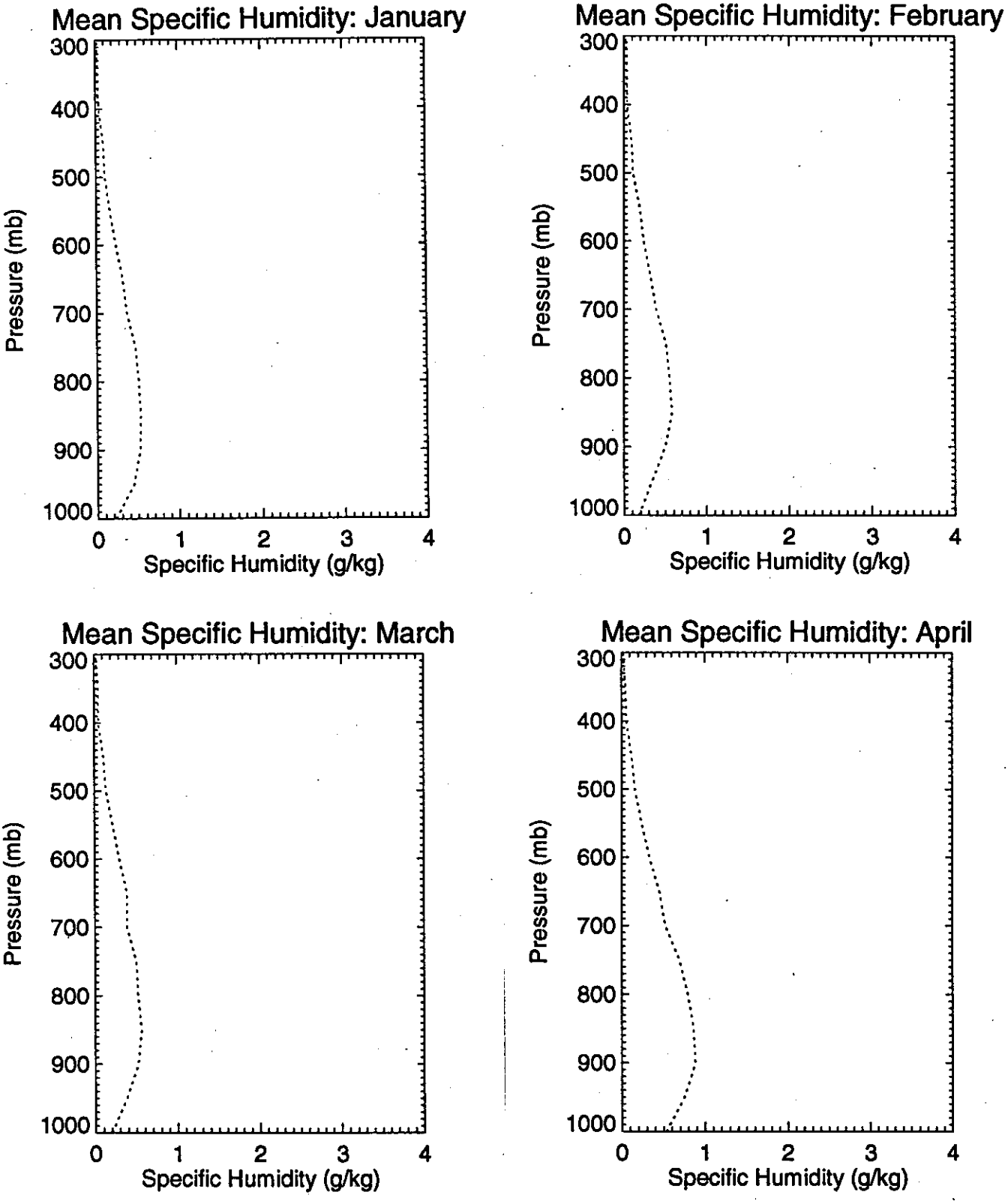
Mean Specific Humidity: January
Mean Specific Humidity: February
Mean Specific Humidity: March
Mean Specific Humidity: April
Pressure (mb)
300
400
500
600
700
800
900
1000
0
1
2
3
4
Specific Humidity (g/kg)

Figure 1.3.2 (Continued)

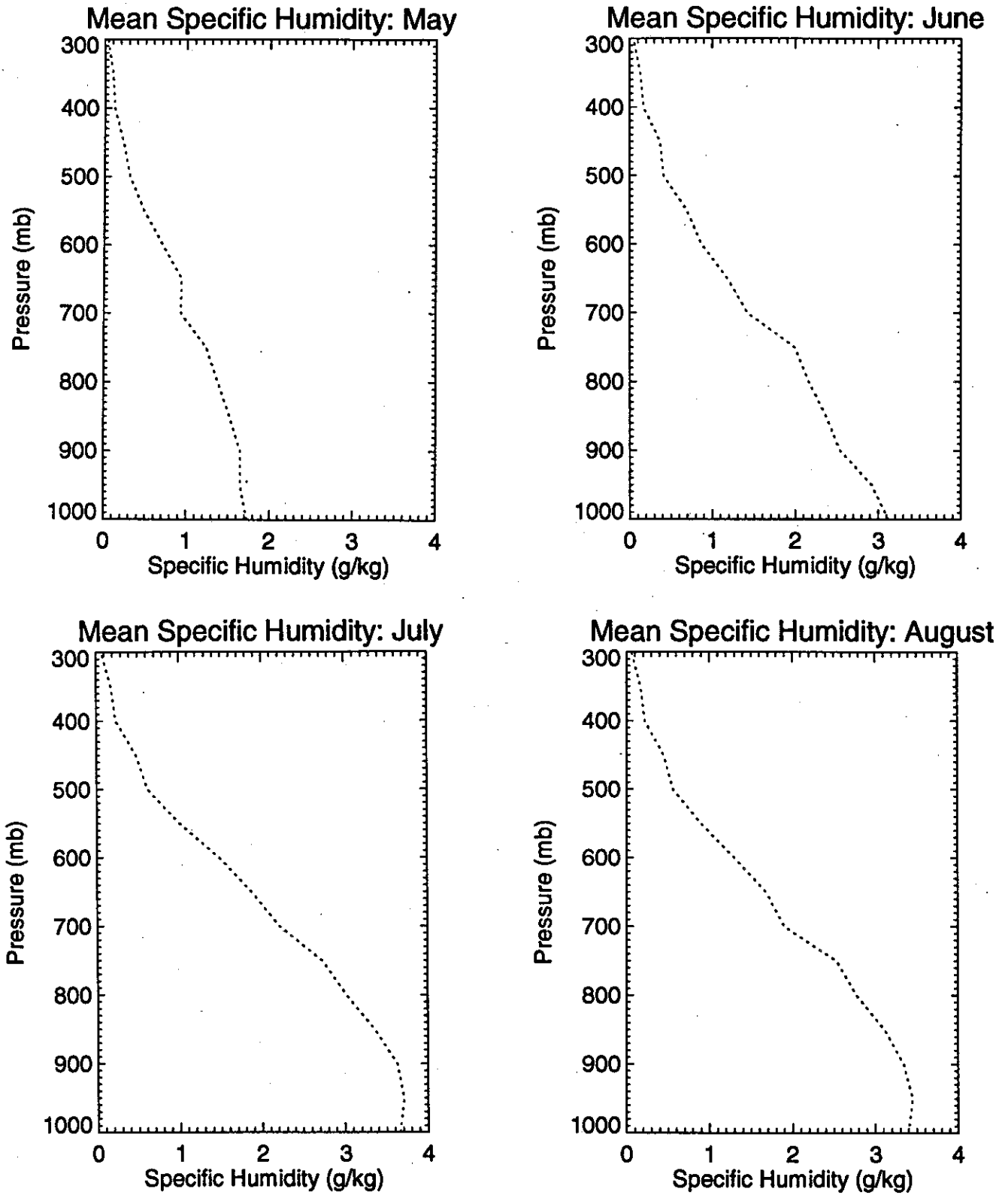

Figure 1.3.2 (Continued)

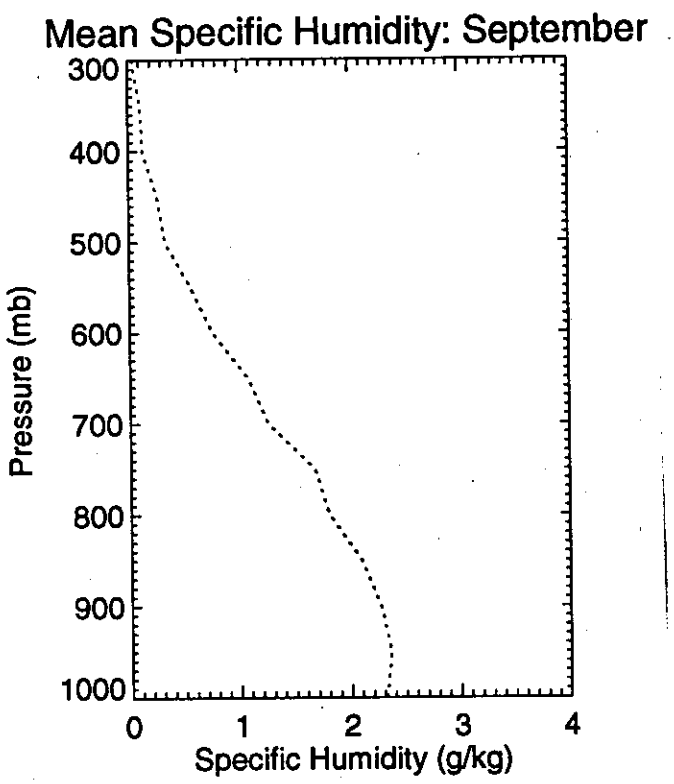

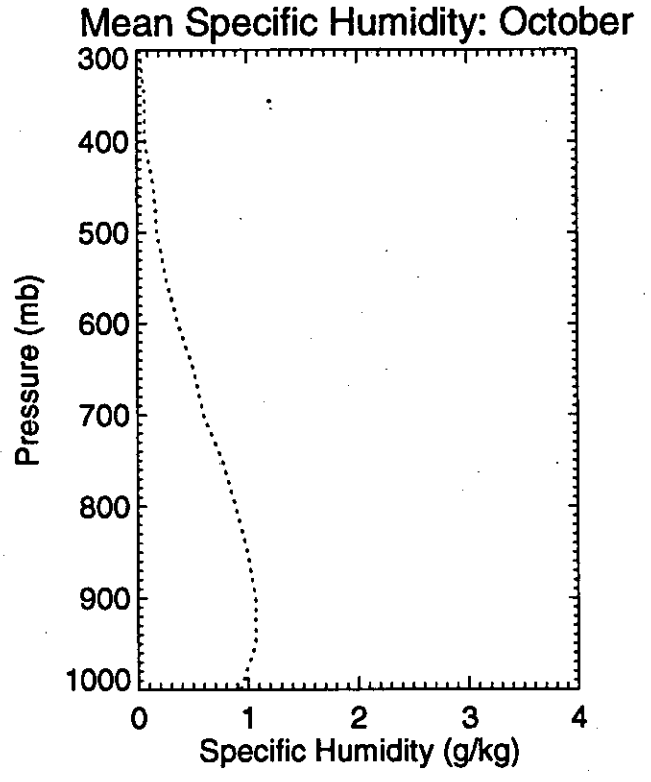

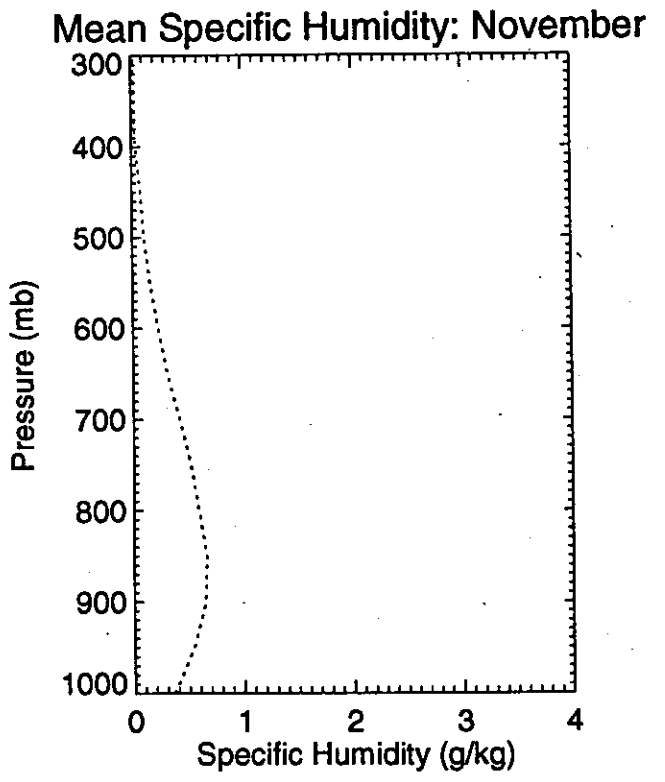

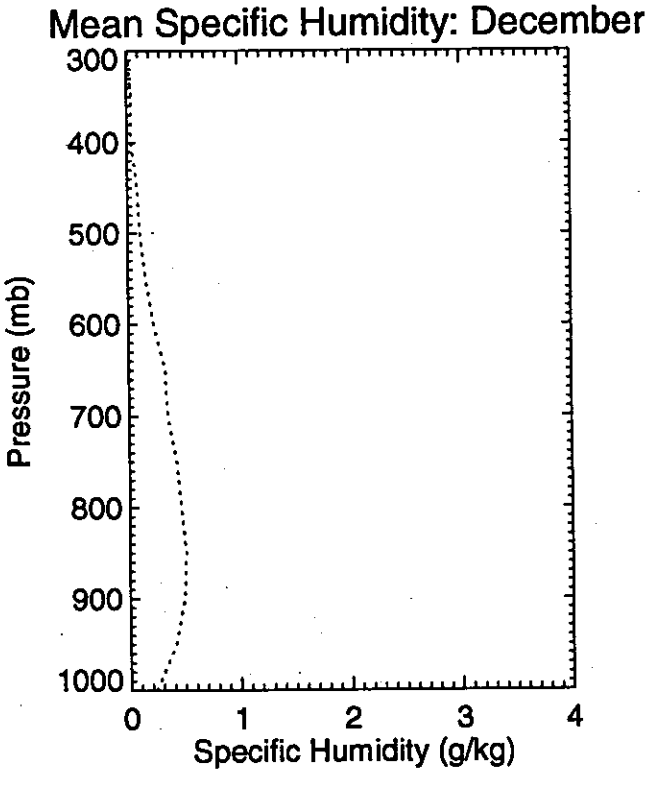

Figure 1.3.3

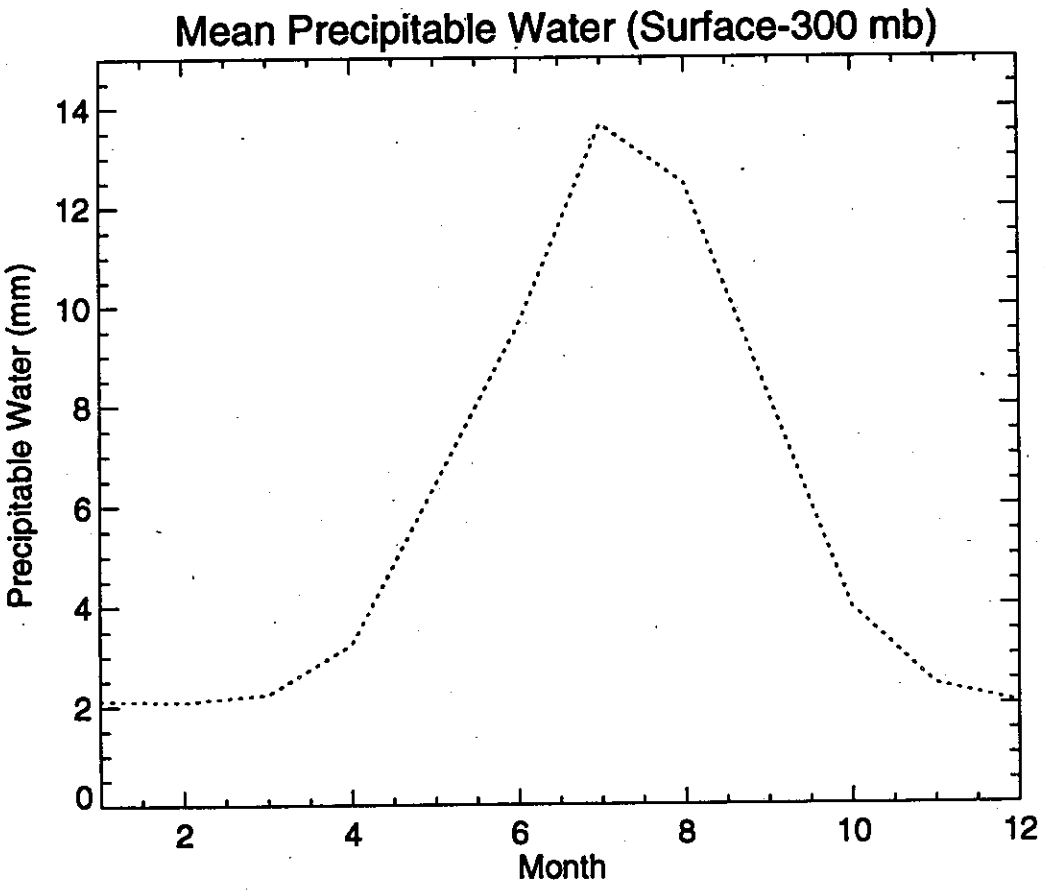
Mean Precipitable Water (Surface-300 mb)
Precipitable Water (mm)
0
2
4
6
8
10
12
14
2
4
6
8
10
12
Month

1.4 COADS Cloud Cover

Mean monthly total cloud cover and low cloud cover (% of the celestial dome covered by cloud and by low cloud, also termed cloud fraction) for the Arctic Ocean (Figure 1.4.1) were analyzed using surface meteorological reports from ships, the Russian NP series of drifting ice station and any other sources (e.g., from field experiments) for the period 1950-1995 contained in the Comprehensive Ocean Atmosphere Data Set (COADS) [Woodruff et al., 1987]. The NP program terminated in 1991. These represent visual observations. Low cloud amount represents the fraction of the celestial dome cloud covered by the lowest reported cloud level. Hahn et al. [1995] discuss potential biases in these data during polar darkness. Observations are summarized for a coarse subset of points from the EASE-Grid. Using a drop-in-the-bucket approach, we assigned any observation within a 600 km radius of each of the grid points to the respective point. We required that the means be based on at least 150 observations, otherwise the grid point value is treated as missing (blank values on the maps). The limitation of the data to marine regions and occasional missing grid values presented difficulties in producing computer-generated isoline maps. Consequently, we display results as character plots. Our analysis procedure is essentially identical to that of Clark et al. [1996] who evaluated Arctic cloud cover, precipitation frequency and temperature characteristics using a shorter COADS record (1980-1993) evaluated over a coarser grid and with a larger search radius. Warren et al. [1988] also provide COADS-derived Arctic Ocean cloud assessments as part of their larger global ocean archive.

Previous surface-based climatologies for the Arctic [Huschke, 1969; Warren et al., 1986; 1988] depict total cloud cover during the winter half of the year ranging from 40-70%. The highest amounts are found over the Atlantic side of the Arctic Ocean where cyclone activity associated with the primary North Atlantic cyclone track is frequent and water vapor is relatively abundant. Cloud cover is typically more limited over land, the sea ice cover and the central Arctic Ocean in particular, where water vapor is less abundant, the boundary layer is more stable, and anticyclonic conditions are common [Shine et al., 1984; Serreze et al., 1993]. Total cloud fractions rise to 70-90% in summer with a rapid increase between April and May, characterized by extensive low-level stratus over the ocean. Summer cloud cover also tends to be more spatially homogeneous.

Our monthly Arctic Ocean climatology shows these patterns. Note in particular the sharp increase between April and May in both total cloud cover and low cloud cover. For most months and especially summer, total cloud cover over the southern Beaufort Sea remains noticeably limited as compared with the rest of the ice-covered ocean. Few moisture-bearing cyclones are found in this area during winter (Section 1.2), reflected in the low values of precipitable water (Section 1.3). In turn, this regional summer minimum is consistent with the SLP distribution (Section 1.1), which shows anticyclonic conditions persisting in this area and a local summer maximum in the distribution of anticyclone centers. On the other hand, this area also shows high zonal vapor fluxes during summer. This Beaufort Sea summer cloud minimum is also evident in the regional analysis by Serreze and Rehder [1990] for June, the July results from the combined Warren et al. [1986, 1988] land and ocean climatologies examined by Schweiger and Key [1994] and the warm and cold season analyses of Clark et al. [1996]

The SHEBA site appears to be at the northern edge of this southern Beaufort Sea cloud minimum. Winter total and low cloud cover at the SHEBA site (Figure 1.4.2) are 55-75% and 35-45%, respectively (depending on the month), climbing to 75-85% and 60-75%, respectively, for summer. The low cloud fraction in particular climbs sharply between April and May, dropping less sharply between September and November. Figure 1.4.3 provides histograms of the frequency of cloud for the SHEBA region based on the individual (daily) COADS records for each month. Here, we use the octal classes originally provided in the COADS archive, which range from 0 (clear) to 8 (overcast). For all months, the most commonly reported condition is overcast skies. One can see clearly the sharp rise in the frequency of overcast skies between April and May. The frequency of clear skies is highest for March (21%) and lowest for September (2%).

Figure 1.4.1

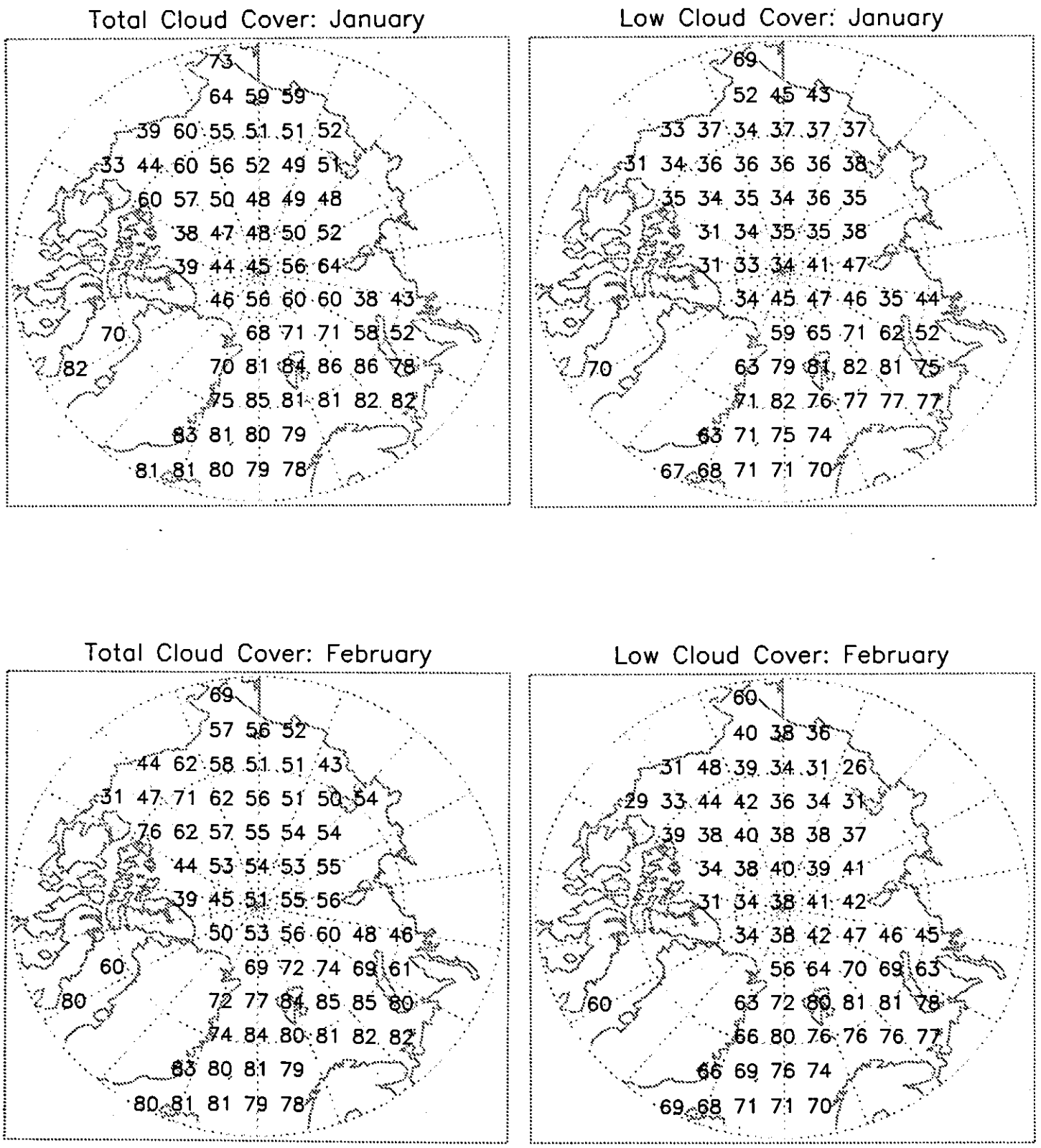

Units: %

Figure 1.4.1 (Continued)

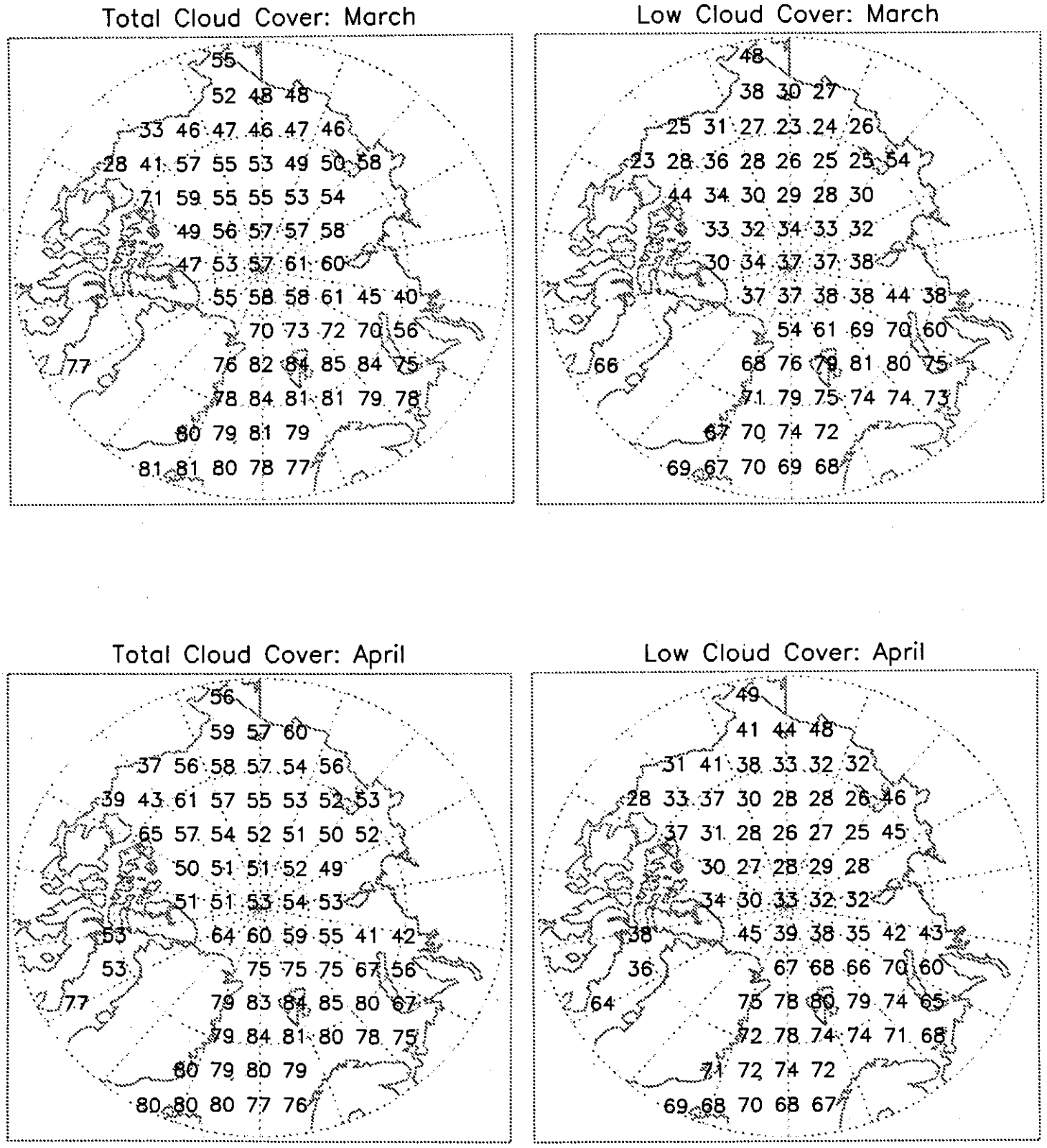

Units: %

Figure 1.4.1 (Continued)

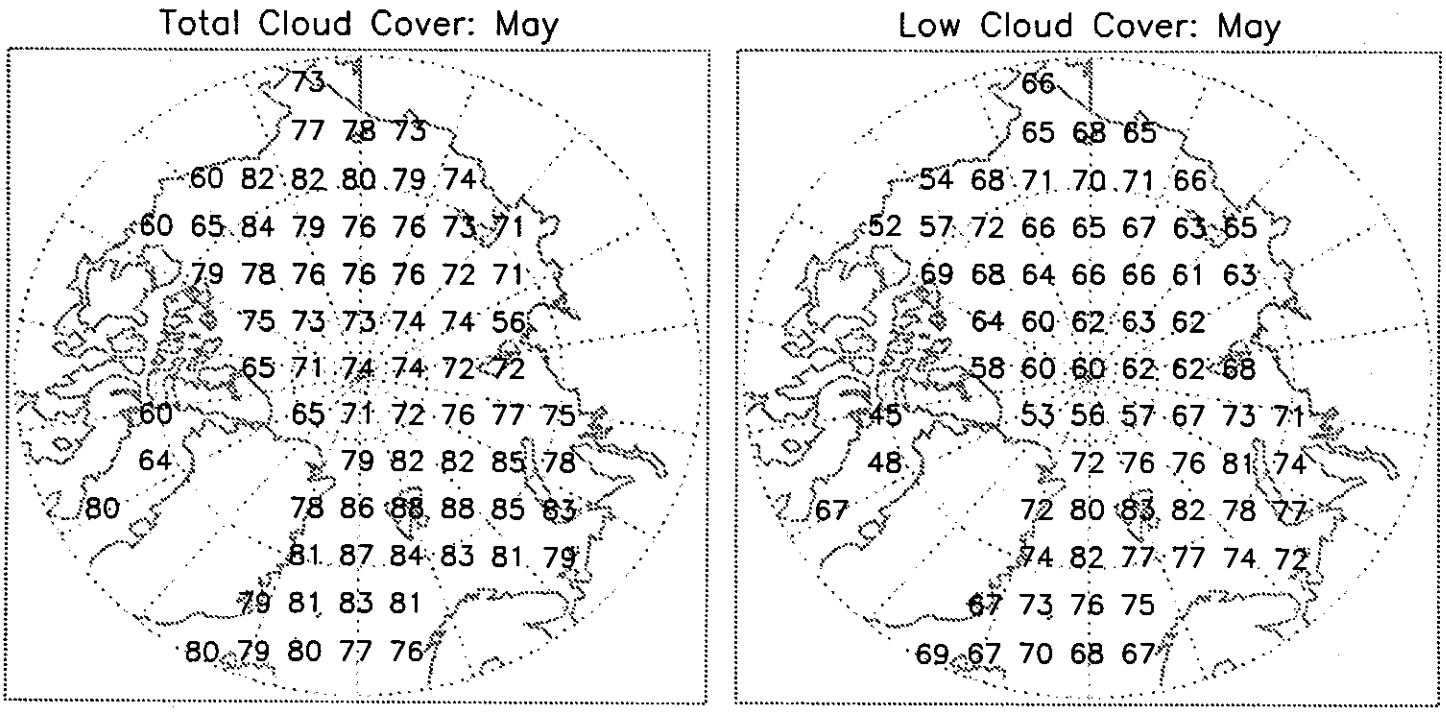

Units: %

Figure 1.4.1 (Continued)

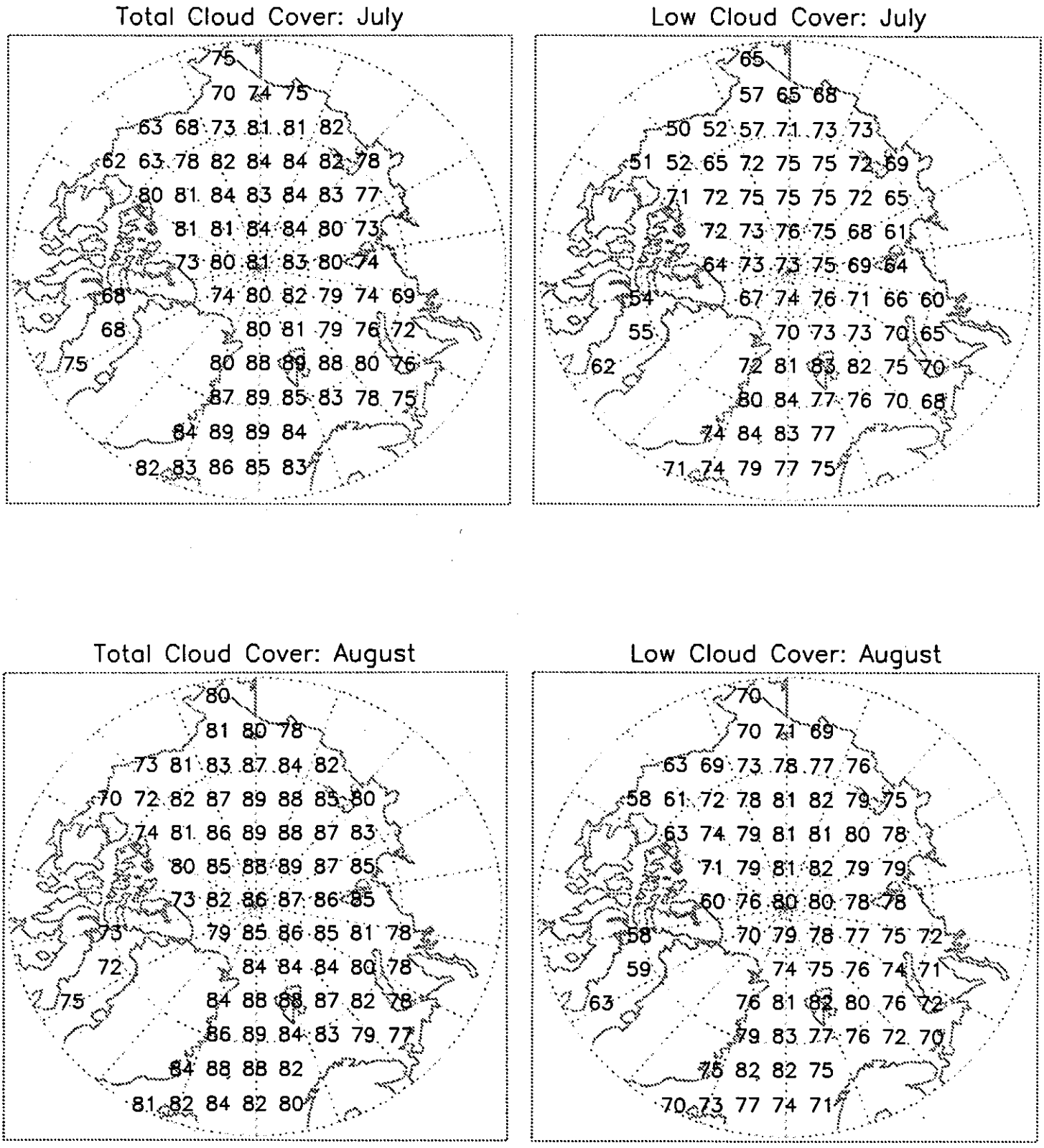

Units: %

Figure 1.4.1 (Continued)

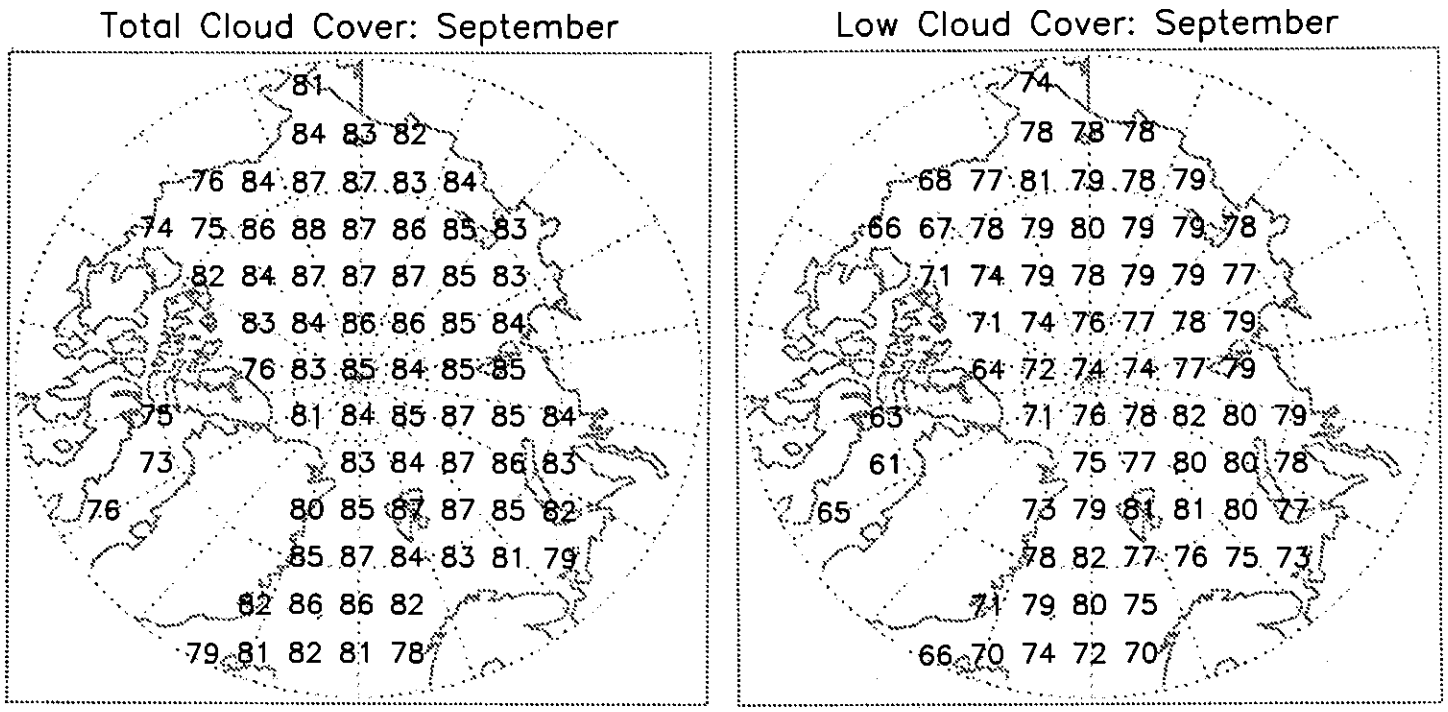

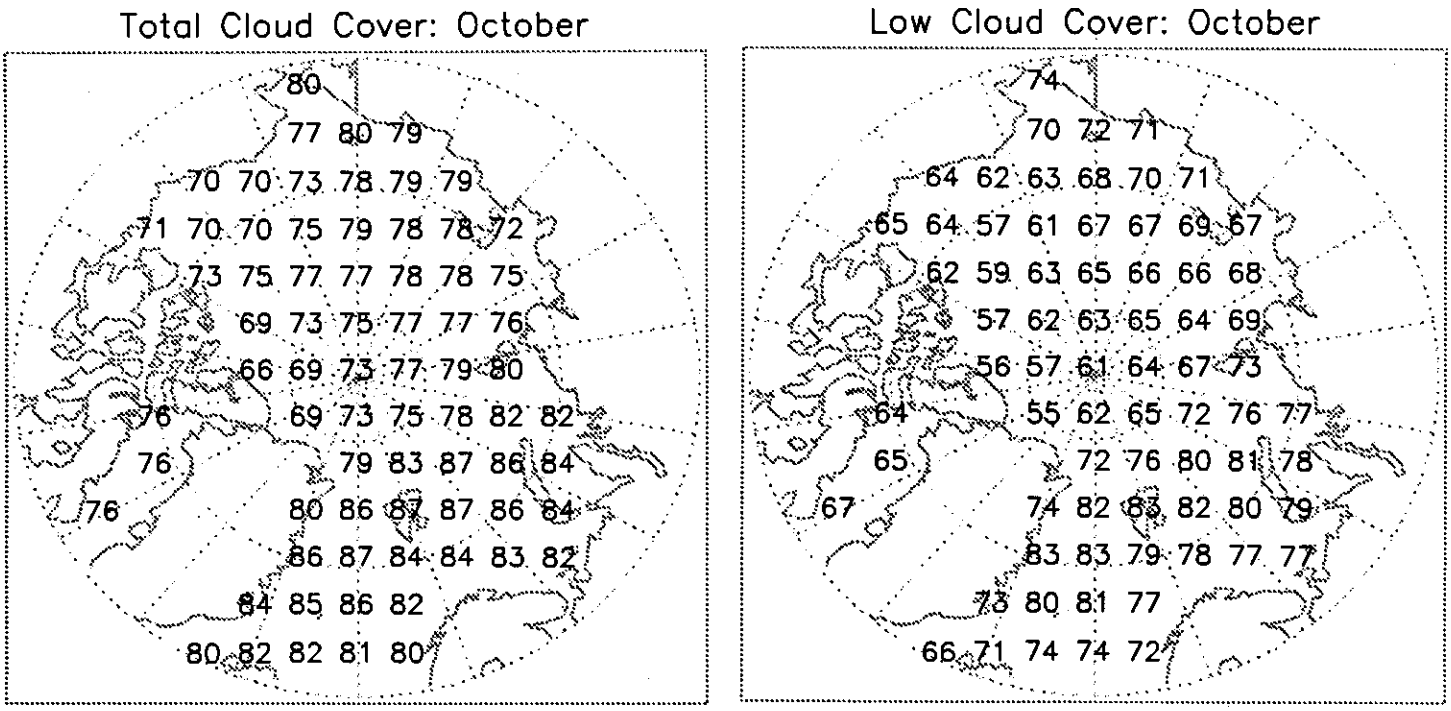

Units: %

Figure 1.4.1 (Continued)

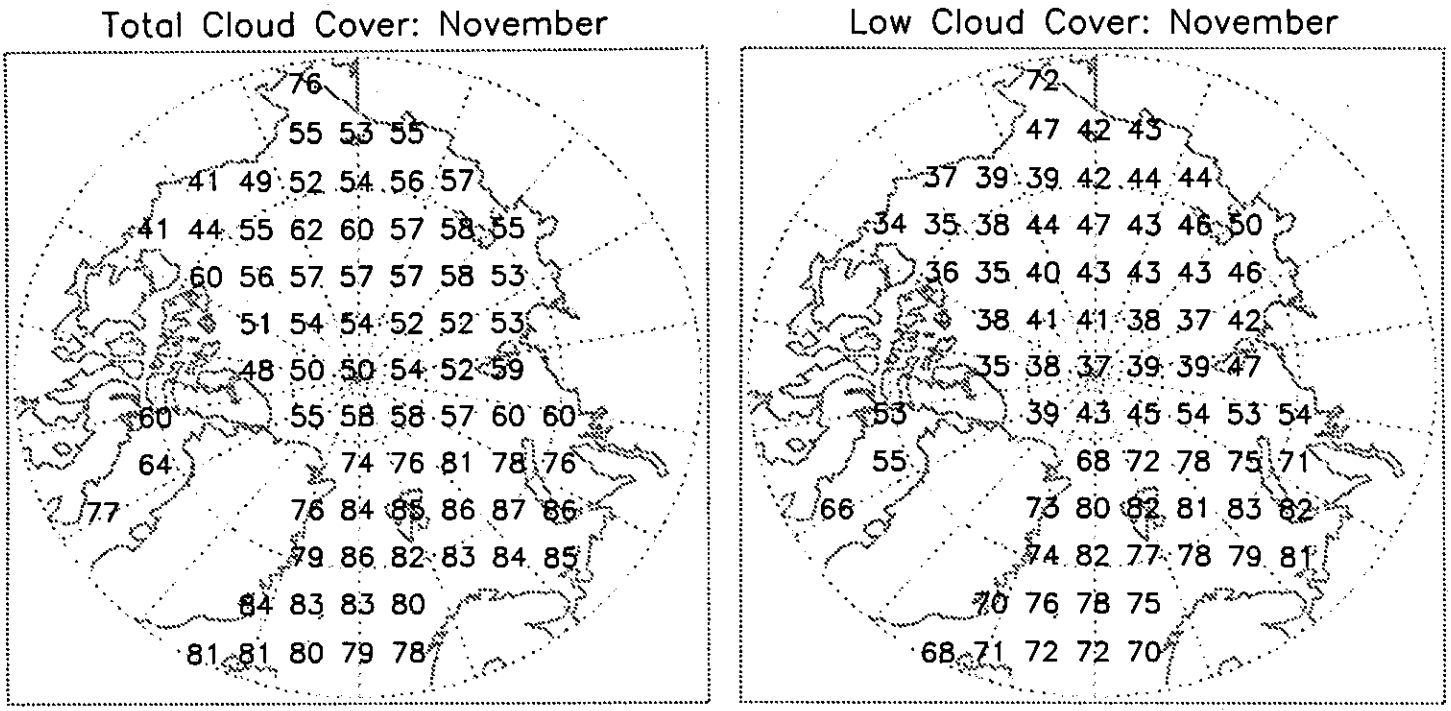

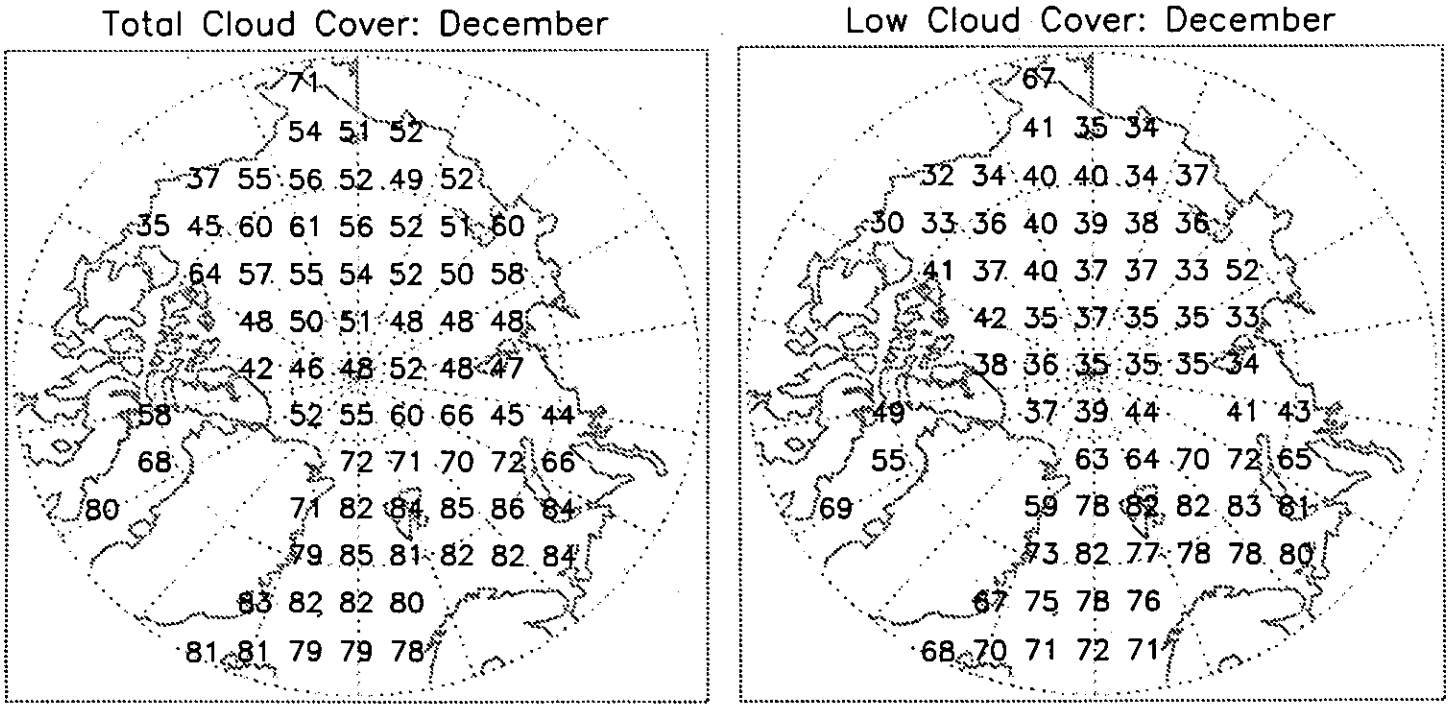

Units: %

Figure 1.4.2

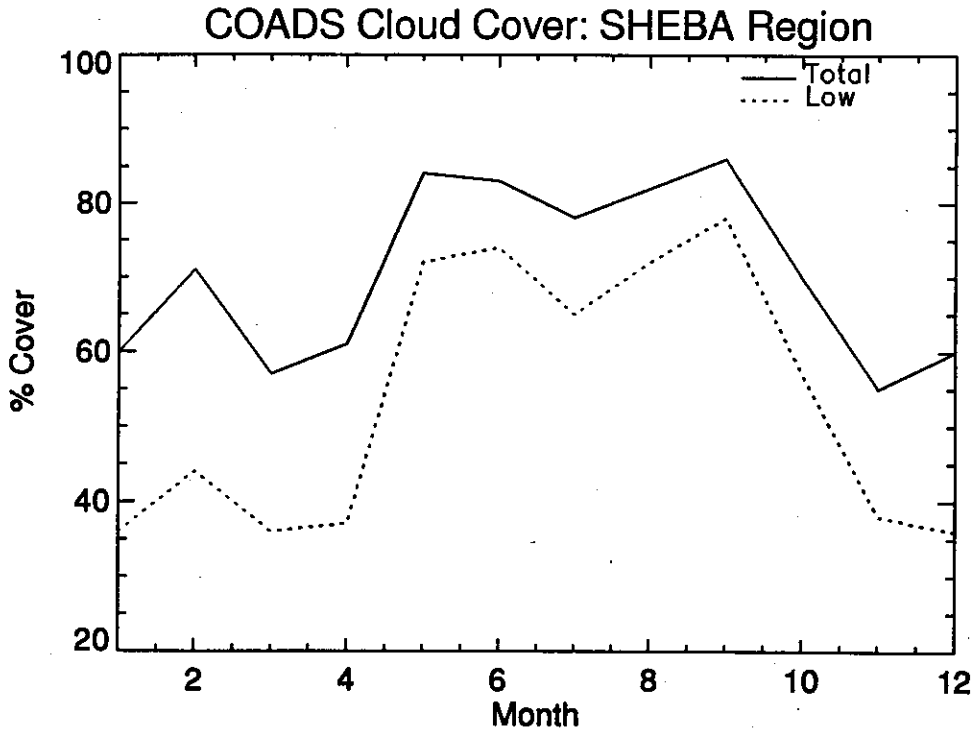
COADS Cloud Cover: SHEBA Region
Total
Low
% Cover
100
80
60
40
20
2
4
6
8
10
12
Month

Figure 1.4.3

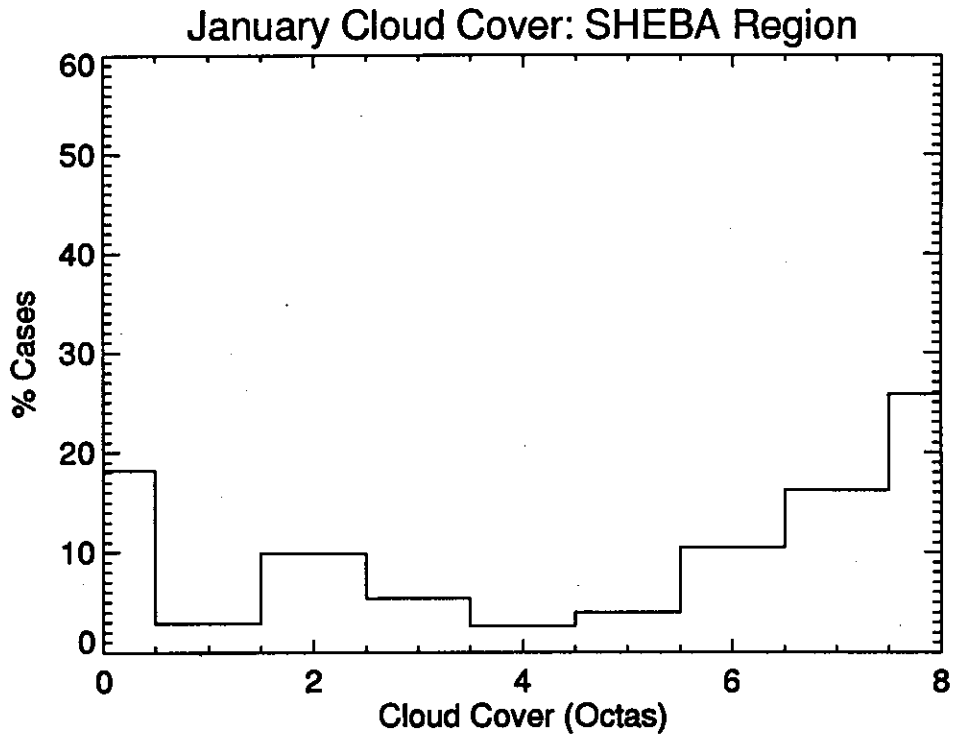
January Cloud Cover: SHEBA Region
% Cases
60
50
40
30
20
10
0
0
2
4
6
8
Cloud Cover (Octas)

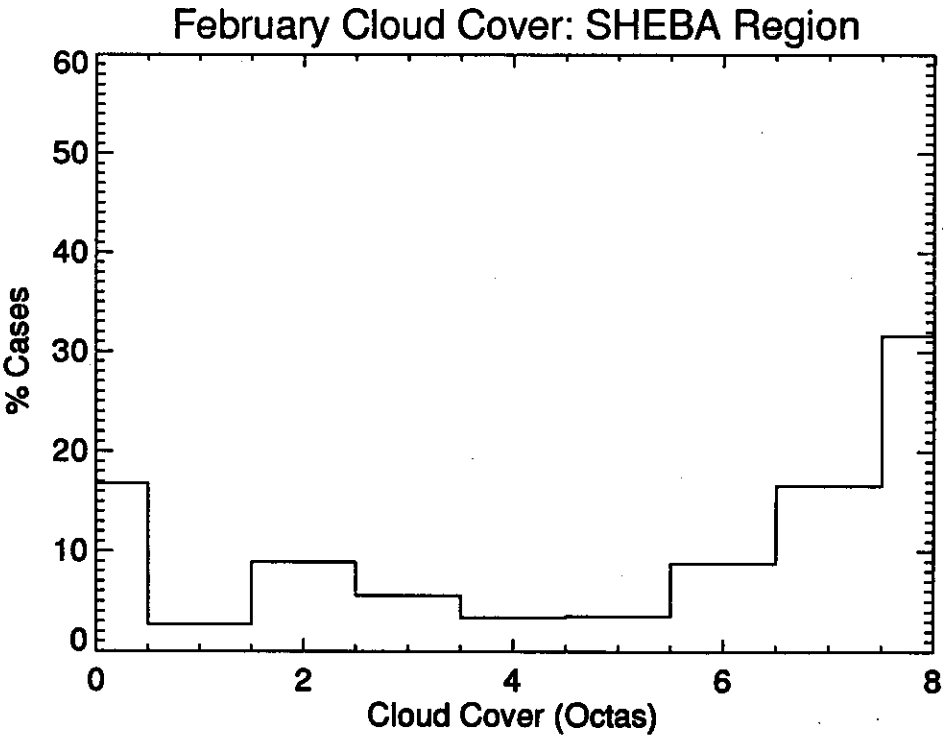
February Cloud Cover: SHEBA Region
% Cases
60
50
40
30
20
10
0
0
2
4
6
8
Cloud Cover (Octas)

Figure 1.4.3 (Continued)

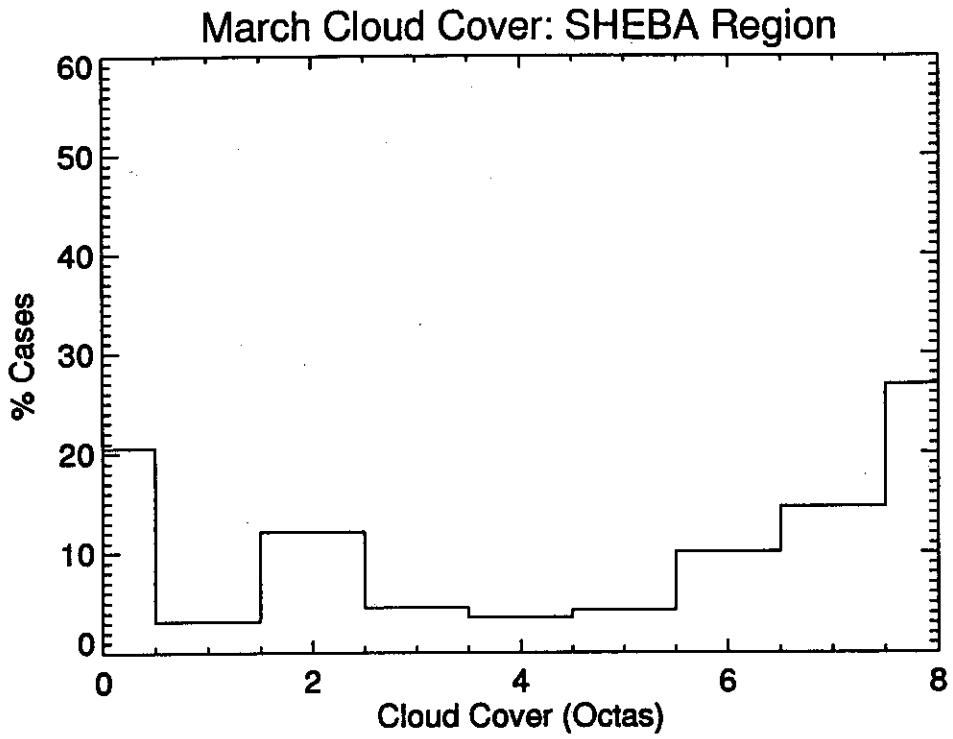

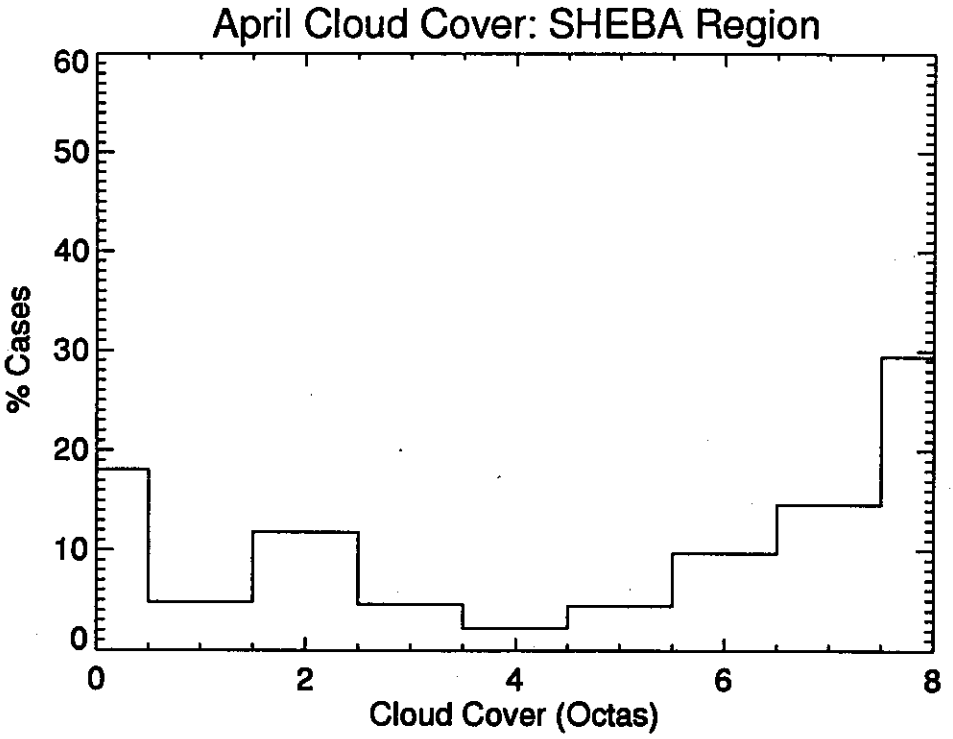

Figure 1.4.3 (Continued)

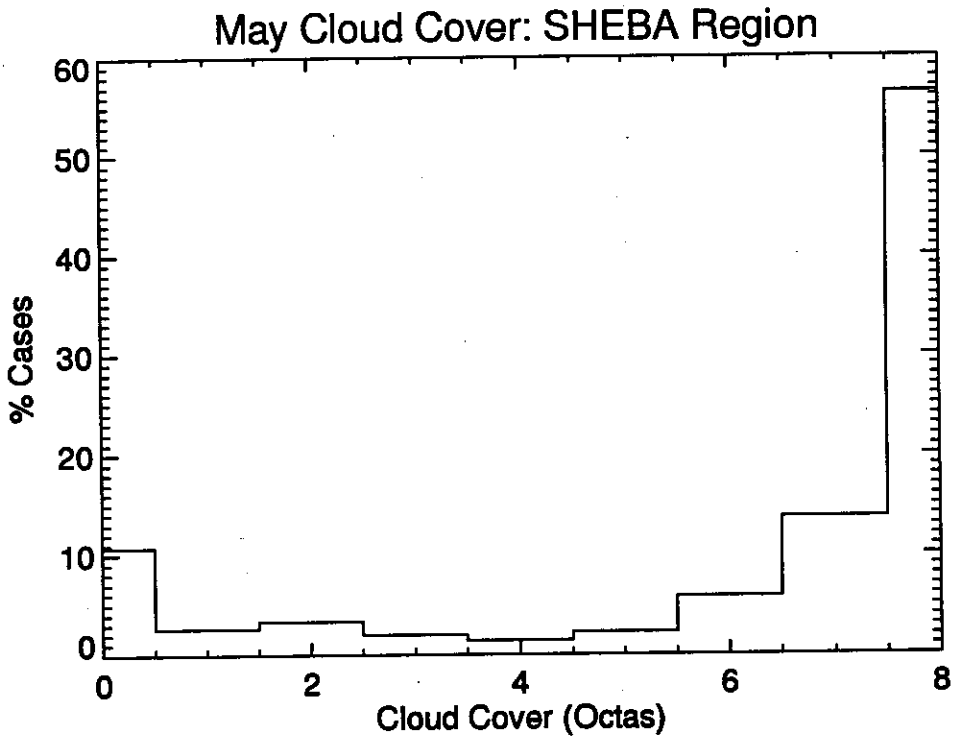

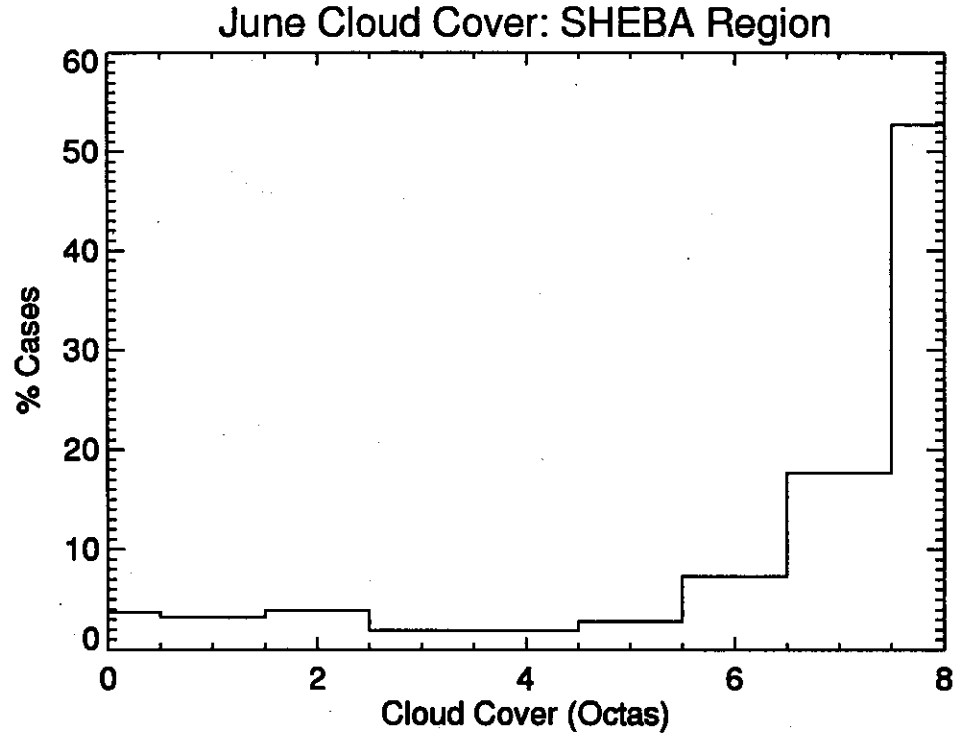

Figure 1.4.3 (Continued)

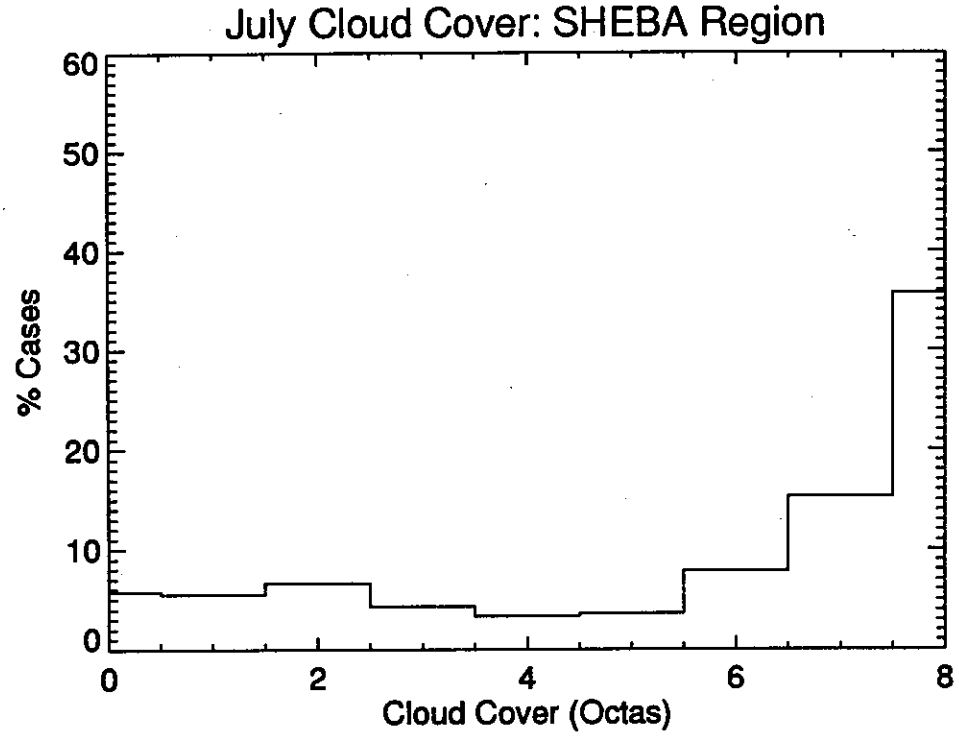

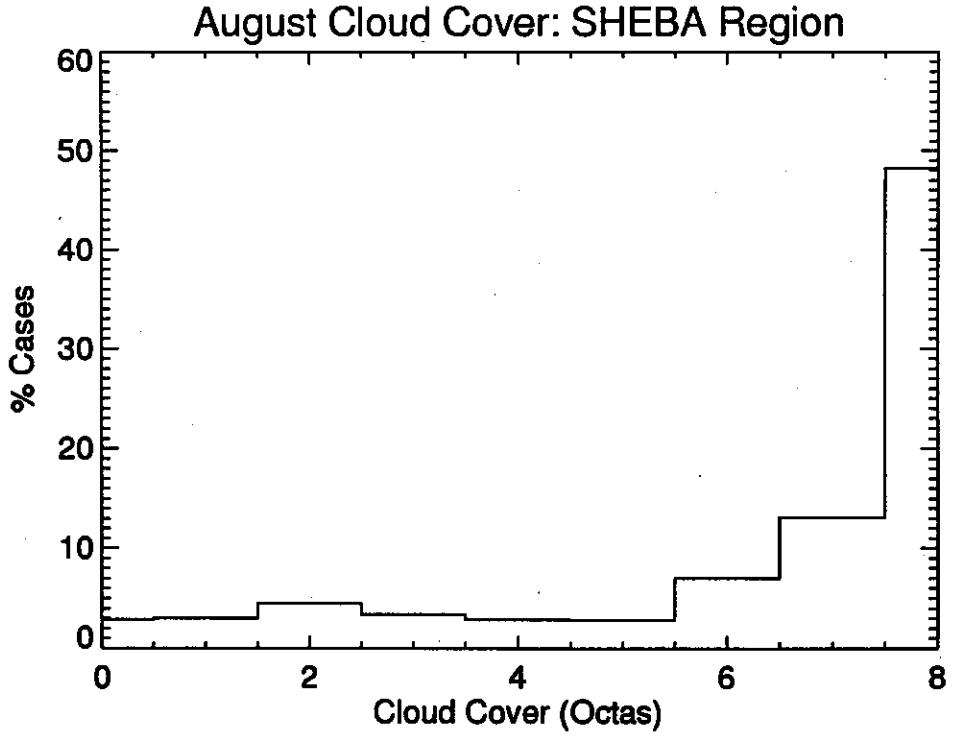

Figure 1.4.3 (Continued)

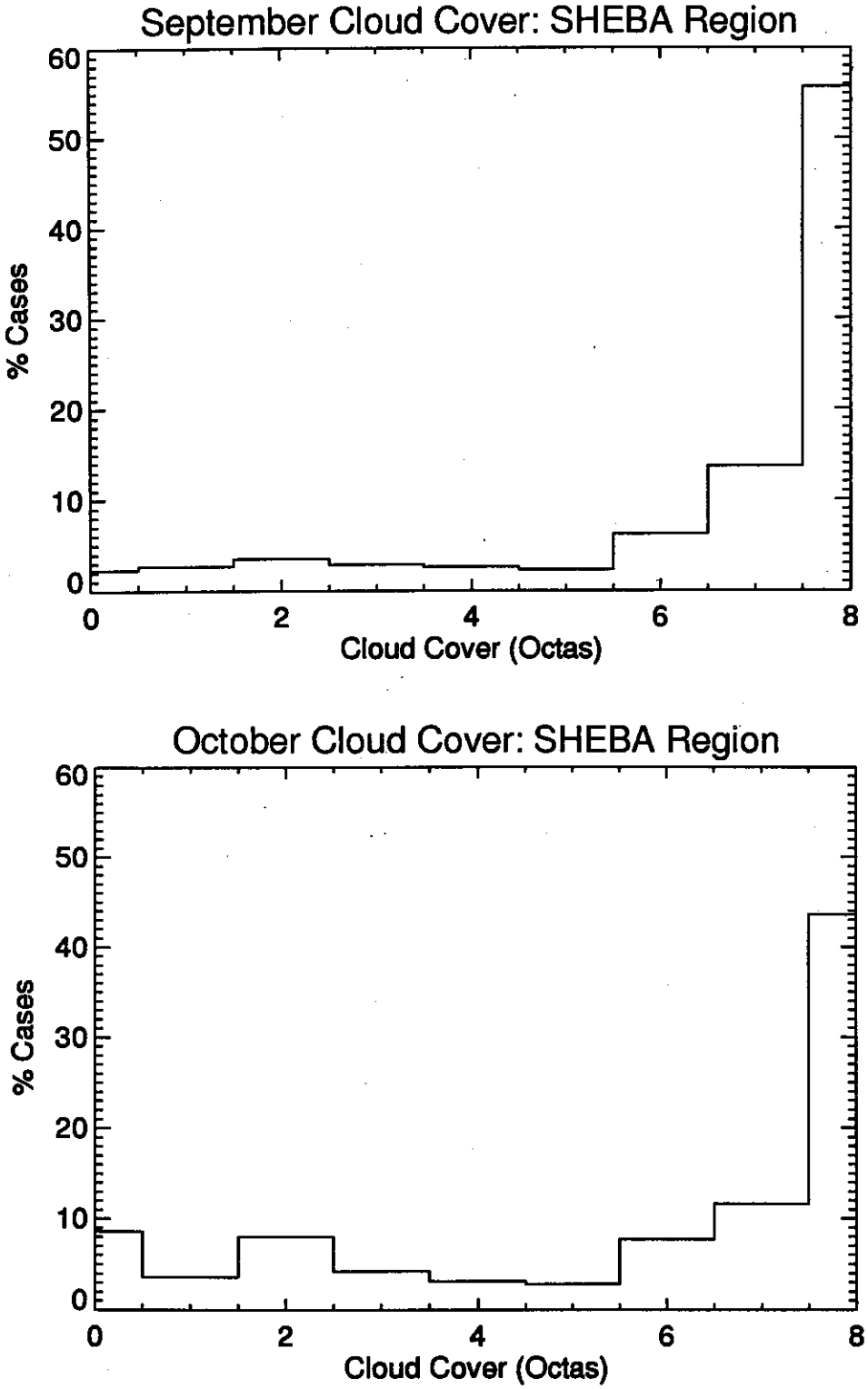

Figure 1.4.3 (Continued)

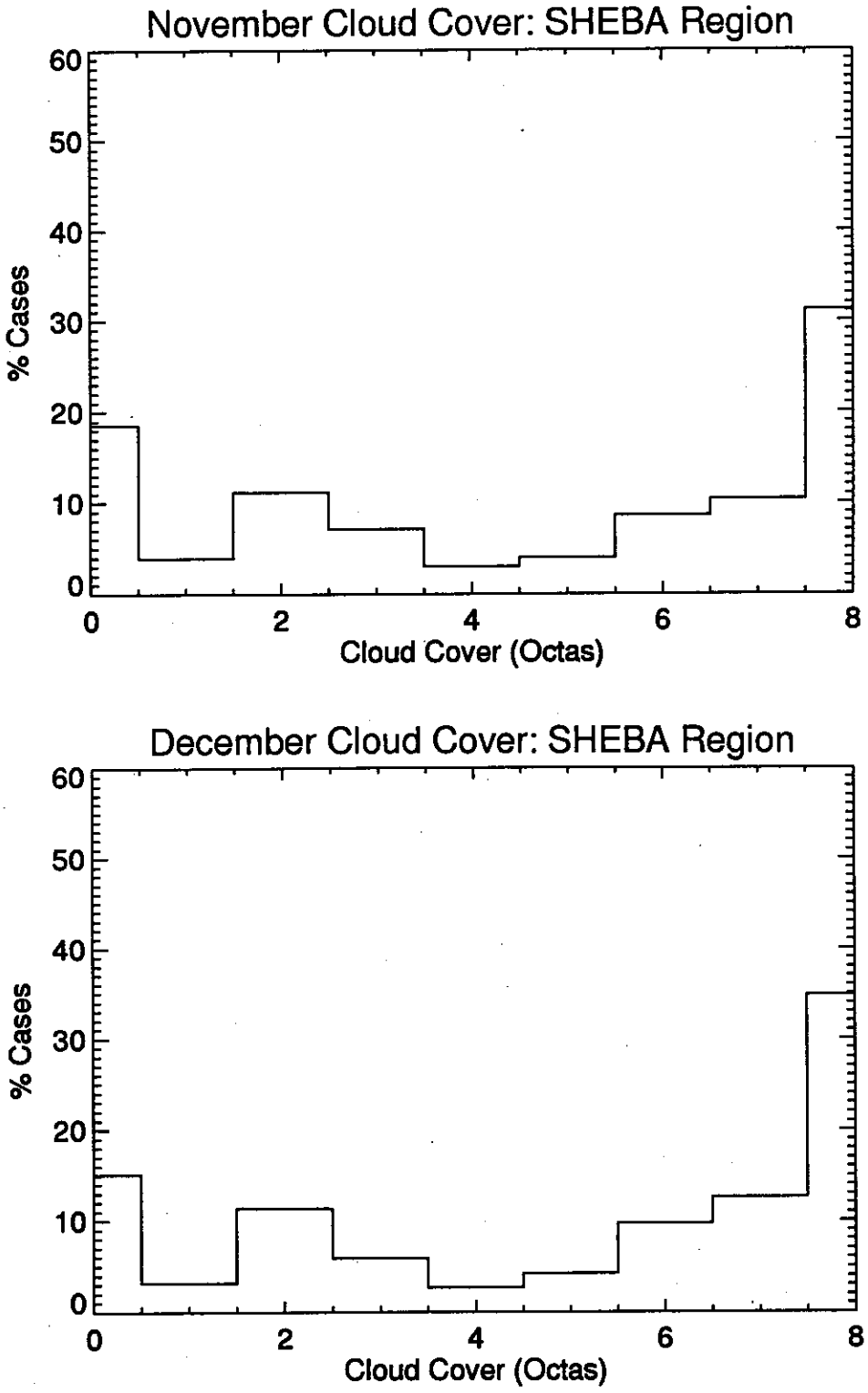

1.5 ISCCP-D2 Cloud Properties

The International Satellite Cloud Climatology Project (ISCCP) monthly 3-hourly 280 km-resolution (C2) data products [Rossow and Schiffer, 1991] are being superseded by a D2 product with improvements in calibration, cloud detection algorithms and the radiative model. The improvements in the cloud detection procedure are particularly important for clouds over snow and ice and result primarily from the addition of the Advanced Very High Resolution Radiometer (AVHRR) 3.7 micrometer channel in the cloud threshold tests. The radiative model has been enhanced to include both ice and liquid-phase clouds. The original model considered liquid clouds only. Rossow et al. [1996] provide additional information. The availability of four years (1986, 1990, 1991, 1992) of D2 data allows for some initial analyses of remotely-sensed Arctic cloud properties to complement the COADS-derived fields in Section 1.4. Figure 1.5.1 provides monthly mean fields of total cloud cover, cloud (visible) optical depth, cloud top pressure and cloud top temperature from the D2 product. In Section 2.3, we provide surface radiation fluxes for the Arctic derived from the earlier C2 products for 1984-1990 [Schweiger and Key, 1994]. Efforts are ongoing to reprocess these fields using the improved D2 product.

ISCCP cloud cover distributions for marine regions reproduce the major features in the COADS analyses, in particular, decreasing cloud cover from the Atlantic side of the Arctic towards the central Arctic Ocean. However, the ISCCP values are higher than the COADS values over the central Arctic Ocean from November through March, but lower from May through October. A relative Beaufort Sea minimum is apparent in the ISCCP fields from June through August, consistent with the SLP analyses. Ignoring the months of polar darkness for which cloud (visible) optical depth is not defined, optical depths for most months show a strong poleward increase, but with the highest values over the Greenland Ice Sheet. This pattern appears suspect. ISCCP investigators are aware of this issue, which may relate to how cloud scattering is modeled in the retrieval process. Cloud top pressures over most of the Arctic Ocean range from 550-700 mb, with some suggestion of an April-June maximum (i.e., cloud top heights are lower for these months). Cloud top pressures tend to decrease over land. Cloud top temperatures over the central Arctic Ocean range from 235 K during winter to about 260 K during summer.

Figure 1.5.1

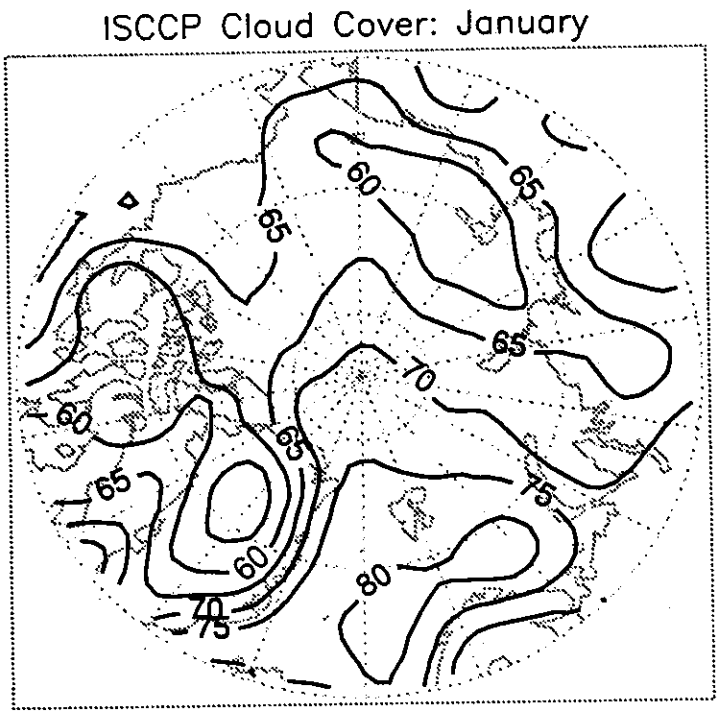

Units: %

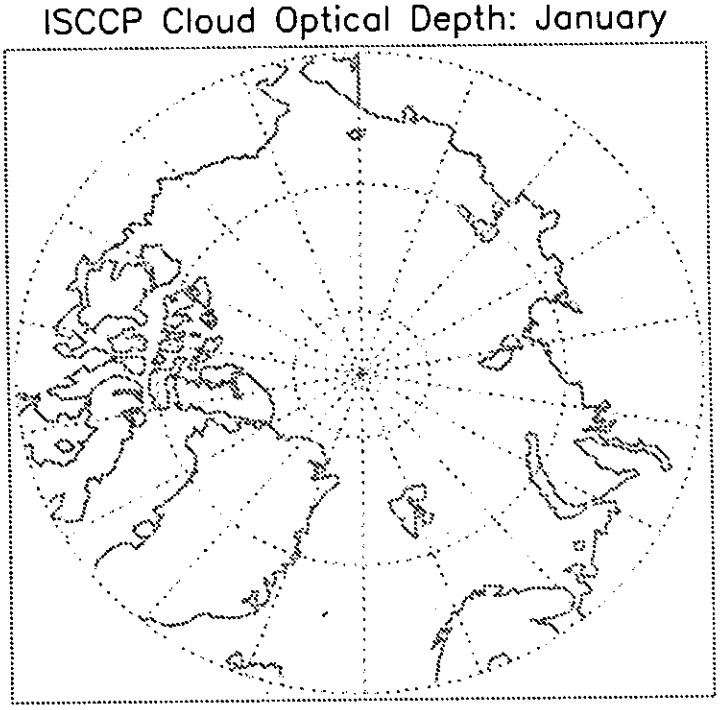

Units: Dimensionless

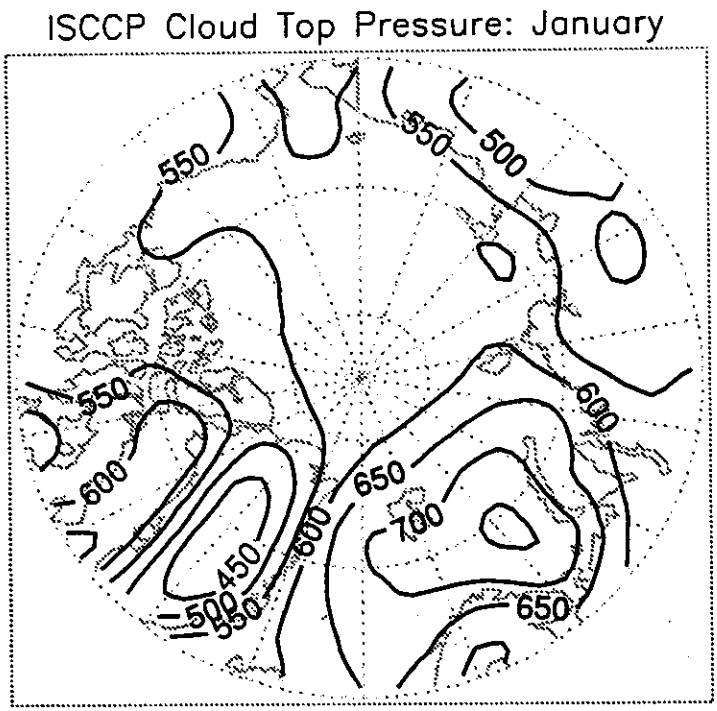

Units: mb

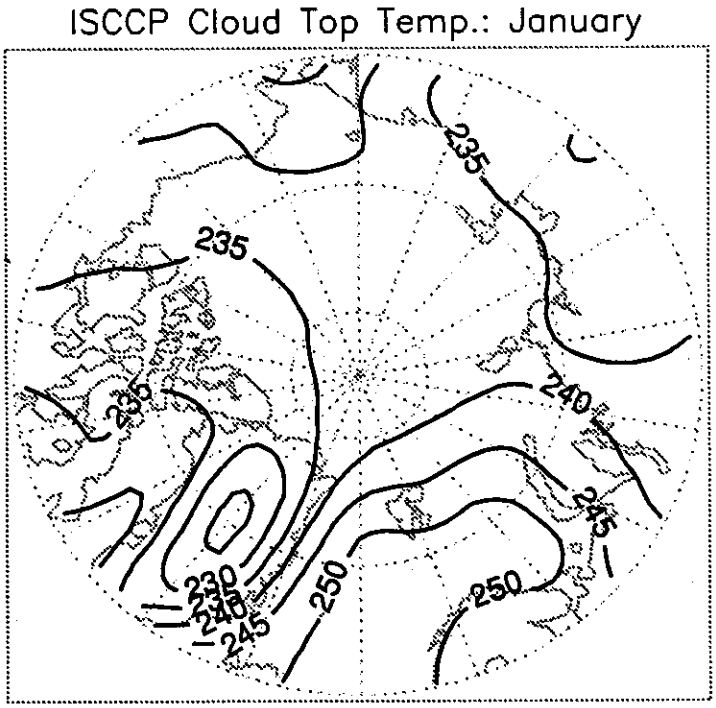

Units: K

Figure 1.5.1 (Continued)

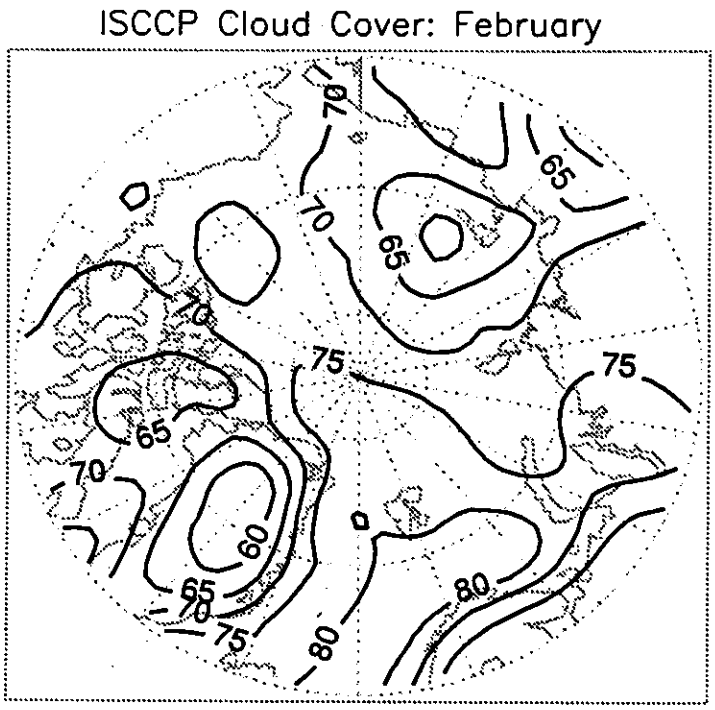

Units: %

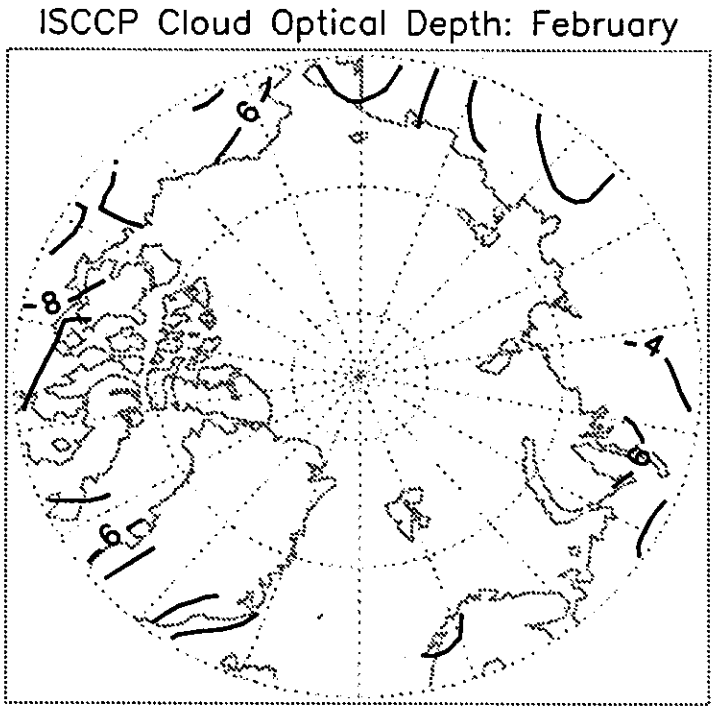

Units: Dimensionless

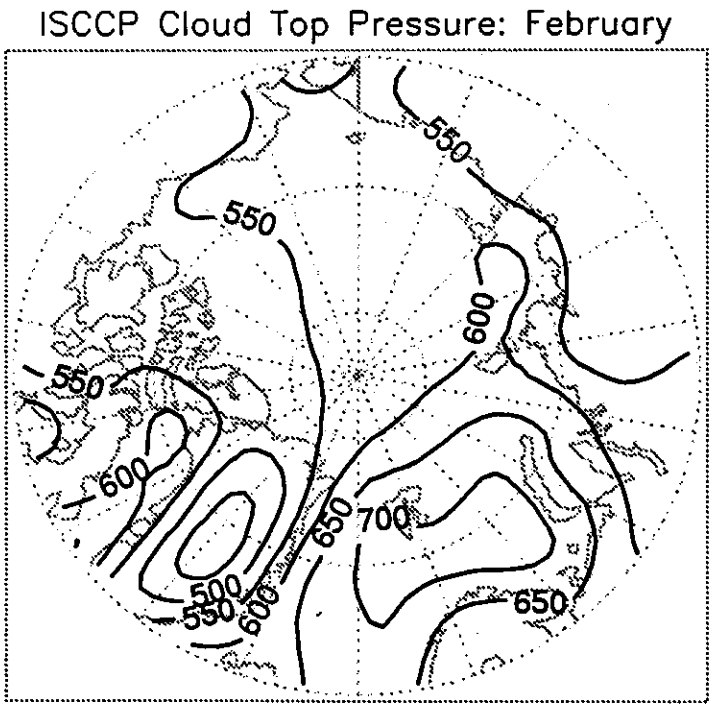

Units: mb

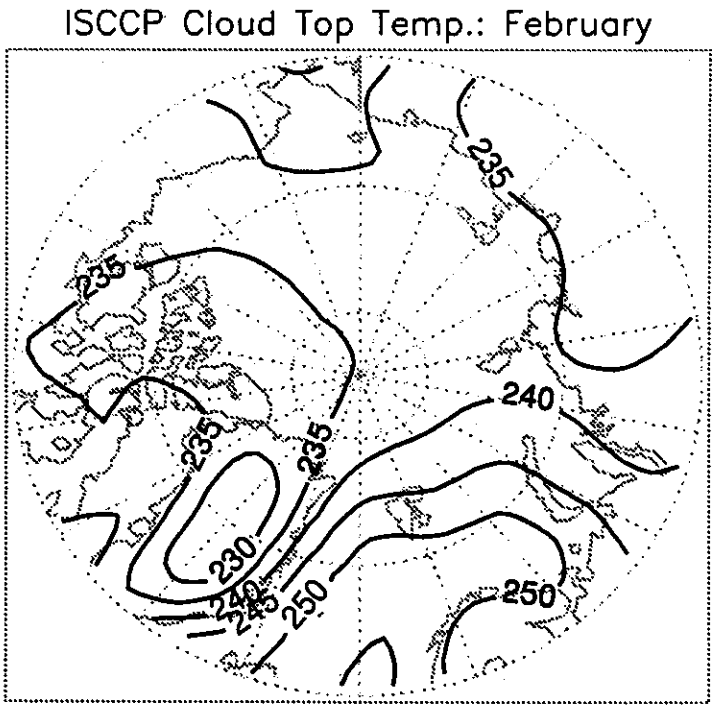

Units: K

Figure 1.5.1 (Continued)

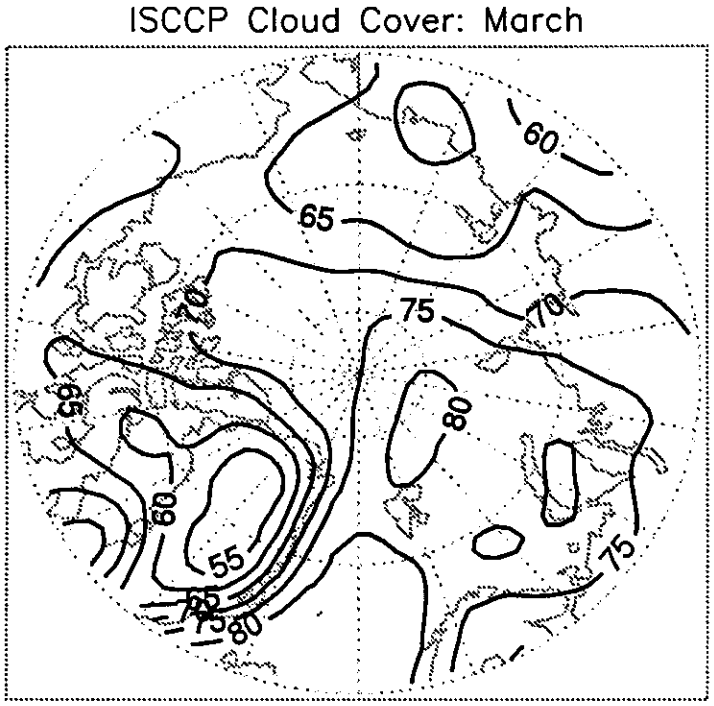

Units: %

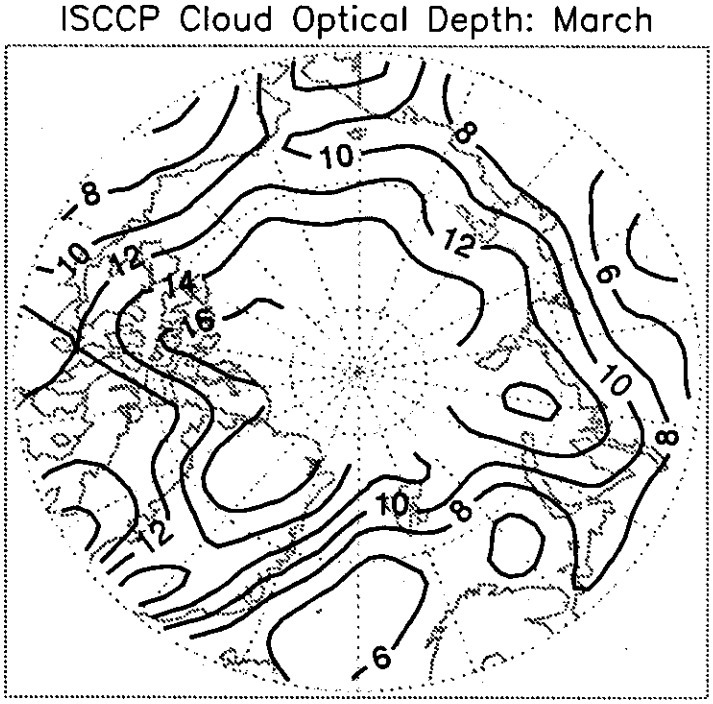

Units: Dimensionless

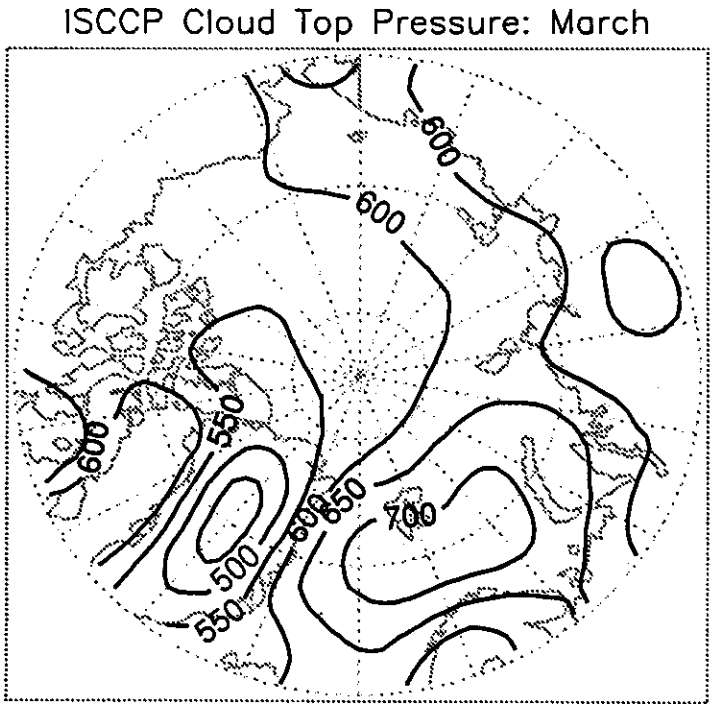

Units: mb

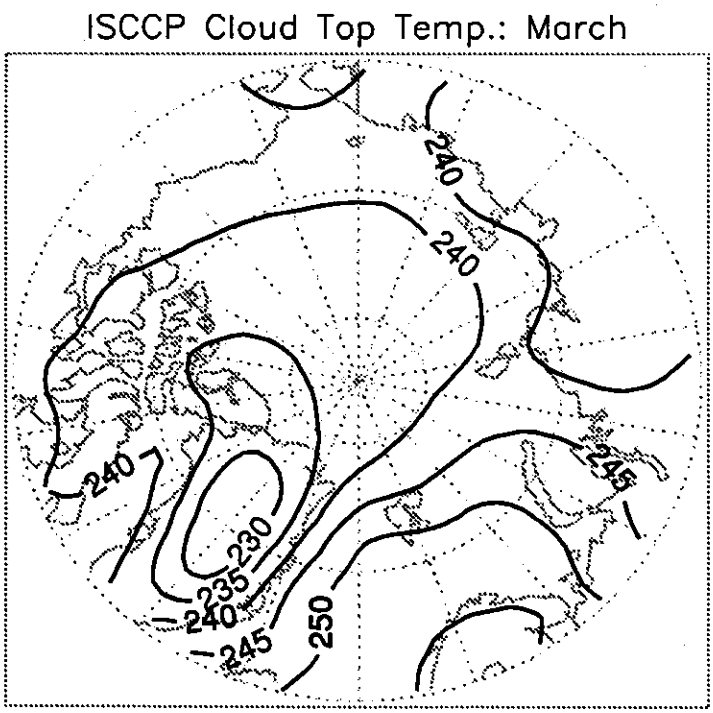

Units: K

Figure 1.5.1 (Continued)

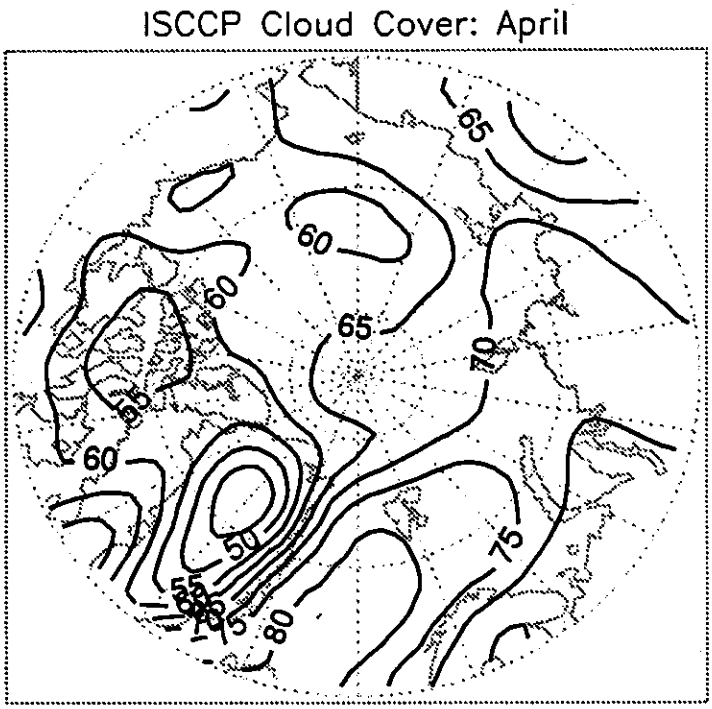

Units: %

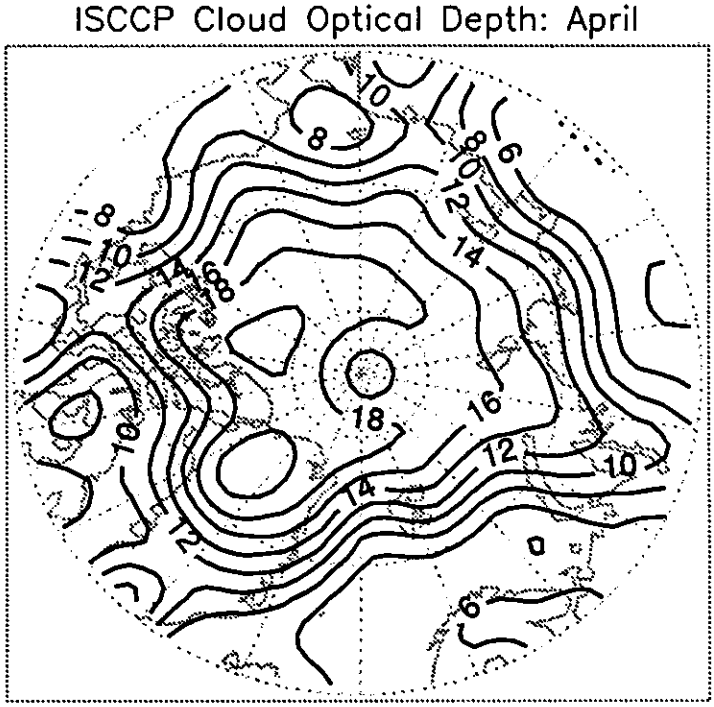

Units: Dimensionless

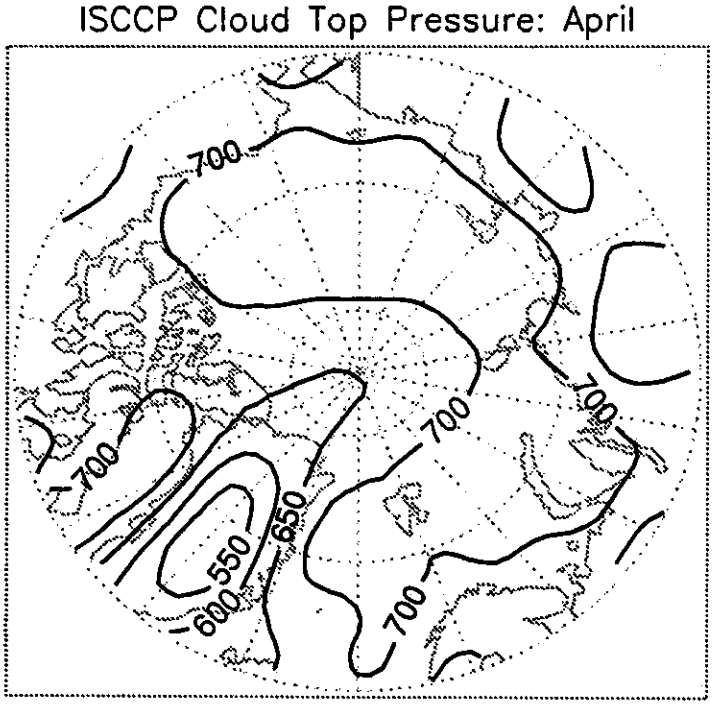

Units: mb

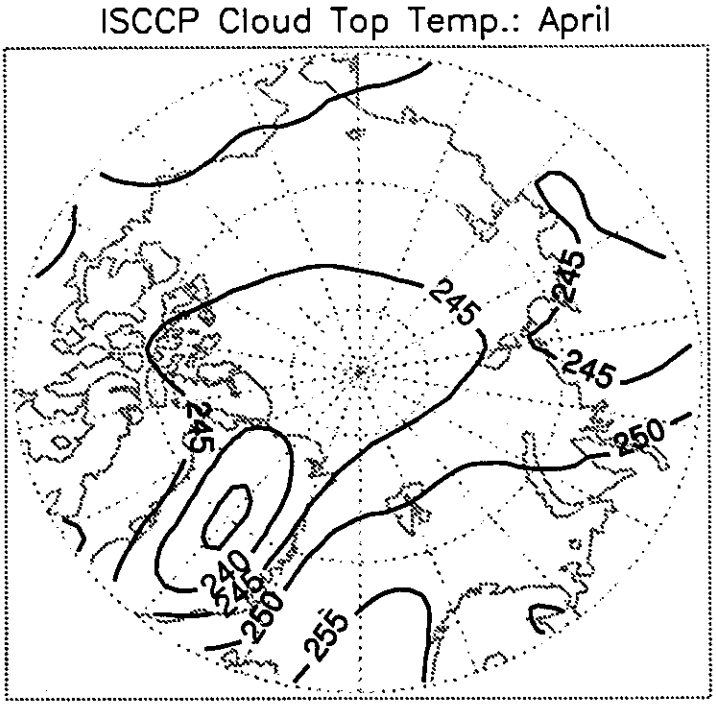

Units: K

Figure 1.5.1 (Continued)

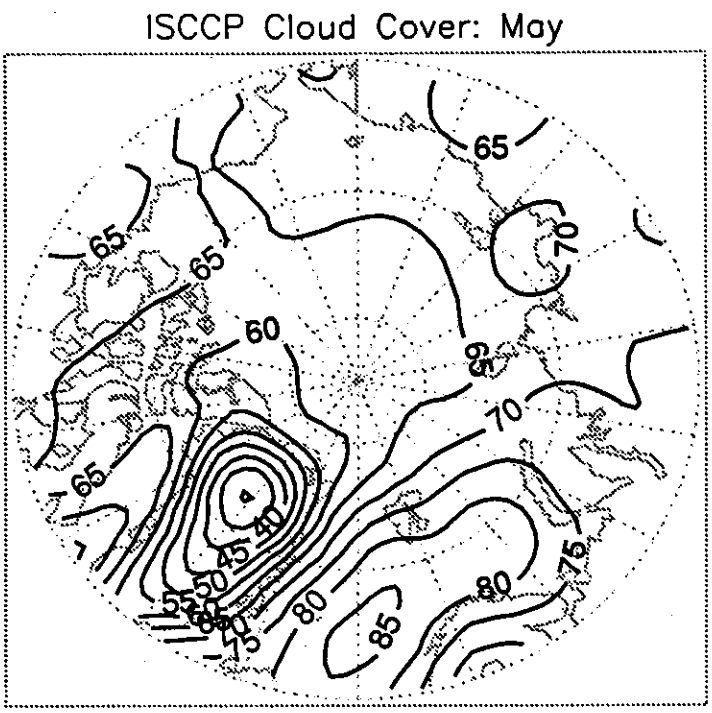

Units: %

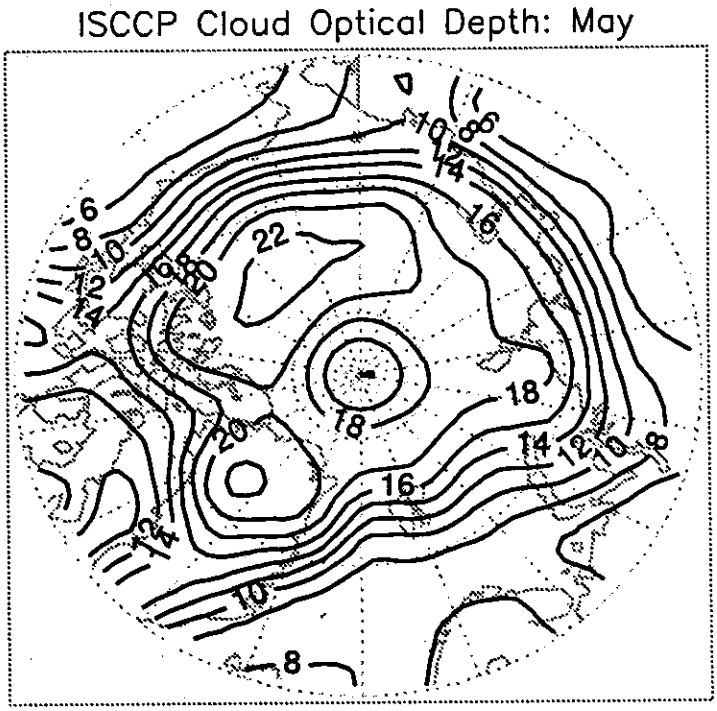

Units: Dimensionless

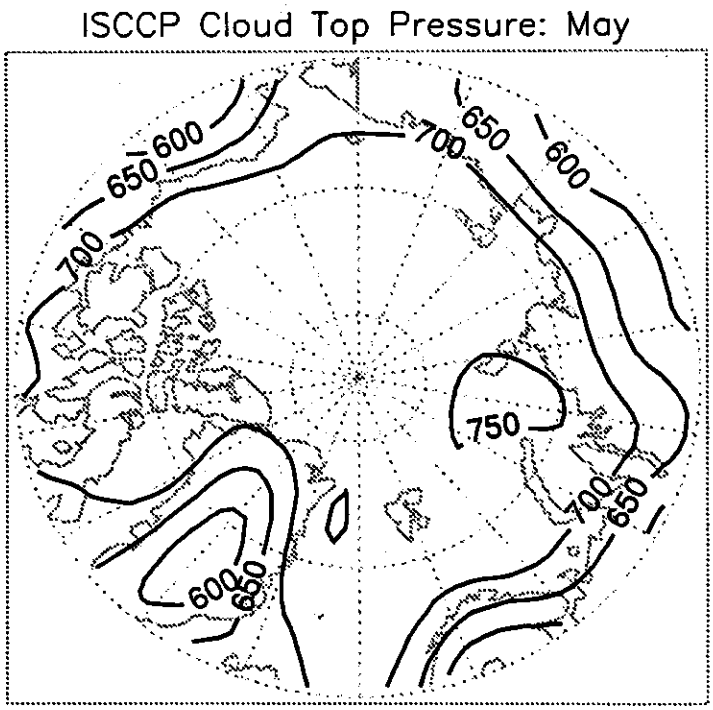

Units: mb

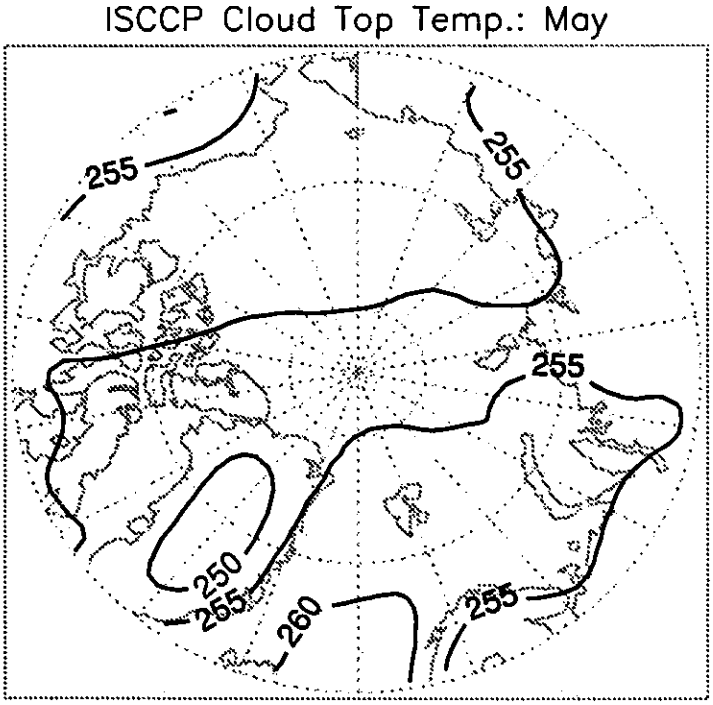

Units: K

Figure 1.5.1 (Continued)

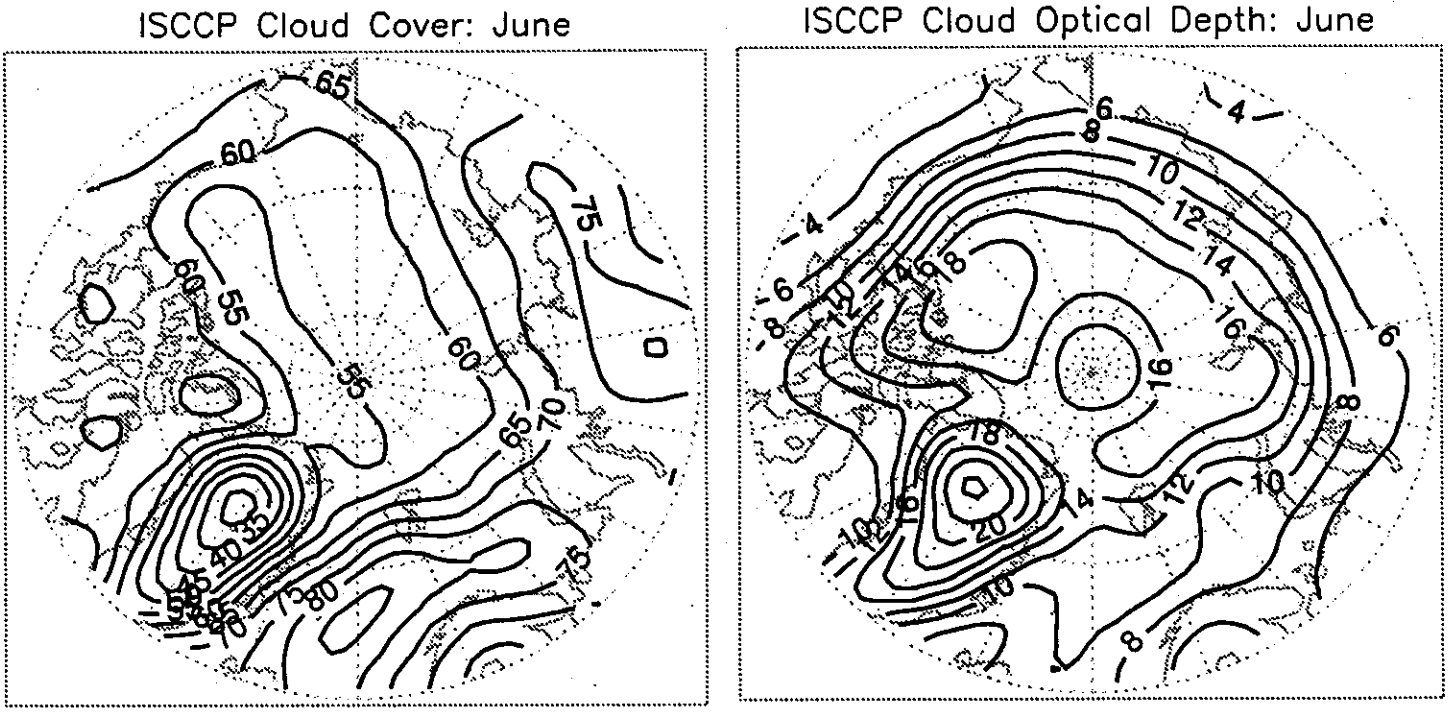

Units: %

Units: Dimensionless

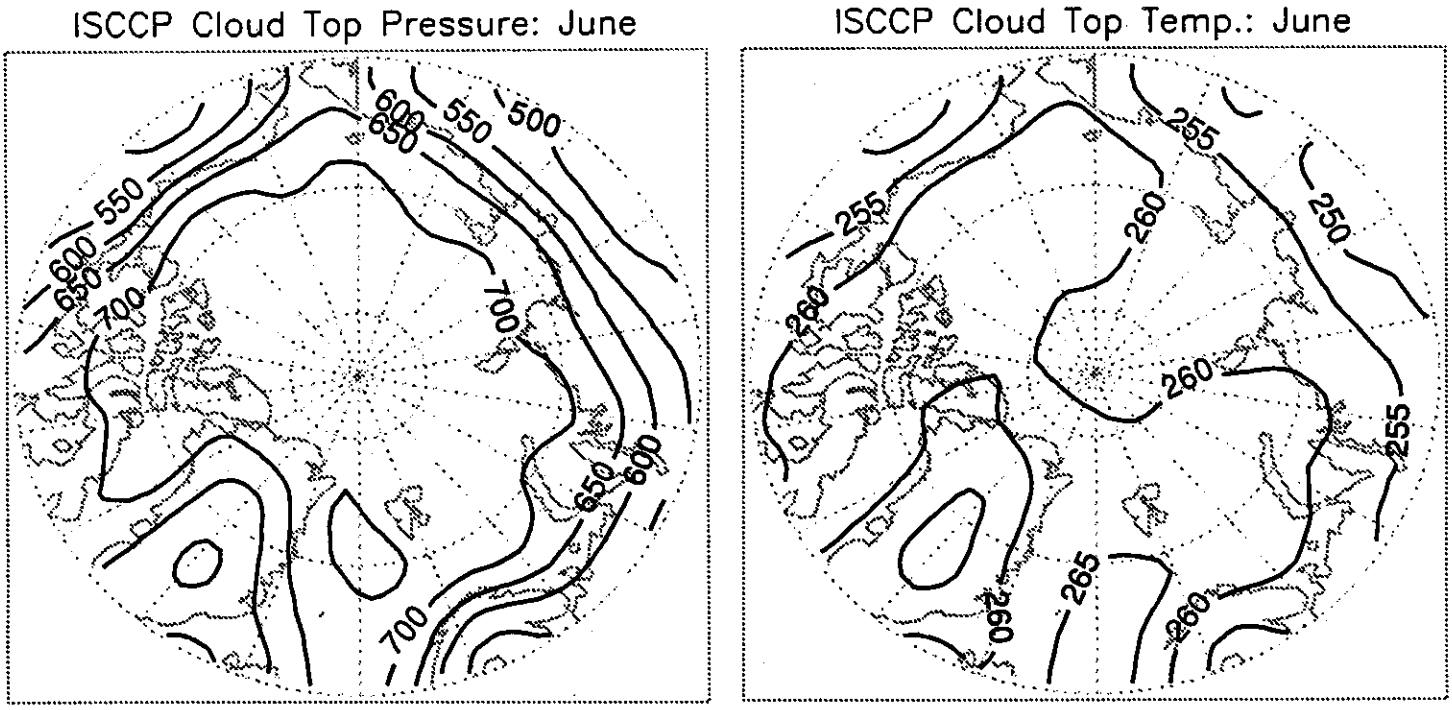

Units: mb

Units: K

Figure 1.5.1 (Continued)

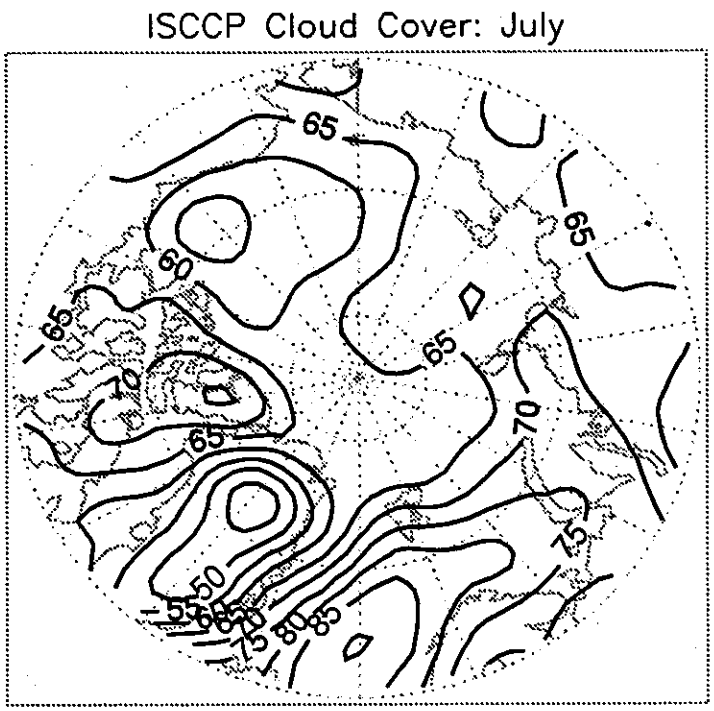

Units: %

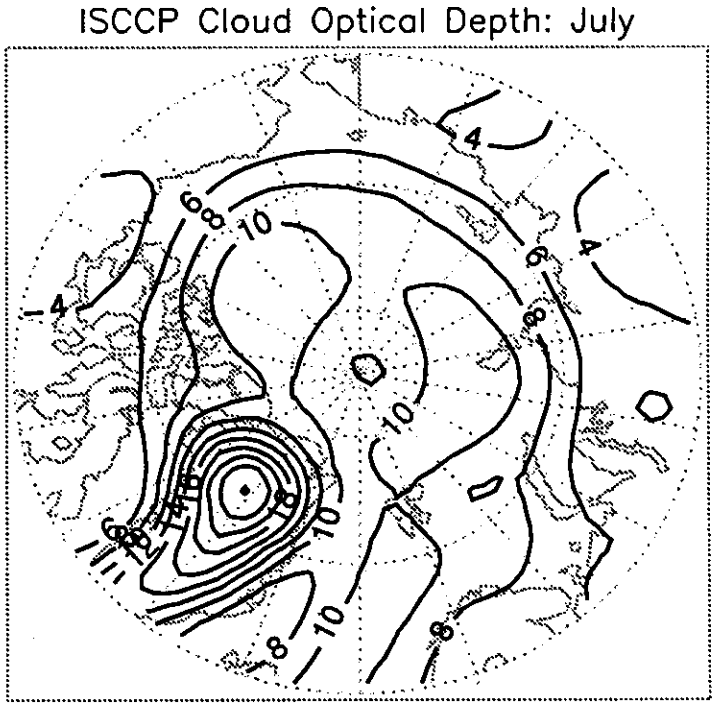

Units: Dimensionless

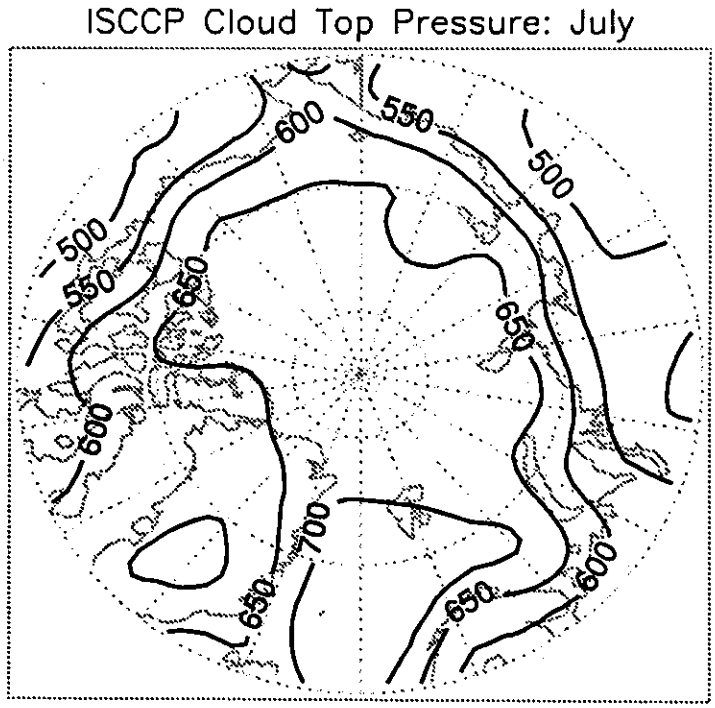

Units: mb

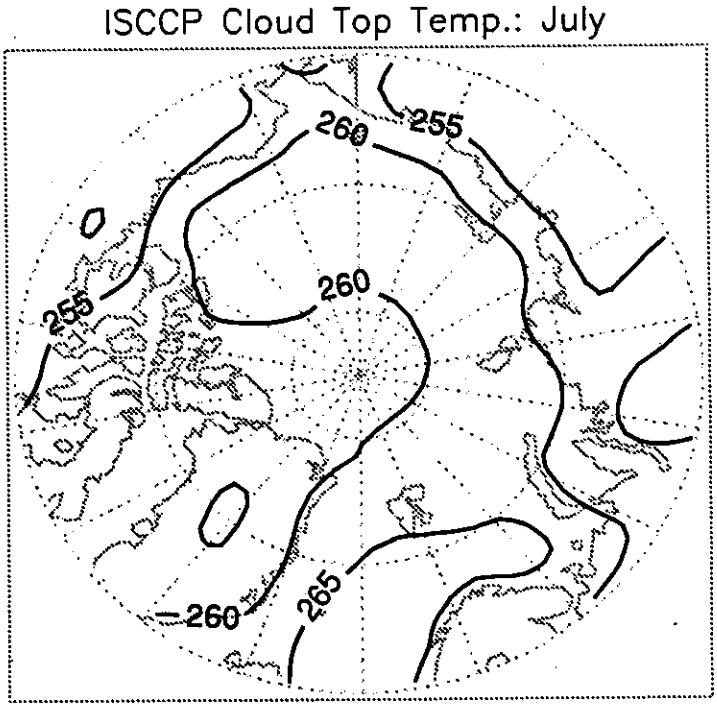

Units: K

Figure 1.5.1 (Continued)

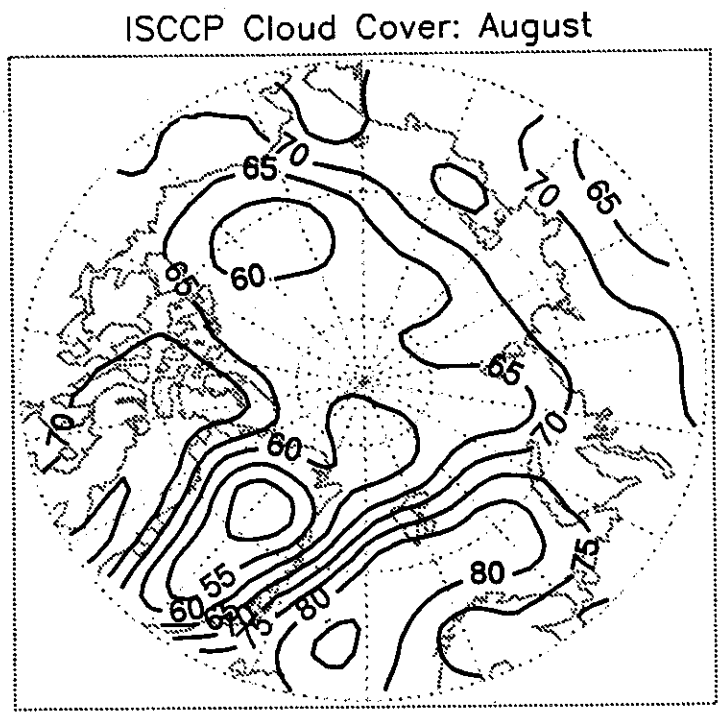

Units: %

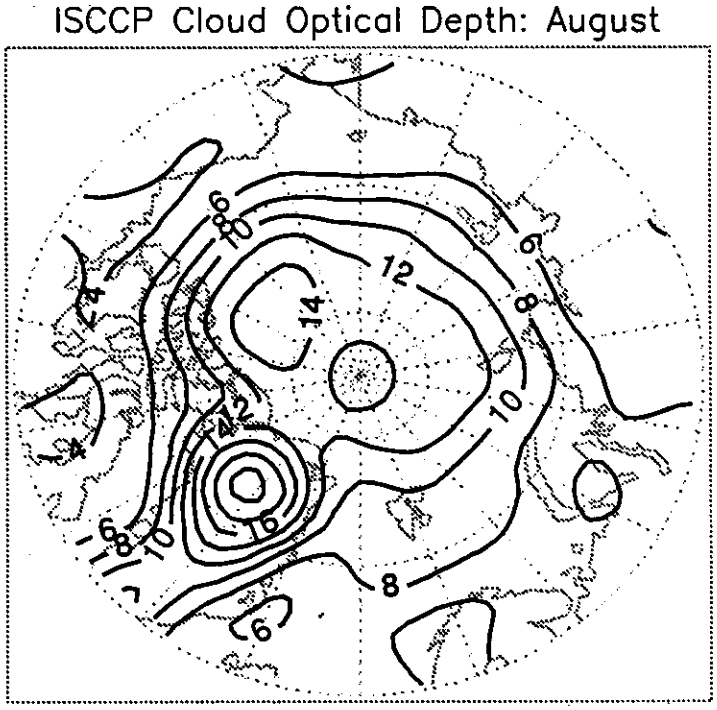

Units: Dimensionless

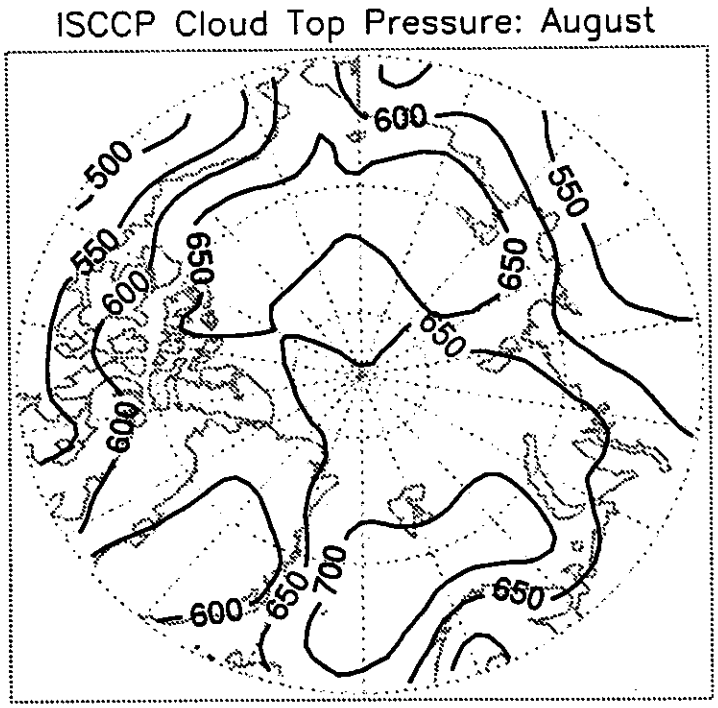

Units: mb

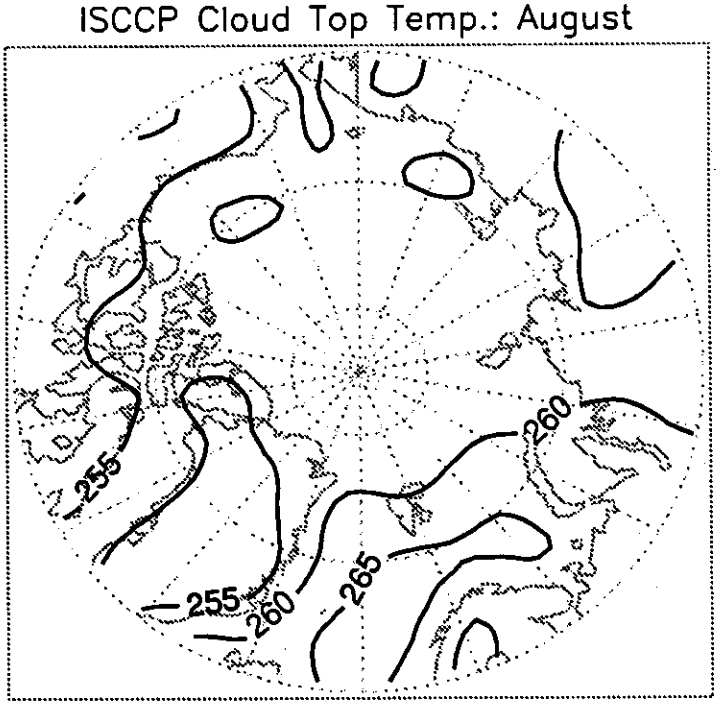

Units: K

Figure 1.5.1 (Continued)

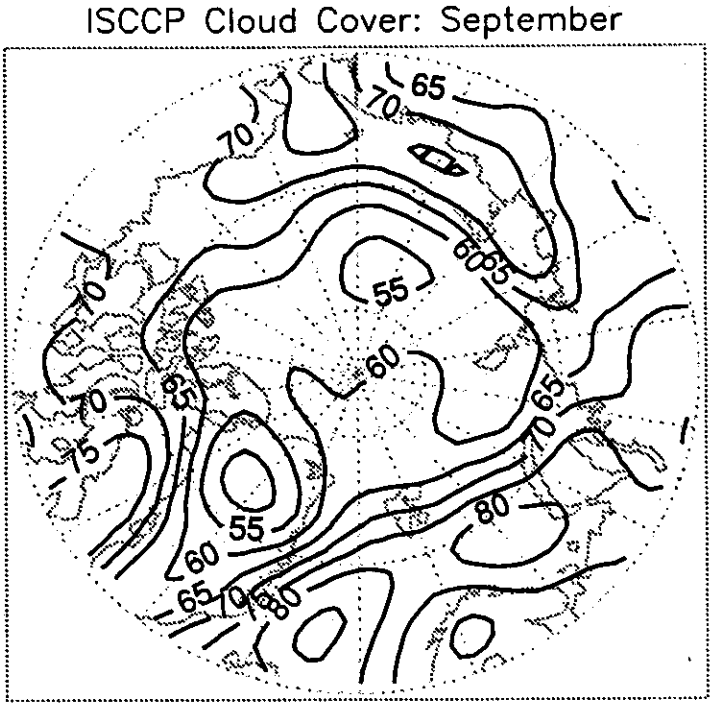

Units: %

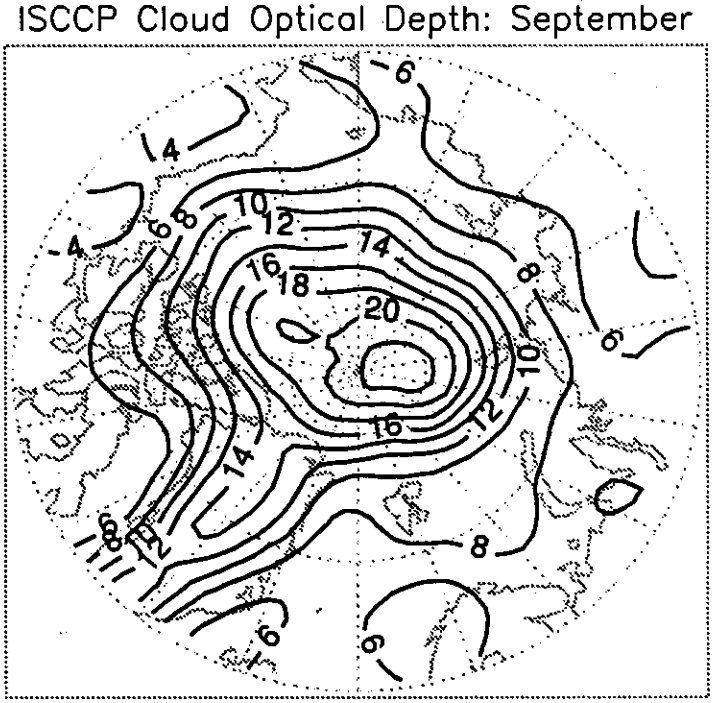

Units: Dimensionless

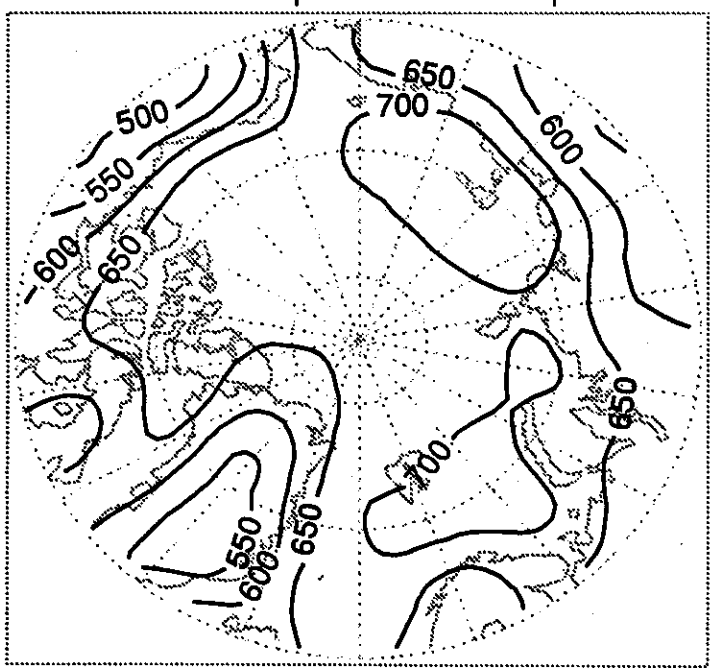

Units: mb

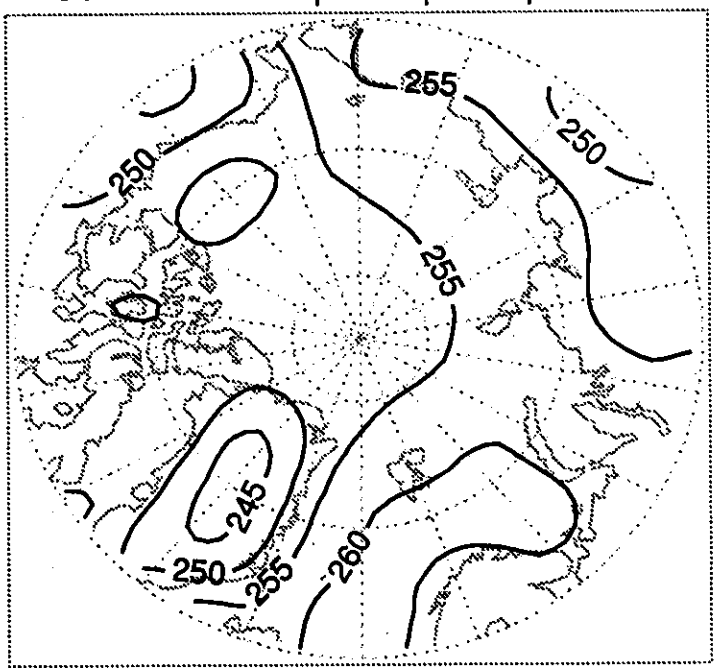

Units: K

Figure 1.5.1 (Continued)

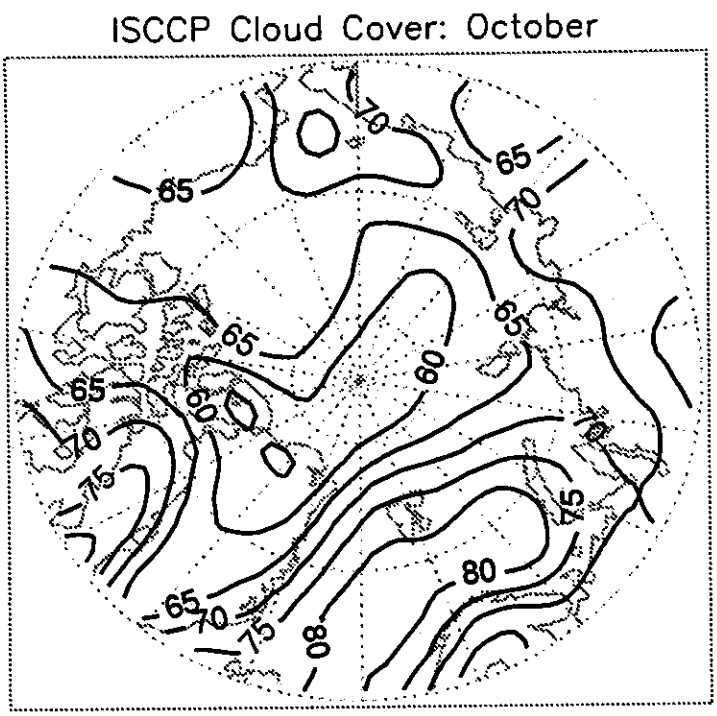

Units: %

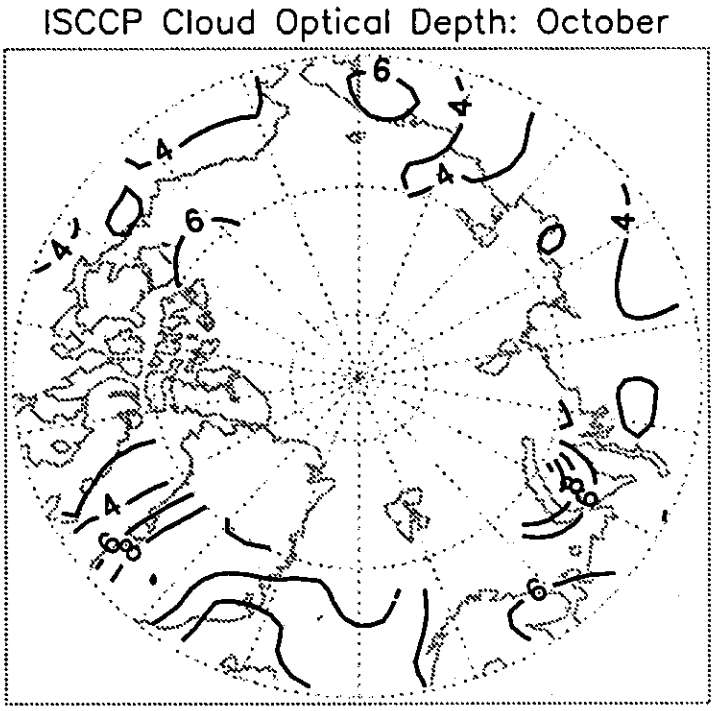

Units: Dimensionless

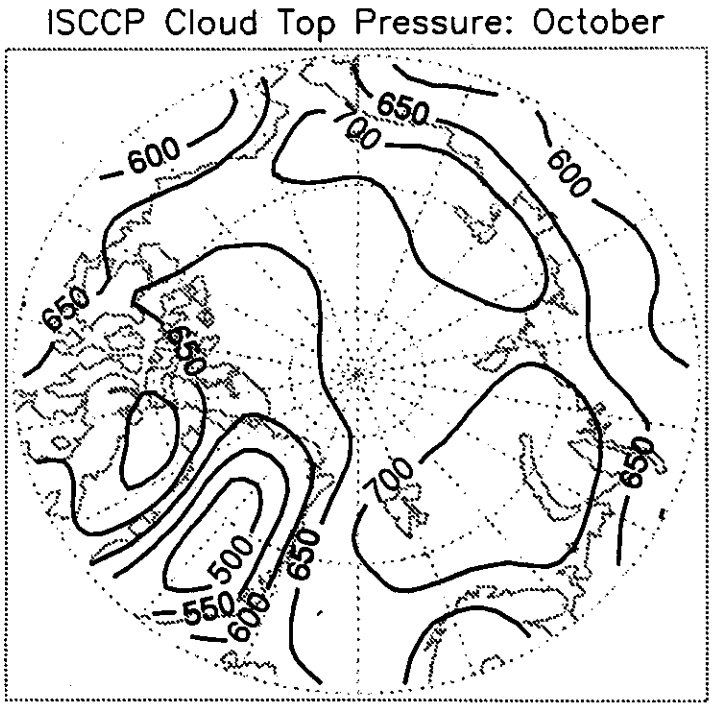

Units: mb

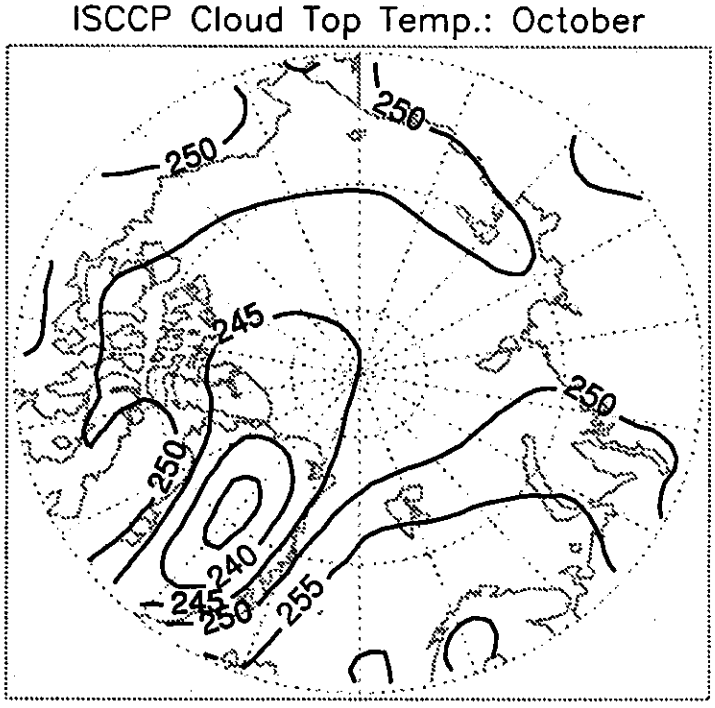

Units: K

Figure 1.5.1 (Continued)

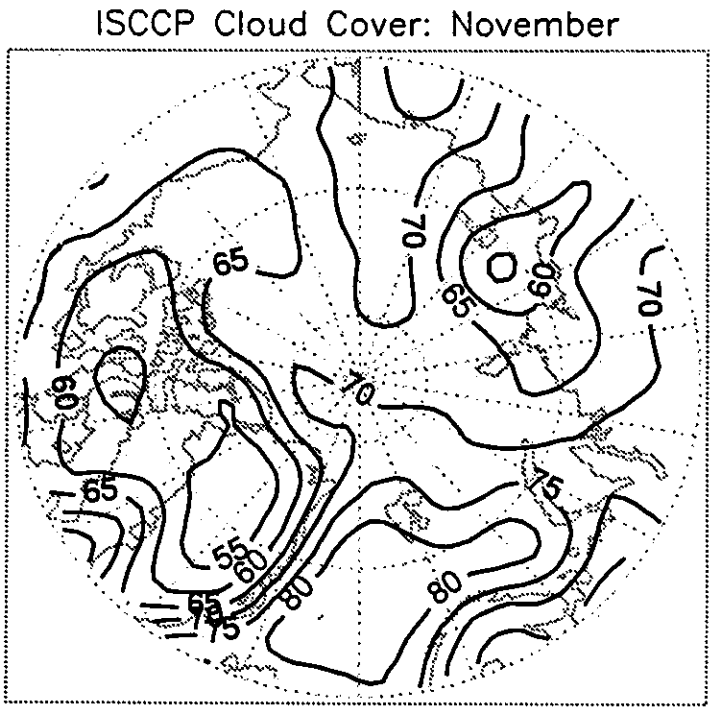

Units: %

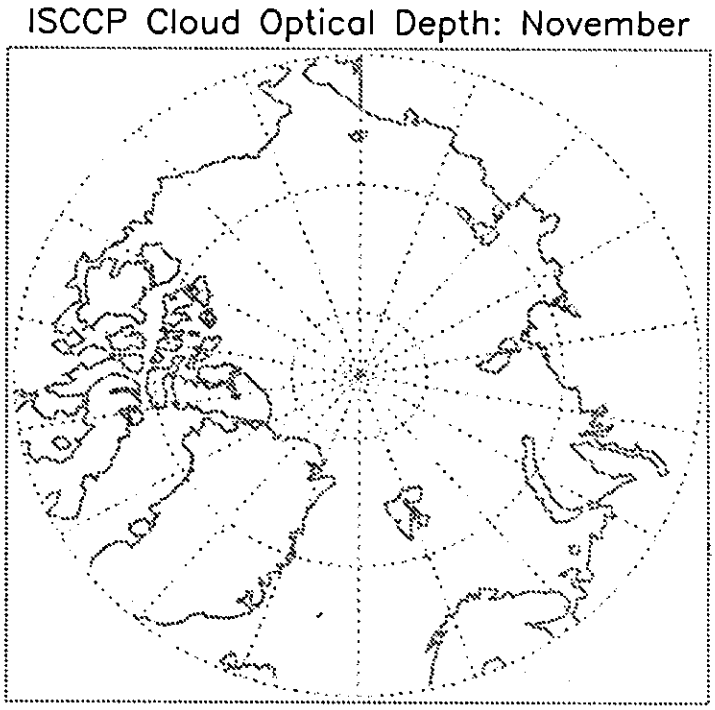

Units: Dimensionless

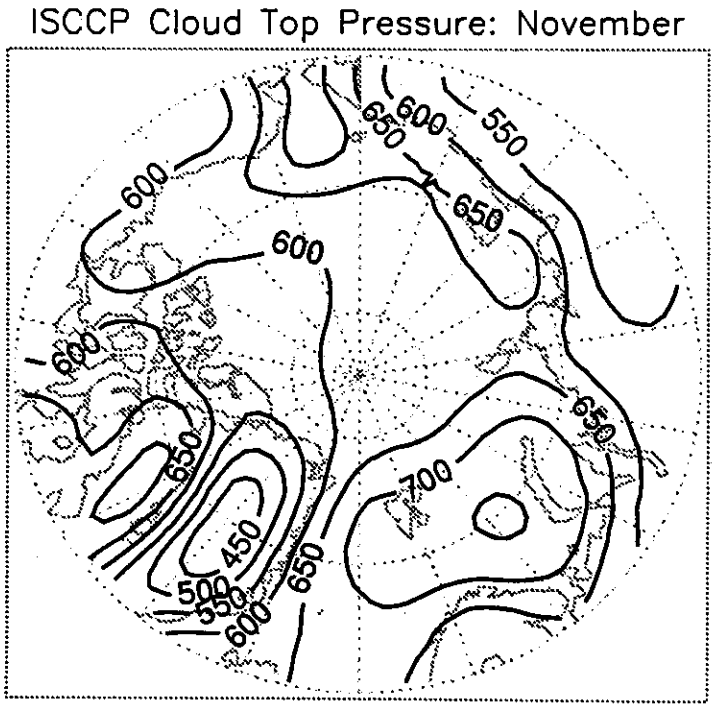

Units: mb

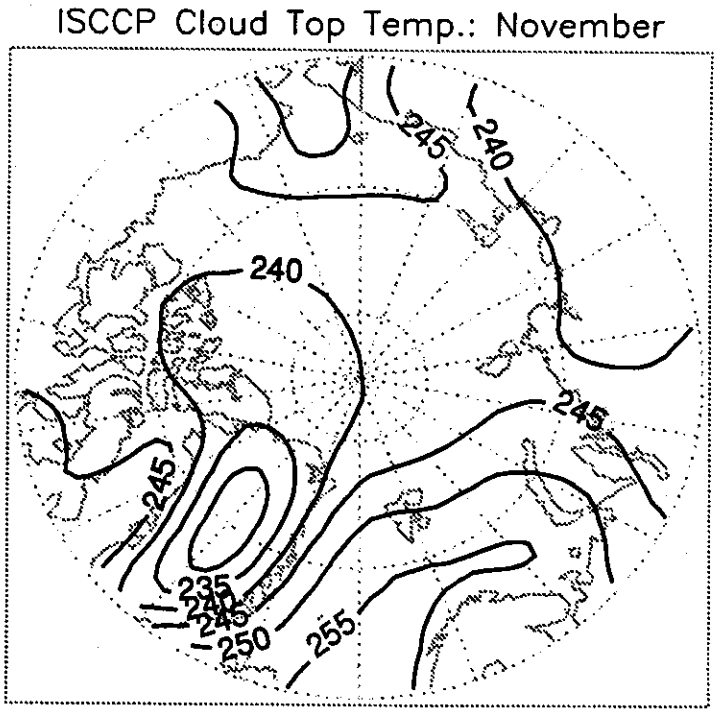

Units: K

Figure 1.5.1 (Continued)

ISCCP Cloud Cover: December

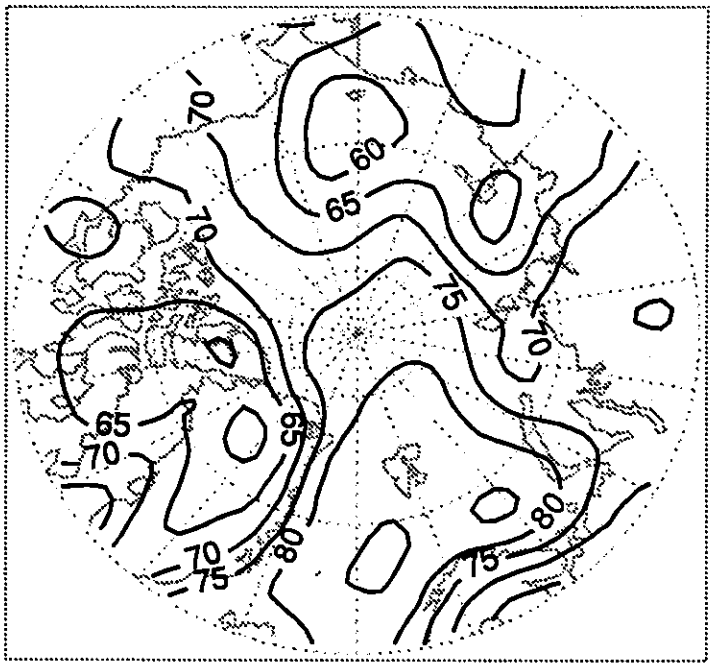

Units: %

ISCCP Cloud Optical Depth: December

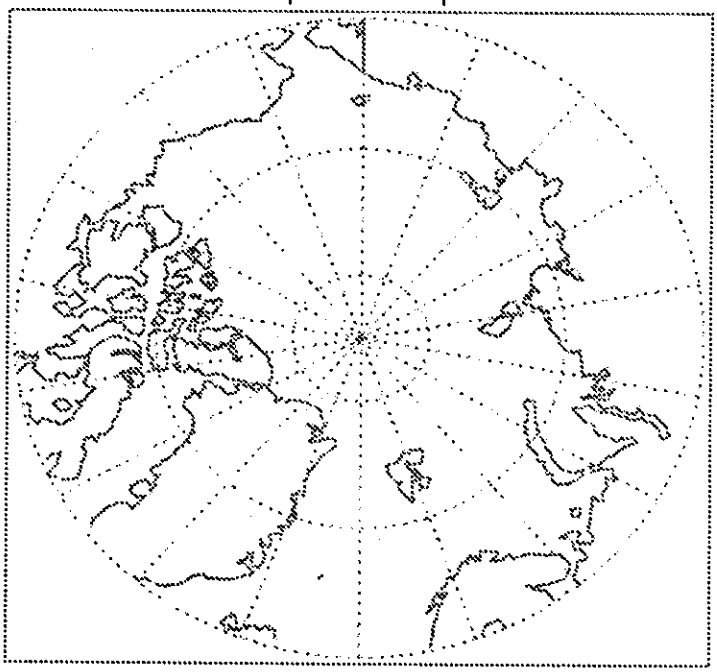

Units: Dimensionless

ISCCP Cloud Top Pressure: December

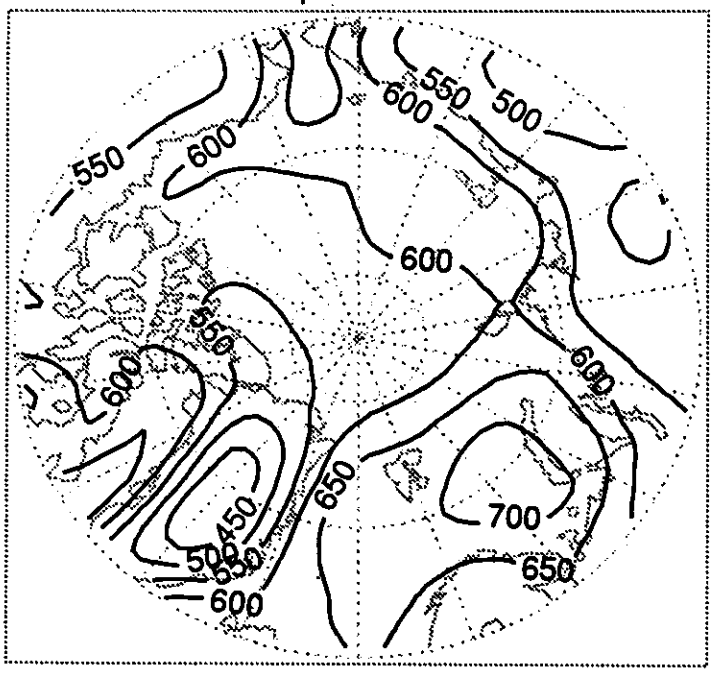

Units: mb

ISCCP Cloud Top Temp.: December

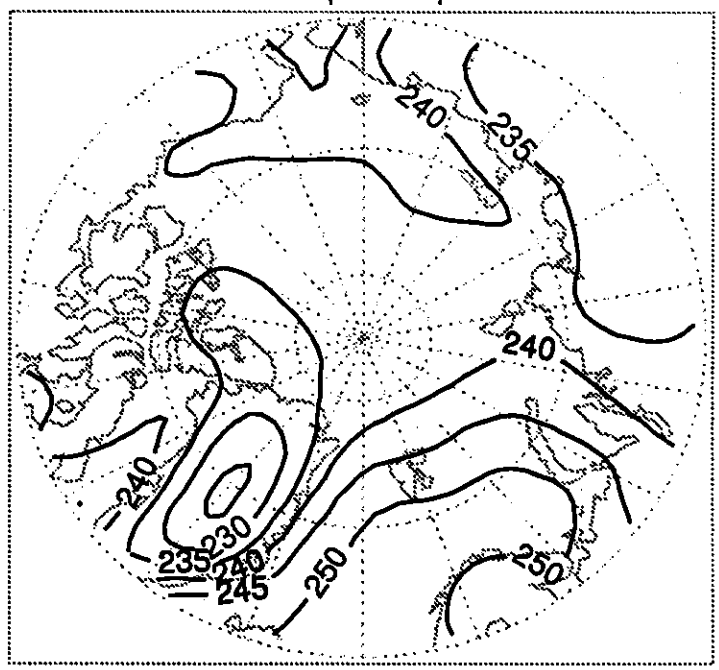

Units: K

2. SURFACE CLIMATE

2.1 Precipitation Totals

The spatio-temporal characteristics of Arctic Ocean precipitation are still uncertain. Mean monthly (Figure 2.1.1) and annual total (Figure 2.1.2) precipitation fields are presented based on the Legates and Willmott [1990] climatology and six-hourly forecasts from the NCEP/NCAR reanalysis [Kalnay et al., 1996], the latter evaluated over the period 1979-1995. For further comparison, Figure 2.1.2 also includes the annual climatology of Bryazgin [1976]. Both the Legates and Willmott and NCEP/NCAR climatologies were interpolated to the EASE-Grid. This interpolation largely eliminates local "bullseyes" in the NCEP/NCAR precipitation fields that result from a processing error in the model output.

The Legates and Willmott [1990] climatology is based on traditional land-based gauge measurements and shipboard estimates from ten different archival sources. A procedure was introduced to mitigate systematic biases caused by wind, wetting of the interior of the gauges and evaporation from the gauge. As far as we are aware, the Legates and Willmott [1990] product represents the best available observationally-based gridded (digital) climatology providing full Arctic coverage. However, we stress that the central Arctic Ocean values rely primarily on interpolation inwards from coastal sites (C. Willmott, pers. comm.). The NCEP/NCAR modeled fields hence provide a useful comparison. The analysis of Bryazgin [1976] is based on gauge-corrected data from fixed stations, aircraft landings and the Russian NP series of manned drifting camps for the period 1916-1974. Maps of annual and monthly mean precipitation compiled by Bryazgin, which contain more recent data, are also published in the "Atlas of the Water Balance of the Northern Polar Area" prepared by Russian scientists at the Arctic and Antarctic Research Institute [Khrol, 1996]. The annual map is very similar to that shown in Figure 2.1.2.

All of the annual maps in Figure 2.1.2 show a well-pronounced precipitation maximum over the Atlantic side of the Arctic where cyclone activity is frequent, with values decreasing towards the central Arctic Ocean. The monthly maps show this Atlantic-side maximum to be most pronounced for winter and weaken during summer, at which time precipitation increases over land areas and the central Arctic Ocean. Based on the Legates and Willmott [1990] climatology, the month of maximum precipitation for the SHEBA region is August (28 mm). By comparison, the NCEP/NCAR model predicts a July peak of about 38 mm. The model values for this area are higher in all months and particularly April-June. From grid-point difference maps (not shown), this appears typical of the model's representation of the Central Arctic. By contrast, it appears that the model values are generally too low for the Atlantic side of the Arctic. Bryazgin's monthly maps published in the Khrol [1996] atlas indicate an August through September precipitation maximum of 20-30 mm.

The annual totals for the SHEBA region summarized from Legates and Willmott are 124 mm, compared to 231 from the NCEP/NCAR model (Figure 2.1.3). The estimated corresponding value from Bryazgin [1976] and the map in the Khrol [1996] atlas is about 150 mm. Based on the general agreement between the two observed fields, an annual total for the SHEBA region of 125-150 mm is a reasonable estimate.

Colony et al. [1997] have summarized precipitation measurements from the Russian NP program collected over the years 1954-1990. The original data are available on a CD-ROM compiled by University of Washington's Polar Science Center and the National Snow and Ice Data Center (NSIDC). The measurements are considered to have an inherent accuracy of 1 mm. The data include corrections for gauge wetting. Corrections for blowing snow

are also incorporated by comparing measured gauge precipitation with snow liquid water equivalent obtained from snow line measurements. Figures 2.1.4 and 2.1.5, reproduced from Colony et al. [1997], are histograms of monthly precipitation for the cold half (November-April) and warm half (June-October) of the year, respectively. These results are based on grouping together all available NP measurements. Most observations are from north of 80°N and along the Eurasian side of the Arctic Ocean for lower latitudes. Figure 2.1.3 suggests that precipitation for these areas is somewhat higher than for the Beaufort Sea, but the results nevertheless provide some sense of the range of conditions that could be encountered in the SHEBA region. Immediately apparent from the histograms is a higher mean over the Central Arctic for the warm half of the year. It appears that months with zero precipitation are rare during the warm half of the year and that occasional months may have precipitation totals exceeding 40 mm. Fewer such extreme events occur during the cold half of the year.

Figure 2.1.1

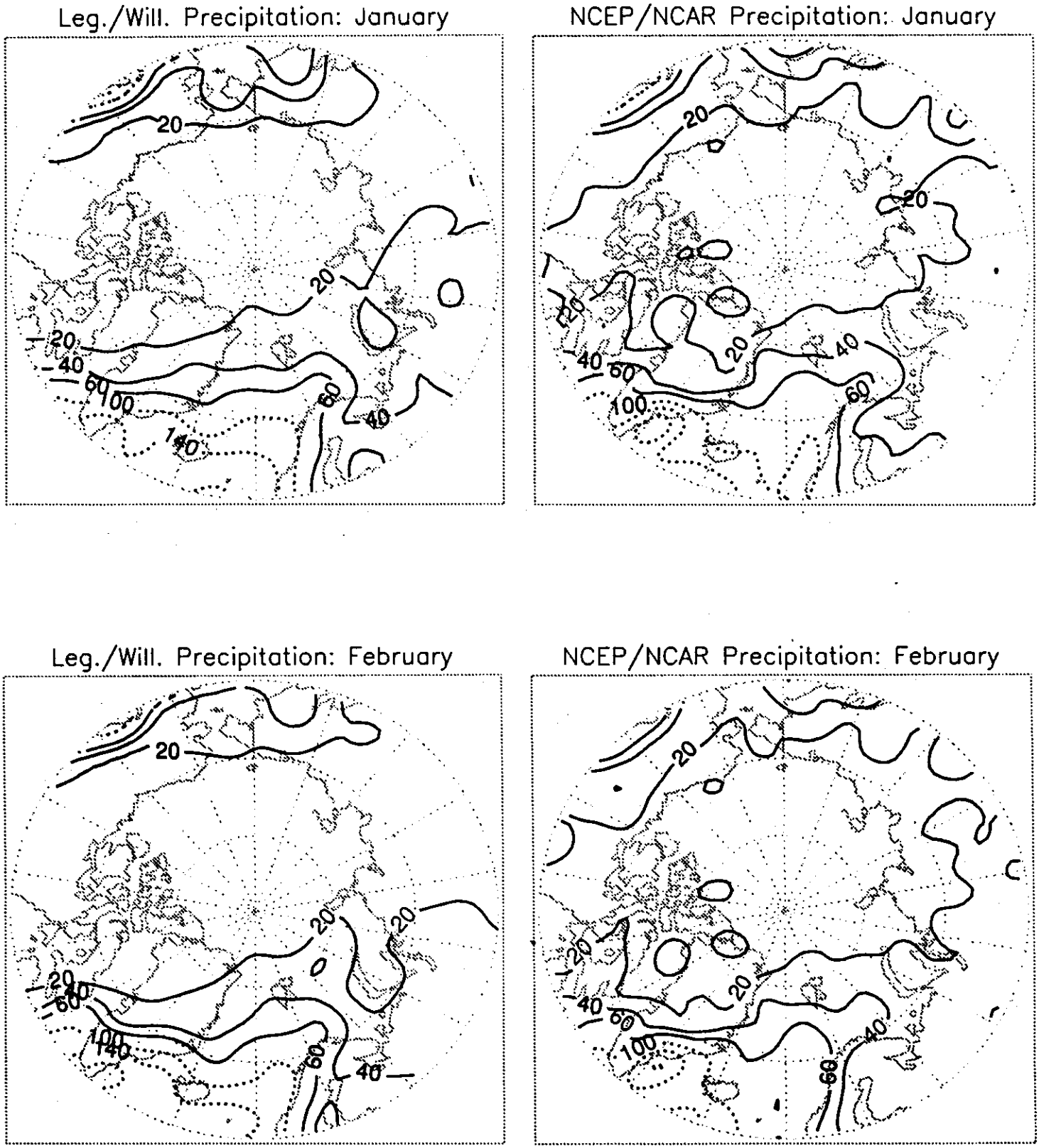

Units: Millimeters
Contours: 0-60 x 20 (solid), 100+ x 40 (dotted)

Figure 2.1.1 (Continued)

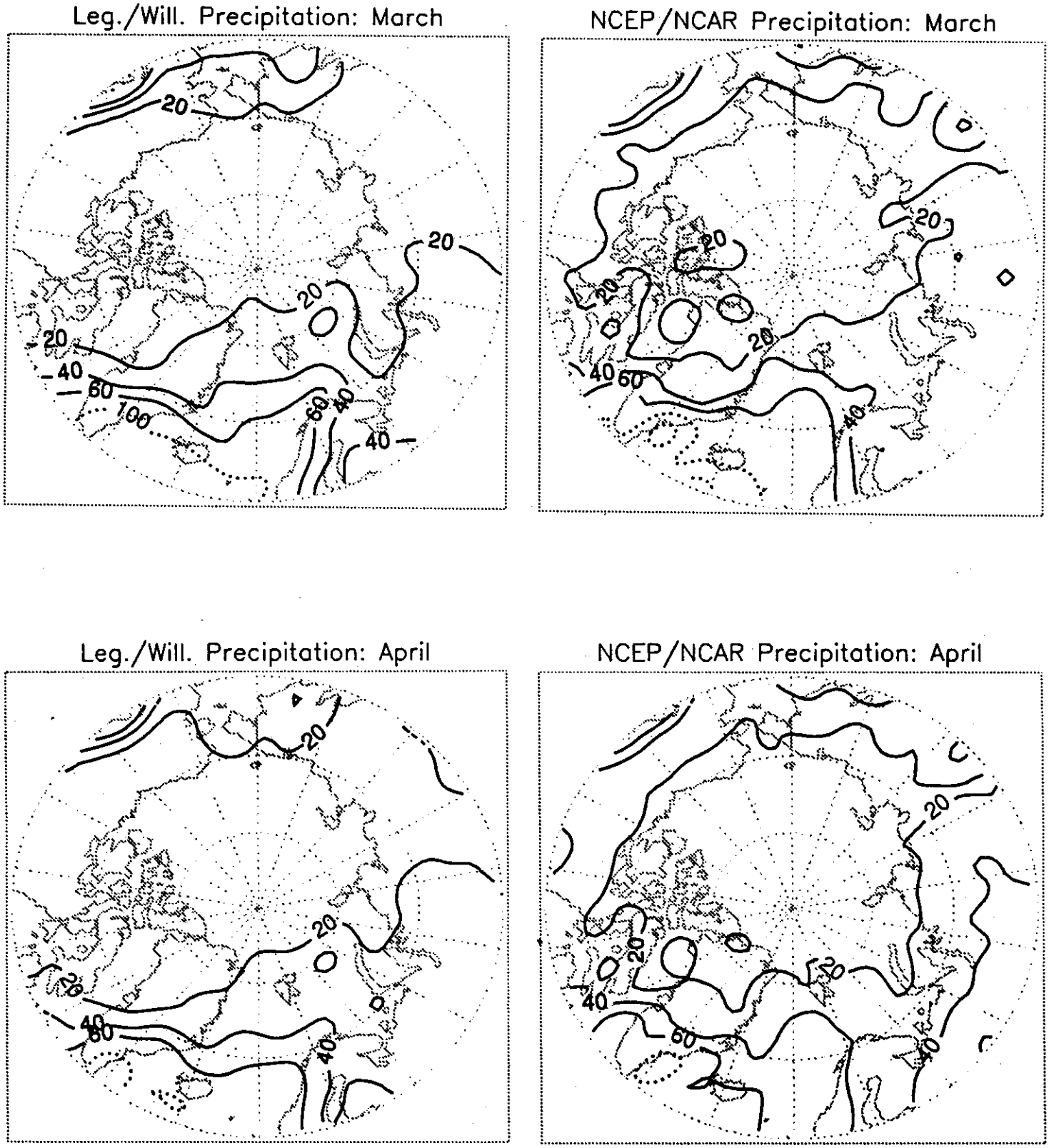

Units: Millimeters
Contours: 0-60 x 20 (solid), 100+ x 40 (dotted)

Figure 2.1.1 (Continued)

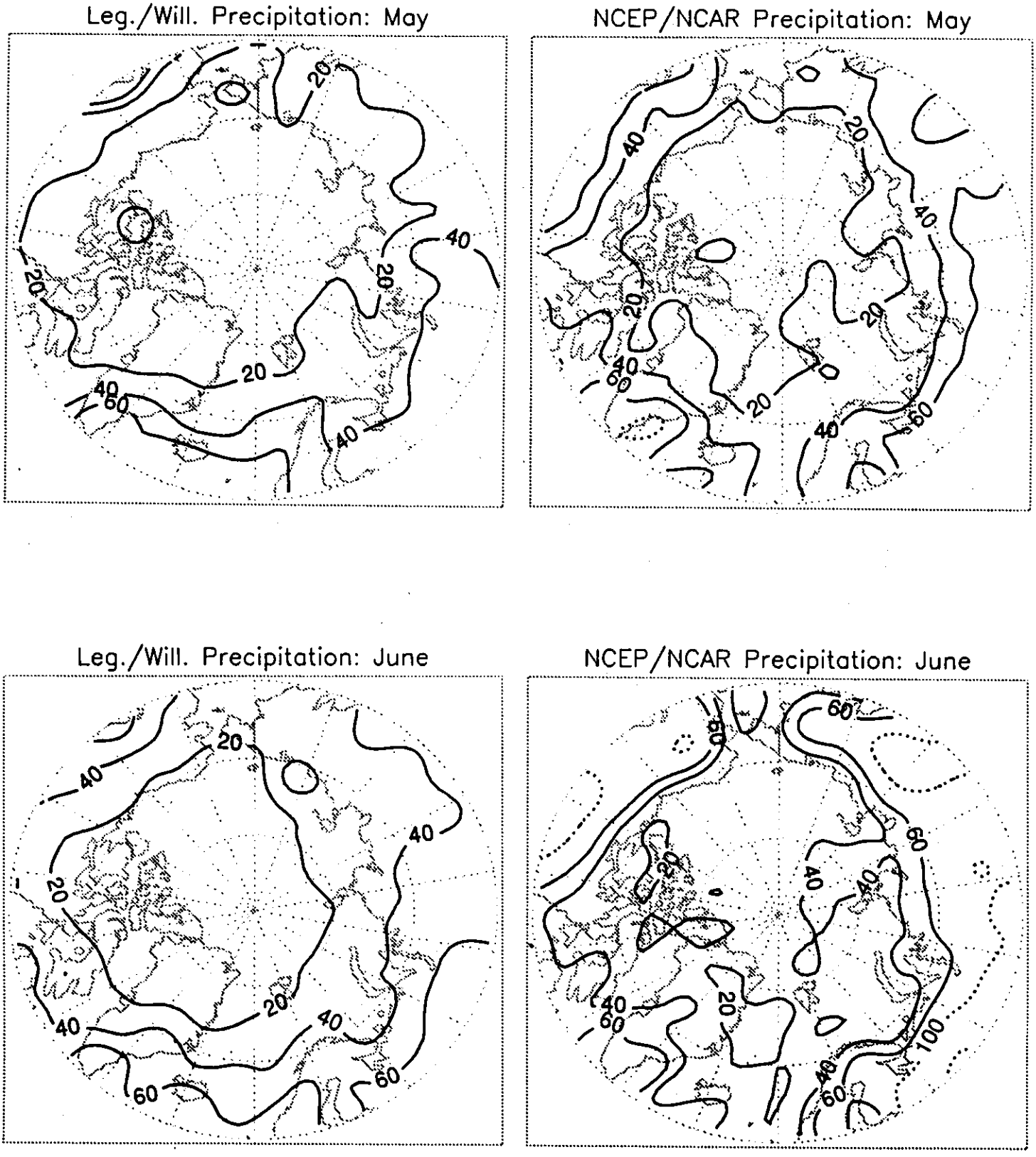

Units: Millimeters
Contours: 0-60 x 20 (solid), 100+ x 40 (dotted)

Figure 2.1.1 (Continued)

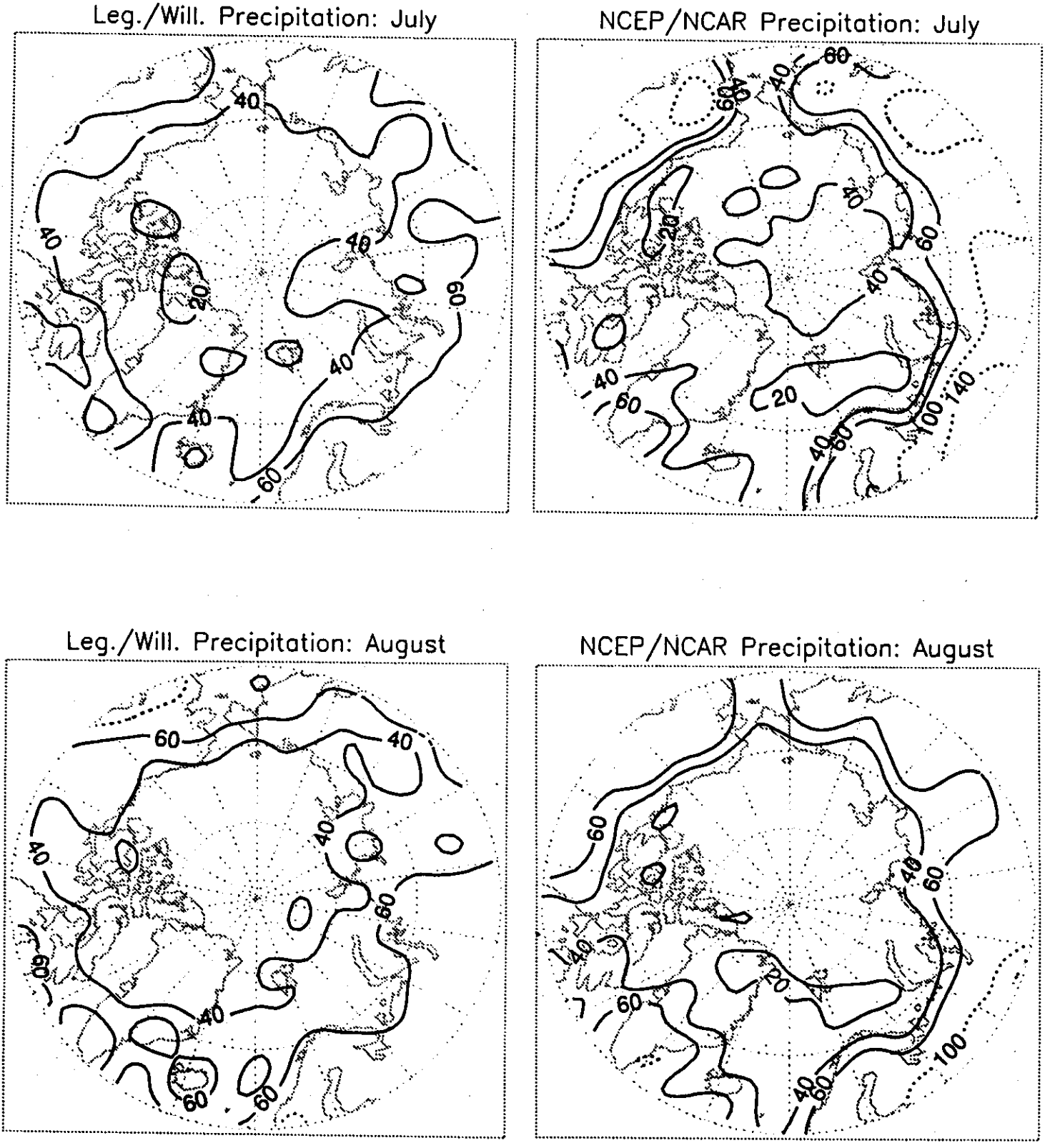

Units: Millimeters
Contours: 0-60 x 20 (solid), 100+ x 40 (dotted)

Figure 2.1.i (Continued)

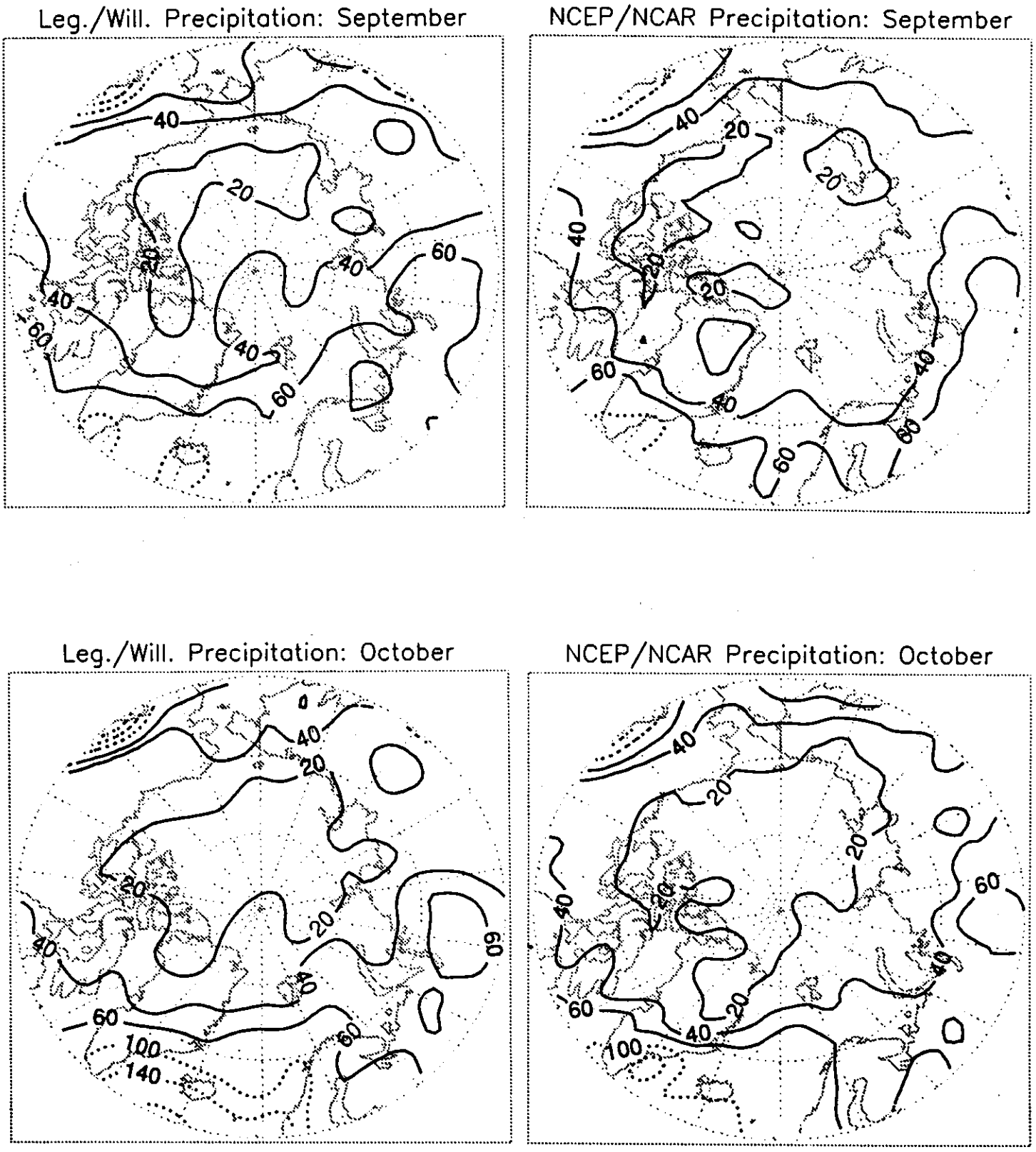

Units: Millimeters
Contours: 0-60 x 20 (solid), 100+ x 40 (dotted)

Figure 2.1.1 (Continued)

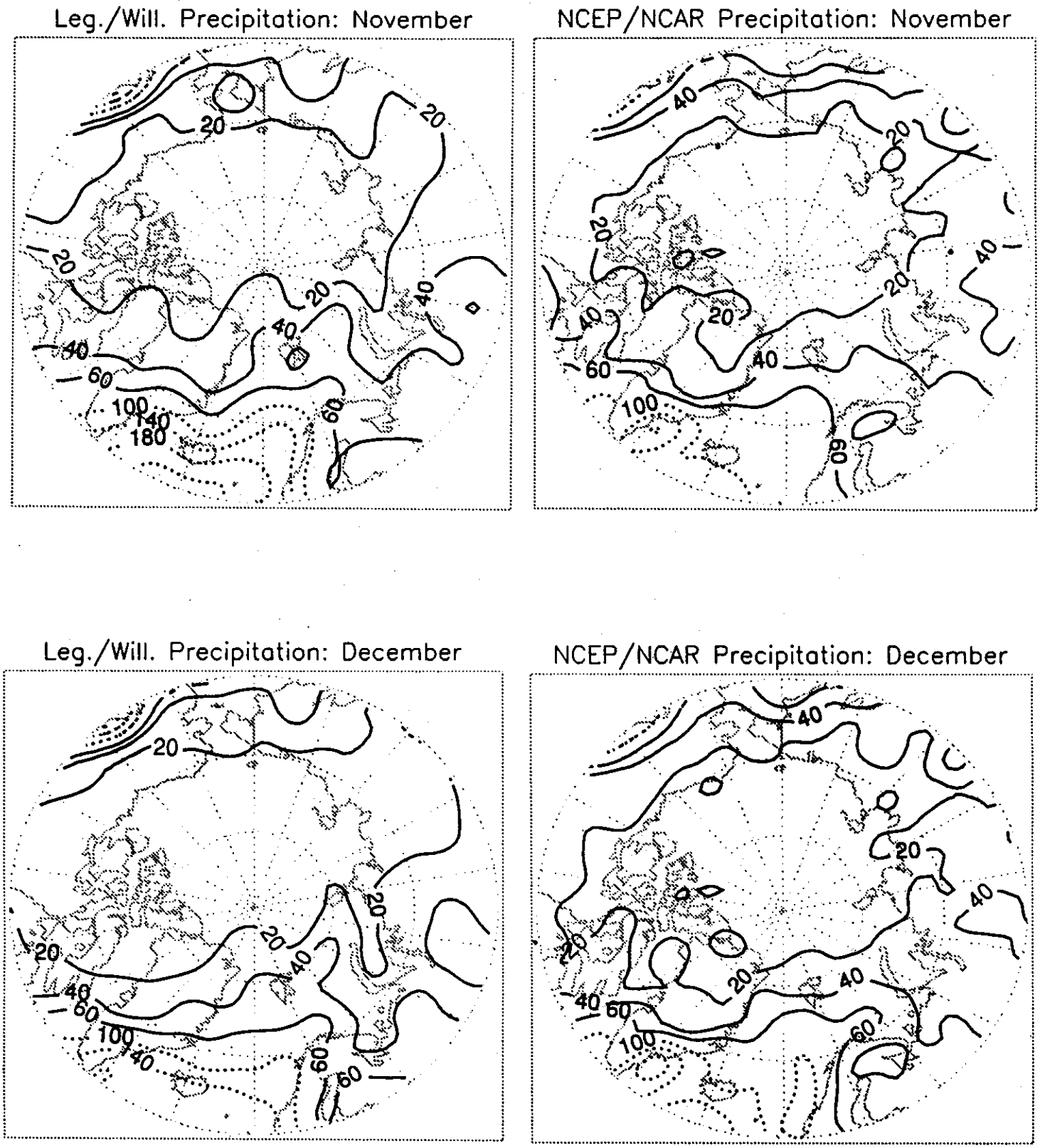

Units: Millimeters
Contours: 0-60 x 20 (solid), 100+ x 40 (dotted)

Figure 2.1.2

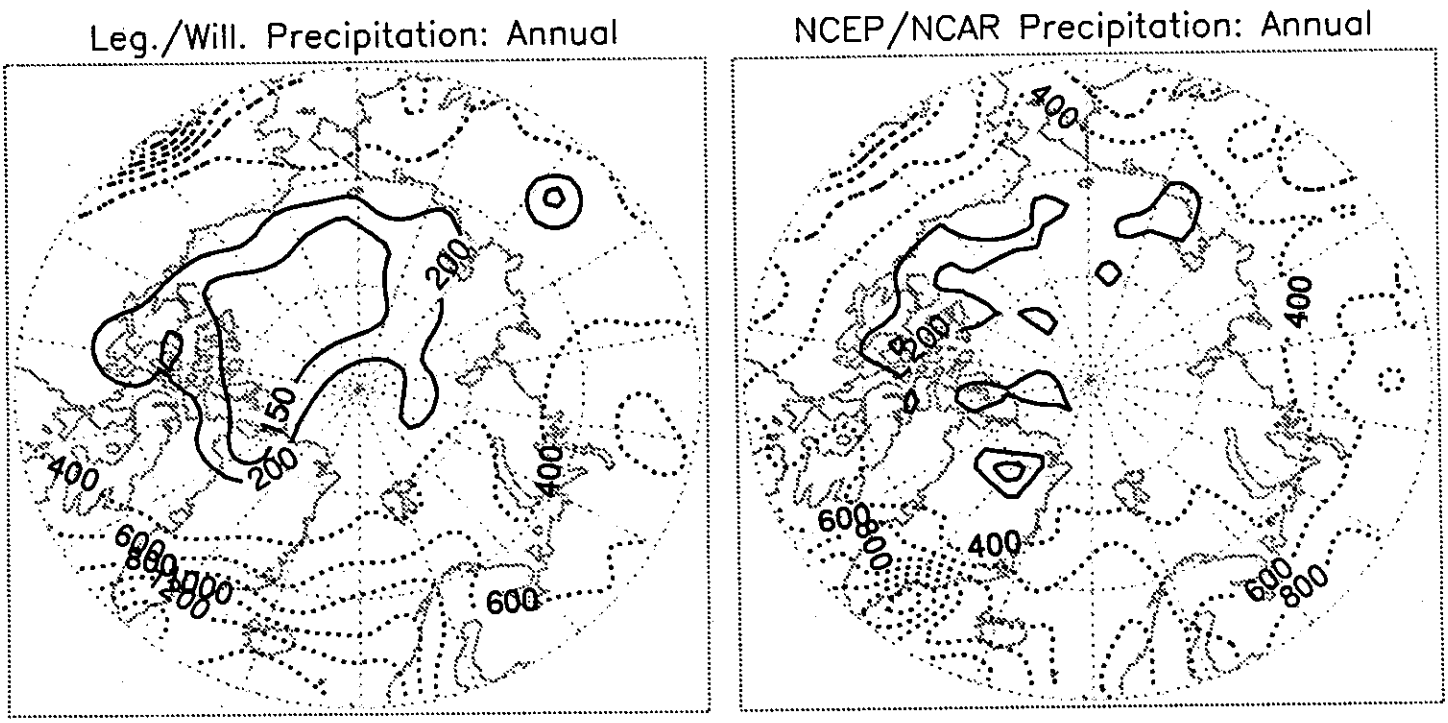

Annual Precipitation (Bryazgin, 1976)

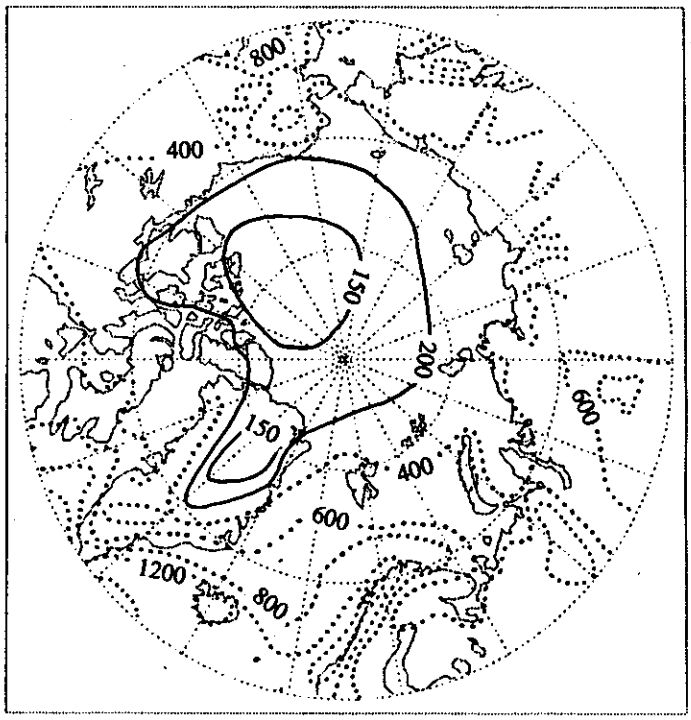

Units: mm
Contours: 0-200 x 50 (solid), 200-2000 x 200 (dotted)

Figure 2.1.3

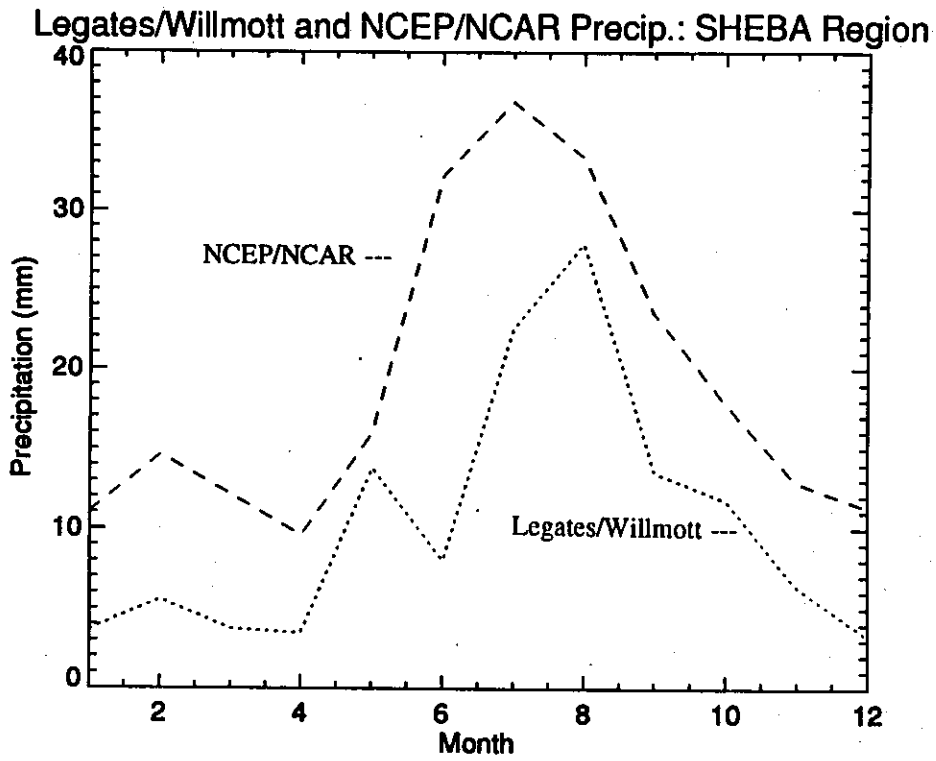
Legates/Willmott and NCEP/NCAR Precip.: SHEBA Region
Precipitation (mm)
Month
NCEP/NCAR ---
Legates/Willmott ---
0
10
20
30
40
2
4
6
8
10
12

Figure 2.1.4

Histogram of Total Precipitation for the Cold Half of the Year (November-May) from Russian North Pole Measurements (Reproduced from Colony et al., 1997).

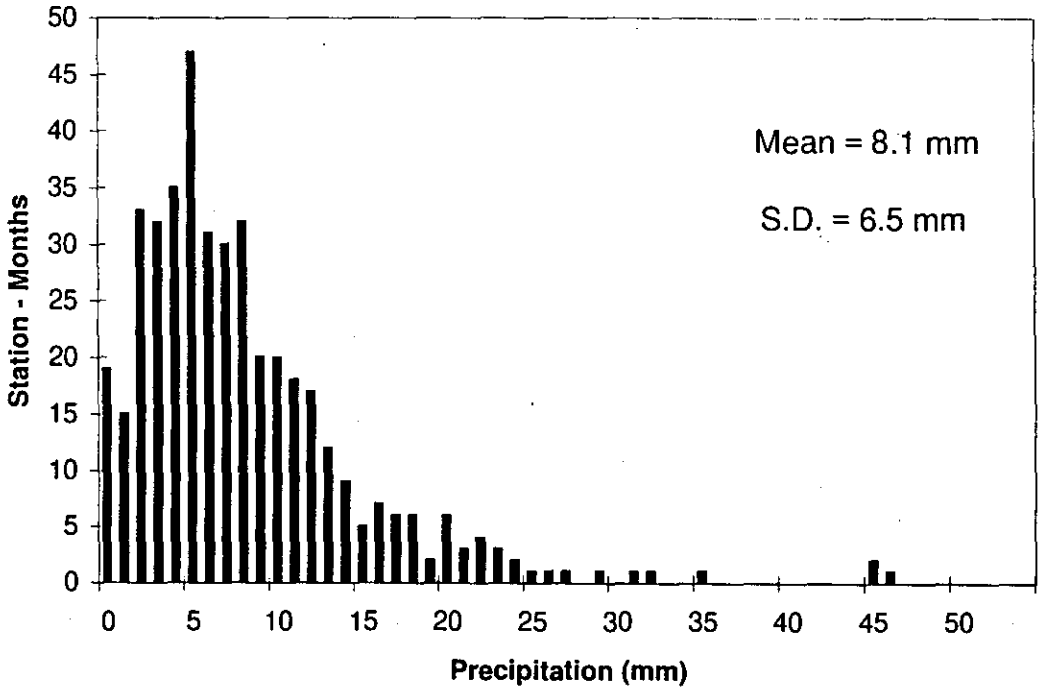

Figure 2.1.5

Histogram of Total Precipitation for the Warm Half of the Year (June-October) from Russian North Pole Measurements (Reproduced from Colony et al., 1997).

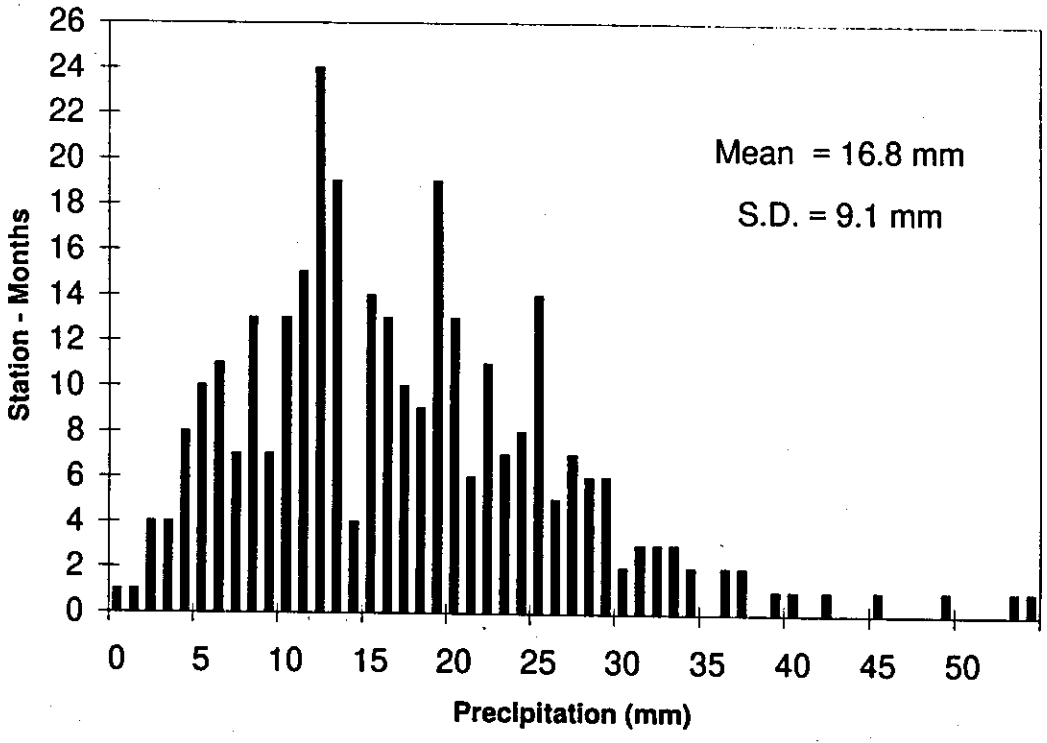

2.2 Precipitation Characteristics

The COADS "present weather" codes for 1950-1995 [Woodruff et al., 1987] used for analyses of cloud conditions (Section 1.4) also allow for evaluation of Arctic Ocean precipitation characteristics (but not amount). Following Petty [1995], the present weather codes (which provide information on the occurrence of precipitation, as well as precipitation phase and intensity) were analyzed in terms of monthly precipitation frequency (the percent of valid weather observations for which precipitation is reported) and the frequencies of solid precipitation, liquid precipitation and moderate/heavy precipitation (with respect to all precipitation reports in which phase and intensity could be determined). Data failing COADS quality-control flags were first eliminated. Cases with missing cloud cover observations were also discarded, limiting reports to those made by human observers as opposed to automated stations. As outlined by Petty [1995] and Clark et al. [1996], who undertook a pilot study of precipitation characteristics as part of their Arctic Ocean study, this mitigates an important ambiguity in interpreting missing weather codes. Starting in 1982, a missing code could either mean that no observation was taken or that no significant weather occurred. This information was not archived by the U.S. Global Telecommunication system until May of 1984. In 1985 a change was added to the World Meteorological Organization (WMO) format for international exchange of keyed log book data to distinguish between the two types, but inconsistencies have been found even subsequent to 1985. Further caveats regarding use of the COADS data are provided by Petty [1995]. Results are summarized for the same Arctic Ocean EASE-Grid locations used for the COADS cloud cover analyses (Figure 2.2.1). We required that each monthly grid point value of precipitation frequency be based on at least 150 present weather observations and that the intensity and phase frequencies be based on at least 150 observations for which phase and frequency could be determined. As with the cloud cover analyses, a 600 km search radius was used.

For the Atlantic side of the Arctic, precipitation frequency and the intensity of moderate/heavy precipitation have a winter maximum and summer minimum, consistent with the seasonality in precipitation totals shown in Section 2.1 and corresponding changes in the strength of the North Atlantic cyclone track. Even during winter, a sizable fraction of Atlantic-side precipitation is in liquid form. Away from the Atlantic side, precipitation frequency exhibits an April minimum but otherwise no obvious seasonal cycle. Most months show a relative minimum in precipitation frequency over the southern Beaufort Sea. This appears to be parallel by a relative minimum in the frequency of moderate/heavy precipitation frequency although results for many grid points are missing due to a lack of sufficient data. For July, typically 40-50% of precipitation over most of the central Arctic falls in liquid form, compared to less than 5% for most winter months. The seasonal cycle in precipitation phase for the SHEBA region (Figure 2.2.2) shows 60% of all precipitation events representing rain during July. About 15% of all reports represent mixed precipitation and the remainder solid precipitation. Because of the problem of missing data, values for several months in this figure rely on data for surrounding grids.

The relative minimum in precipitation frequency over the southern Beaufort Sea is in accord with the generally anticyclonic conditions in this region and is also reflected in reduced cloud cover. However, the COADS results for this region (and the central Arctic in general) show no evidence for the summer maximum in precipitation amounts to be accompanied by pronounced increases in either precipitation frequency or intensity. In part, this may represent an artifact of the comparatively few COADS present weather observations in the Beaufort Sea. A related problem is that given the broad range of conditions represented by the moderate/heavy precipitation class, seasonal changes in precipitation intensity within this low-precipitation region may be largely masked.

Figure 2.2.1

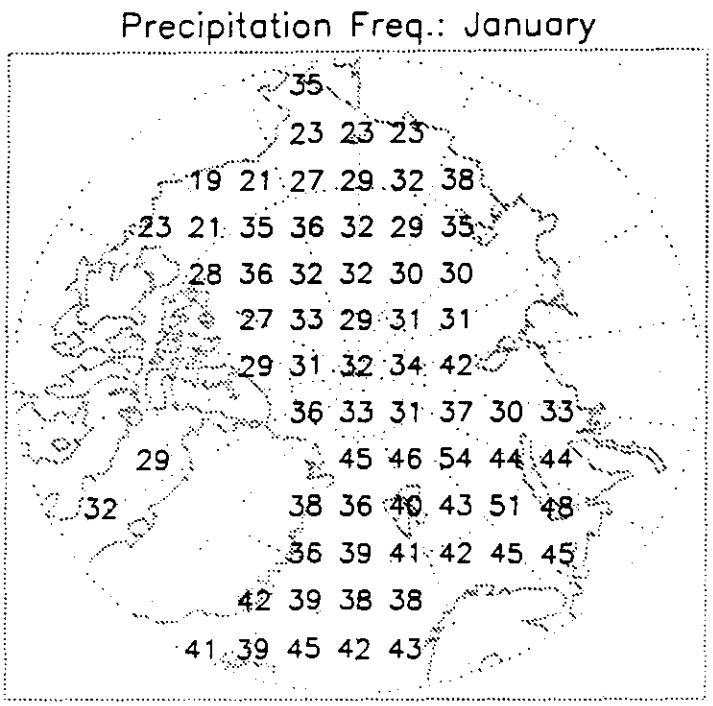

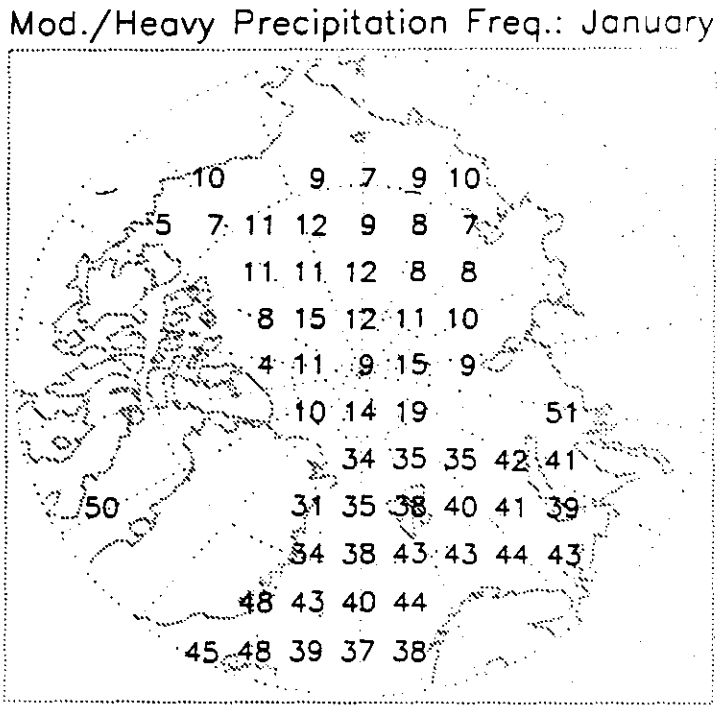

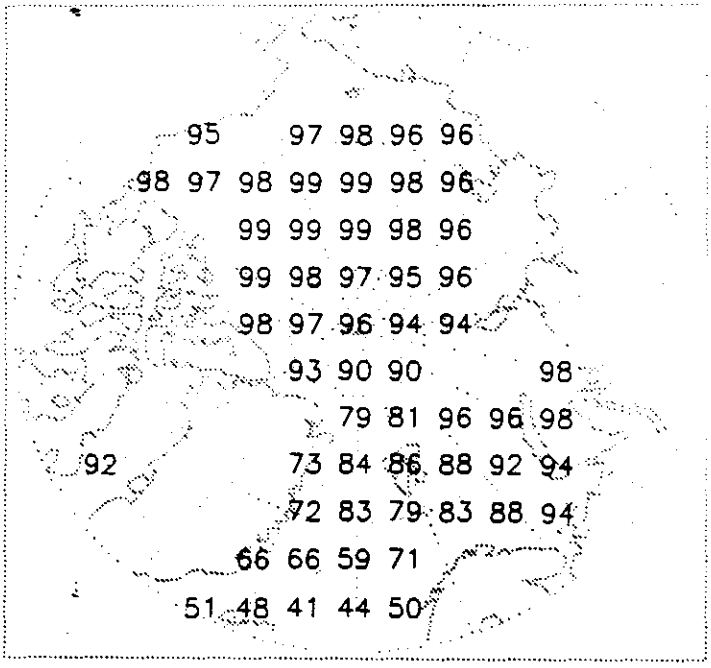

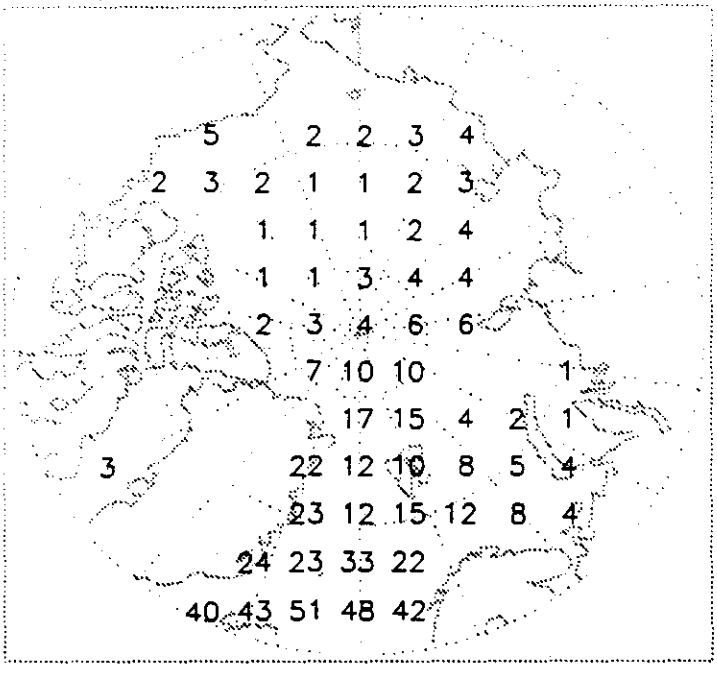

Units: % Frequency

Figure 2.2.1 (Continued)

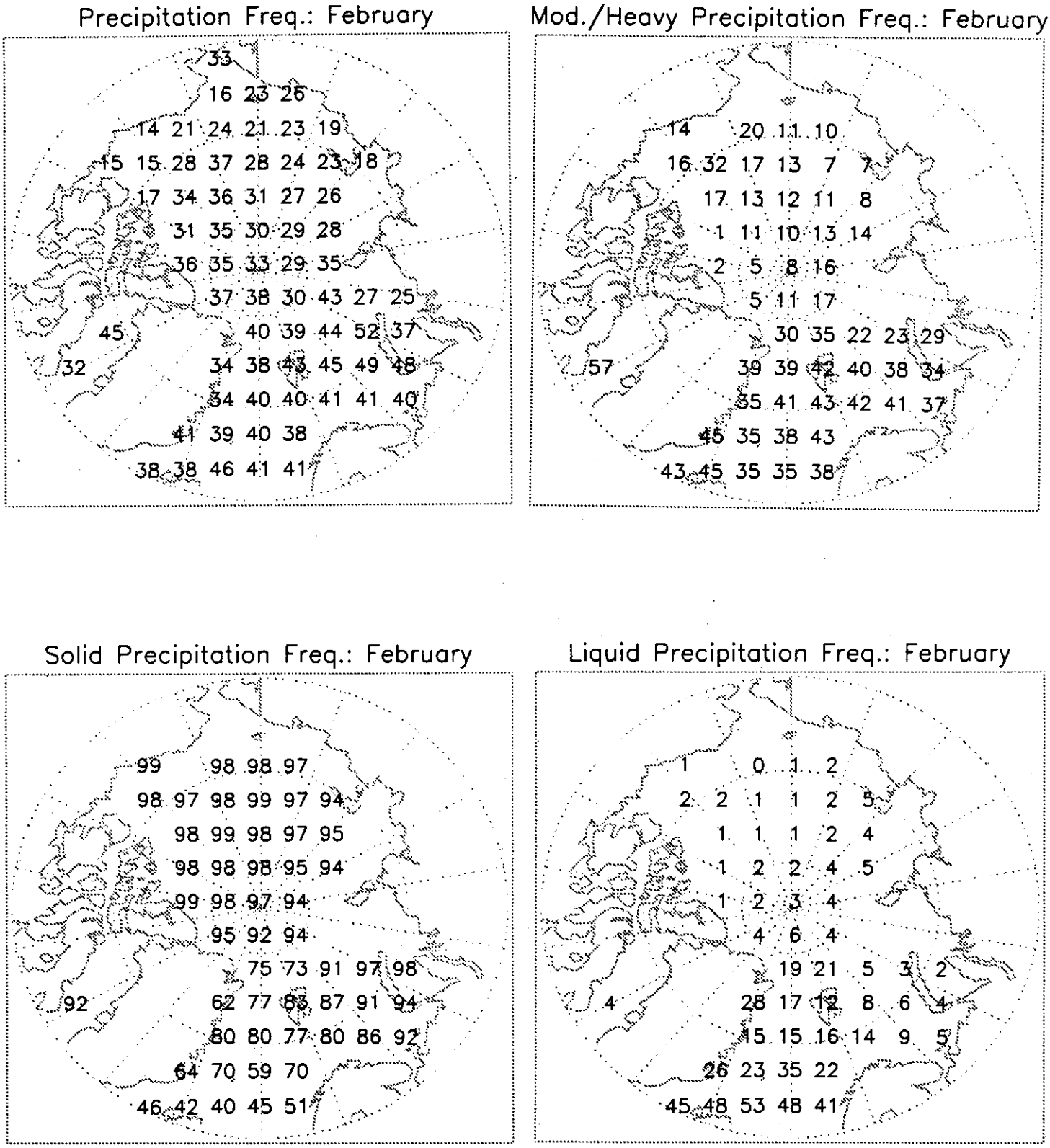

Units: % Frequency

Figure 2.2.1 (Continued)

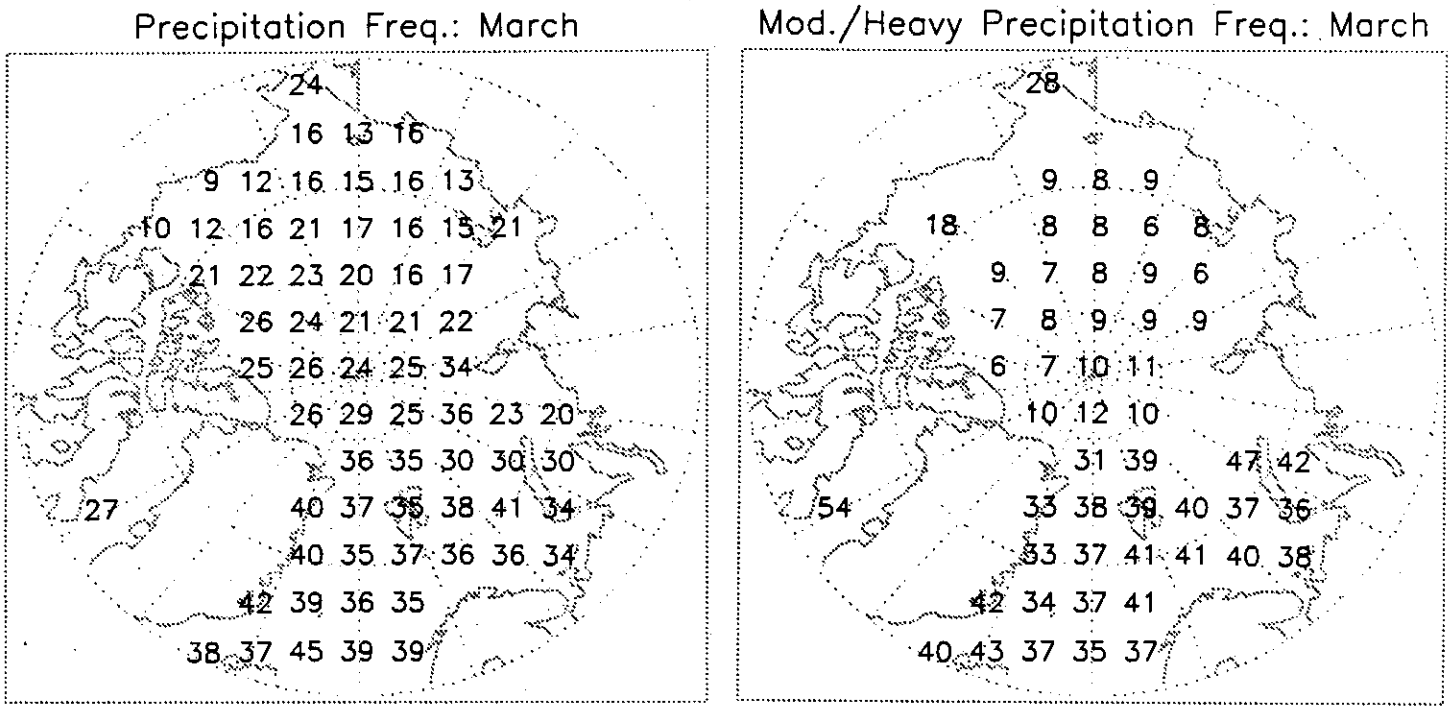

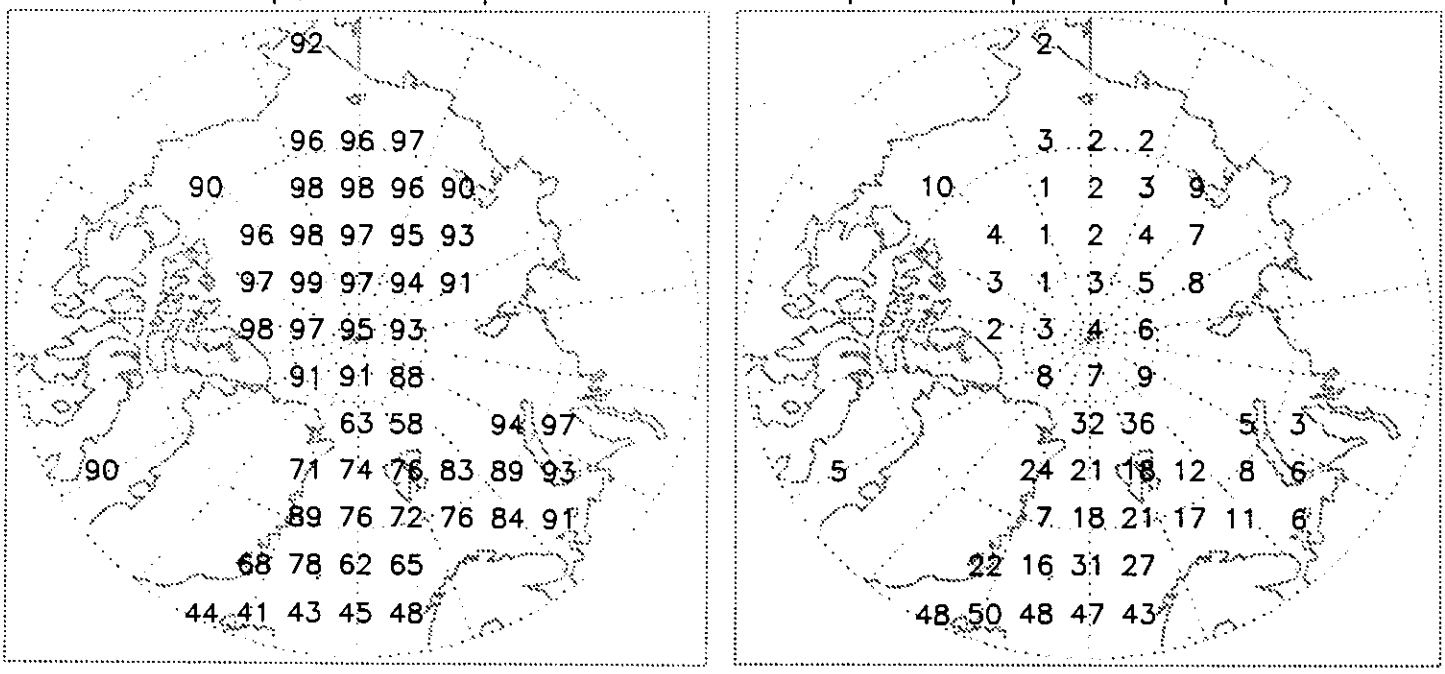

Units: % Frequency

Figure 2.2.1 (Continued)

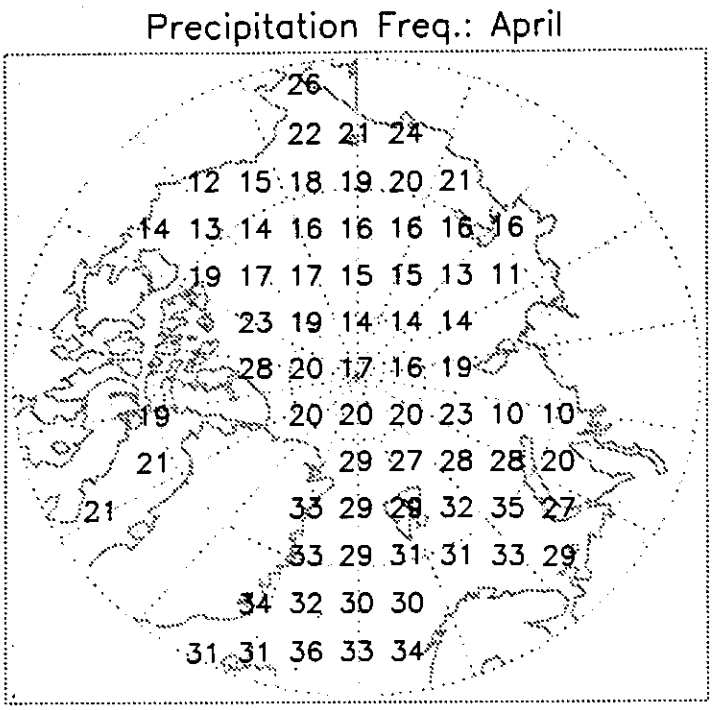

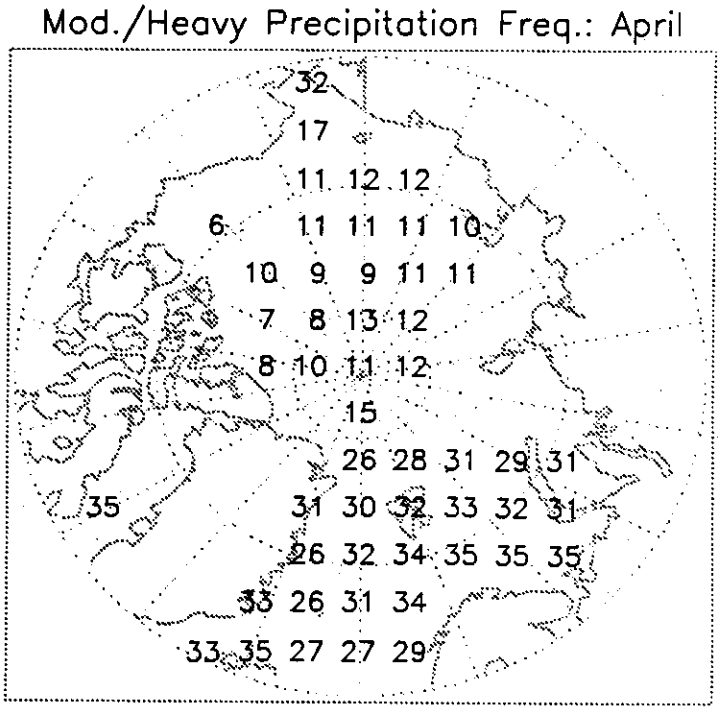

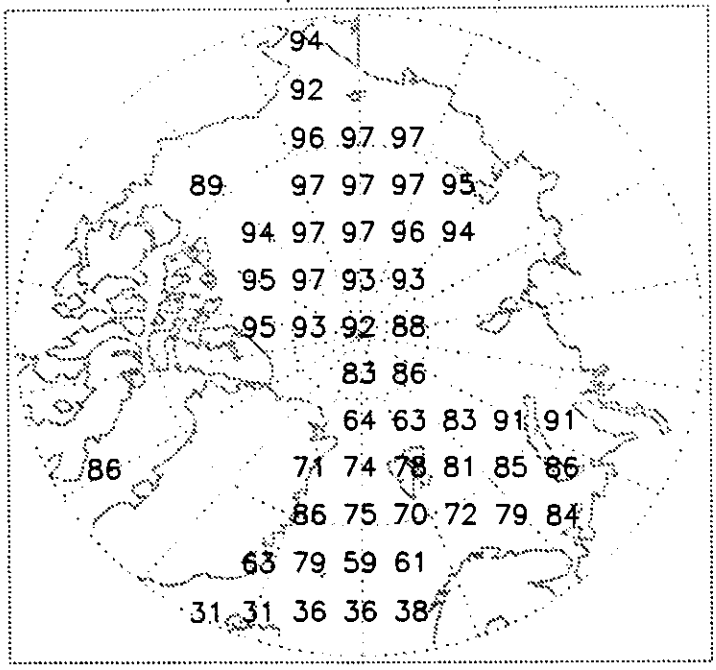

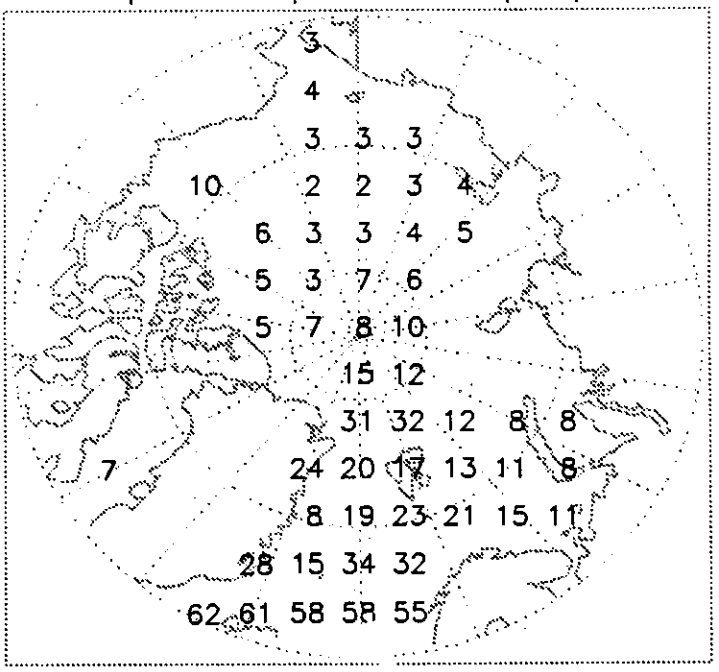

Units: % Frequency

Figure 2.2.1 (Continued)

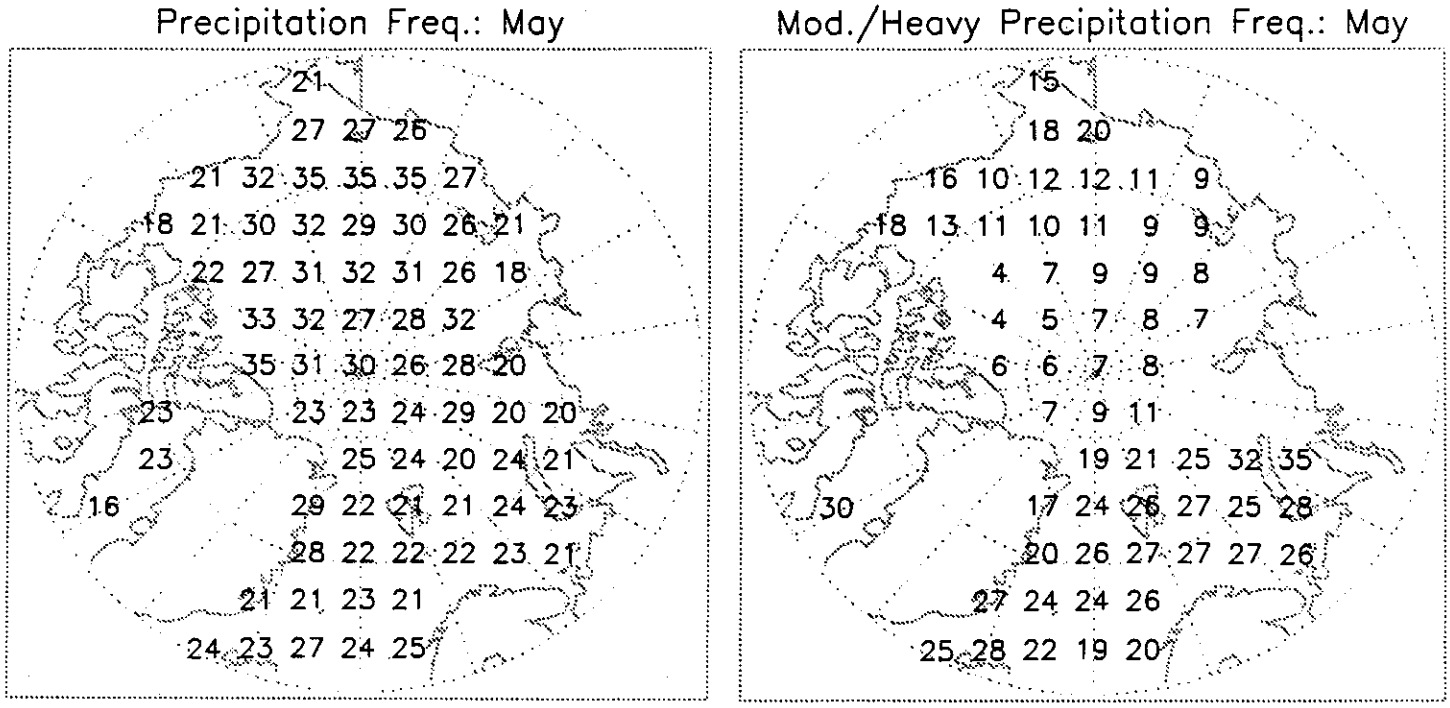

Units: % Frequency

Figure 2.2.1 (Continued)

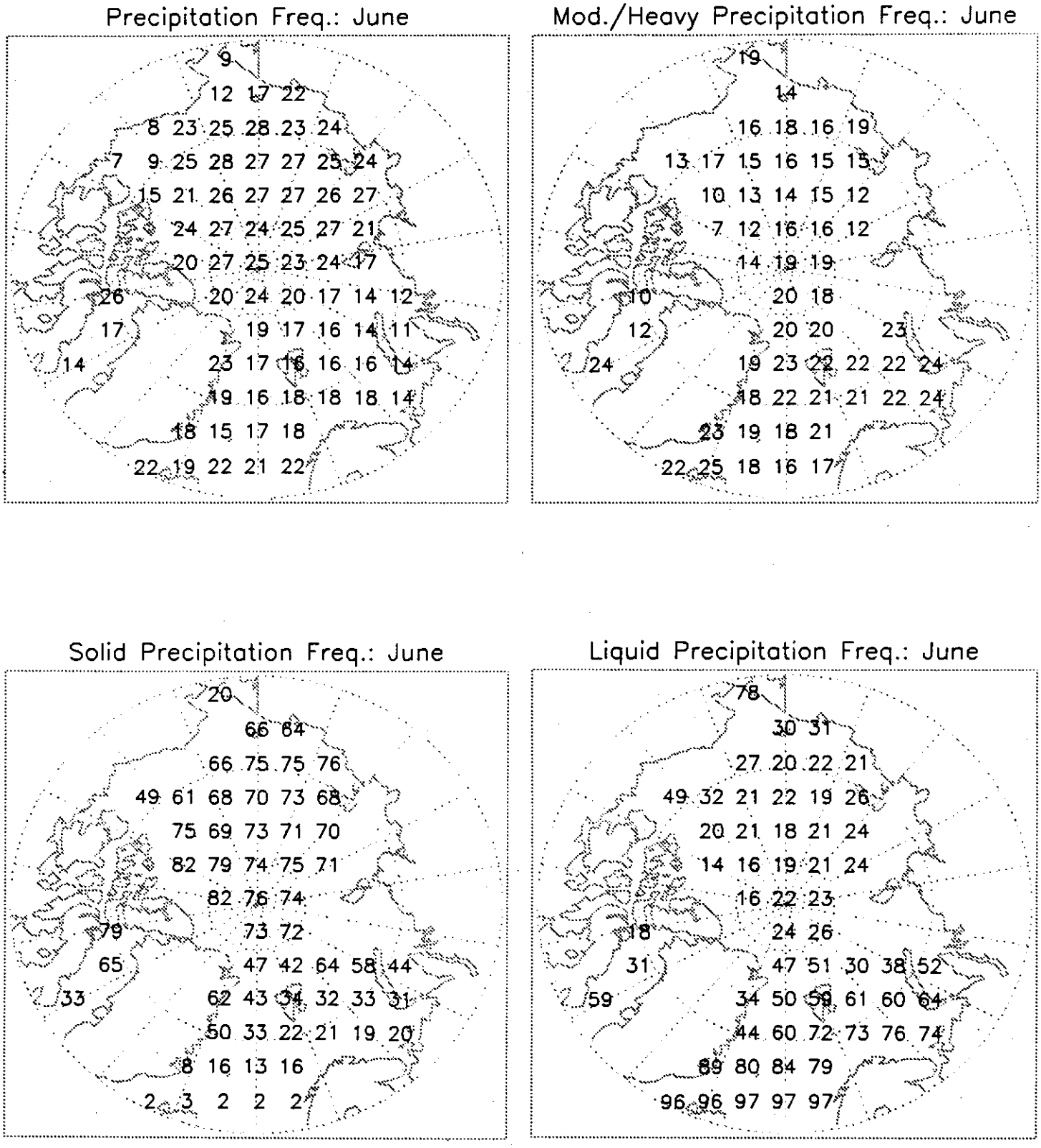

Units: % Frequency

Figure 2.2.1 (Continued)

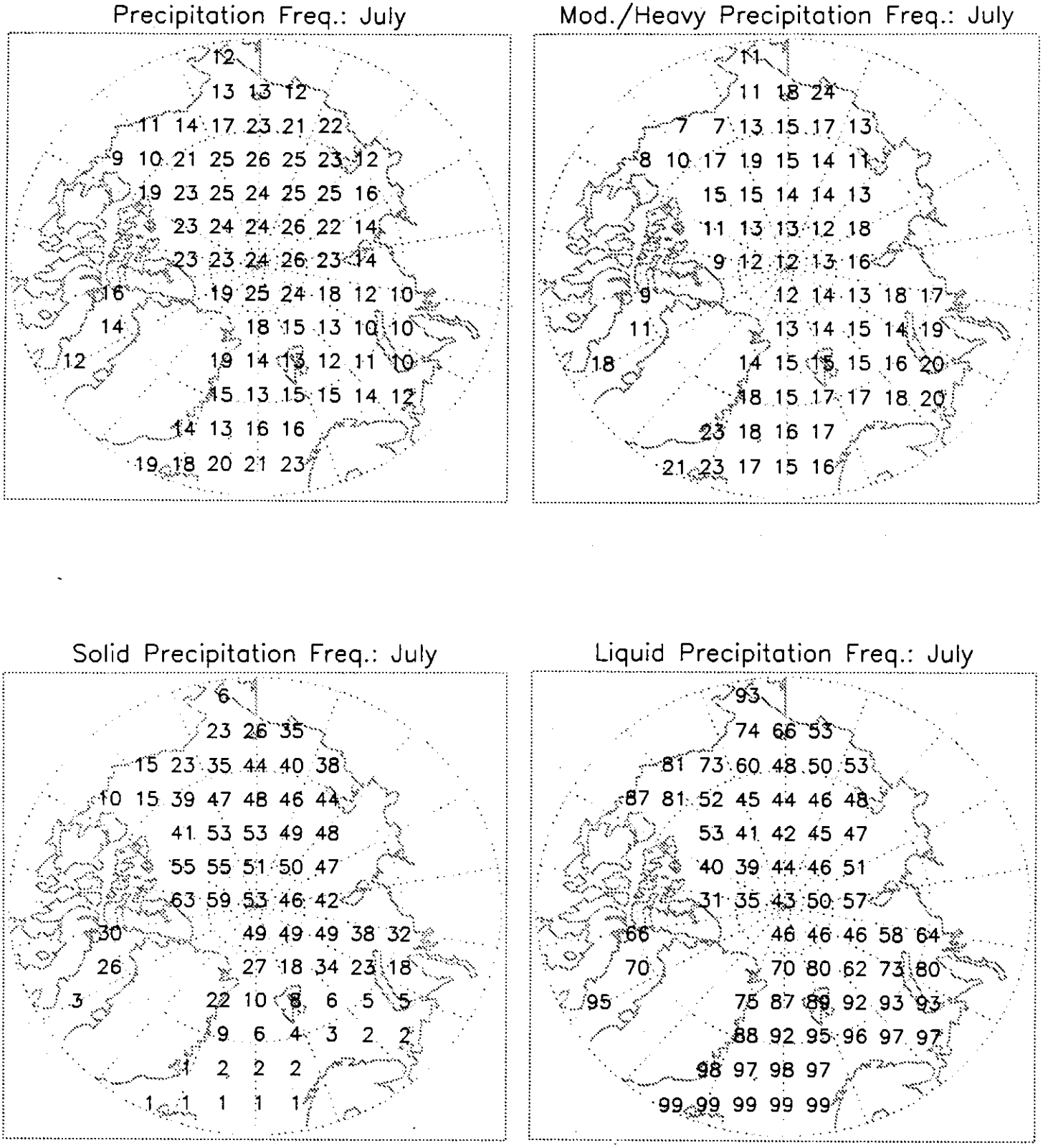

Units: % Frequency

Figure 2.2.1 (Continued)

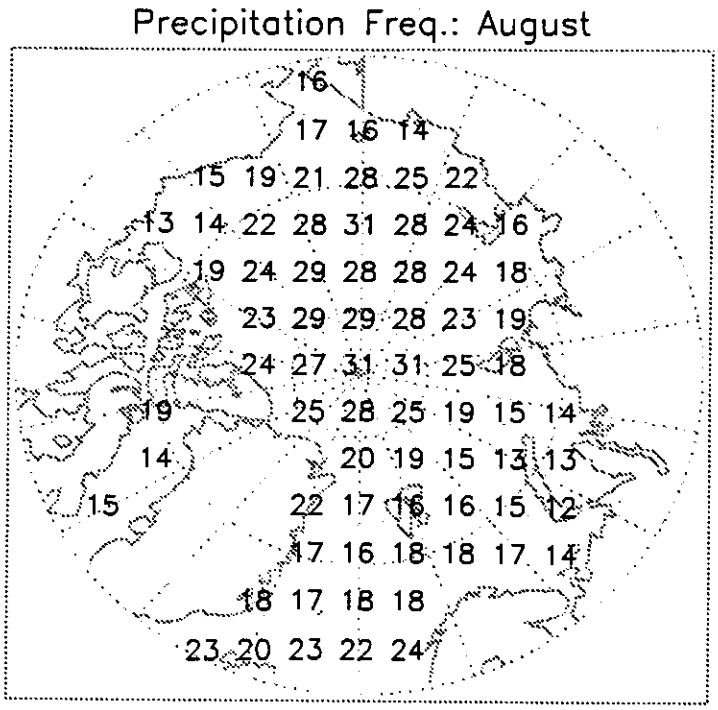

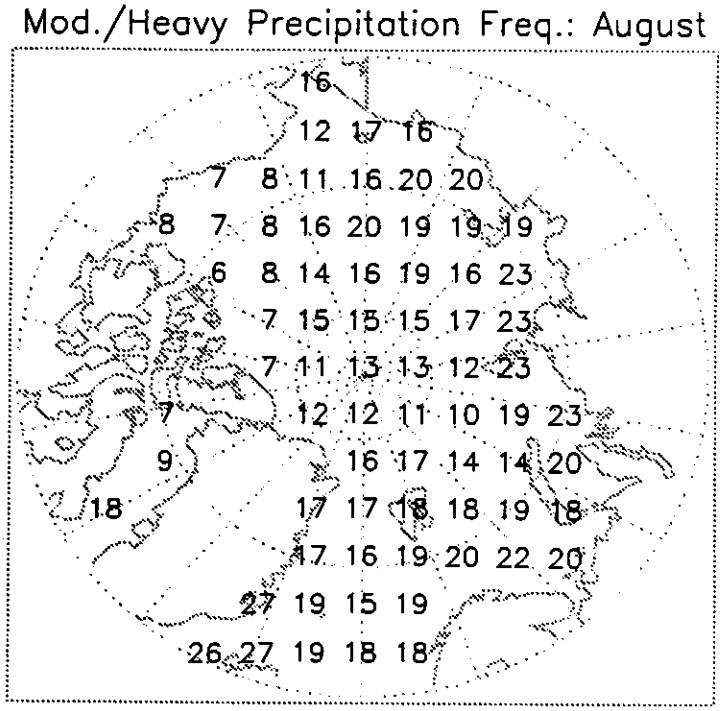

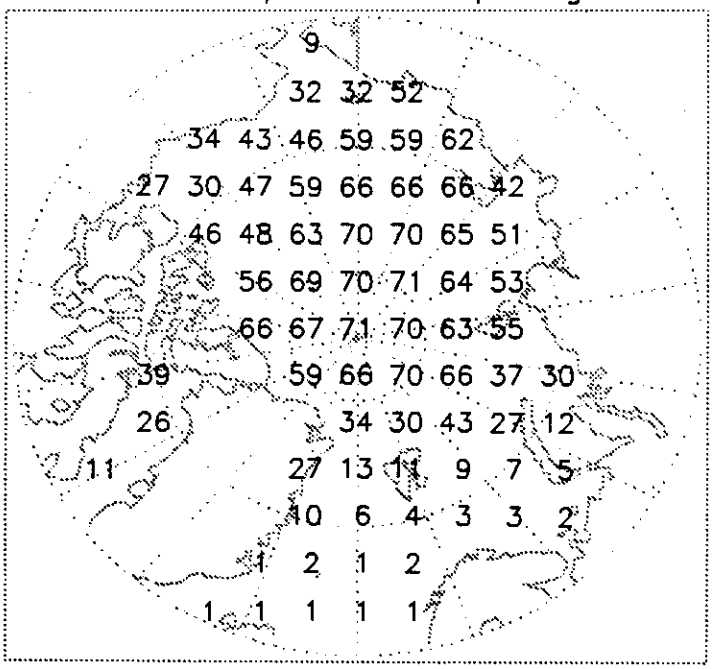

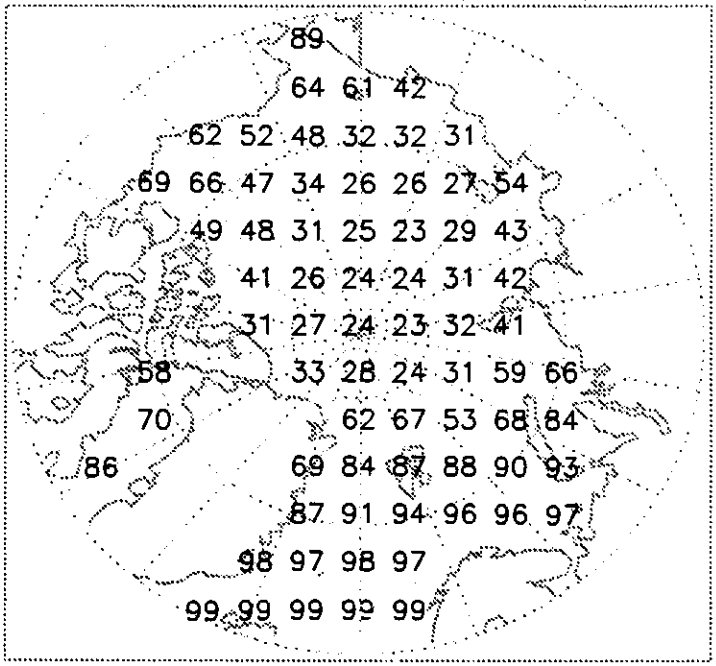

Units: % Frequency

Figure 2.2.1 (Continued)

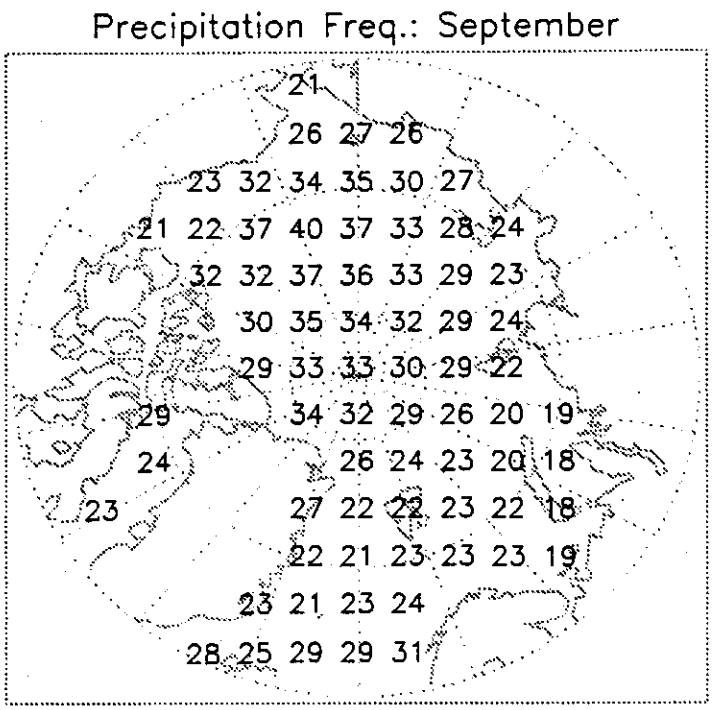

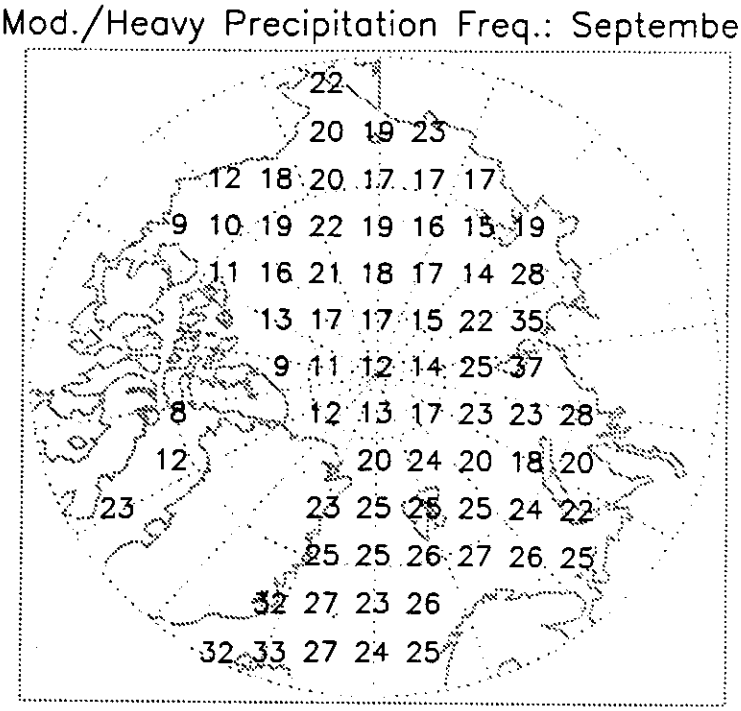

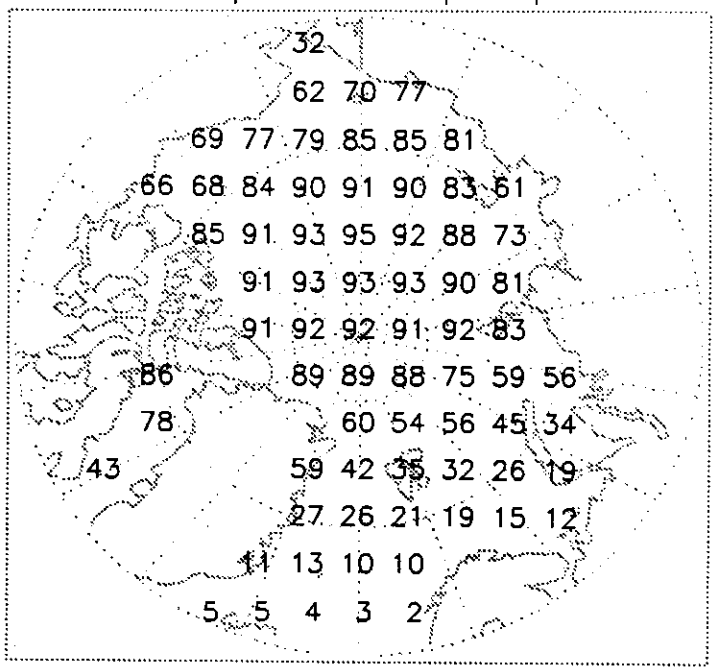

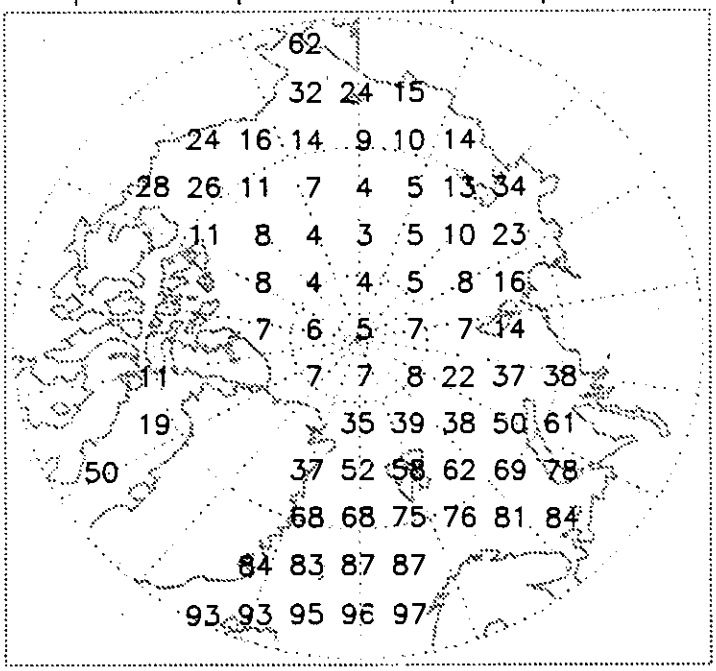

Units: % Frequency

Figure 2.2.1 (Continued)

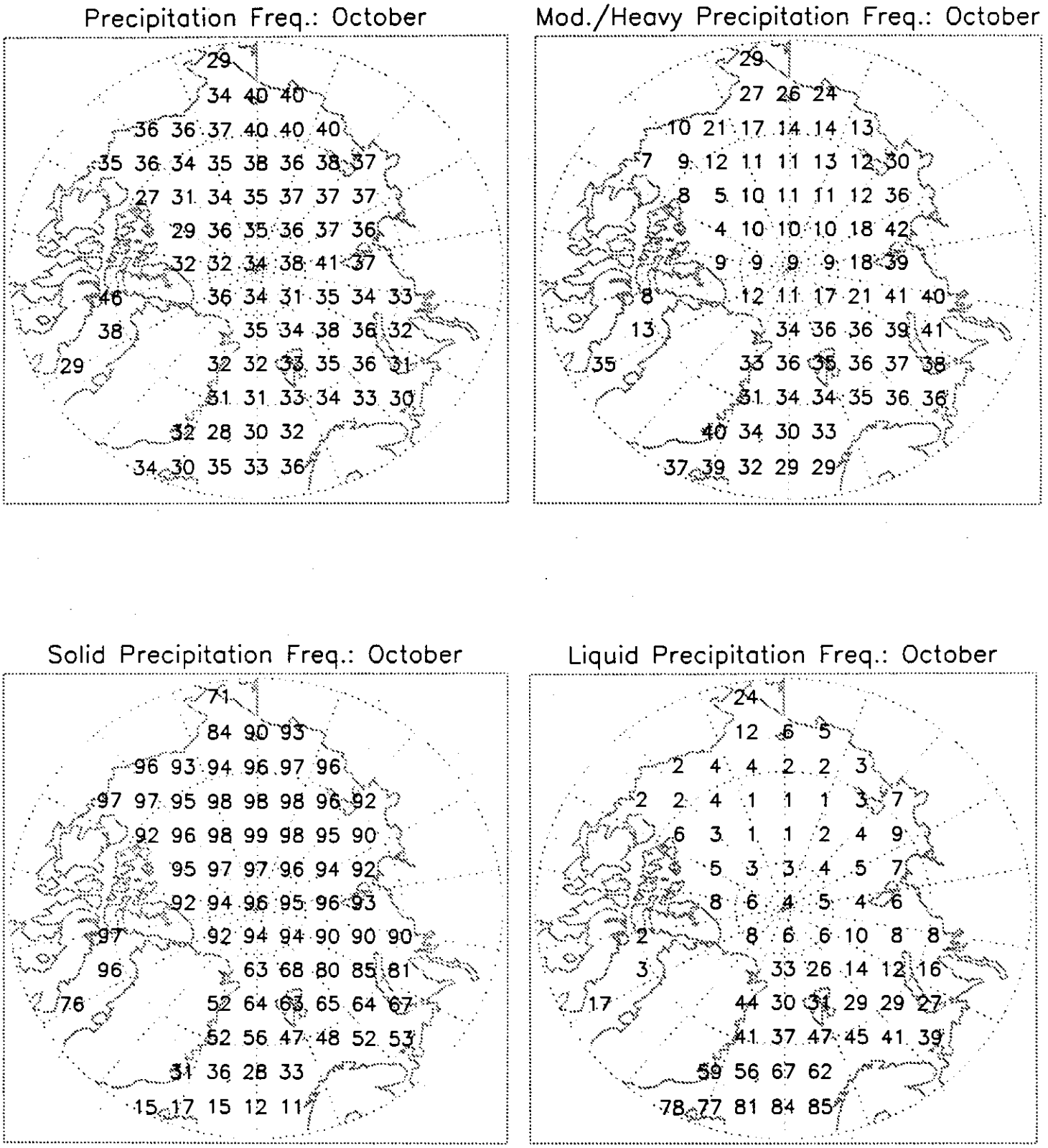

Units: % Frequency

Figure 2.2.1 (Continued)

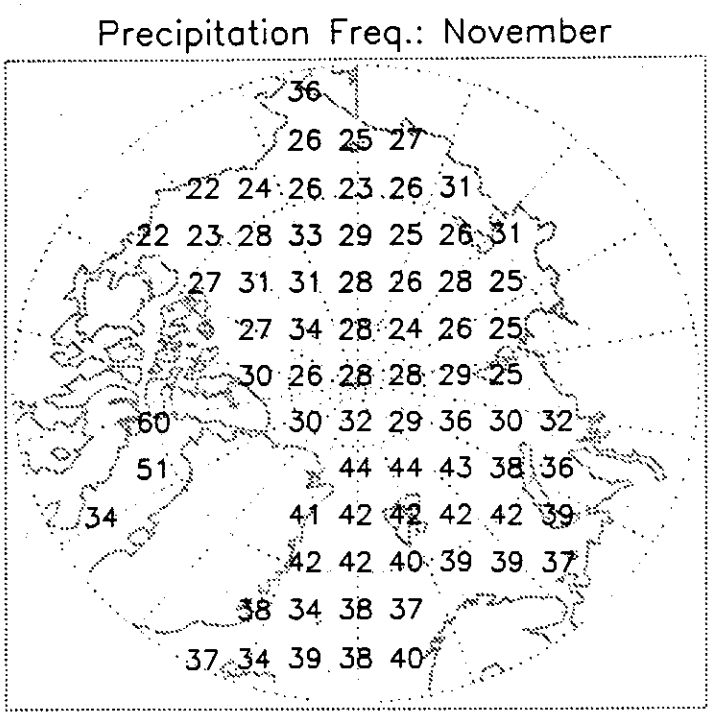

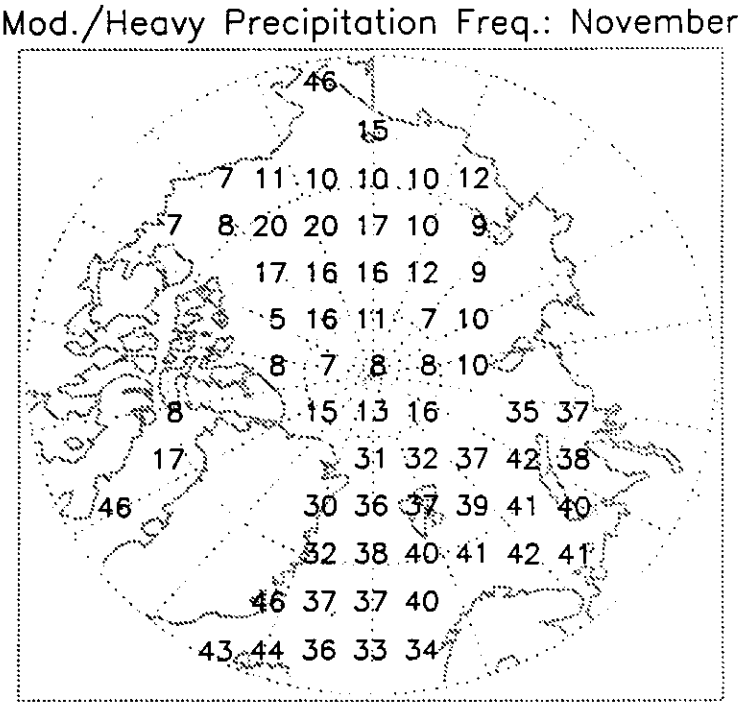

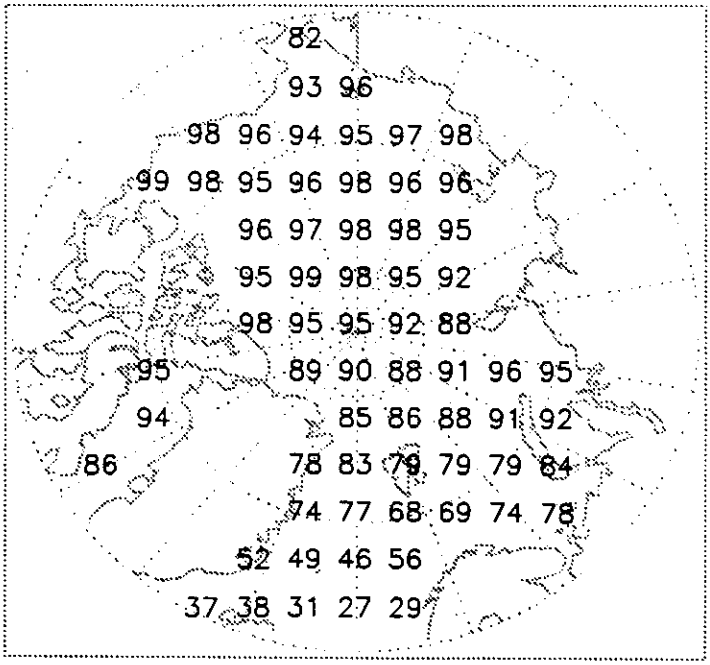

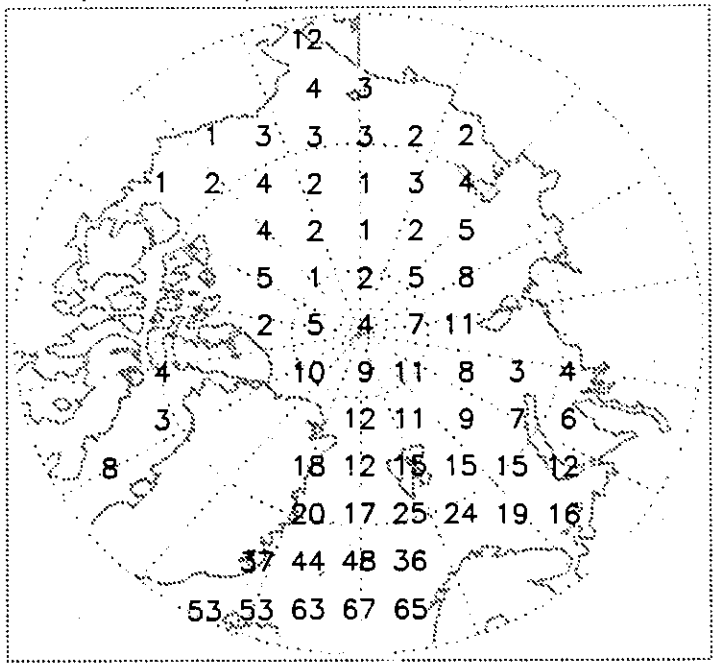

Units: % Frequency

Figure 2.2.1 (Continued)

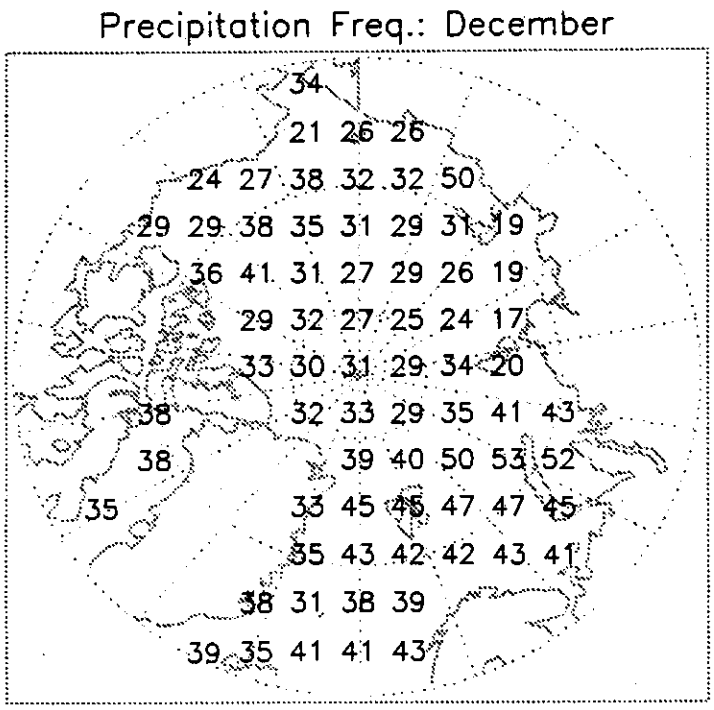

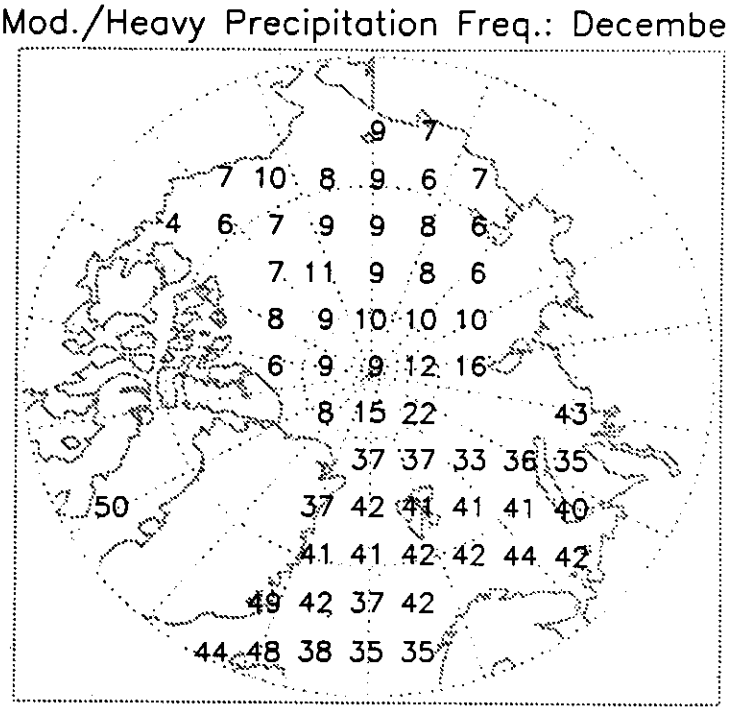

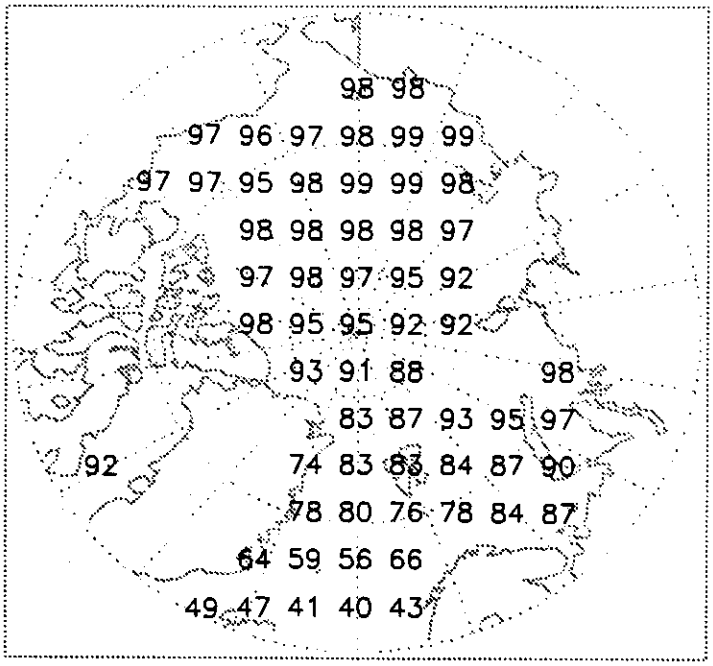

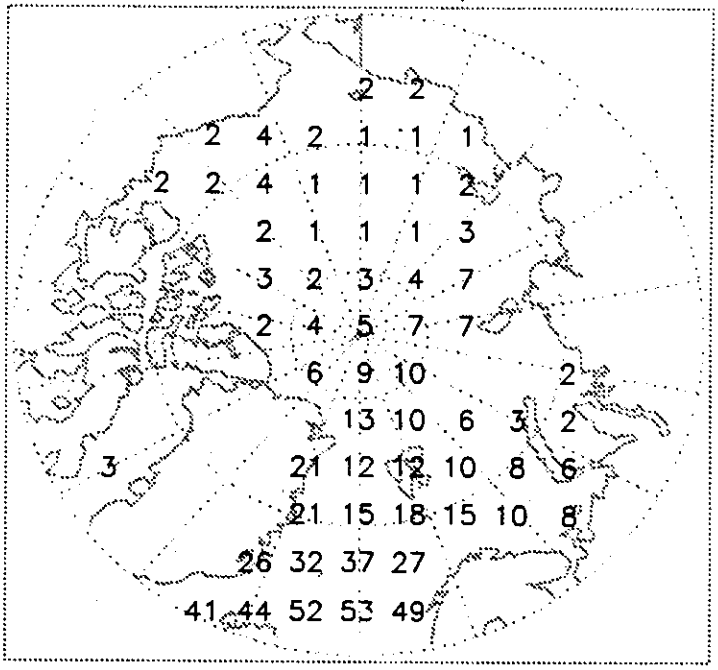

Units: % Frequency

Figure 2.2.2

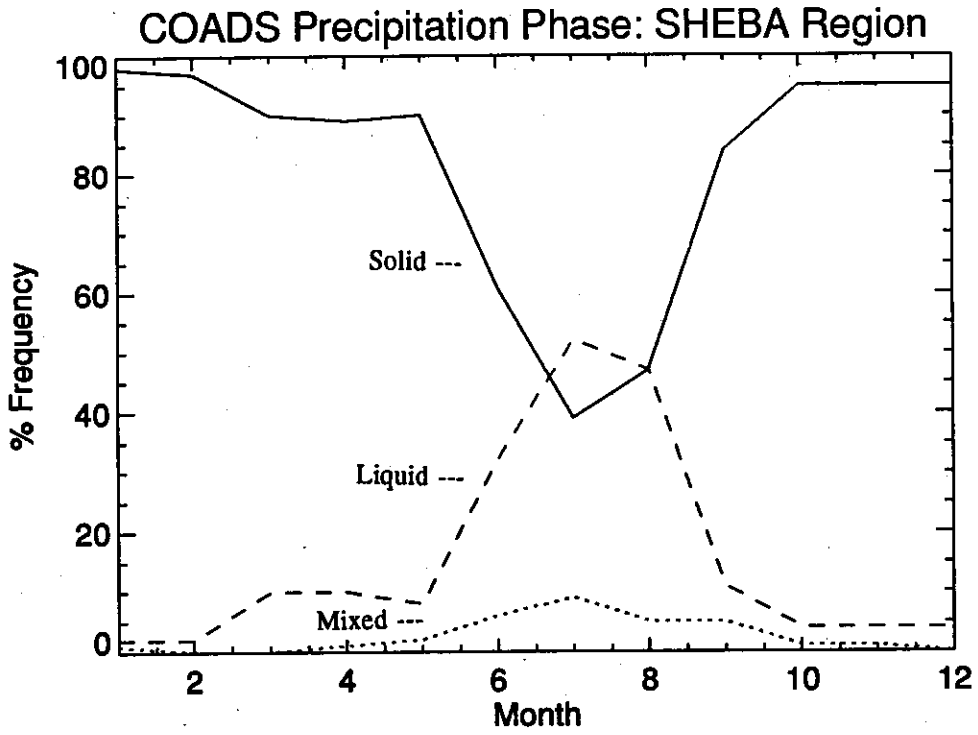
COADS Precipitation Phase: SHEBA Region
% Frequency
Month
Solid ---
Liquid ---
Mixed ---
0
20
40
60
80
100
2
4
6
8
10
12

2.3 Surface Radiation Climate

Data from various sources have been used to compile a new gridded monthly climatology of global (downwelling shortwave) radiation for the region north of 65°N [Serreze et al., 1997a]. The data sources outlined below are indicated by the characters plotted in Figure 2.3.1

Ocean data (*) comprise monthly mean fluxes from the Russian drifting stations NP-2 through NP-31 spanning 1950-1991, obtained from a CD-ROM compiled by University of Washington's Polar Science Center and the National Snow and Ice Data Center (NSIDC) (see also Marshunova and Mishin, 1994), the U.S. ice island "T-3", digitized from data tables in Marshunova and Chernigovskii [1971] and the technical report of Weller and Holmgren [1974] and U.S. station "Arlis II", digitized from tables provided by Roulet [1969]. The major sources of land data are the Global Energy Balance Archive [Ohmura and Gilgen, 1991], representing 57 land stations north of 60°N (GB), the NOAA Solar and Meteorological Surface Observations archive (nine Alaskan sites north of 60°N (S) and the Atmospheric Environment Service (14 Canadian Arctic sites) (C). More limited observations were obtained for other sites from Gavrilova [1963] (G) and field experiments for Broughton Island, the Carey Islands, Cape Herschel and Coburg Island [Jacobs et al., 1974; Steffen, 1976] (F). Limited monthly data were also obtained for six sites over the Greenland Ice Sheet from the Program for Arctic Regional Climate Assessment (P) (headed by K. Steffen, University of Colorado and sponsored by the National Aeronautics and Space Administration and the National Science Foundation). The above archives were found to provide poor coverage of the North Atlantic between about 60°N-65°N and for coastal Greenland. To provide coverage over these areas, it was necessary to resort to estimated values, based on consideration of cloud cover, the extraterrestrial flux and non-cloud scattering and absorption [see Vowinkel and Orvig, 1964]. For coastal Greenland stations and Jan Mayen we made use of estimates by Marshunova and Chernigovskii [1971] (MC). For the North Atlantic, a series of points was chosen from isoline maps of Smetannikovoi [1983] (SM).

Briefly, we passed the drifting station data through a Cressman interpolation to provide long-term means for as many Arctic Ocean grid points as the data would permit, using the 100x100 km version of the EASE-Grid. Long-term means from the land stations were then appended to these values, with the combined data set then passed through a second interpolation to the EASE-Grid, providing essentially complete coverage north of 65°N . Due to the irregular spatial distribution of the data, use of the raw values in the interpolation procedure may introduce biases related to solar zenith angle. Therefore, the interpolation was based instead on values expressed as the difference between the observed global radiation (G_{obs}) and an estimate of the clear-sky downwelling shortwave flux (G_{clr}). The adjustment by G_{clr} normalizes the data with respect to latitudinal variations in solar zenith angle/day length and associated path-length dependencies of non-cloud atmospheric absorption and scattering. It also acts to normalize the data with respect to a minor non-cloud effect of surface albedo (G_{clr} tends to increase with respect to albedo due to the effects of multiple scattering). After the interpolation, G_{clr} was added back to the interpolated values. G_{clr} was computed using a neural network version [Key et al., 1996] of the two-stream radiative transfer model used by Schweiger and Key [1994] in the computation of radiative fluxes (all components) from the ISCCP-C2 monthly cloud product [Rossow and Schiffer, 1991] for 1984-1990 . The clear-sky flux calculations were done using ISCCP-C2 all-sky surface albedos [Schweiger et al., 1993] with an aerosol optical depth of 0.05

representing background tropospheric conditions, month-specific total precipitable water ranging from 1.0 mm (January) to 10 mm (August), and total column ozone of 7 g m^{-2}.

The primary influences on spatio-temporal variations in surface global radiation are solar zenith angle/daylength, path length and clouds. To isolate the net effect of clouds, we also calculated an effective cloud transmittance t for each grid cell:

$$t = G_{obs}/G_{clr}$$

The quantity t is a cloud property because the effects of the atmosphere are removed through the use of the surface clear-sky global radiation rather than the top-of-atmosphere flux. It takes a value of one for clear sky (assuming that the modeled G_{clr} is error free), and decreases toward zero with increasing cloud optical thickness. It is not a true cloud transmittance because: 1) the true transmittance is the ratio of downwelling shortwave fluxes immediately below and above the cloud; 2) it will include the effects of multiple scattering between the surface and cloud as well as the surface and atmosphere, which are in turn related to surface albedo; 3) the cloud amount is unknown. The effect of the first and second factors is that our "transmittance" values are biased high by 1-2%. The unknown cloud amount is related to effective cloud transmittance and the true cloud transmittance by

$$t = (1-f) + f\, t_{cld}$$

where f is the cloud fraction and t_{cld} is the actual cloud transmittance. We therefore use the term "effective" to identify these shortcomings.

The model used by Schweiger and Key [1994] to calculate the ISCCP-C2 radiative fluxes is modified from Tsay et al. [1989]. It uses a delta-Eddington two-stream approximation for long wave calculations. Gas absorption for water vapor, ozone, CO_2 and oxygen is parameterized using an exponential sum fitting technique with 24 bands at varying intervals without overlap for the shortwave region, and 105 bands at 20 cm intervals including overlap of gases for the longwave region. Cloud amount, height and optical thickness are set to the values reported in the ISCCP-C2 data set. Cloud physical thickness is calculated from the above parameterization with effective radius and liquid water concentration consistent with the ISCCP-C2 retrieval algorithm. During winter no cloud optical thickness is reported in the ISCCP-C2 data set so the mean summer value of 10.5 is used instead. For each grid cell, separate calculations are performed for cloud free and cloudy conditions. Results are linearly averaged with the fractional area of cloud and clear sky as weights. Consistent with the C2 analysis, emissivity is assumed to be unity. Spectral albedos in the 24 bands are estimated from the single channel reflectance (0.6 mm) reported in the C2 data set as a combination of (potentially) open water, meltponds, bare ice, and snow-covered ice with either 300 mm or 1000 mm snow grain size. The spectral albedos for these surfaces are in part extracted from the literature and in part computed using a 4-stream model. Broadband surface albedos are then estimated from the spectral values. Comparisons with Serreze et al. [1997a] indicate that the ISCCP-C2 global radiation fluxes are too high by typically 20-40 W m^{-2} during summer. This is primarily due to underestimates in cloud fraction of 5-35% [Schweiger and Key, 1992] although the effect may be partly offset by the ISCCP-C2 cloud optical thicknesses being too high. From comparisons with the regional climatology of Marshunova [1961] for the central Arctic Ocean, downwelling longwave fluxes appear to be too low due to underestimates in low

cloud amount. Albedos, however, compare favorably to other existing climatologies [Schweiger et al., 1993]. Despite these uncertainties, we consider the ISCCP-C2 longwave fluxes, net fluxes and albedos as the best available estimates to examine spatio-temporal variability. Some of the existing problems should be resolved with the improved ISCCP "D" products. As discussed in Section 1.5, efforts are underway to calculate fluxes using these data.

From a consideration of the strength and weaknesses in the data sets described above, we select the following spatial fields for presentation: 1) global radiation fluxes for the months March-October representing the new Serreze et al. [1997a] climatology (Figure 2.3.2); 2) effective cloud transmittance t for April through September (Figure 2.3.3) also from Serreze et al. [1997a] (March and October are not presented as t is strongly influenced by errors in measurement and estimation of clear-sky fluxes under extreme solar zenith angles); 3) ISCCP-C2 surface albedos, also for April through September (Figure 2.3.4); 4) an estimate of the seasonal cycle of ice-only surface albedo for the central Arctic Ocean (Figure 2.3.5) compiled by A. Omhura (pers. comm.) from NP drifting station observations north of 75°N (the median albedo based in individual monthly means as well as the estimated standard deviation); 5) ISCCP-C2 downwelling longwave, net longwave and net allwave fluxes, as well as the net cloud forcing at the surface for January through December (Figure 2.3.6). The net cloud forcing represents the difference in the net allwave, all sky (clear plus cloudy) flux and the clear sky flux. Seasonal cycles of selected variables for the SHEBA site are provided in Figures 2.3.7 and 2.3.8.

The fields of global radiation for March, September and October from Serreze et al. [1997a] (Figure 2.3.2) show a primarily zonal pattern, illustrating the dominant effects of the strong latitudinal decrease in the clear-sky flux (G_{clr}) for these months. Comparatively high values for these months are found over the southern part of the Greenland ice sheet. April through August are instead dominated by a strong asymmetric pattern. Central Greenland shows a pronounced peak from May through August. While reflecting the elevation effect on path length, this pattern also illustrates the tendency for the high central portions of ice sheet to be above the bulk of cloud cover. In turn, fluxes decreases sharply towards the Atlantic side of the Arctic due to attenuation by cloud cover. However, as summer cloud fractions show less spatial variability than for spring and autumn, this implies that the summer Atlantic-side radiation signal is strongly a function of mean cloud optical depth. There is also some tendency in summer months for a latitudinal increase in global radiation fluxes, most apparent for June, when G_{clr} shows a marked increase with latitude. Although cloud cover attenuates the flux, the higher central Arctic values in summer, likely in part, also manifest the partially offsetting effects of the high albedo of the sea ice in promoting multiple scattering between the surface and clouds. For June, the month of maximum insolation, fluxes over the high-elevation Greenland ice sheet peak at more than 340 W m^{-2}, but with values in excess of 300 W m^{-2} found over the Pacific side of the central Arctic Ocean extending southward into the Beaufort and near the SHEBA site. As noted earlier, June cloud cover is comparatively limited over the Beaufort Sea, particularly over its southern part. Fluxes of less than 200 W m^{-2} characterize the Atlantic side in the Norwegian and Barents seas.

The spatial patterns of effective cloud transmittance (t) from Serreze et al. [1997a] for April through August (Figure 2.3.3) are similar to the patterns of global radiation in showing the highest values over Greenland (above 0.80), fairly high values over the ice-covered central Arctic Ocean with values falling towards the Atlantic side of the Arctic. This demonstrates dominance of cloud effects on the spatial distribution of global radiation flux for these months. As cloud cover during summer tends to be more spatially homogeneous, the summer pattern for t also argues for a greater optical thickness of

Atlantic-side clouds. For the ice-covered central Arctic Ocean, t ranges from 0.75-0.85 in April, falling to 0.60-0.65 in September. June in particular shows relatively high values over the Beaufort Sea. In contrast to April through August, September shows no marked relationship between G_{obs} and t, demonstrating the effects of the strong latitudinal gradient in the clear-sky flux for this month.

Surface albedos from the ISCCP-C2 data (2.3.4), which represent regional values that include the effects of ice concentration and melt ponds, are highest in April and for the central Arctic Ocean and Beaufort Sea, ranging from 0.70-0.75. Central Arctic Ocean values drop quickly during June-August due primarily to melt. Much lower values for all months over the Atlantic sector and along the coasts represent the effects of open water and low concentration ice. The ice-only values for the central Arctic (Figure 2.3.5) are of course higher than the ISCCP albedos in all months. Based on these data, ice-only albedos for the SHEBA field region can be expected to exceed 0.80 during spring prior to melt and in autumn after freezeup and the deposition of fresh snowfall, falling to 0.60-0.65 during summer melt.

As seen in Figure 2.3.6, the spatial pattern of the ISCCP-C2 downwelling longwave fluxes largely follows the distribution of cloud fraction. The net longwave flux is slightly negative for all regions for every month. For the central Arctic Ocean, the net allwave radiation (the sum of the net shortwave and net longwave fluxes) turns positive in April, returning to negative values during September. The net cloud forcing at the surface is positive for all regions from September through April. It turns negative over the Atlantic side of the Arctic during May and is negative everywhere from June through August. This is understood in that while cloud cover always acts to turn the net longwave flux more positive, it reduces the net shortwave flux. During winter, only longwave fluxes are present. During summer, the cloud forcing on the net longwave and shortwave fluxes compete, but the effect on the net shortwave flux dominates for several months. Put differently, during September through April, cloud cover acts to increase the net allwave surface flux, while during summer, cloud cover decreases the flux.

Based on the Serreze et al. [1997a study global radiation for the SHEBA region peaks in July at slightly over 300 W m^{-2} (Figure 2.3.7). ISCCP results for the SHEBA region indicate a peak in net allwave radiation during June and July of about 100 W m^{-2} (Figure 2.3.8) This largely represents the effect of high global radiation fluxes combined with a seasonal reduction in surface albedos.

http:// stratus.ssec.wisc.edu

products

data

Figure 2.3.1

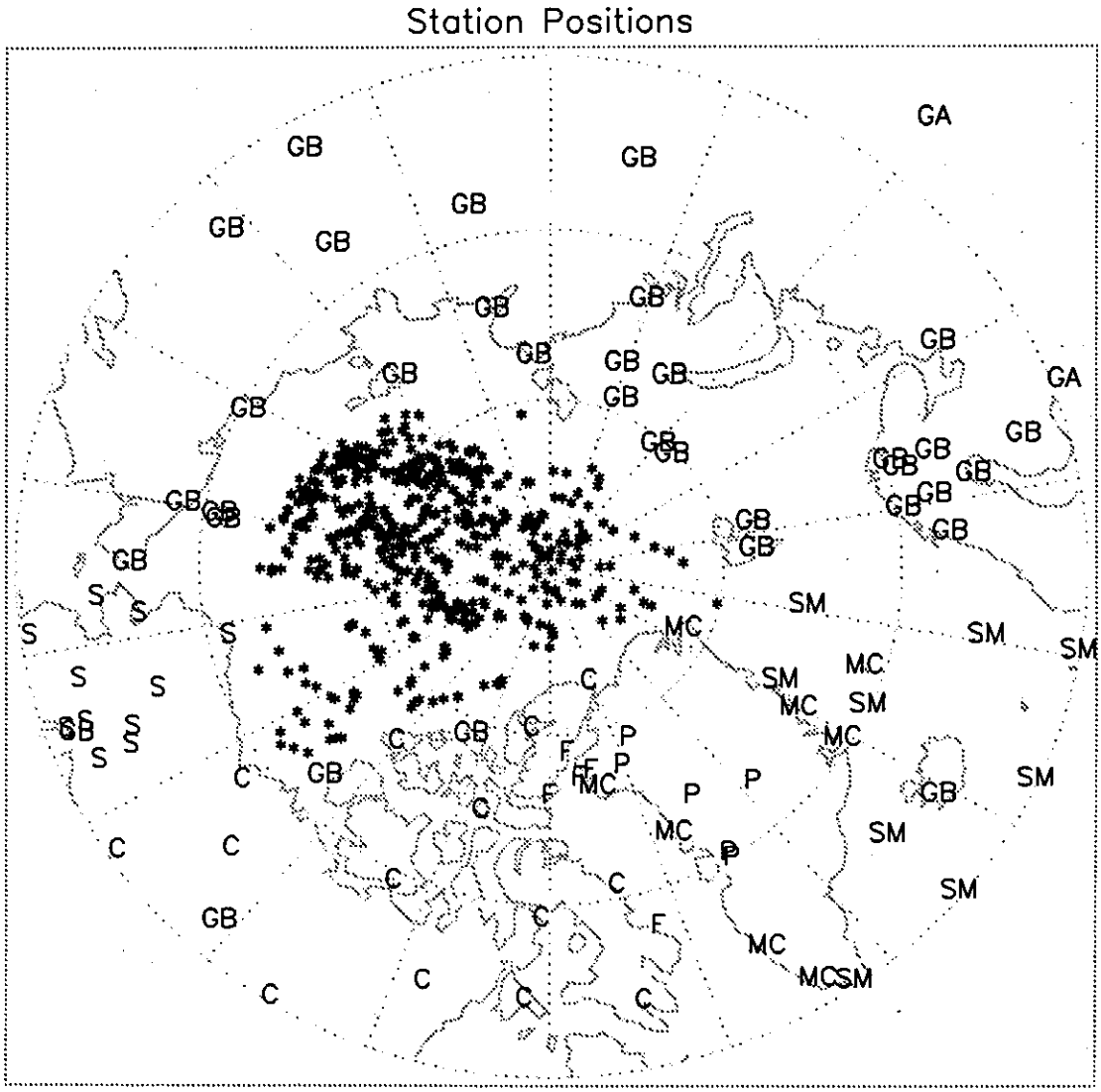

Figure 2.3.2

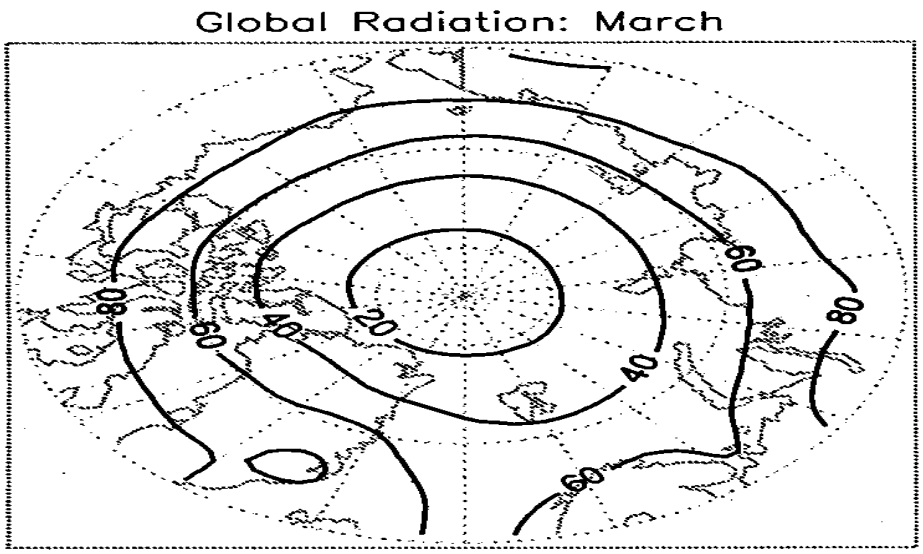

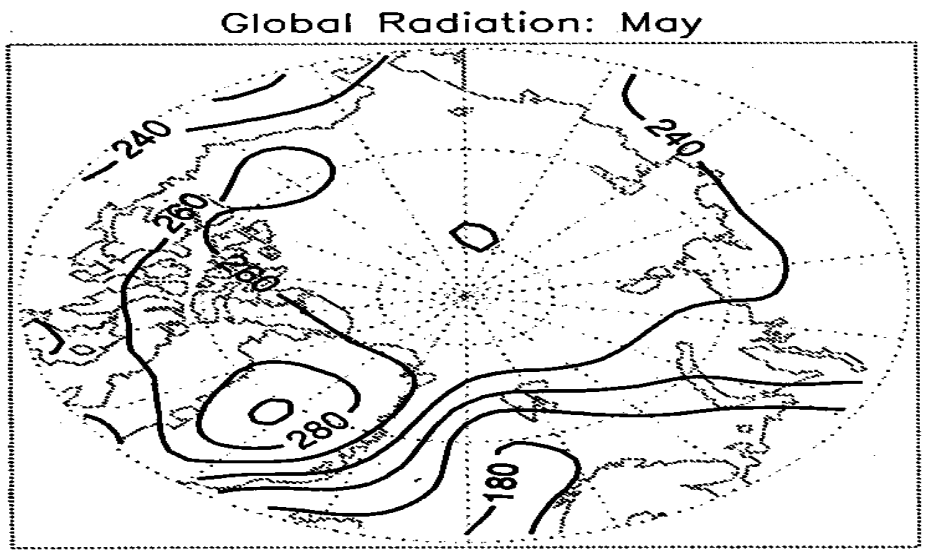

Units: W m^{-2}

Figure 2.3.2 (Continued)

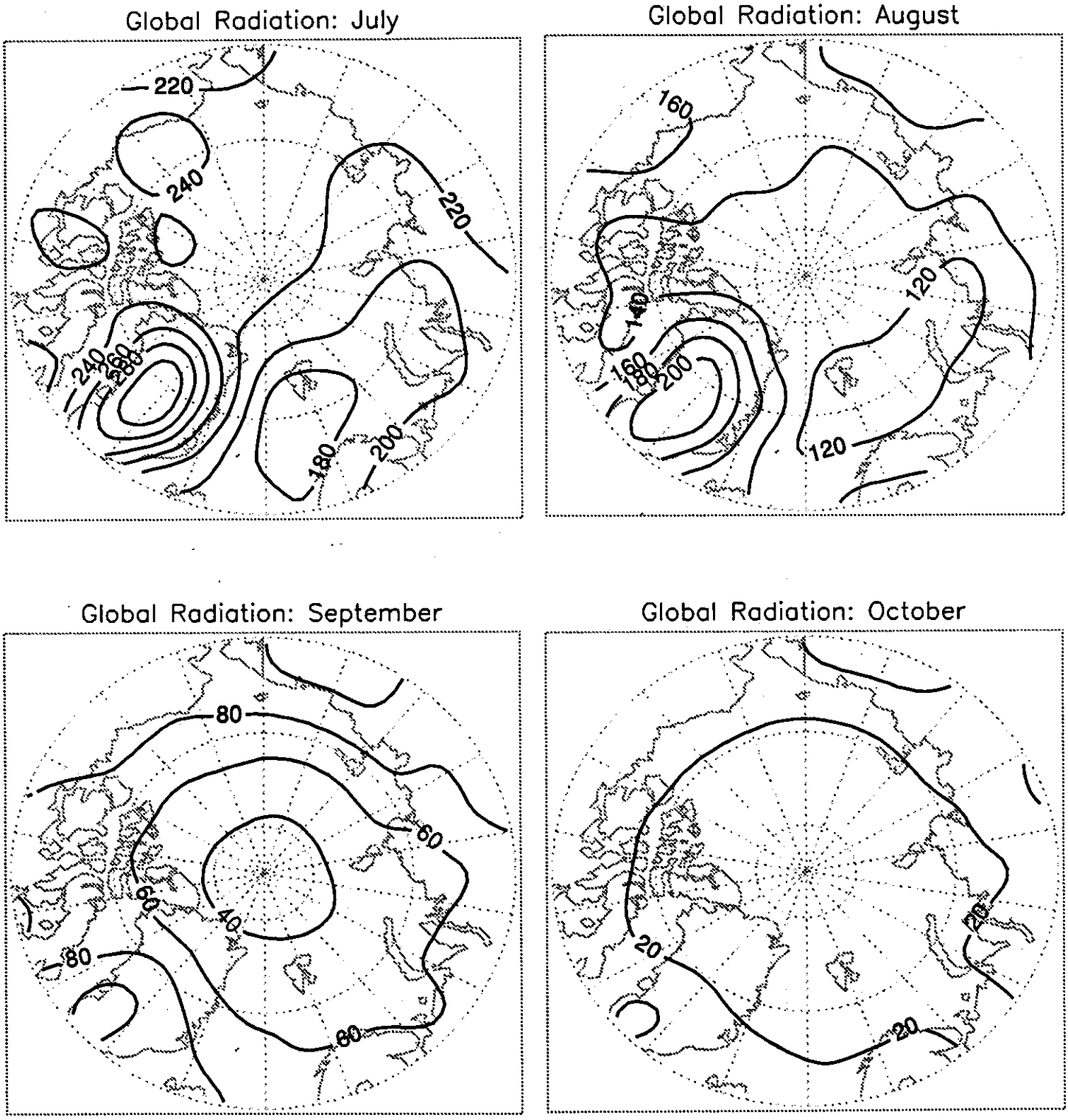

Units: W m^{-2}

Figure 2.3.3

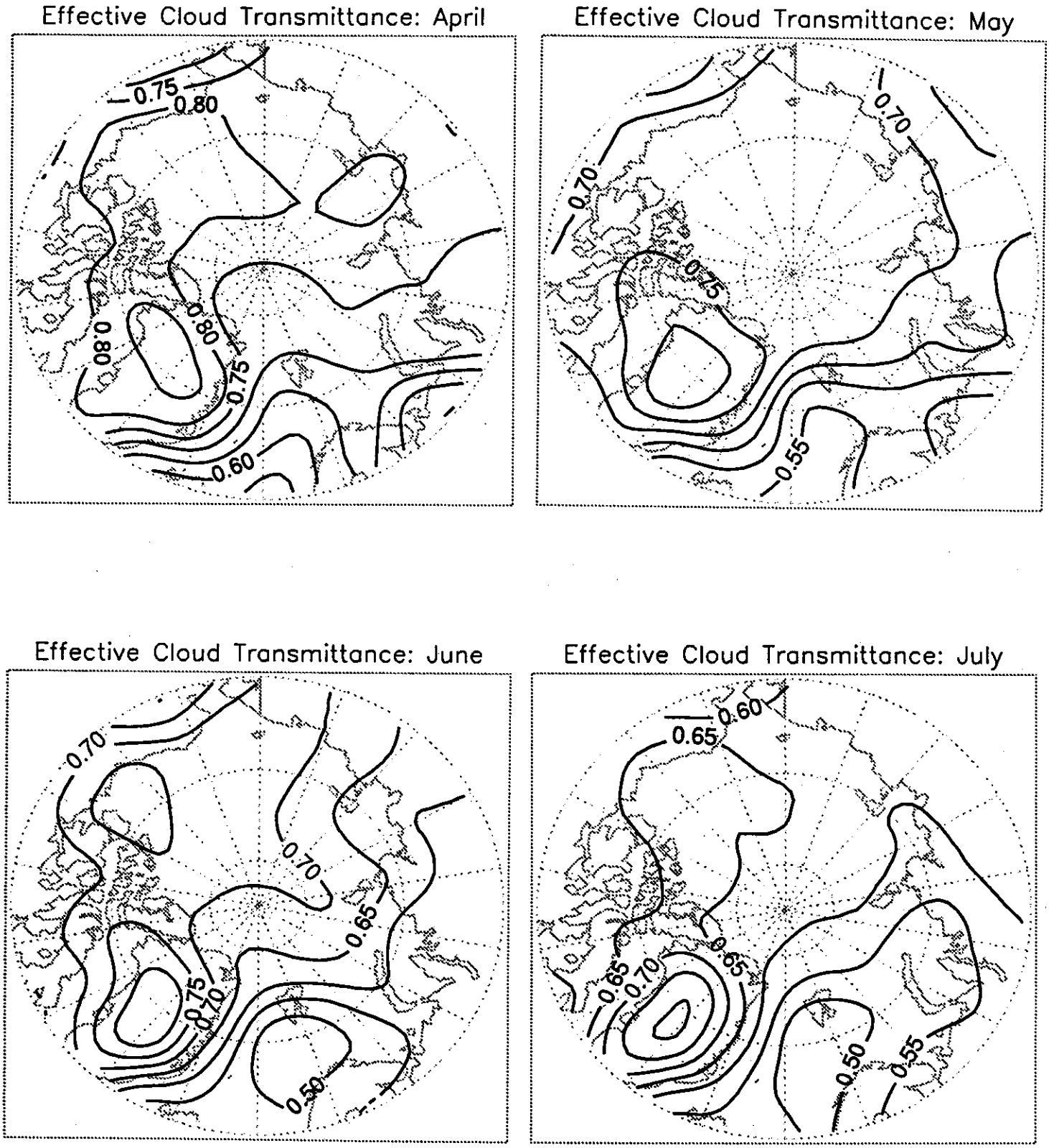

Units: Dimensionless

Figure 2.3.3 (Continued)

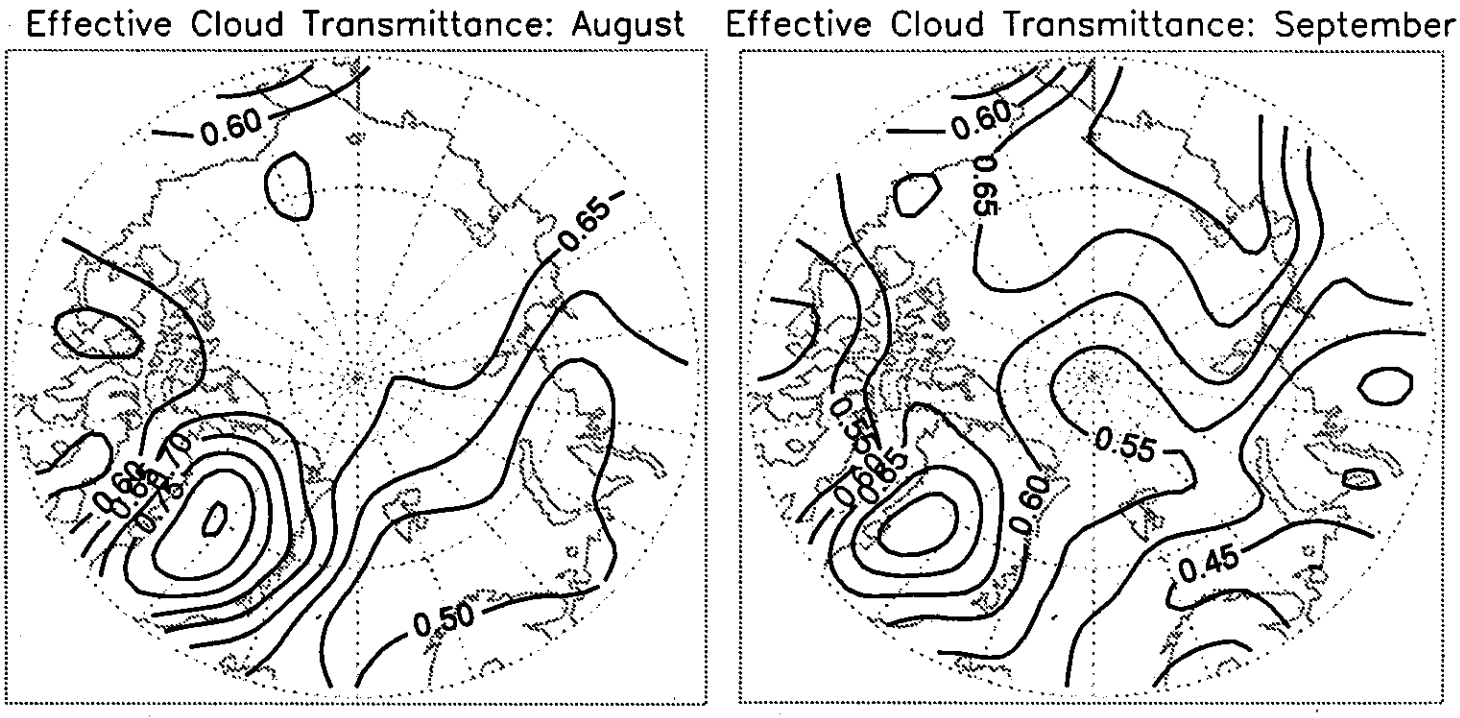

Units: Dimensionless

Figure 2.3.4

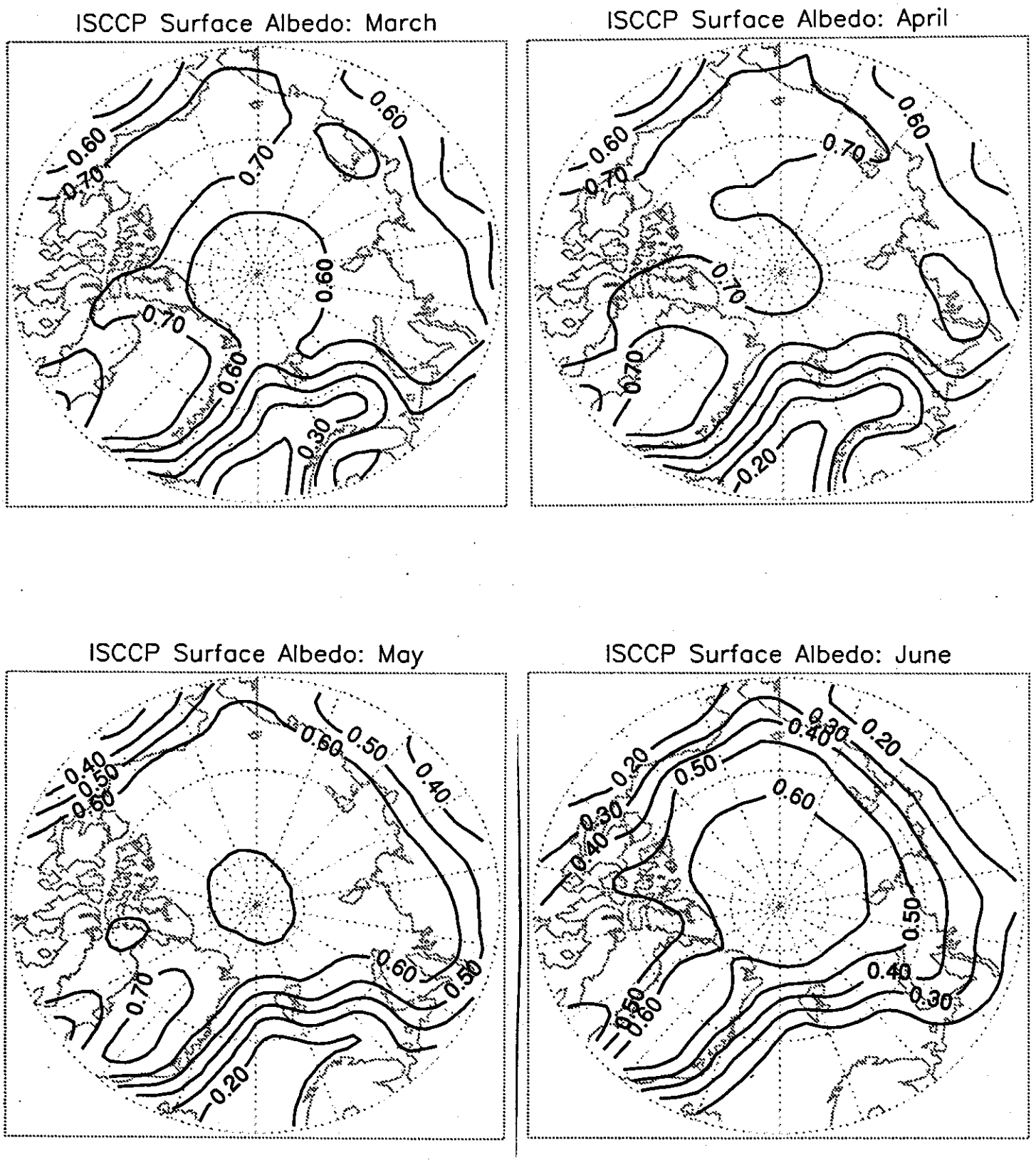

Units: Dimensionless

Figure 2.3.4 (Continued)

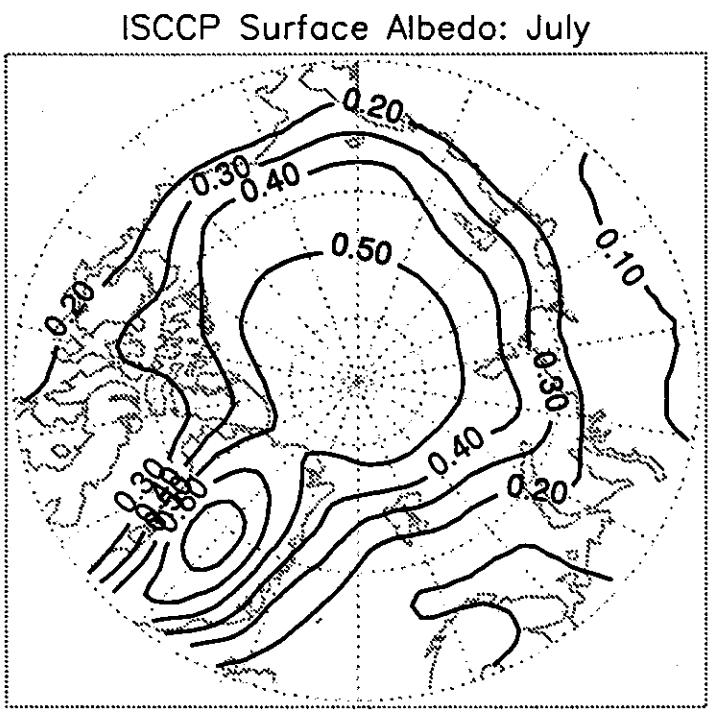

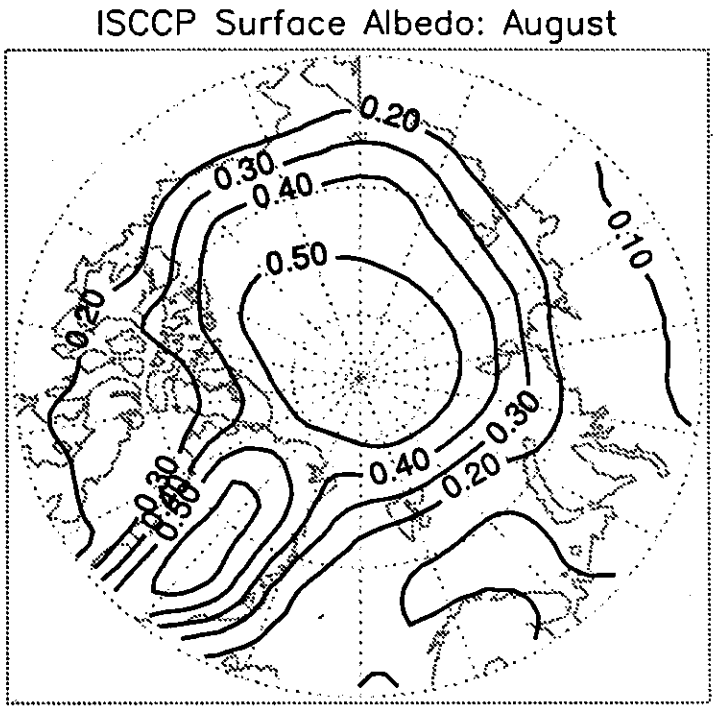

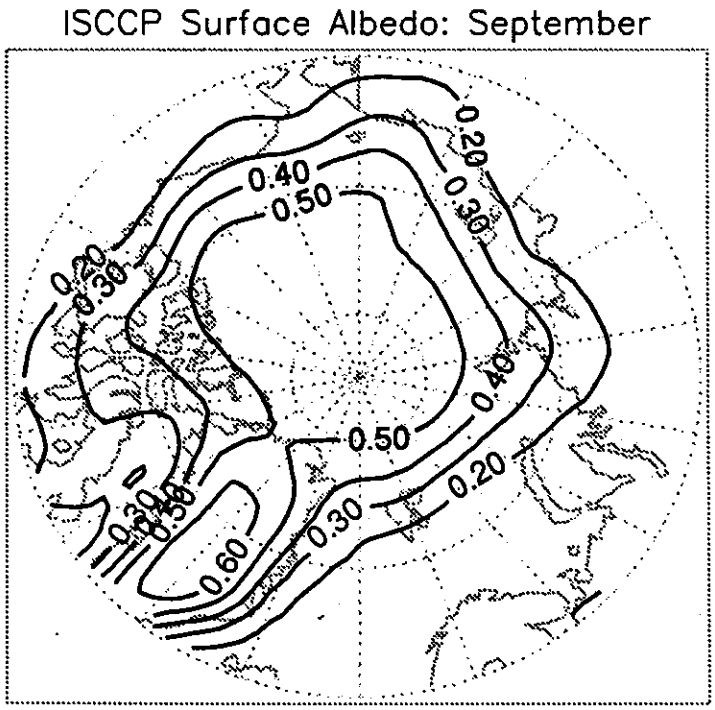

$$\sum_{i=1}^{N} \alpha_i f_i$$

Units: Dimensionless

Figure 2.3.5

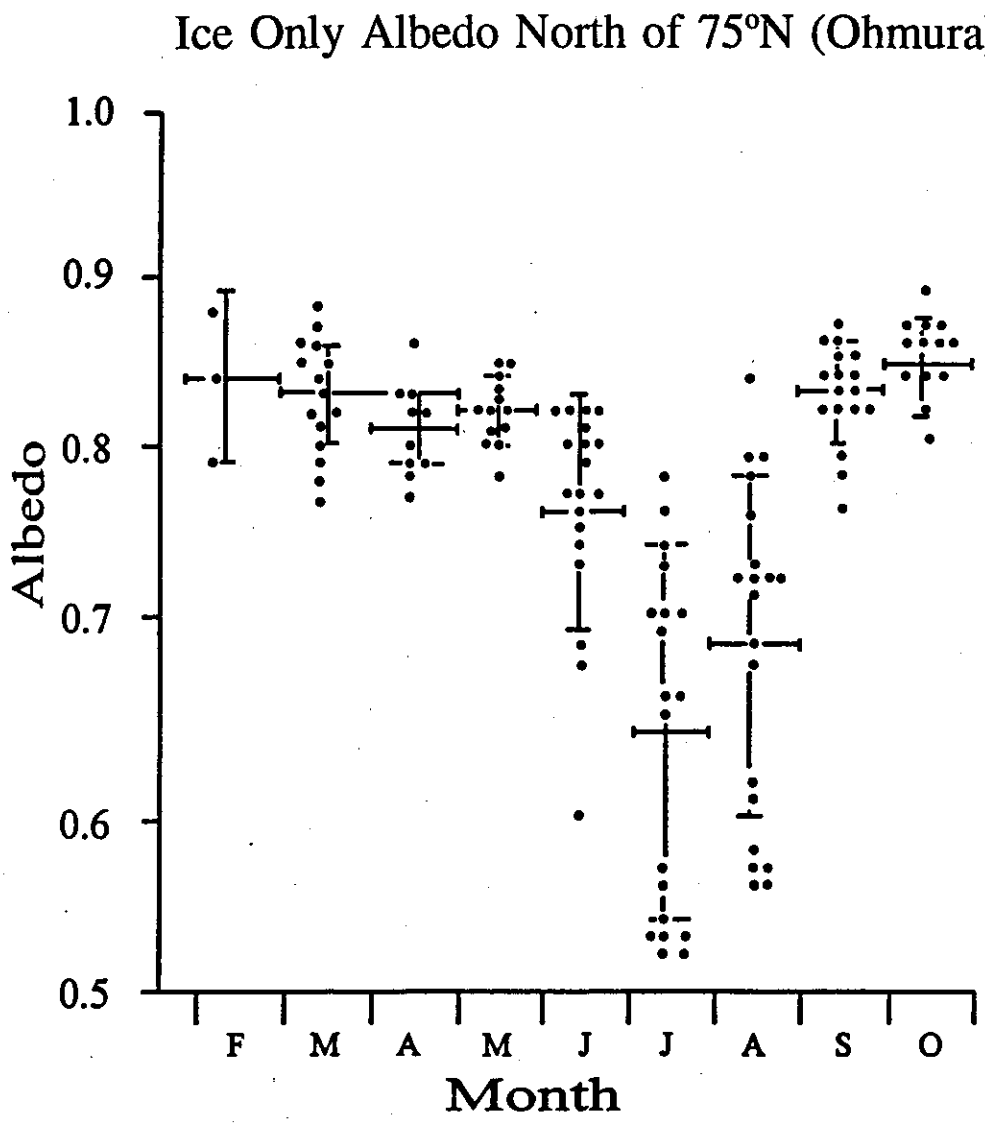
Ice Only Albedo North of 75°N (Ohmura)
1.0
0.9
0.8
0.7
0.6
0.5
Albedo
F
M
A
M
J
J
A
S
O
Month

Figure 2.3.6

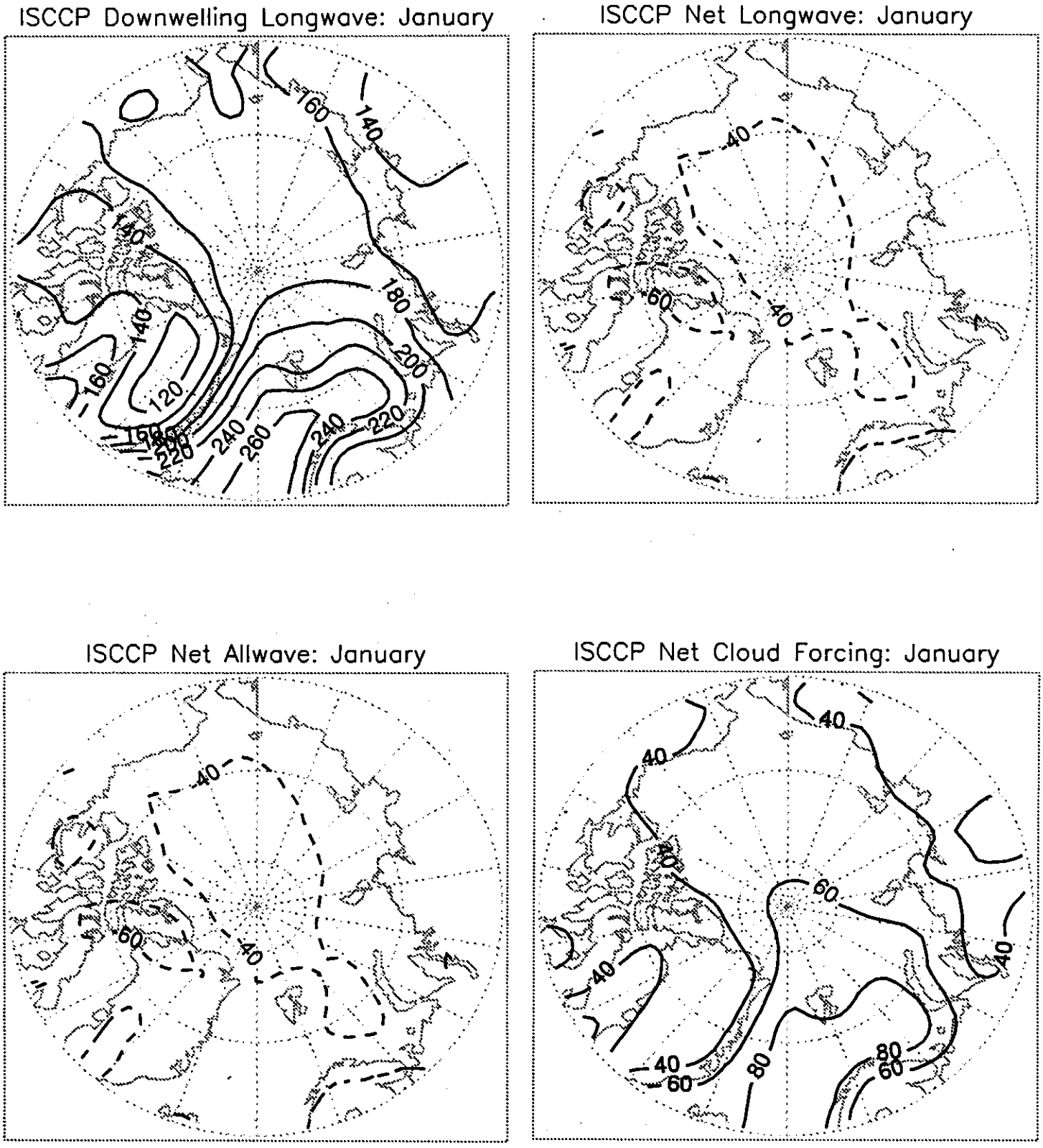

Units: W m^{-2} (Negative Contours Dashed)

Figure 2.3.6 (Continued)

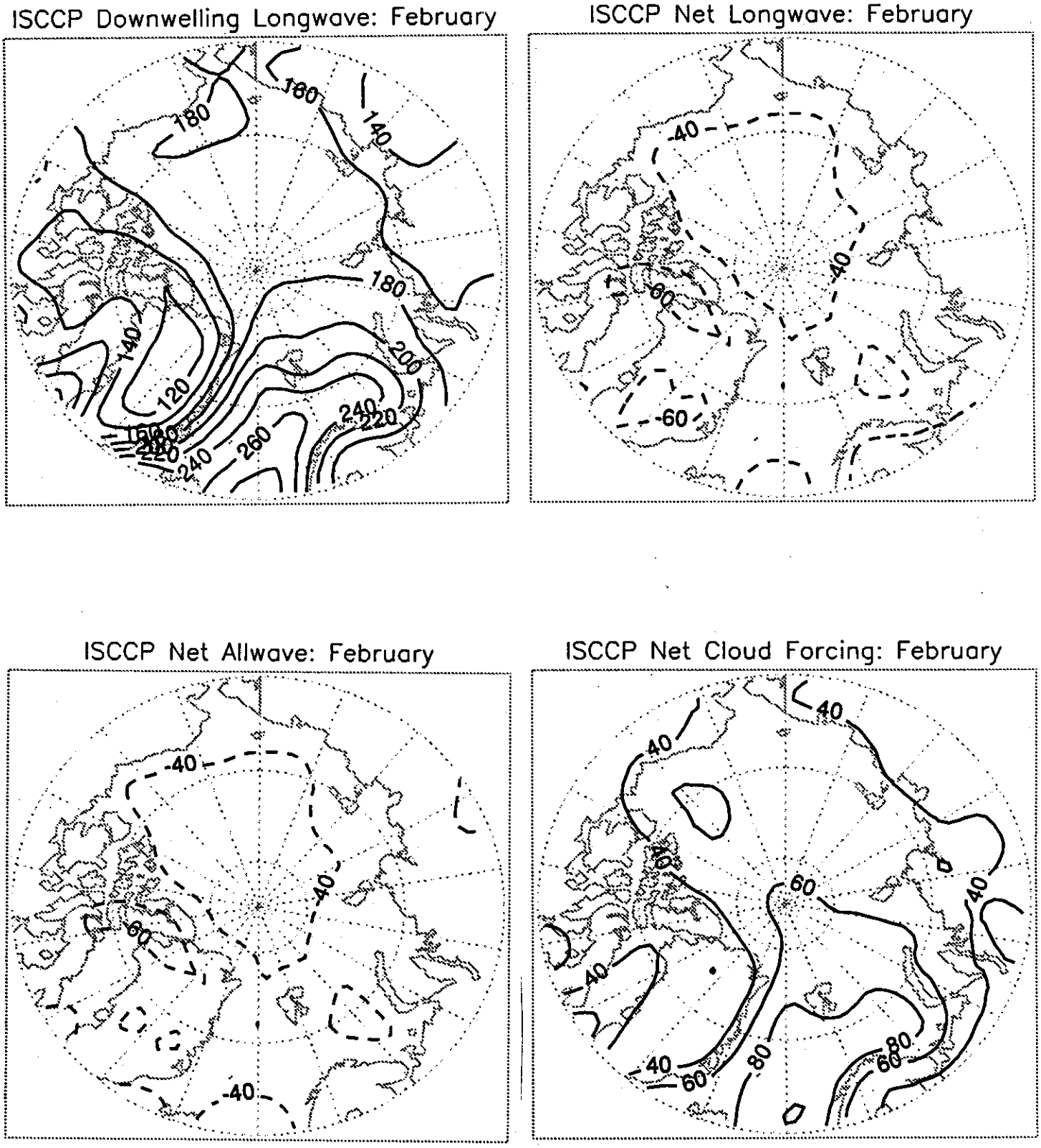

Units: W m^{-2} (Negative Contours Dashed)

Figure 2.3.6 (Continued)

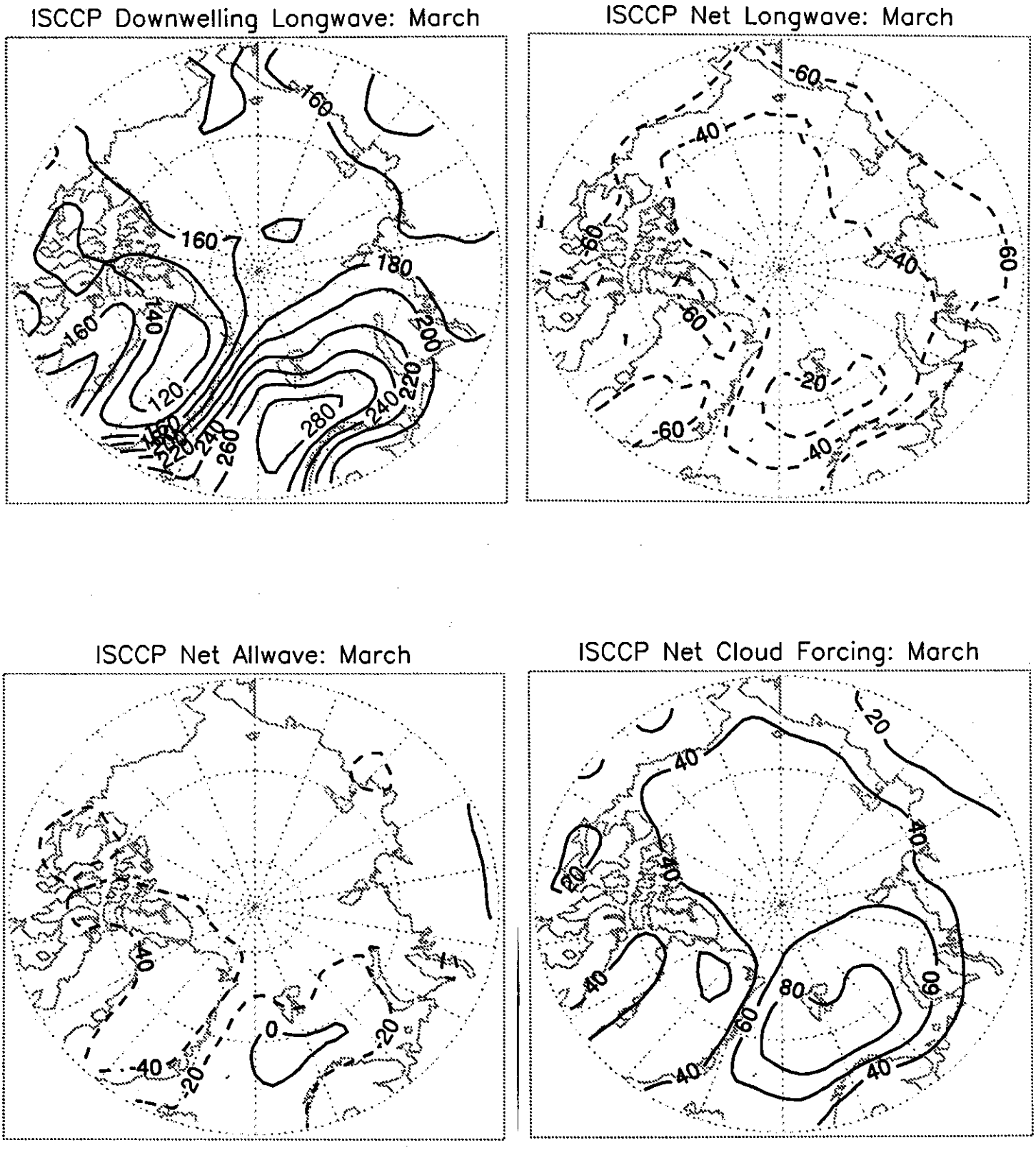

Units: W m^{-2} (Negative Contours Dashed)

Figure 2.3.6 (Continued)

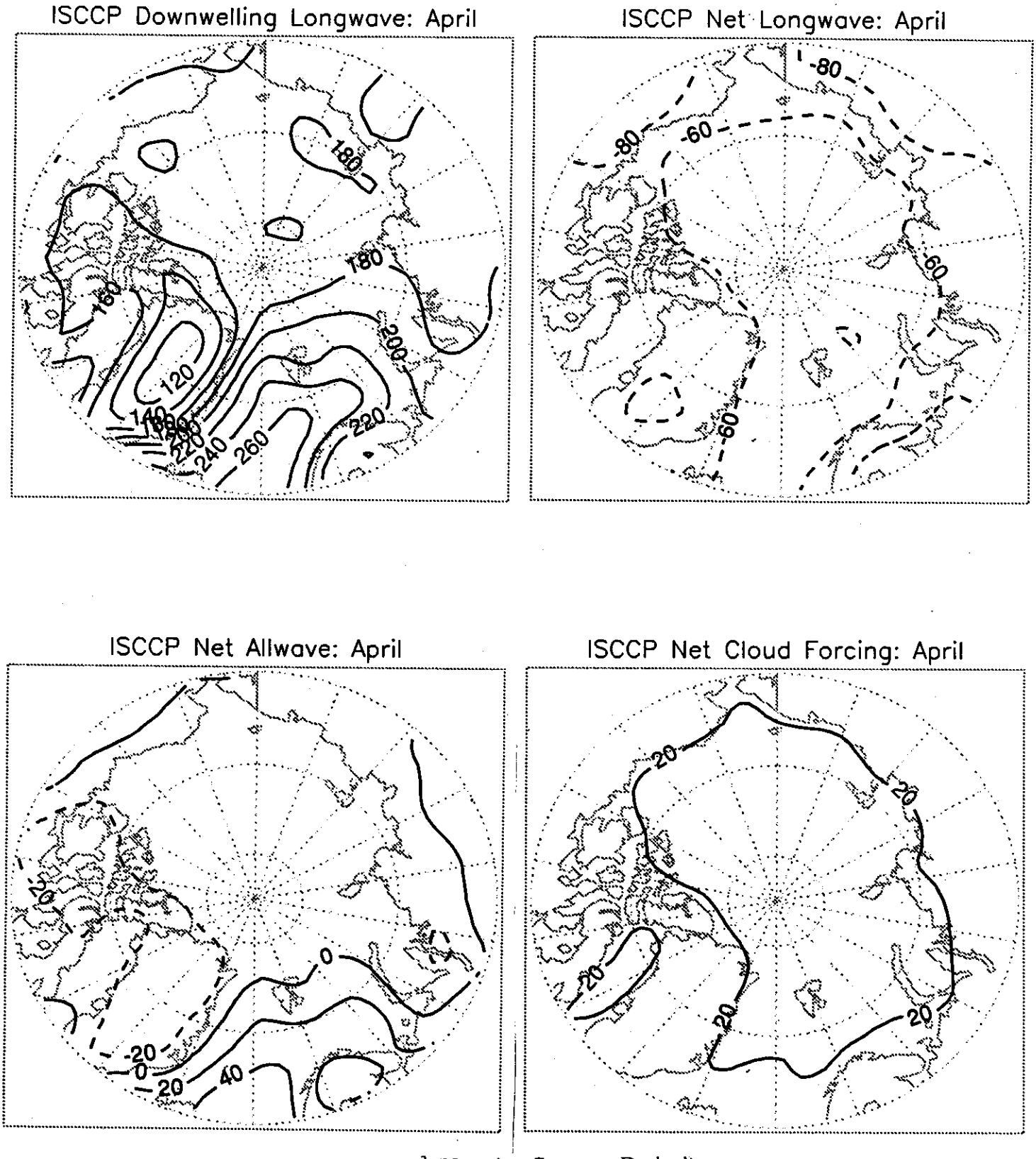

Units: W m^{-2} (Negative Contours Dashed)

Figure 2.3.6 (Continued)

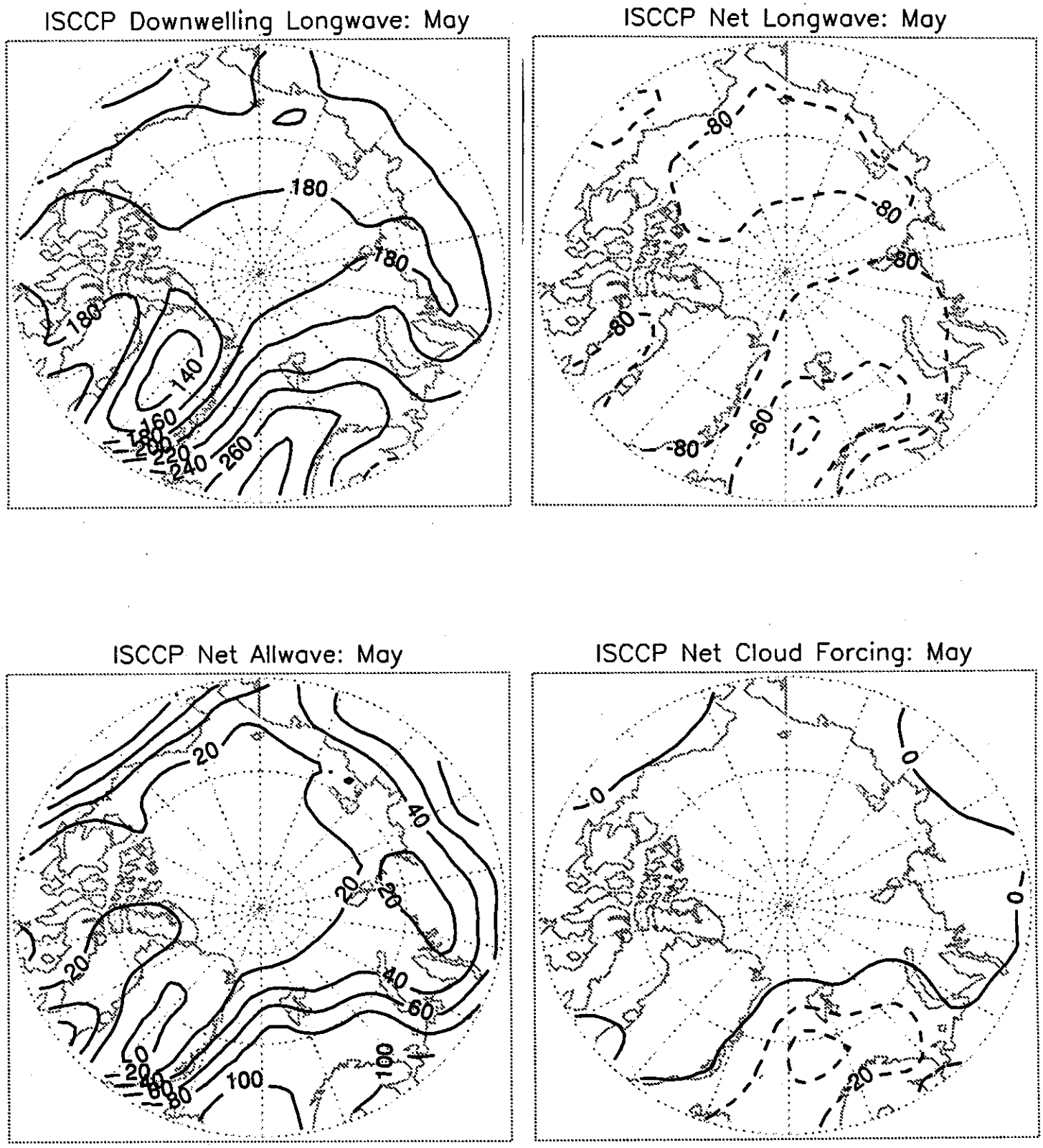

Units: W m^{-2} (Negative Contours Dashed)

Figure 2.3.6 (Continued)

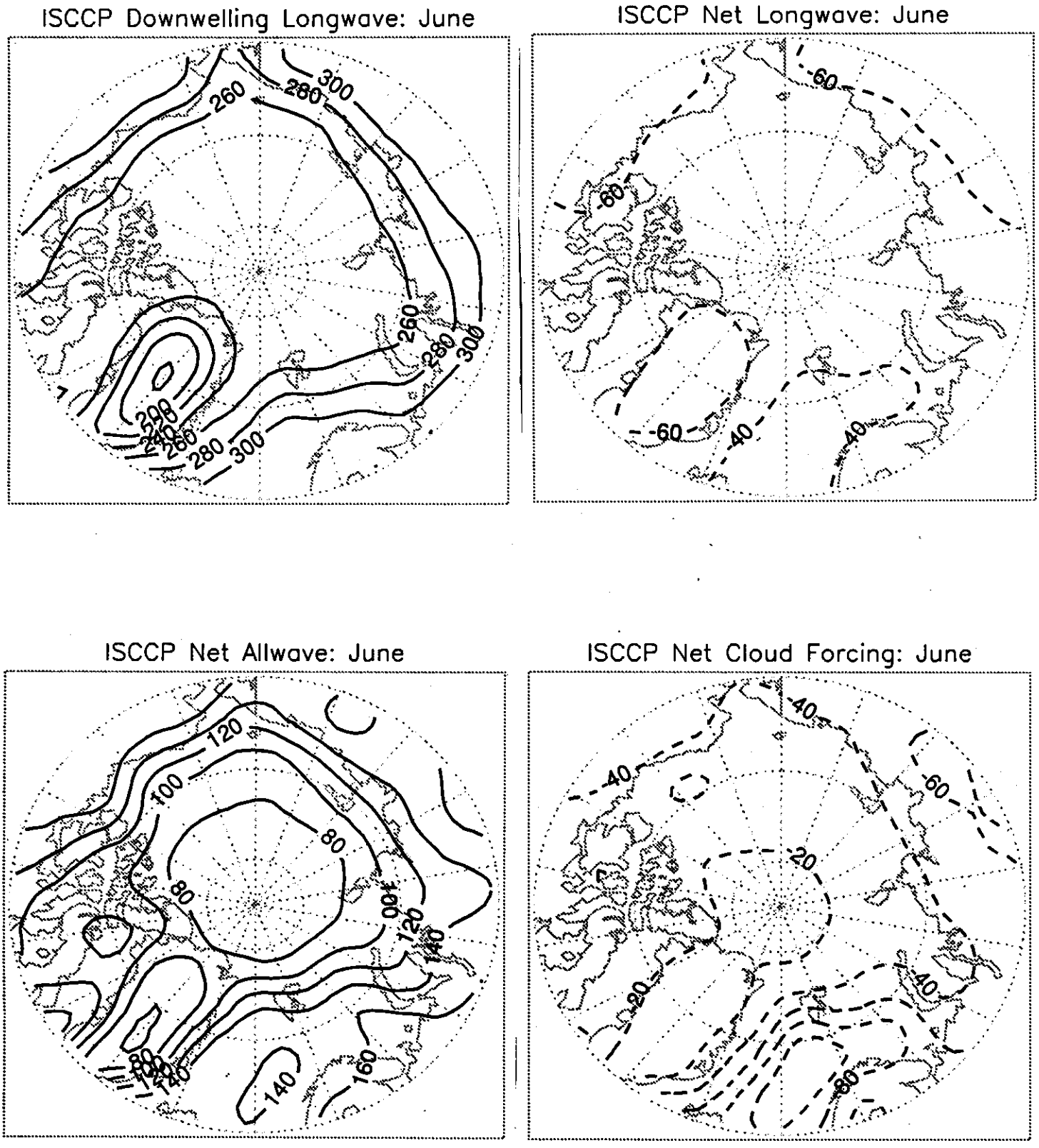

Units: W m^{-2} (Negative Contours Dashed)

Figure 2.3.6 (Continued)

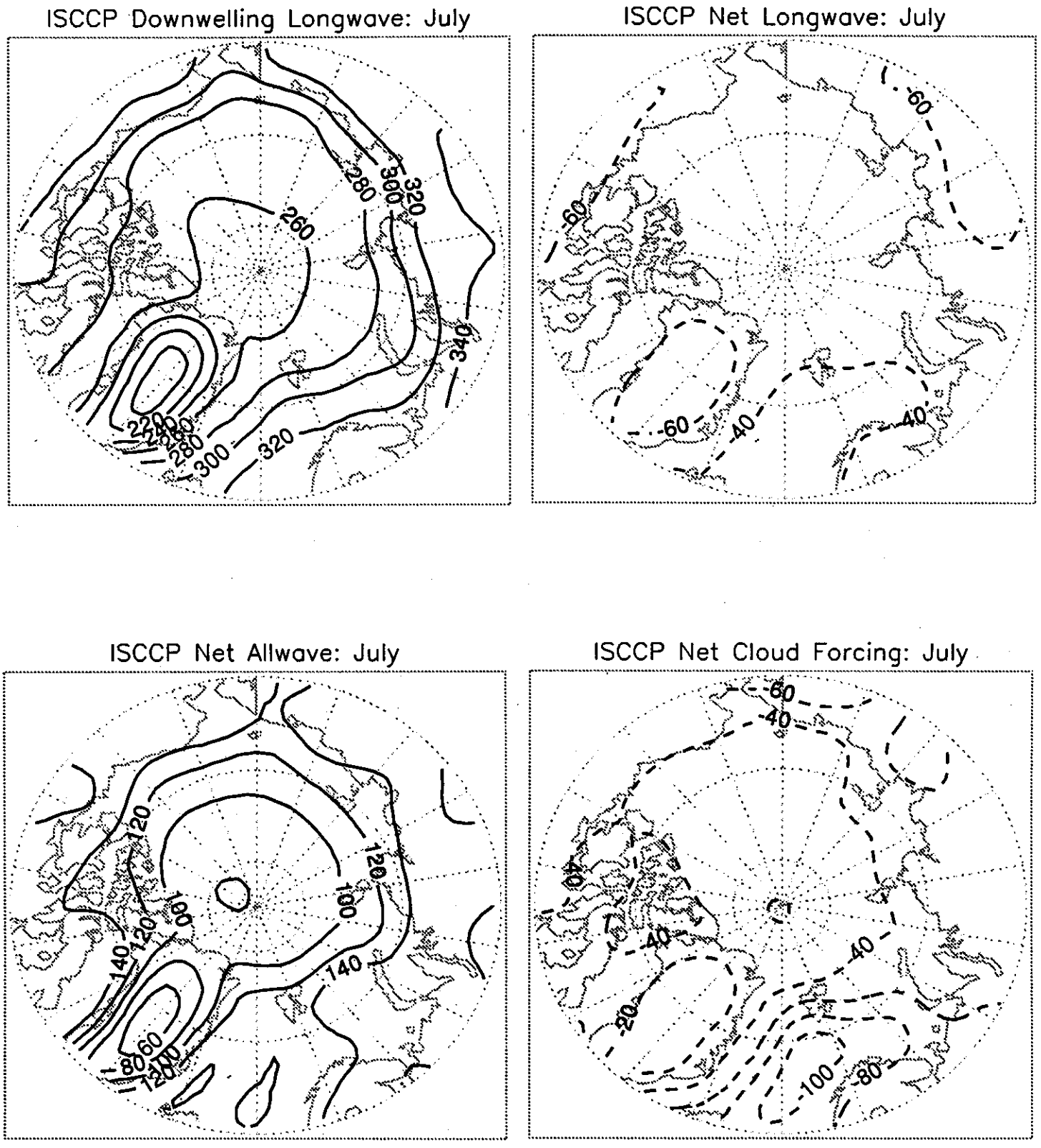

Units: W m^{-2} (Negative Contours Dashed)

Figure 2.3.6 (Continued)

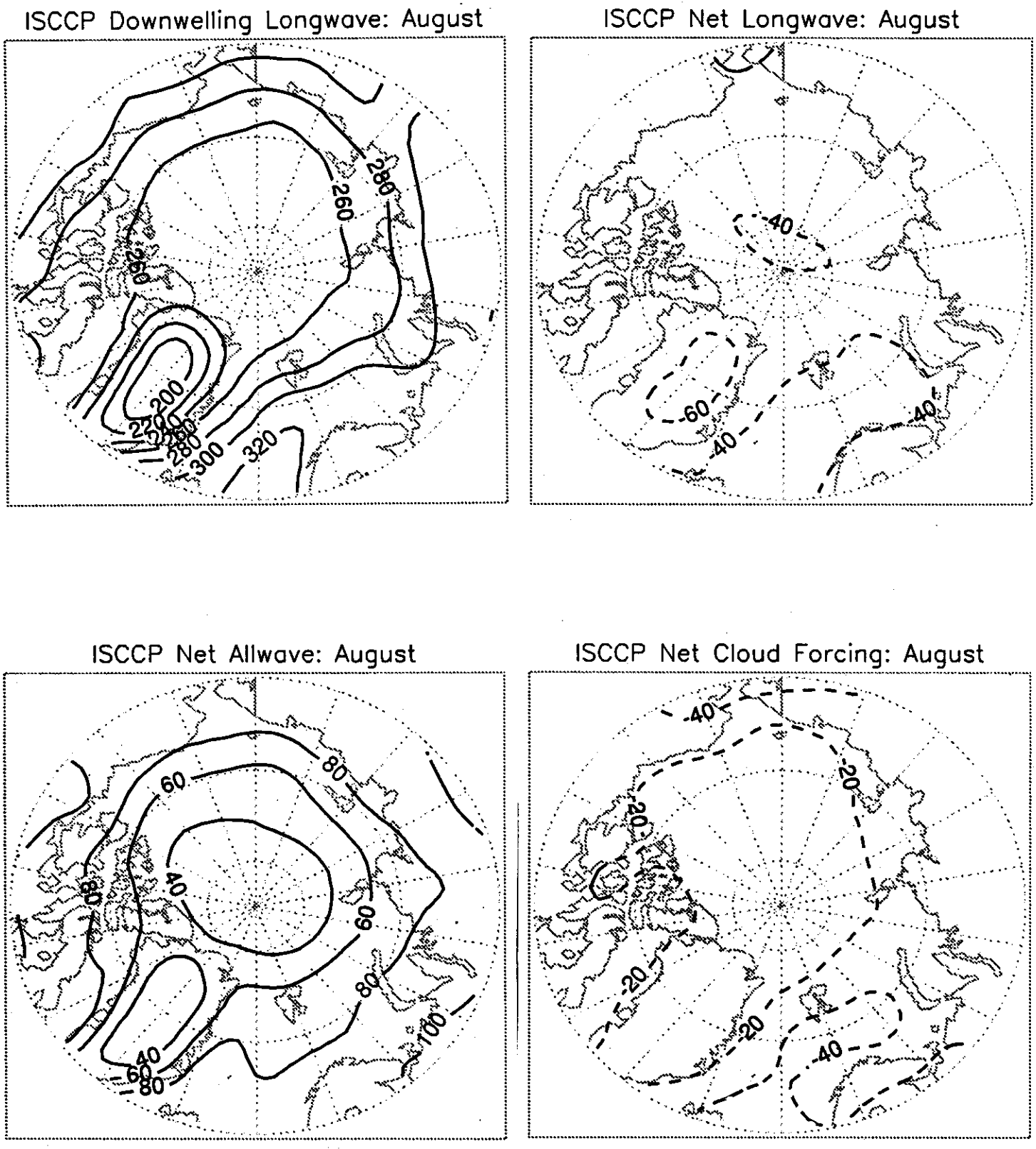

Units: W m^{-2} (Negative Contours Dashed)

Figure 2.3.6 (Continued)

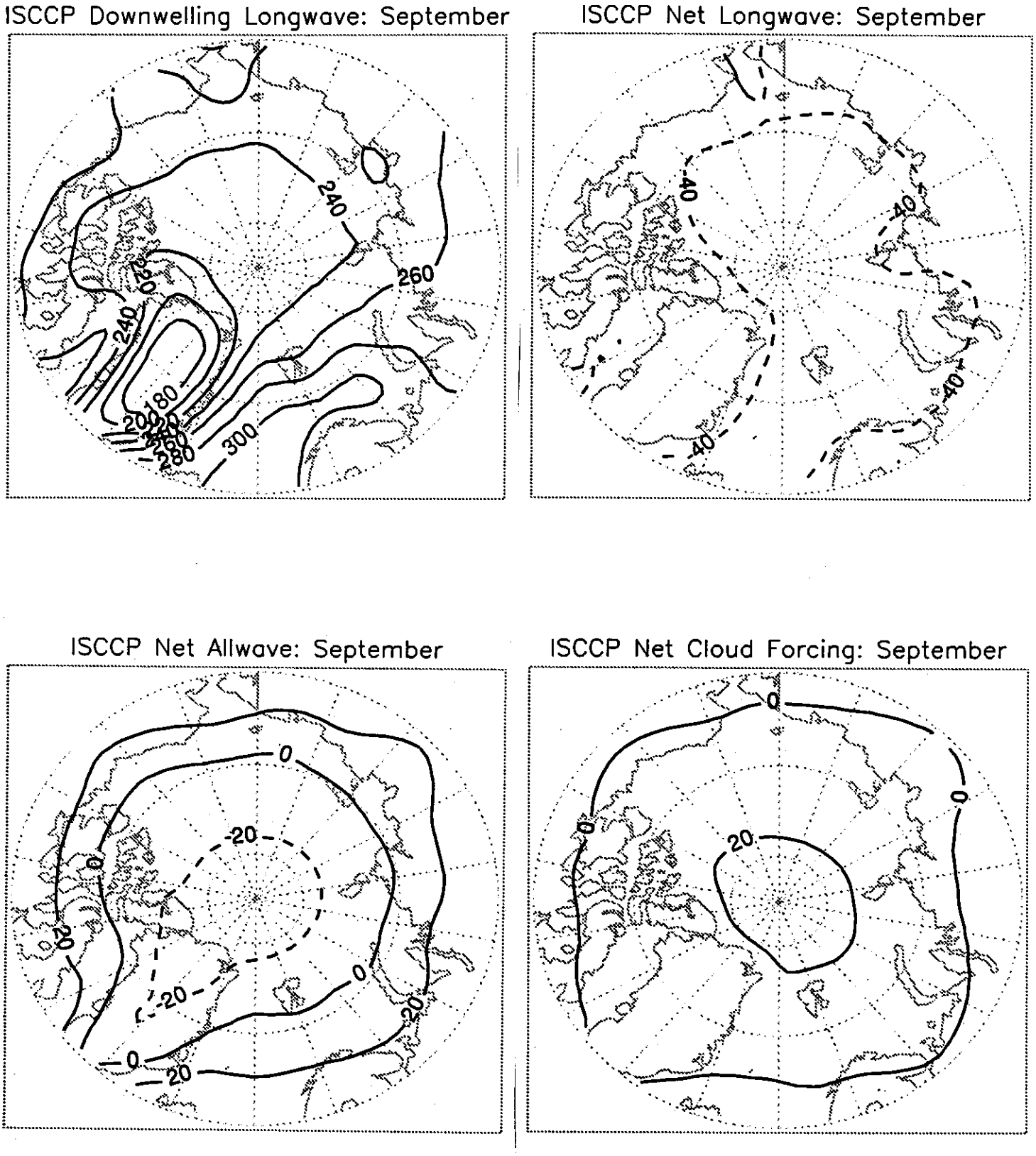

Units: W m^{-2} (Negative Contours Dashed)

Figure 2.3.6 (Continued)

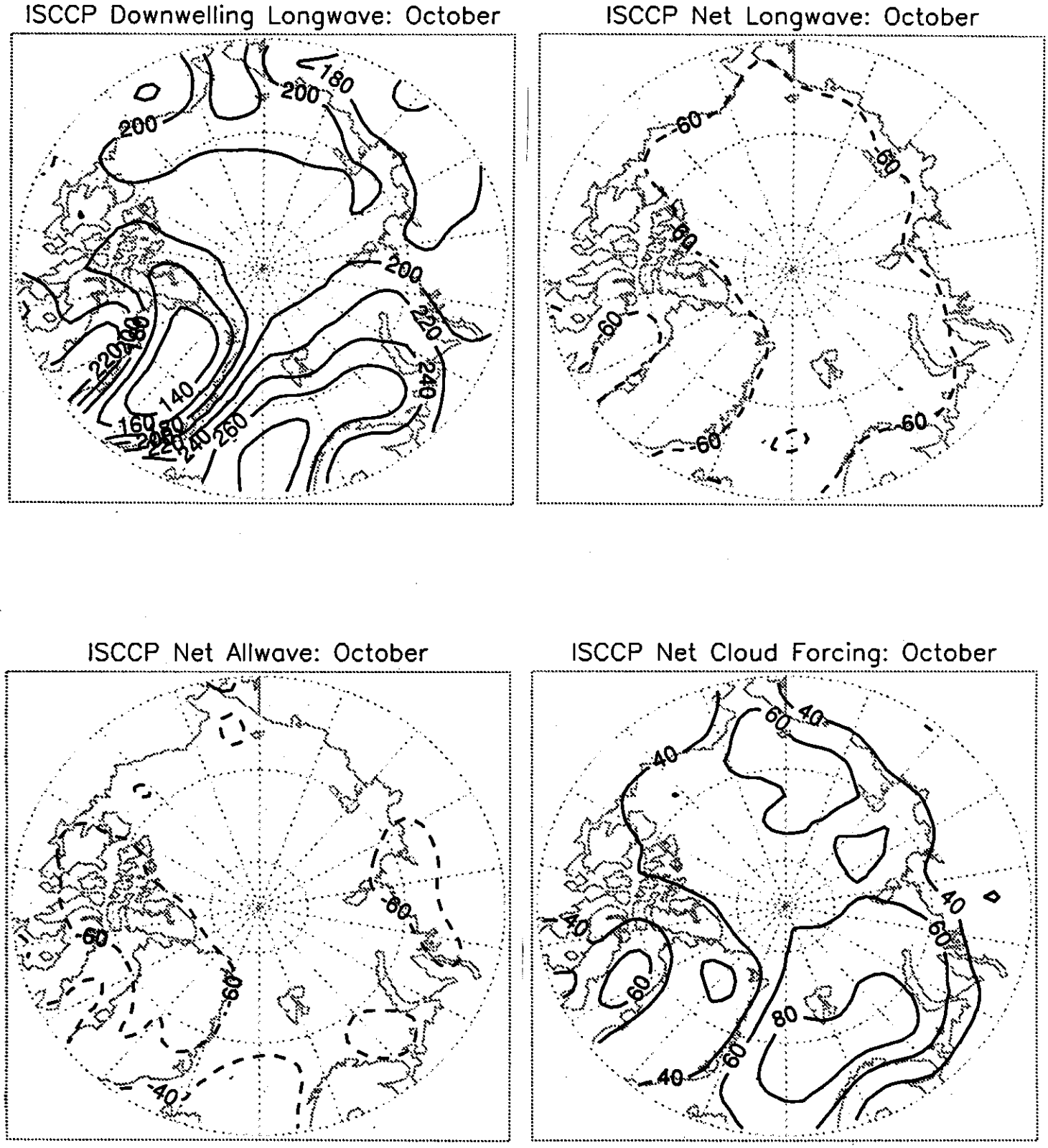

Units: W m^{-2} (Negative Contours Dashed)

Figure 2.3.6 (Continued)

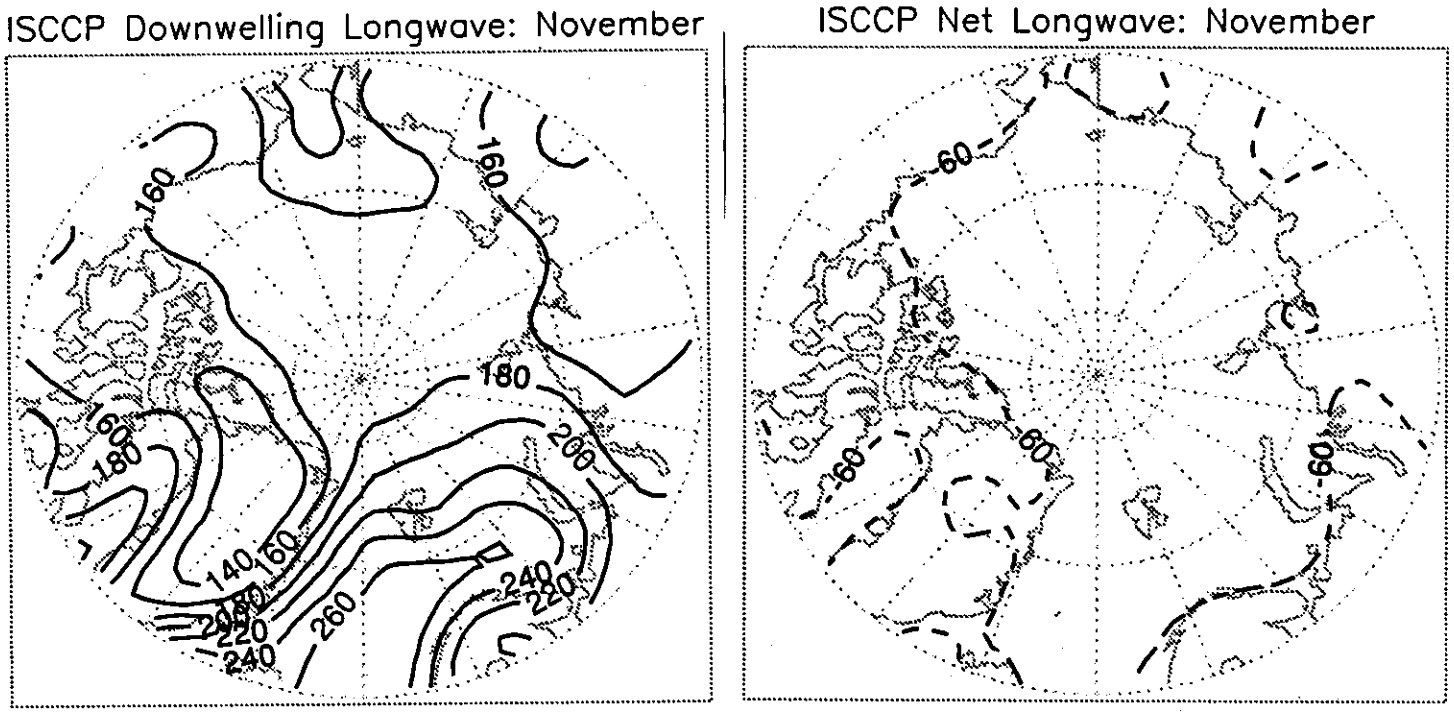

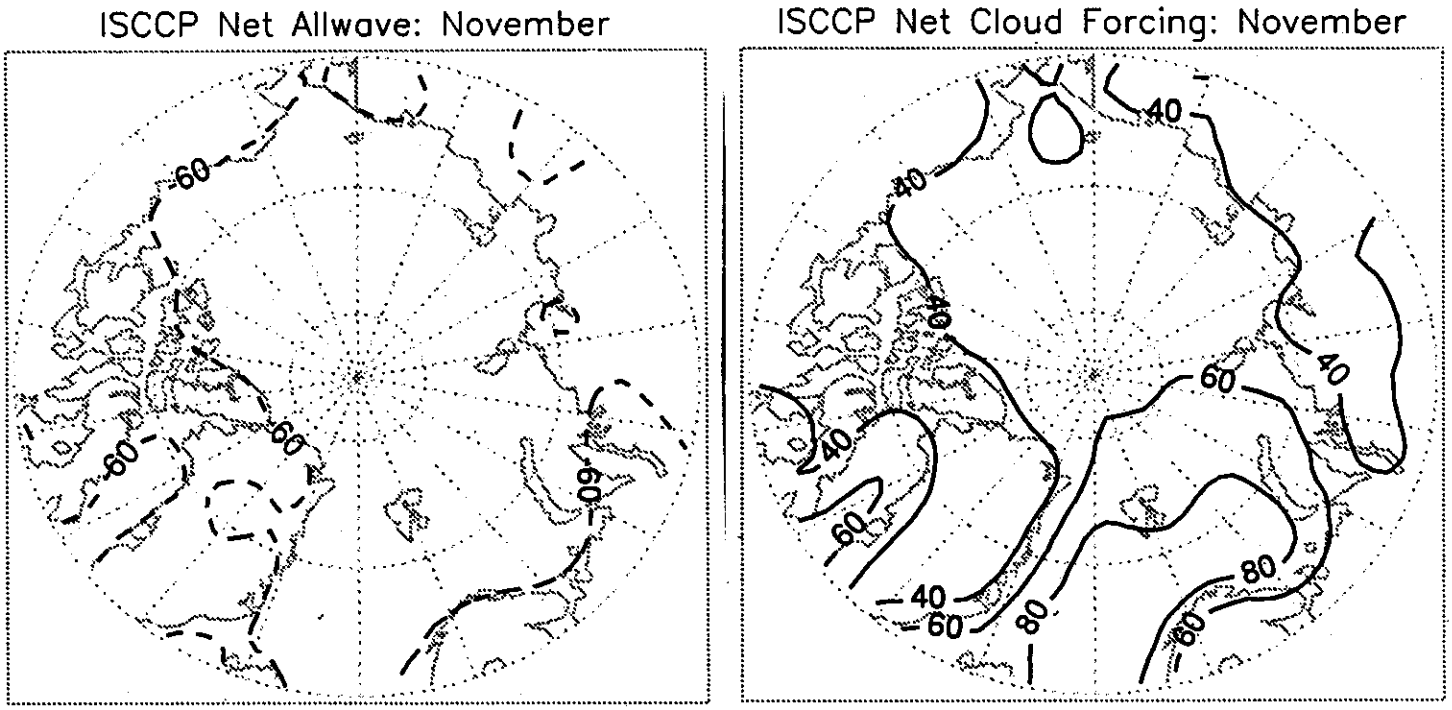

Units: W m^{-2} (Negative Contours Dashed)

Figure 2.3.6 (Continued)

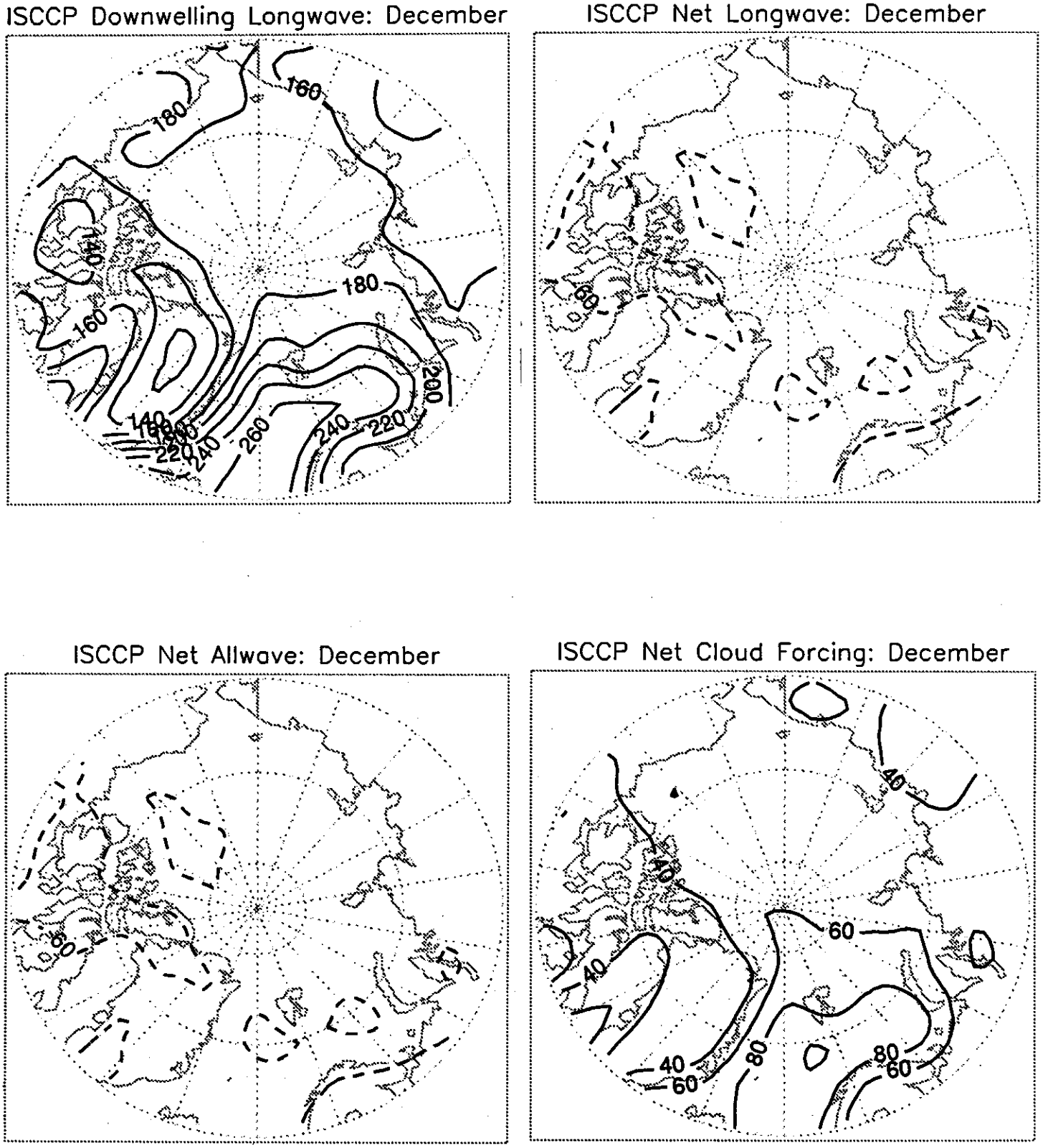

Units: W m^{-2} (Negative Contours Dashed)

Figure 2.3.7

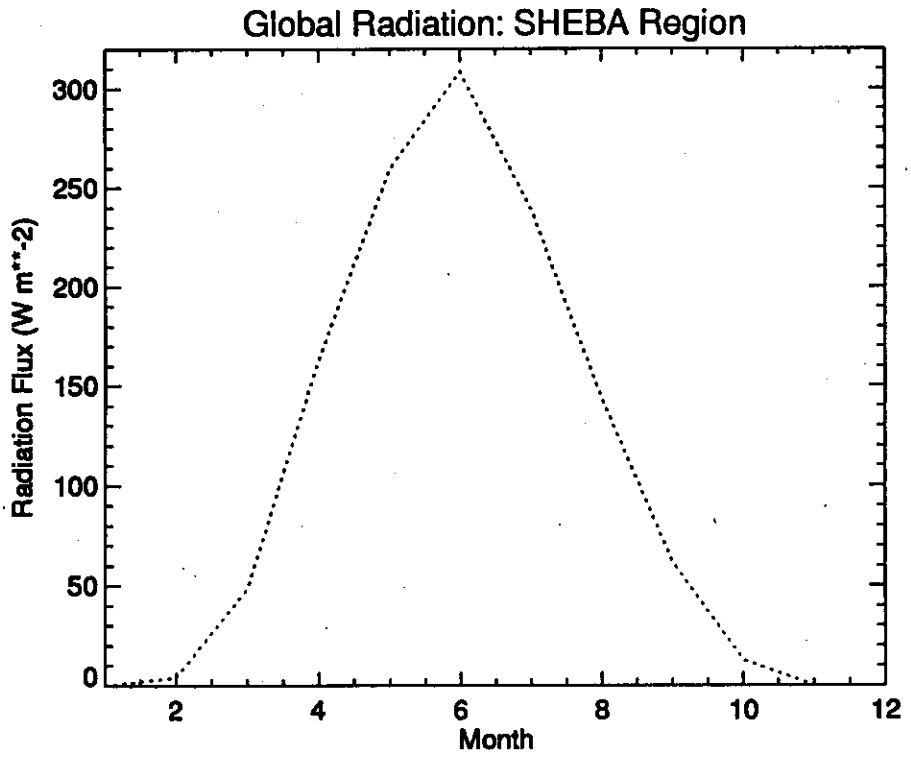

Figure 2.3.8

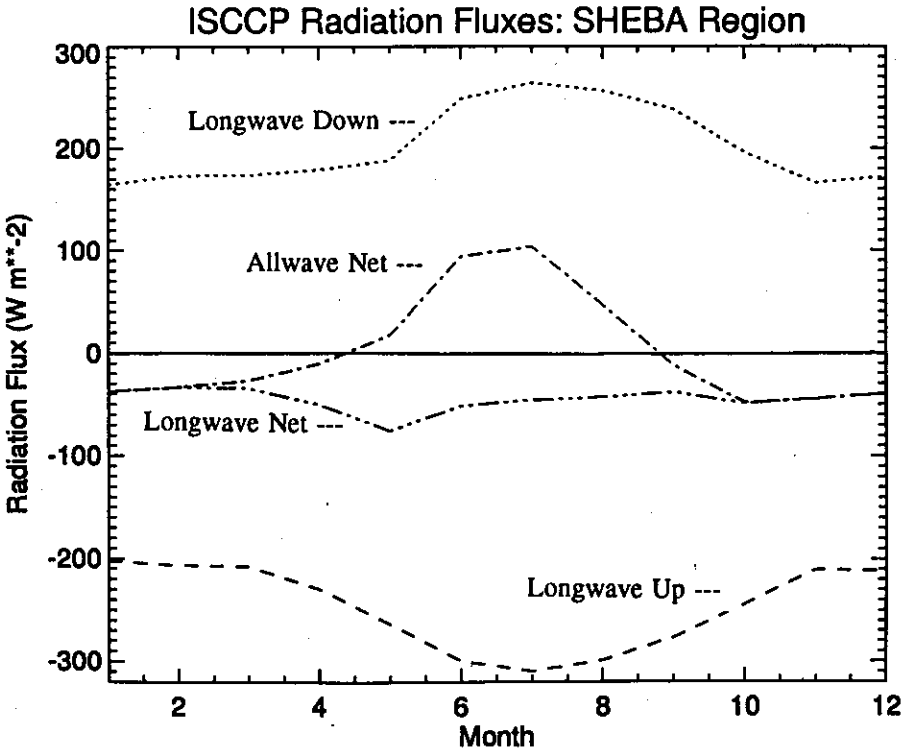

2.4. 2-Meter and Tropospheric Temperatures

Characteristics of Arctic Ocean 2-meter temperatures and have been summarized using a data set prepared by the Earth Observing System (EOS) Polar Exchange at the Sea Surface (POLES) project of the University of Washington. This data set represents a blend of observations from land stations, ships, drifting NP ice camps, and drifting buoys from the International Arctic Buoy Program (IABP). Temperatures, error estimates, and other quality control information are provided four times per day. The period of record used here is 1979-1993. The data represent 2-meter temperatures, with the caveat that the drifting buoys, which are placed on the ice surface, may not be entirely representative of this level. In particular, the buoy measurements can be affected by the insulating effects of snow cover and by solar heating. Estimated errors in the station observations are about 0.1°C and about 2.0°C for the drifting buoys. The data and documentation are available at http://psc.apl.washington.edu/poles/POLES.html. Additional information is provided by Munoz and Martin [1995] and Schweiger and Francis [1995]. We have interpolated the POLES data set to the EASE-Grid. Monthly mean temperatures and the absolute range in monthly mean temperatures for the Arctic Ocean (Figure 2.4.1) are shown along with seasonal cycles (Figure 2.4.2) and monthly histograms (Figure 2.4.3) for the SHEBA site, the latter based on the six-hourly data. We also provide monthly vertical temperature profiles (tropospheric temperatures) at the SHEBA site (Figure 2.4.4). These were compiled using the Arctic water vapor characteristics data set described by Serreze et al. [1995] and outlined in Section 1.3.

Temperatures increase sharply from the central Arctic Ocean to the Atlantic side during winter, spring and autumn, contrasting with a primarily zonal distribution during summer. The temperature range is large (10-20°C) for all of the Arctic during winter, tending to be highest north of Novaya Zemlya, reflecting variability in cyclones activity and warm advection in this region. Temperature ranges are much smaller in summer due to the dampening effects of the melting ice surface. For the SHEBA region, an average seasonal low of about -30°C (243 K) is indicated for January and February, but with a large range of 13-15°C between extreme years. The peak temperature during July is slightly above freezing, with a range of about 5°C. These results are well evident in the histograms. Winter months show broad, flat distributions with occasional values below -40°C. Moving from spring into summer, the distributions shift to the right towards higher mean temperatures and become sharply peaked. Tropospheric temperatures for the SHEBA site show the characteristic strong low-level, surface-based temperature inversion in winter months. For January, the inversion top is at about the 900 mb level, with a temperature difference across the inversion of about 10°C. No pronounced inversion is seen in the mean fields for May through September, although inversions are present in many individual soundings.

Figure 2.4.1

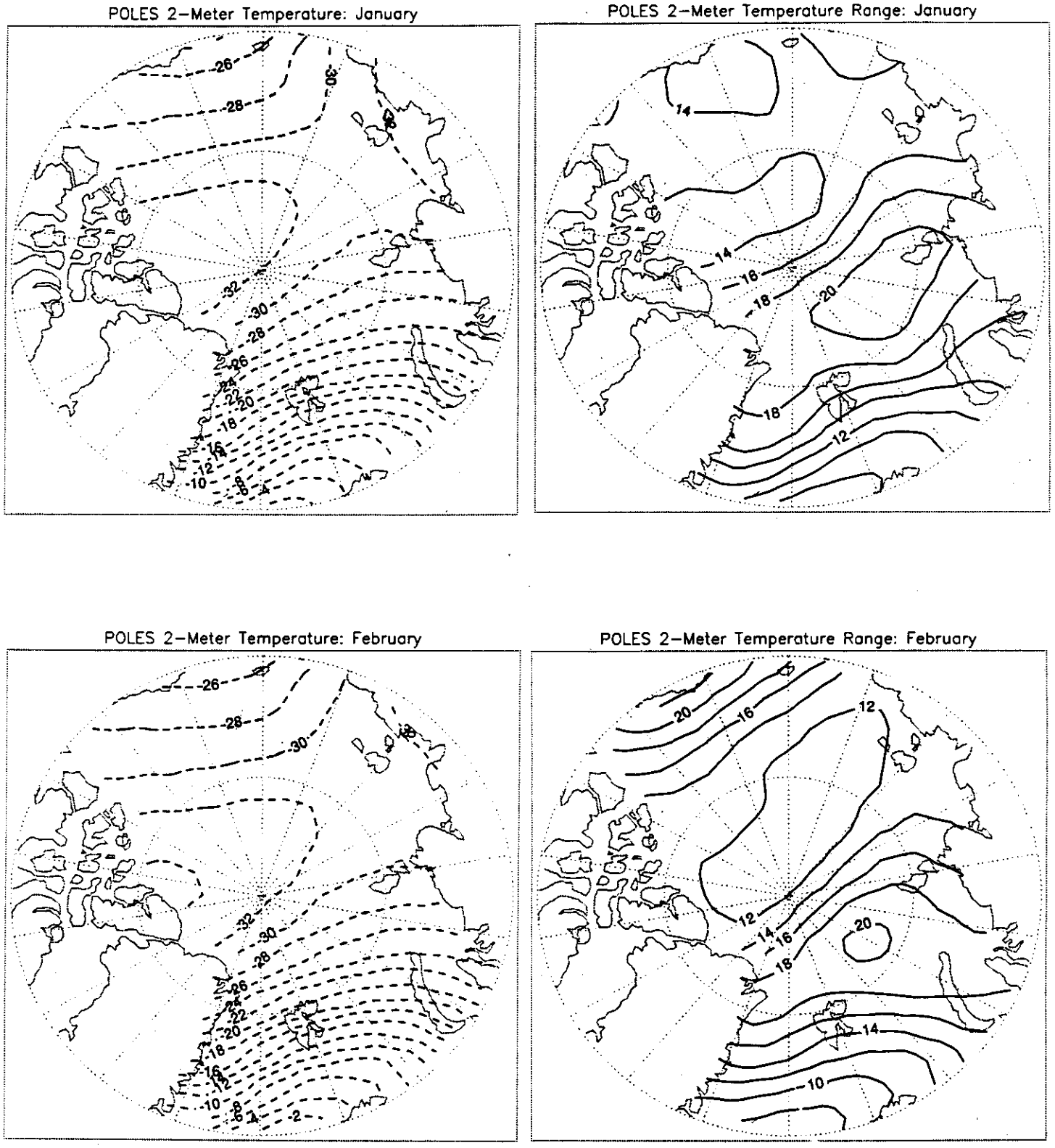

Units: °C (Negative Contours Dashed)

Figure 2.4.1 (Continued)

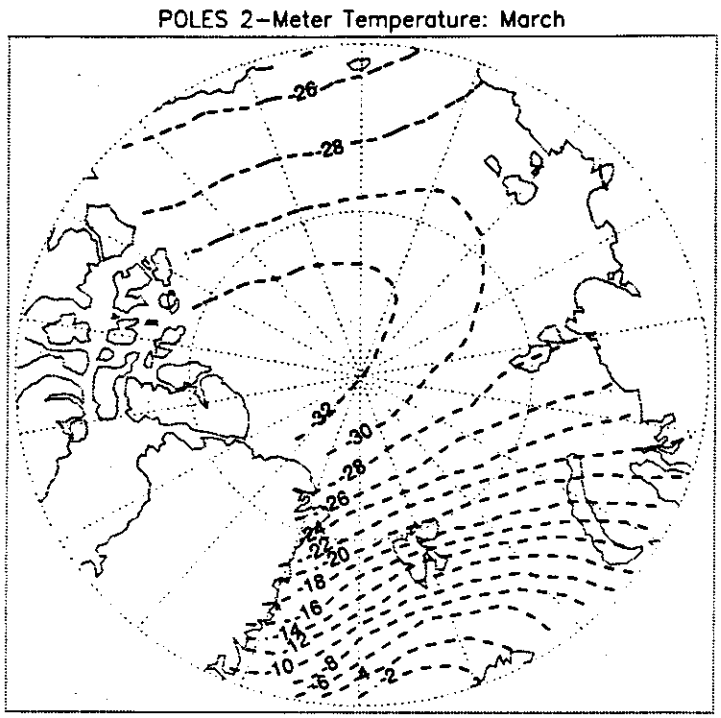

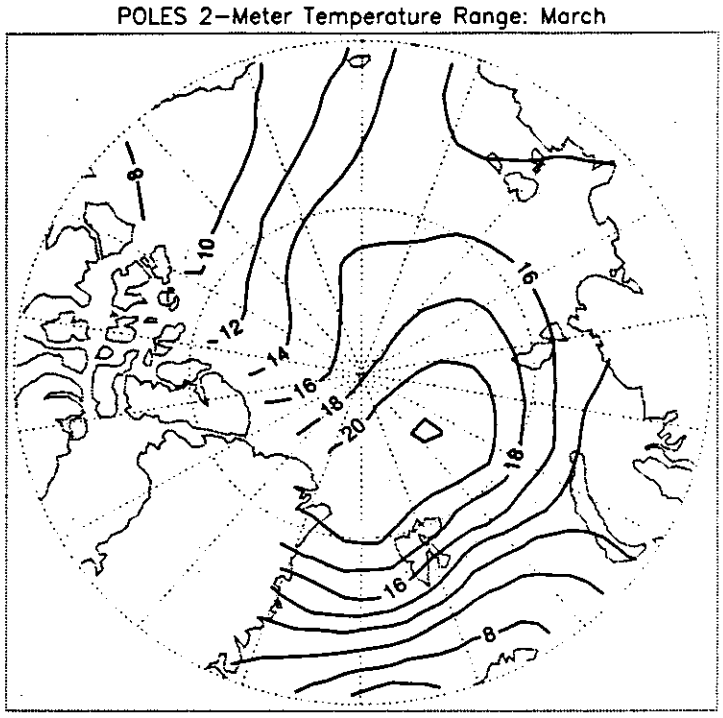

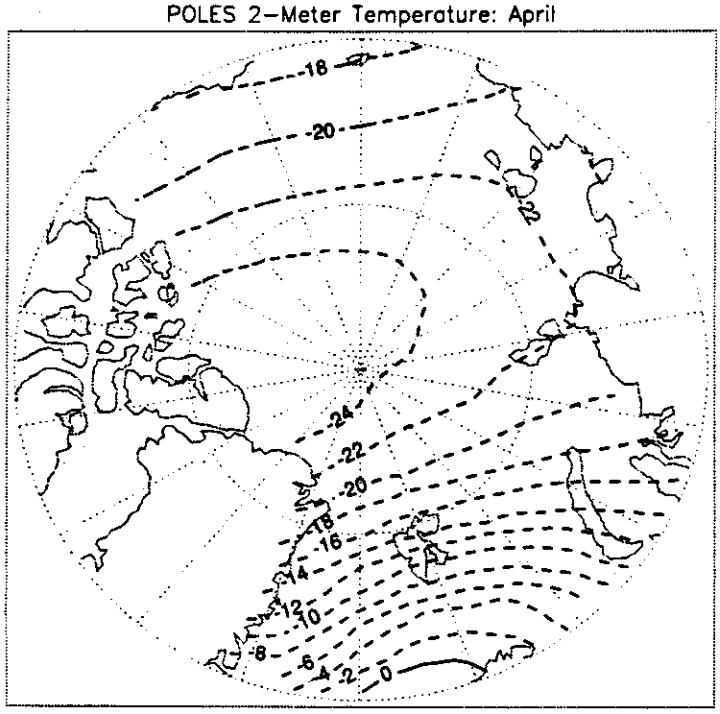

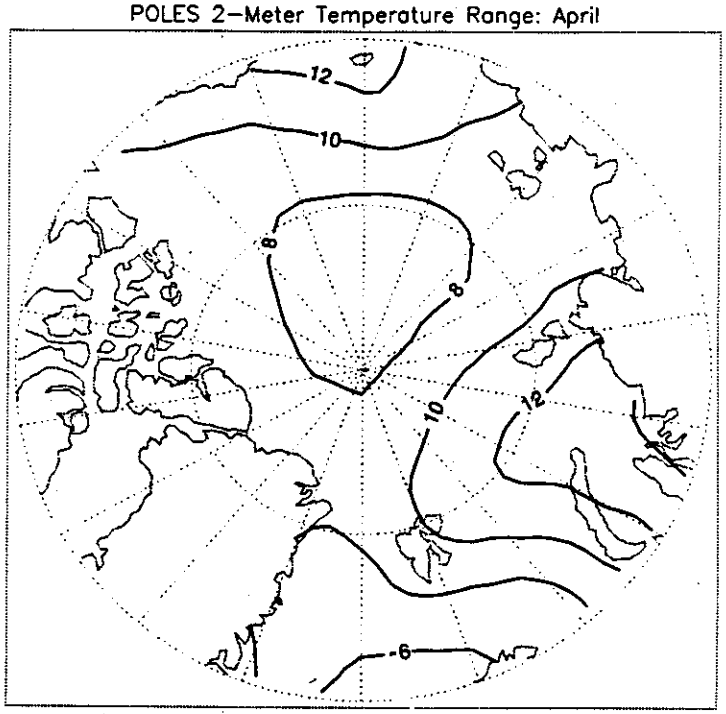

Units: °C (Negative Contours Dashed)

Figure 2.4.1 (Continued)

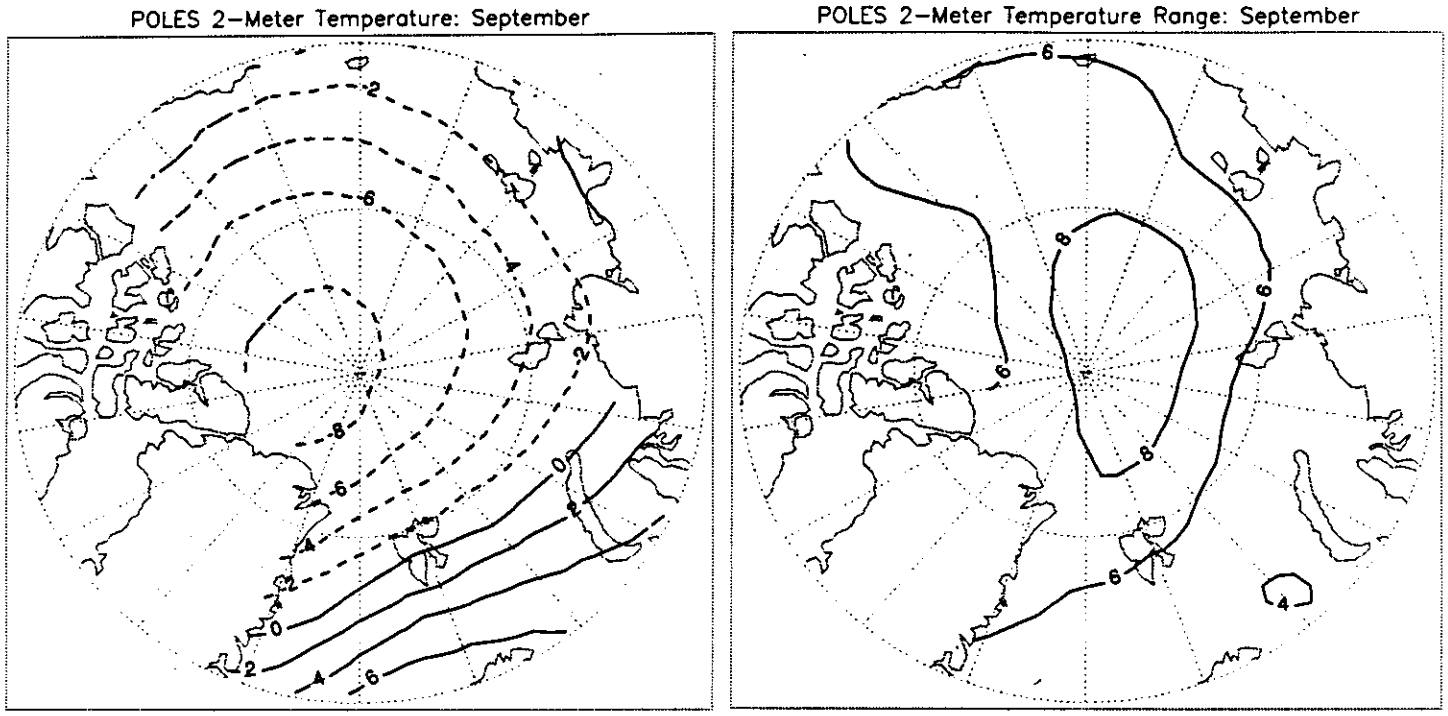

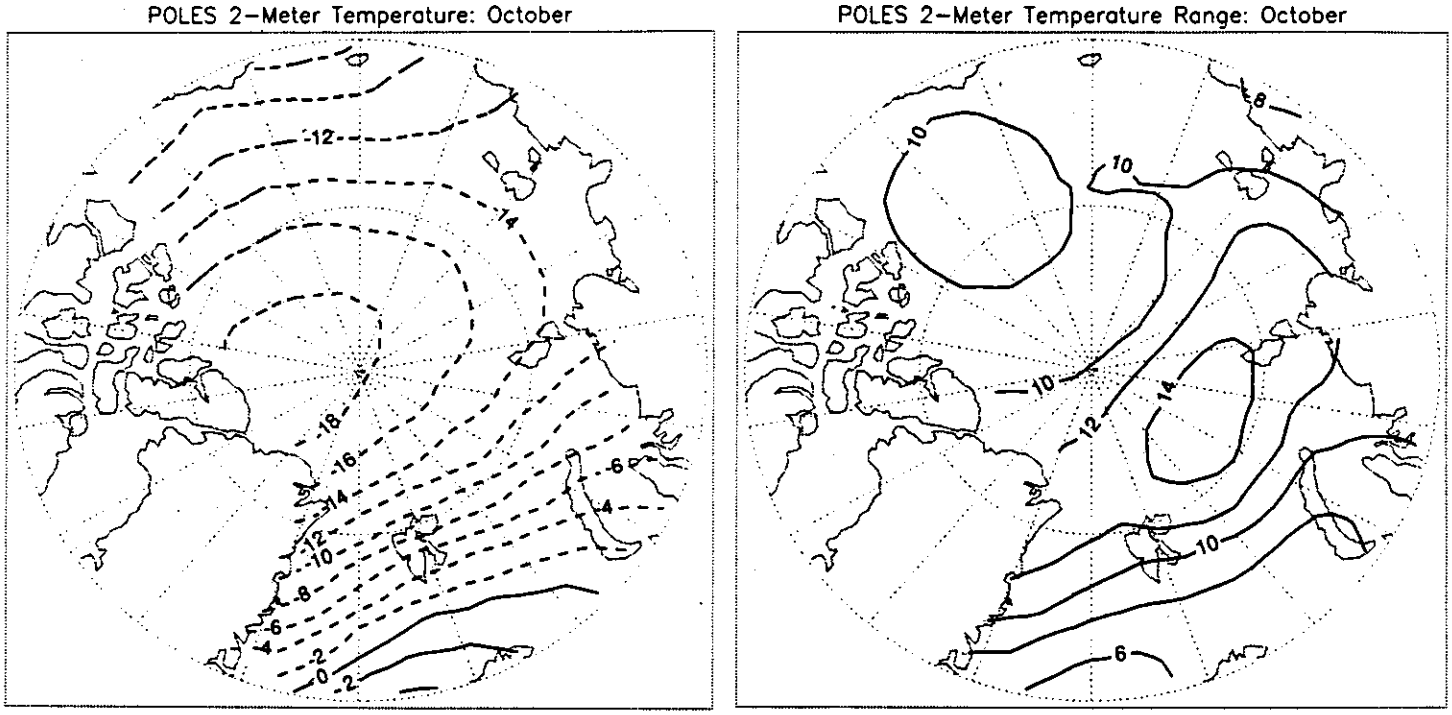

Units: °C (Negative Contours Dashed)

Figure 2.4.1 (Continued)

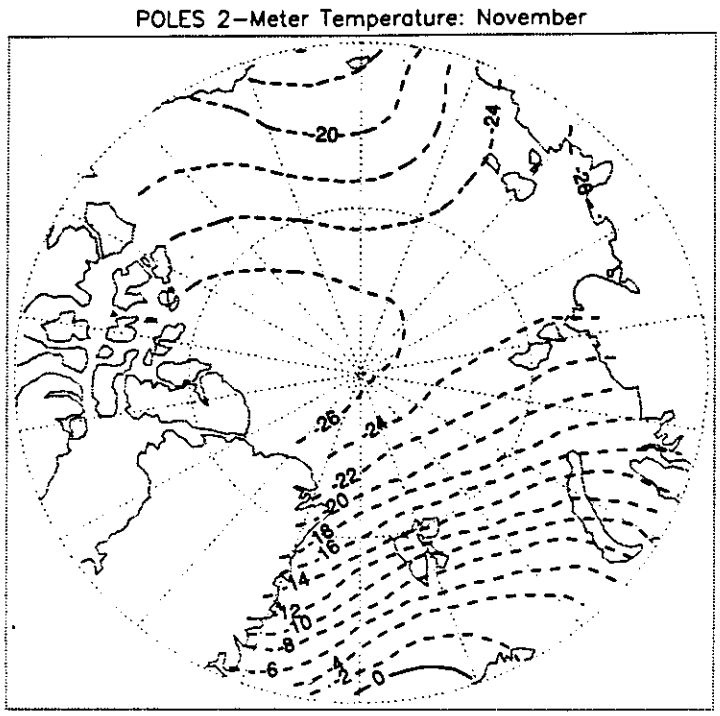

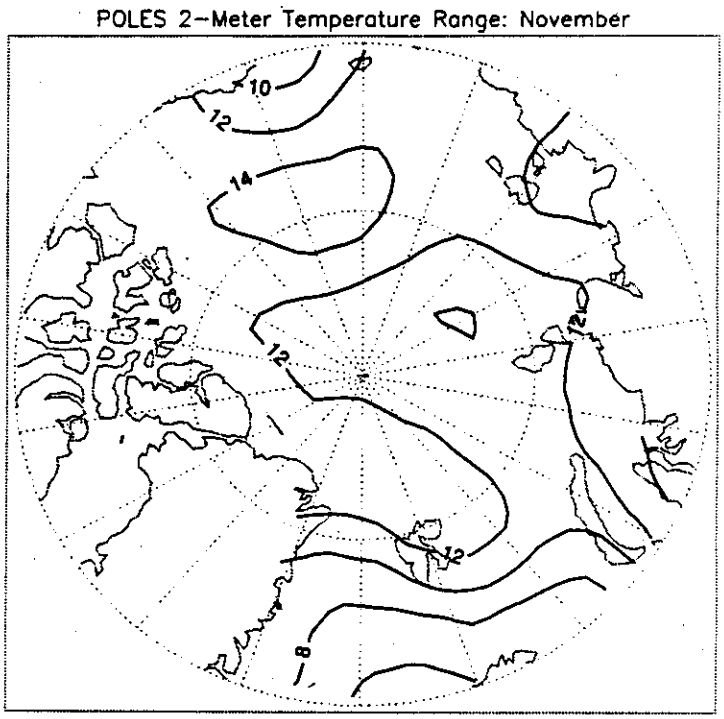

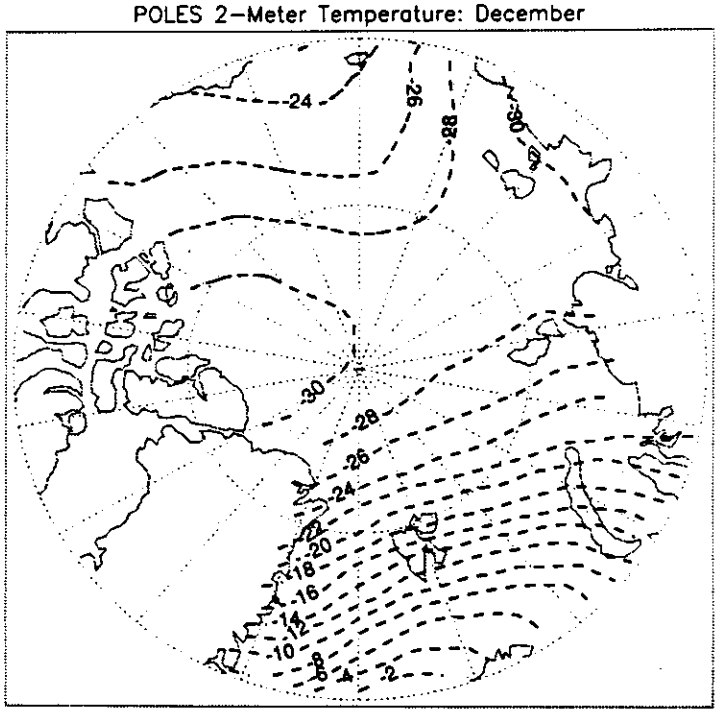

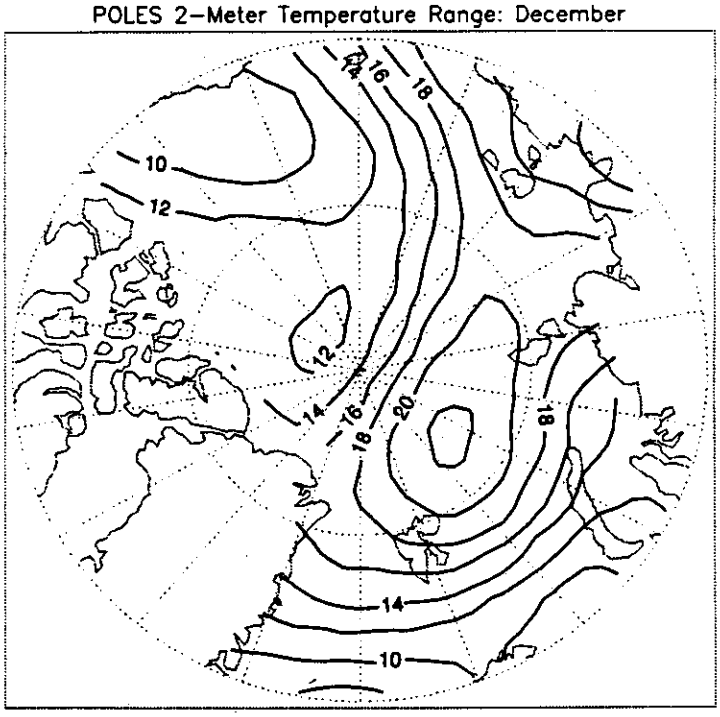

Units: °C (Negative Contours Dashed)

Figure 2.4.2

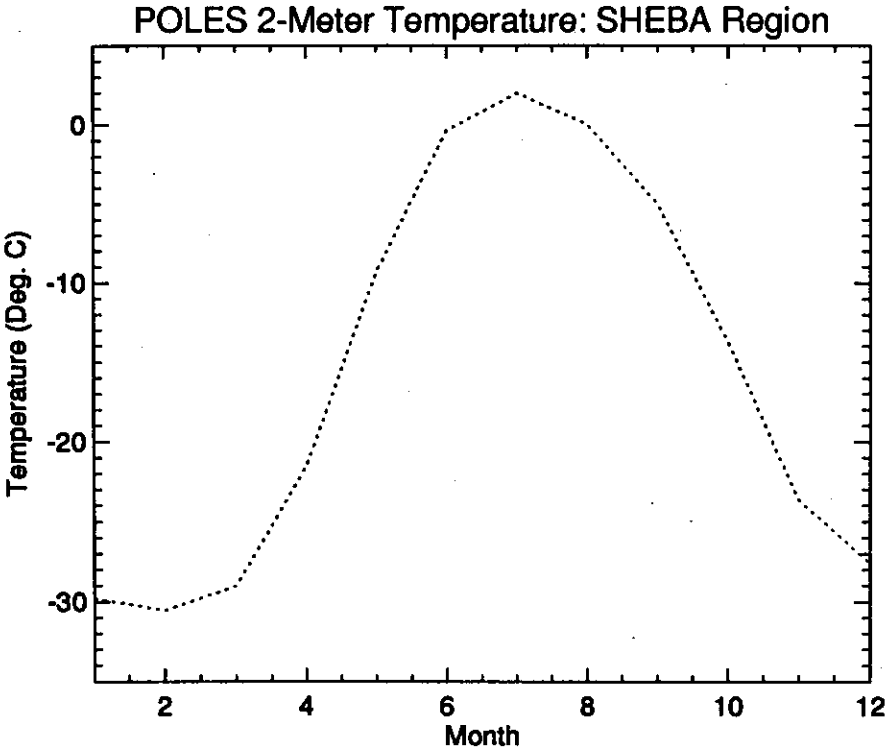
POLES 2-Meter Temperature: SHEBA Region
Temperature (Deg. C)
0
-10
-20
-30
2
4
6
8
10
12
Month

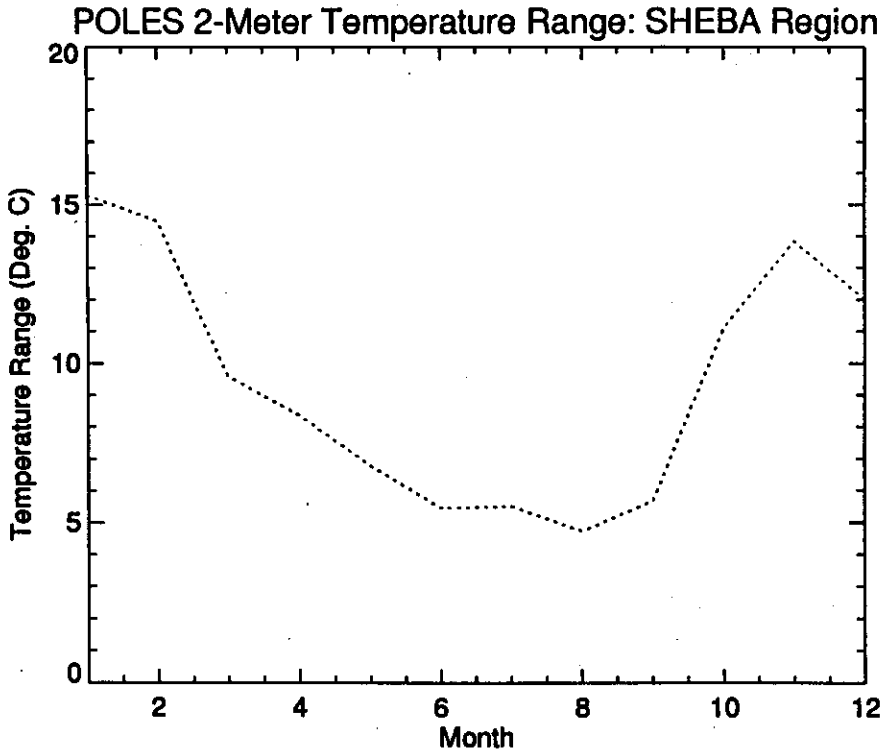
POLES 2-Meter Temperature Range: SHEBA Region
Temperature Range (Deg. C)
20
15
10
5
0
2
4
6
8
10
12
Month

Figure 2.4.3

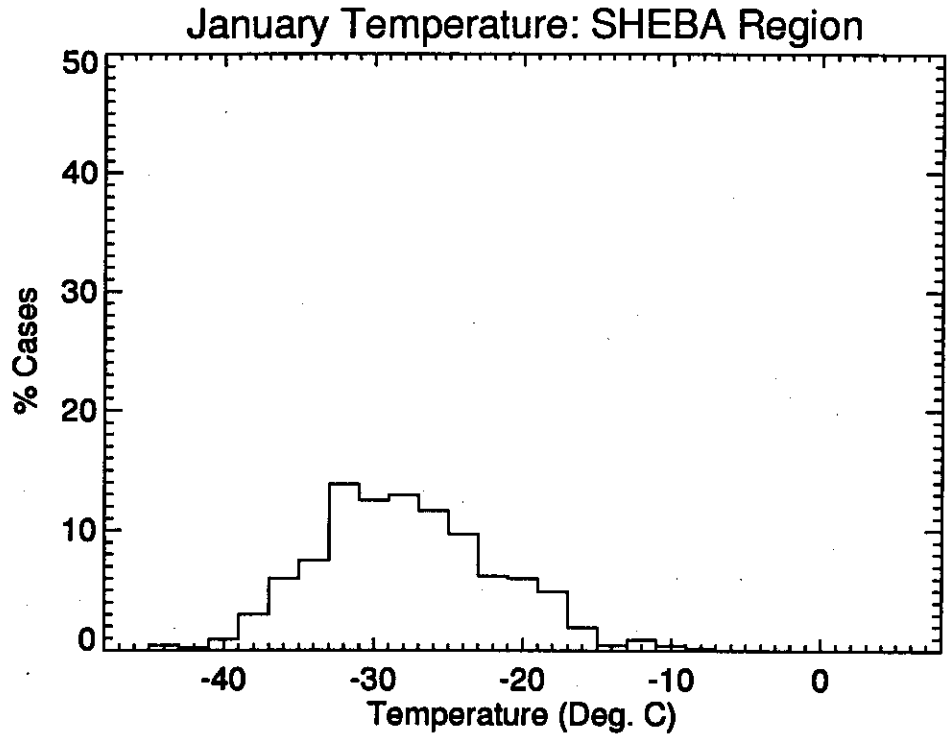
January Temperature: SHEBA Region
% Cases
50
40
30
20
10
0
-40
-30
-20
-10
0
Temperature (Deg. C)

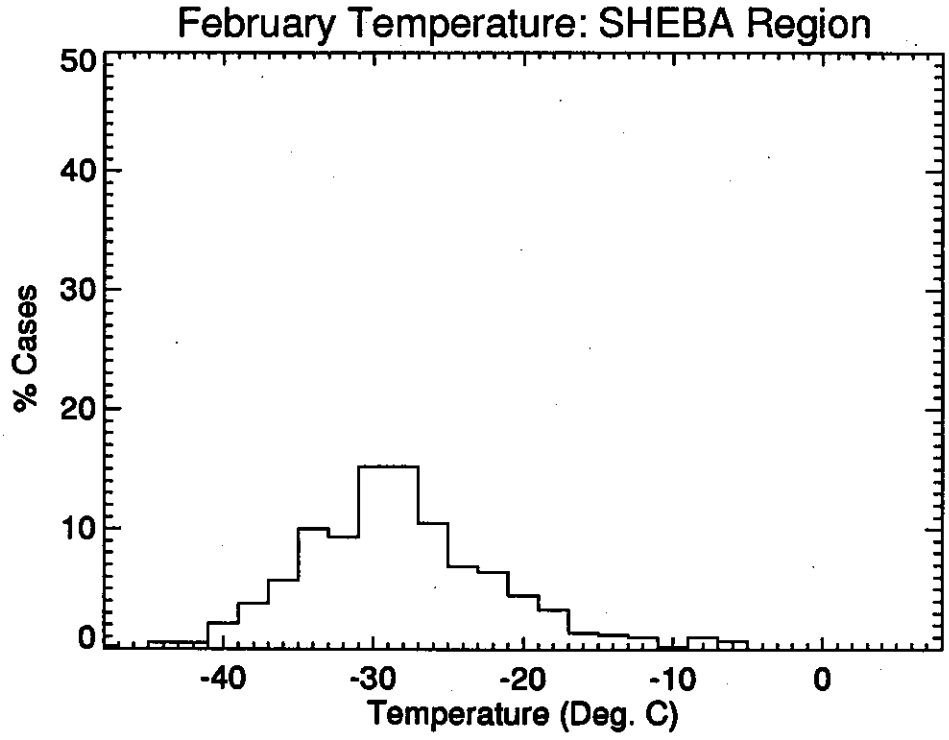
February Temperature: SHEBA Region
% Cases
50
40
30
20
10
0
-40
-30
-20
-10
0
Temperature (Deg. C)

Figure 2.4.3 (Continued)

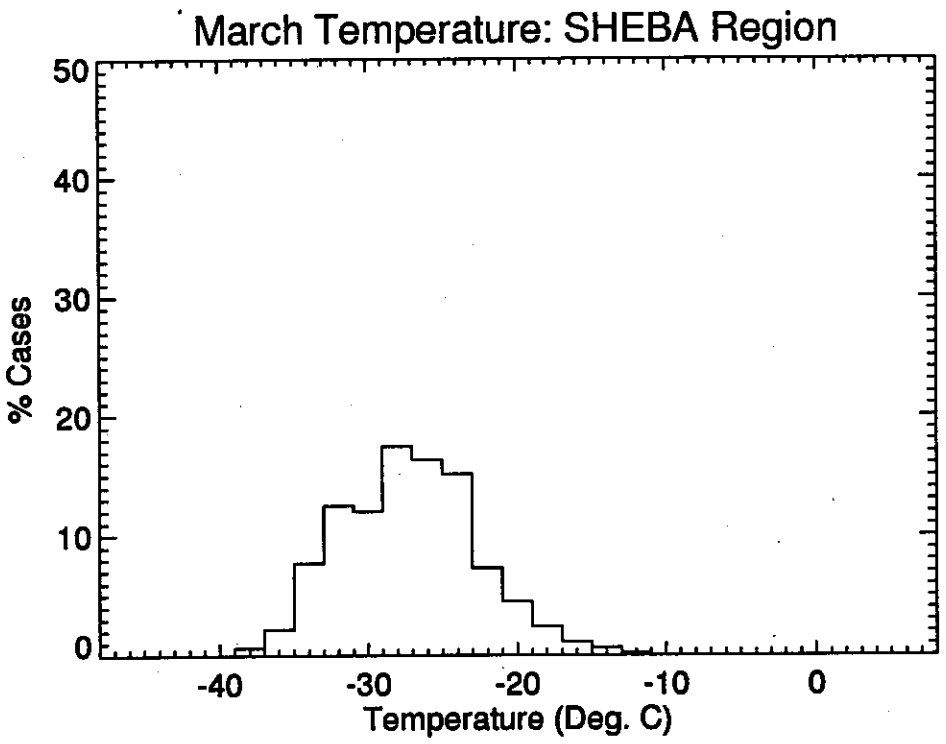

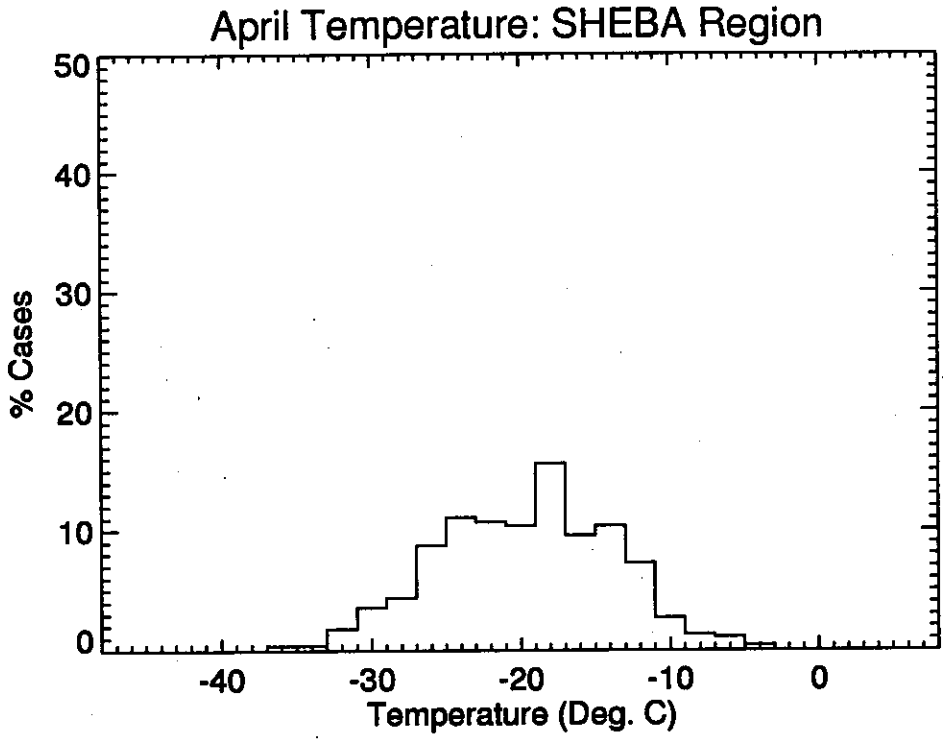

Figure 2.4.3 (Continued)

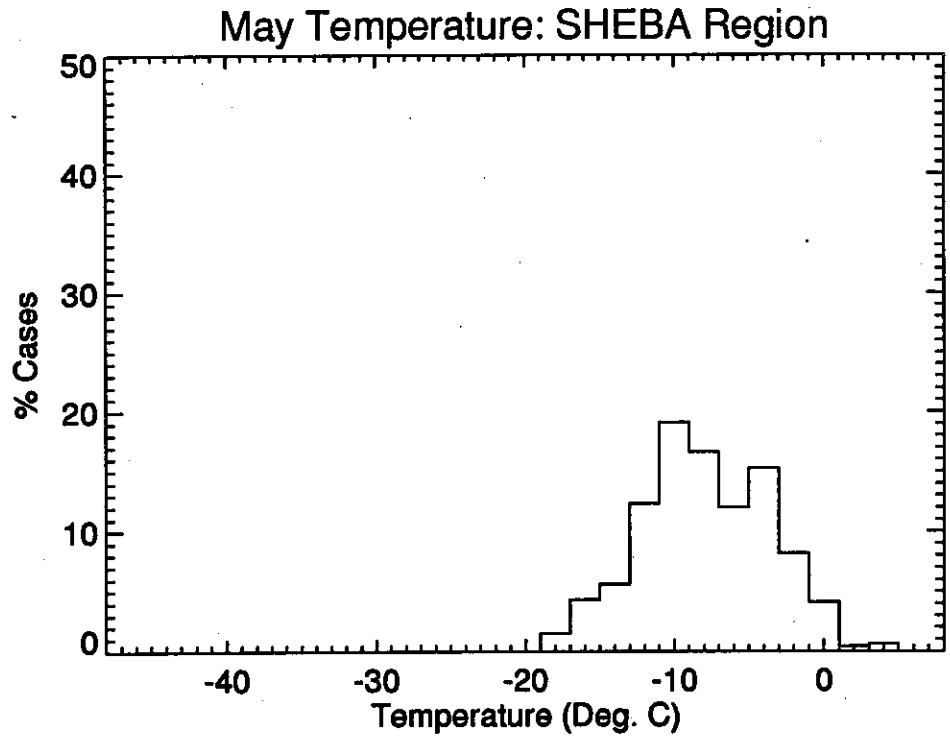

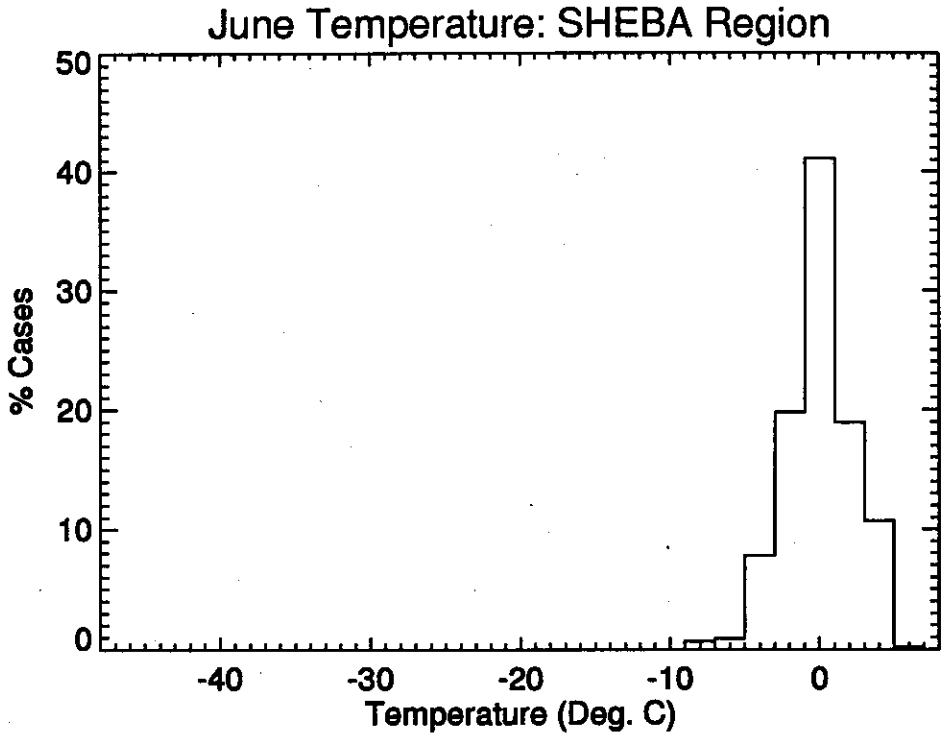

Figure 2.4.3 (Continued)

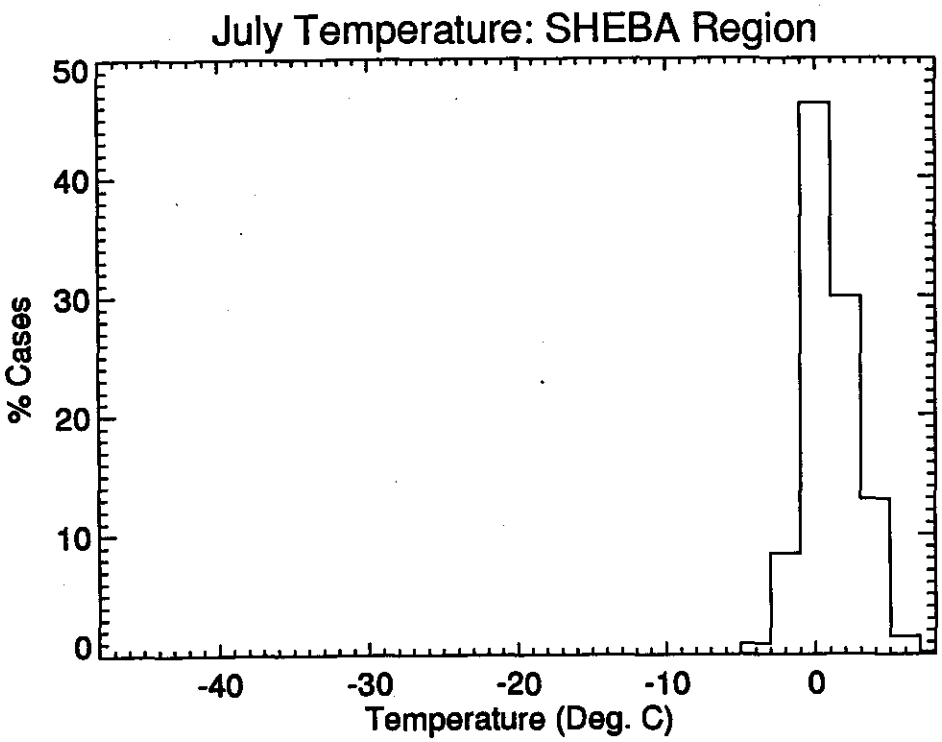

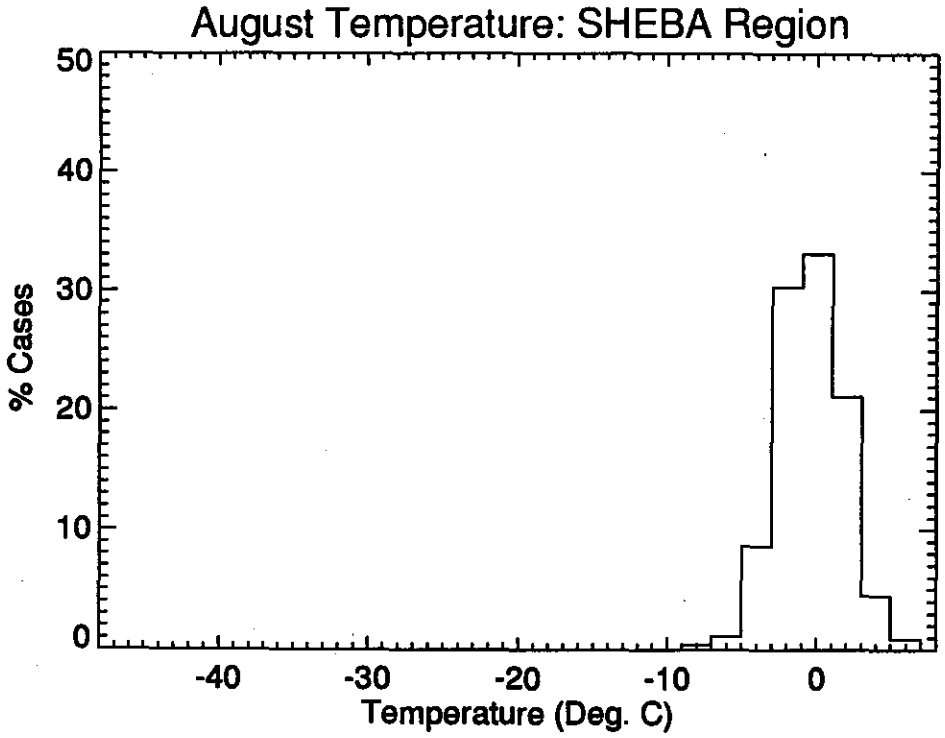

Figure 2.4.3 (Continued)

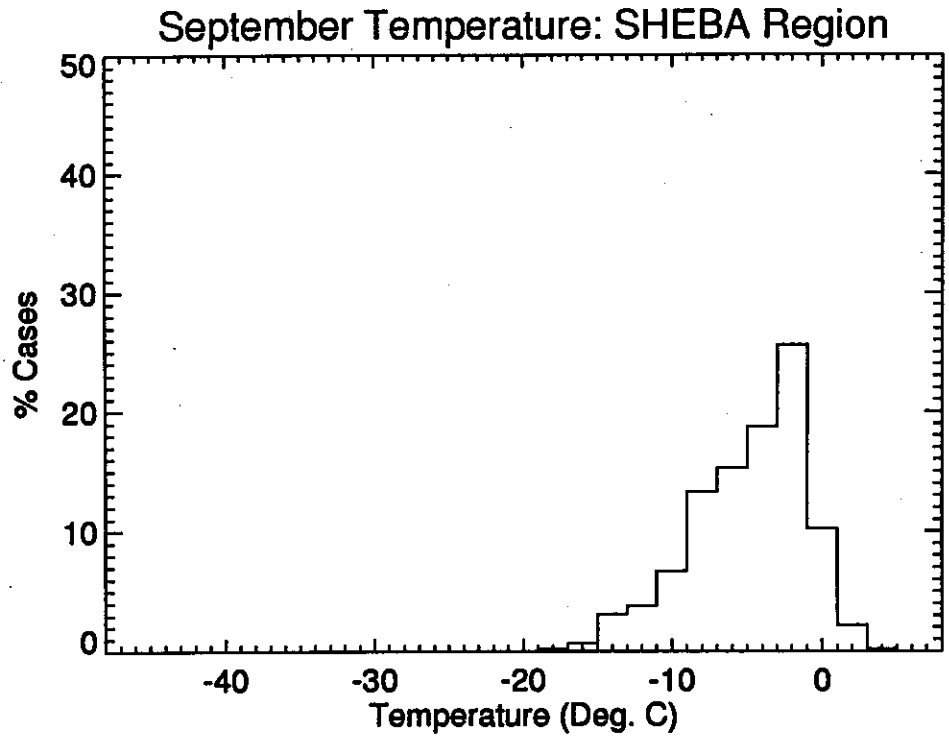

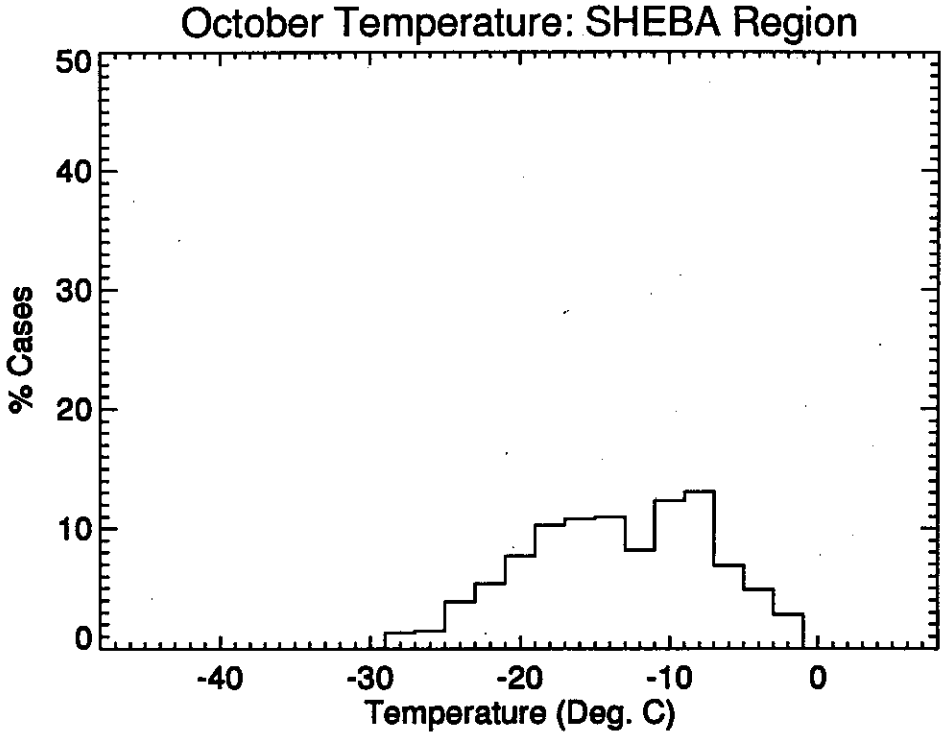

Figure 2.4.3 (Continued)

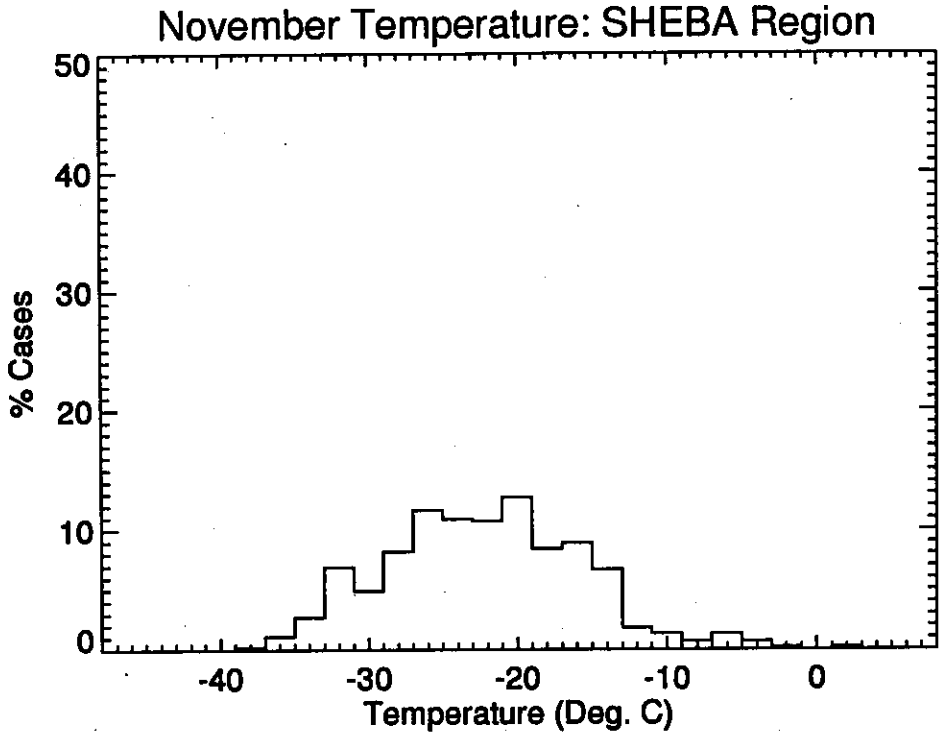

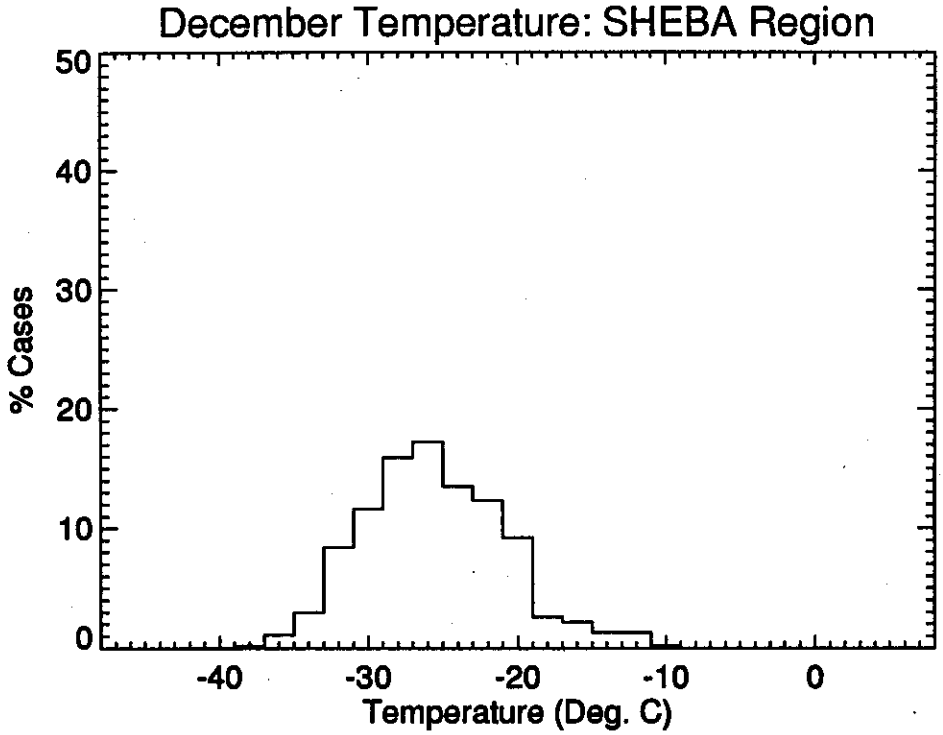

Figure 2.4.4

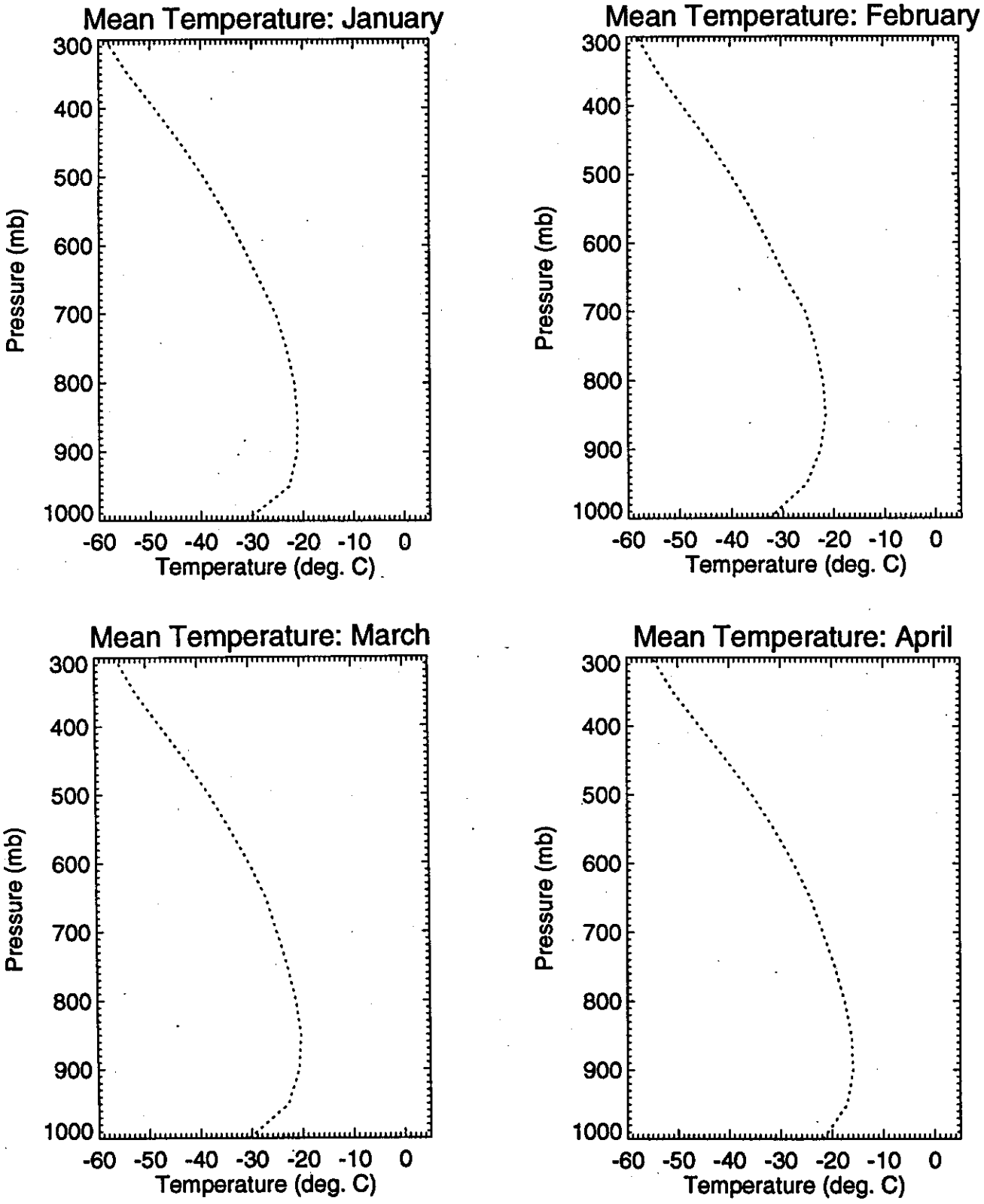
Mean Temperature: January
Pressure (mb)
300
400
500
600
700
800
900
1000
-60 -50 -40 -30 -20 -10 0
Temperature (deg. C)
Mean Temperature: February
Pressure (mb)
300
400
500
600
700
800
900
1000
-60 -50 -40 -30 -20 -10 0
Temperature (deg. C)
Mean Temperature: March
Pressure (mb)
300
400
500
600
700
800
900
1000
-60 -50 -40 -30 -20 -10 0
Temperature (deg. C)
Mean Temperature: April
Pressure (mb)
300
400
500
600
700
800
900
1000
-60 -50 -40 -30 -20 -10 0
Temperature (deg. C)

Figure 2.4.4 (Continued)

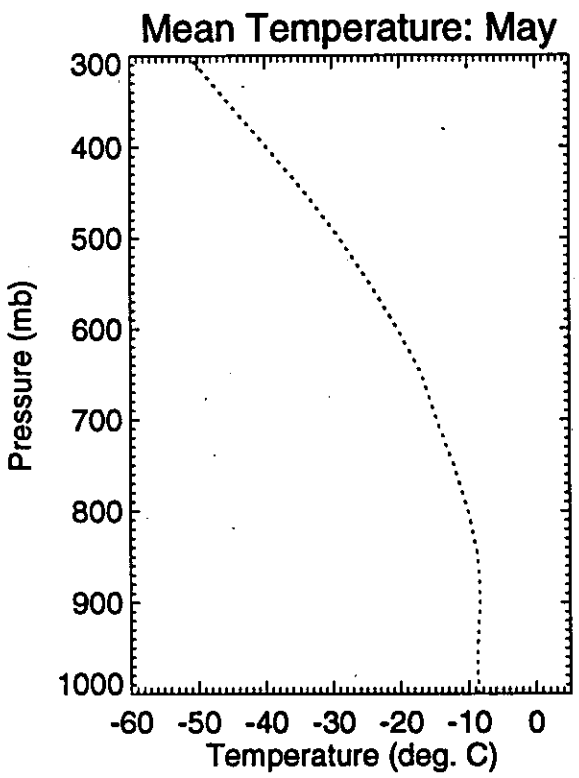

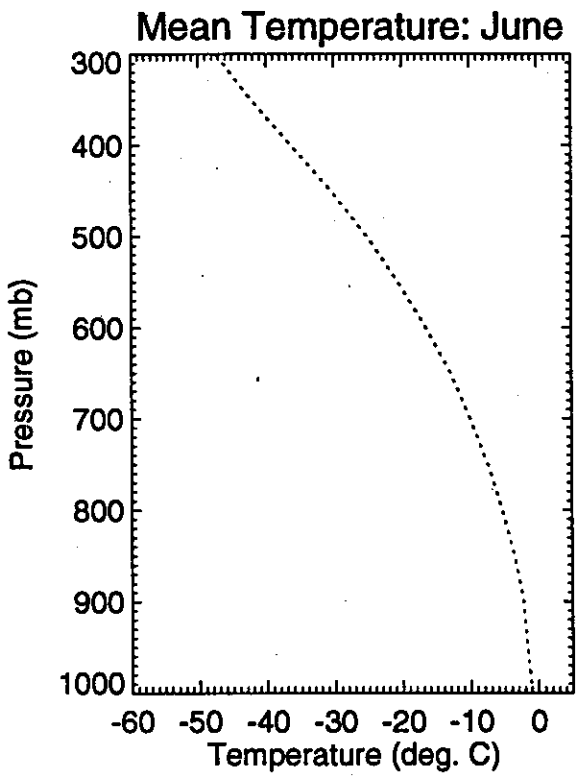

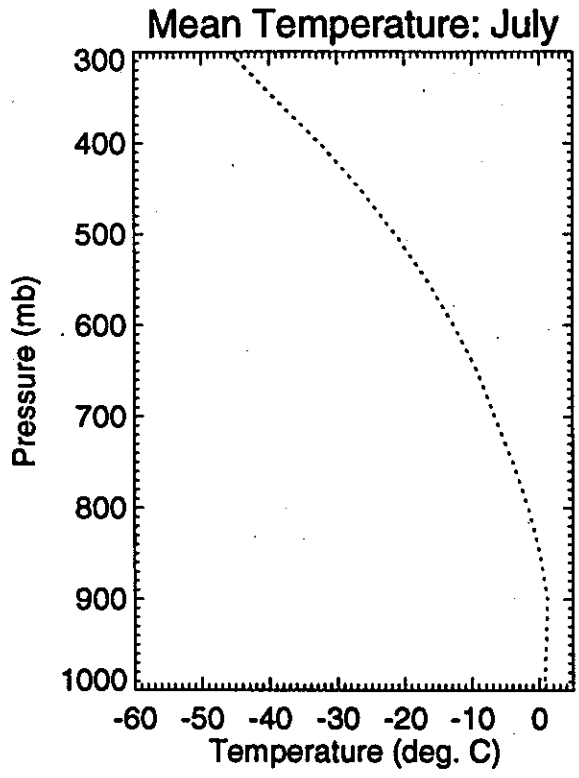

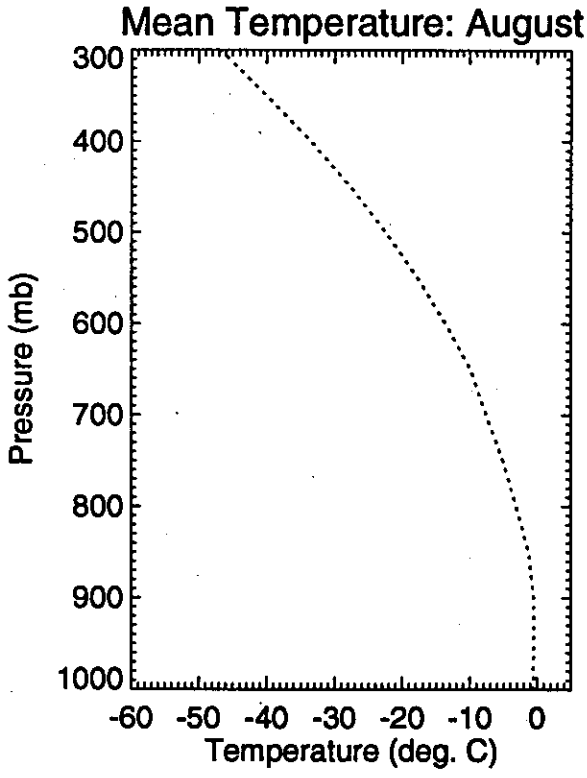

Figure 2.4.4 (Continued)

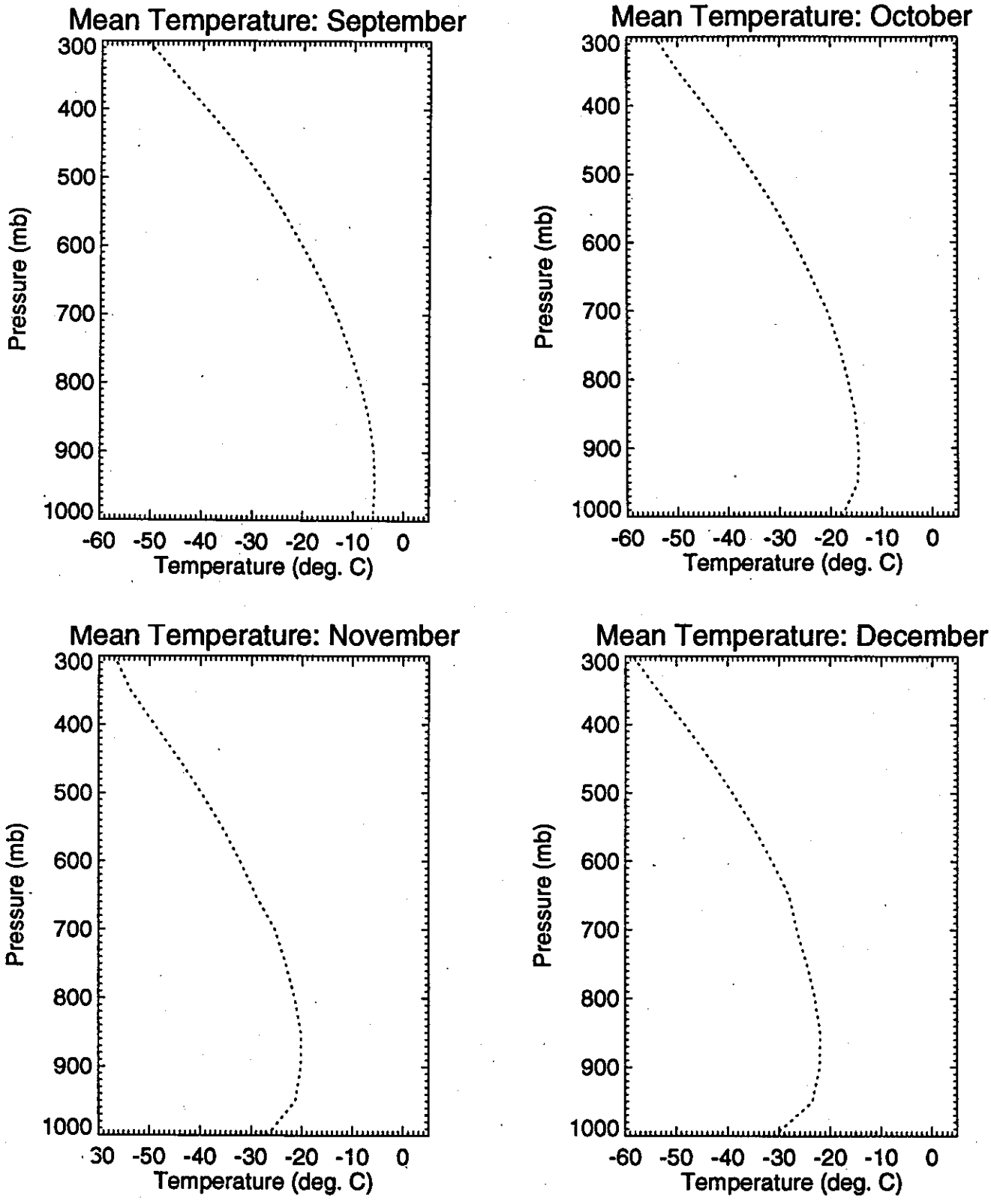

2.5 Surface Winds

Mean monthly surface winds (m s^{-1}), based on COADS reports for the period 1950-1995 for EASE-Grid locations over the Arctic Ocean are shown in Figure 2.5.1. Histograms of wind speed in m s^{-1} for each month for the SHEBA region, based on the individual COADS reports are shown in Figure 2.5.2. As with the other COADS-based analyses, the monthly means are based on a 600 km search radius and a minimum of 150 cases for each grid point, with results presented as character plots rather then isolines because of the missing data problem. To get enough cases for the histograms of daily wind speed, we used a larger 750 km search radius and required a minimum of 200 cases for each month.

Winter months show a distinct increase in mean wind speeds from the central Arctic Ocean of typically 4-5 m s^{-1} towards the Atlantic side of the Arctic, where values may exceed 10 m s^{-1}. This is in accord with the generally weak and often anticyclonic circulation of the former region as compared to frequent cyclone activity for the latter region. Mean wind speeds for summer and early autumn months are more spatially homogeneous, largely due to decreases over the Atlantic sector associated with a reduction in storm frequency and intensity. Note that summer wind speeds appear to increase somewhat along the Siberian and Alaskan coasts. The histograms of daily wind speed for the SHEBA region show a pronounced flattening during summer and autumn, with more cases of high wind speeds. This can be interpreted as a response to the influx of cyclones into the central Arctic Ocean during these months (see Section 1.2).

Figure 2.5.1

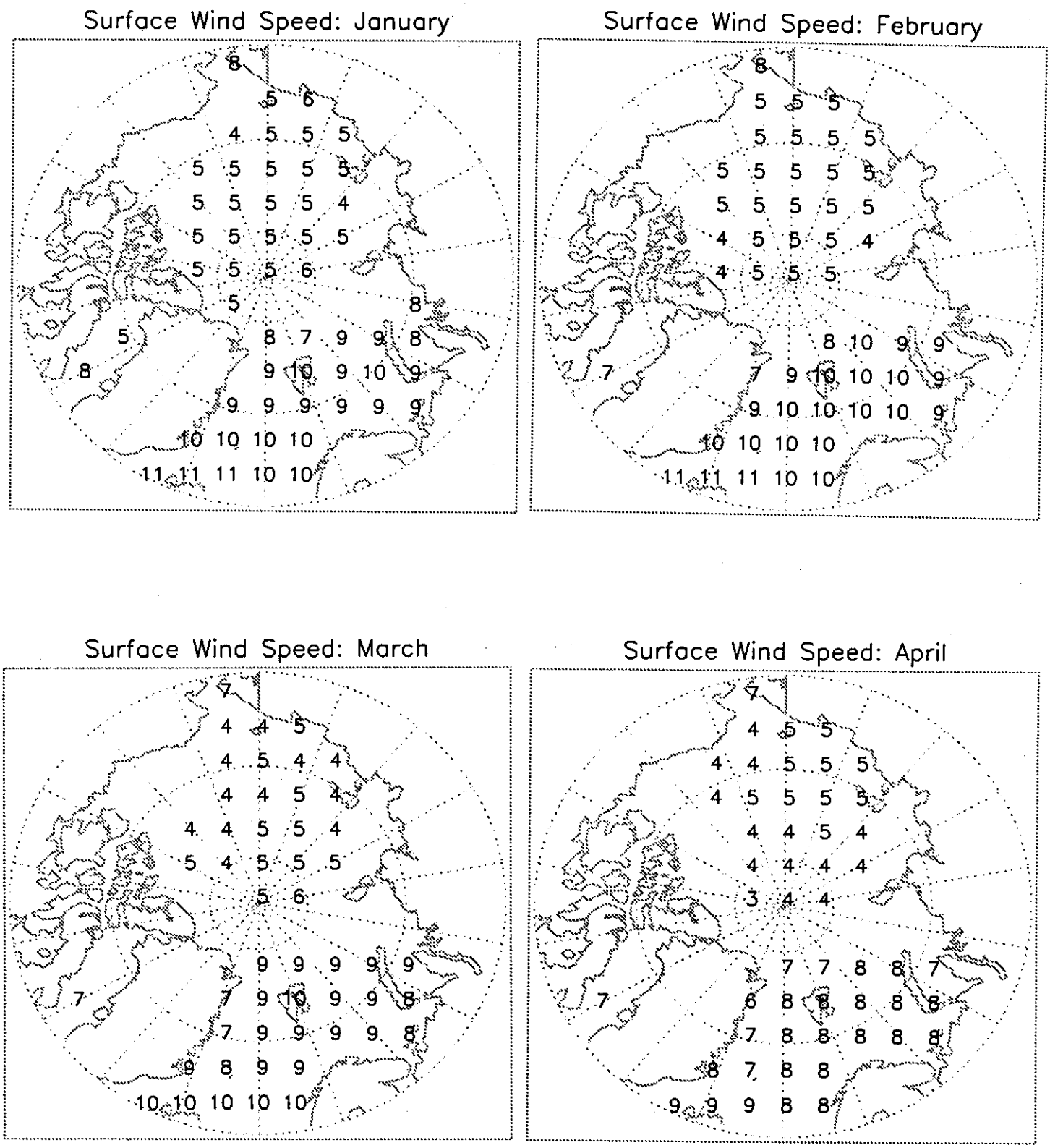

Units: m s^{-1}

Figure 2.5.1 (Continued)

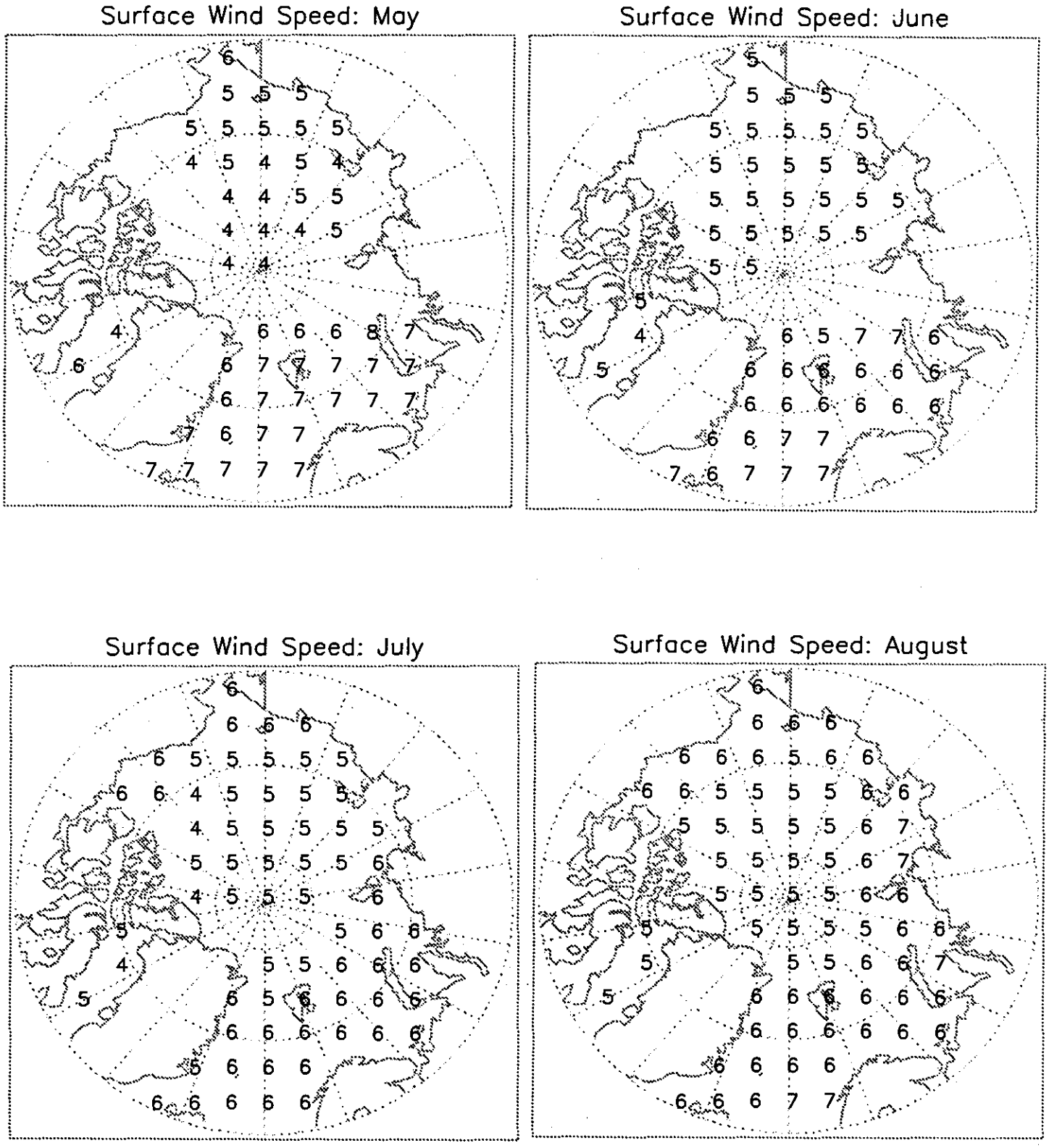

Units: m s^{-1}

Figure 2.5.1 (Continued)

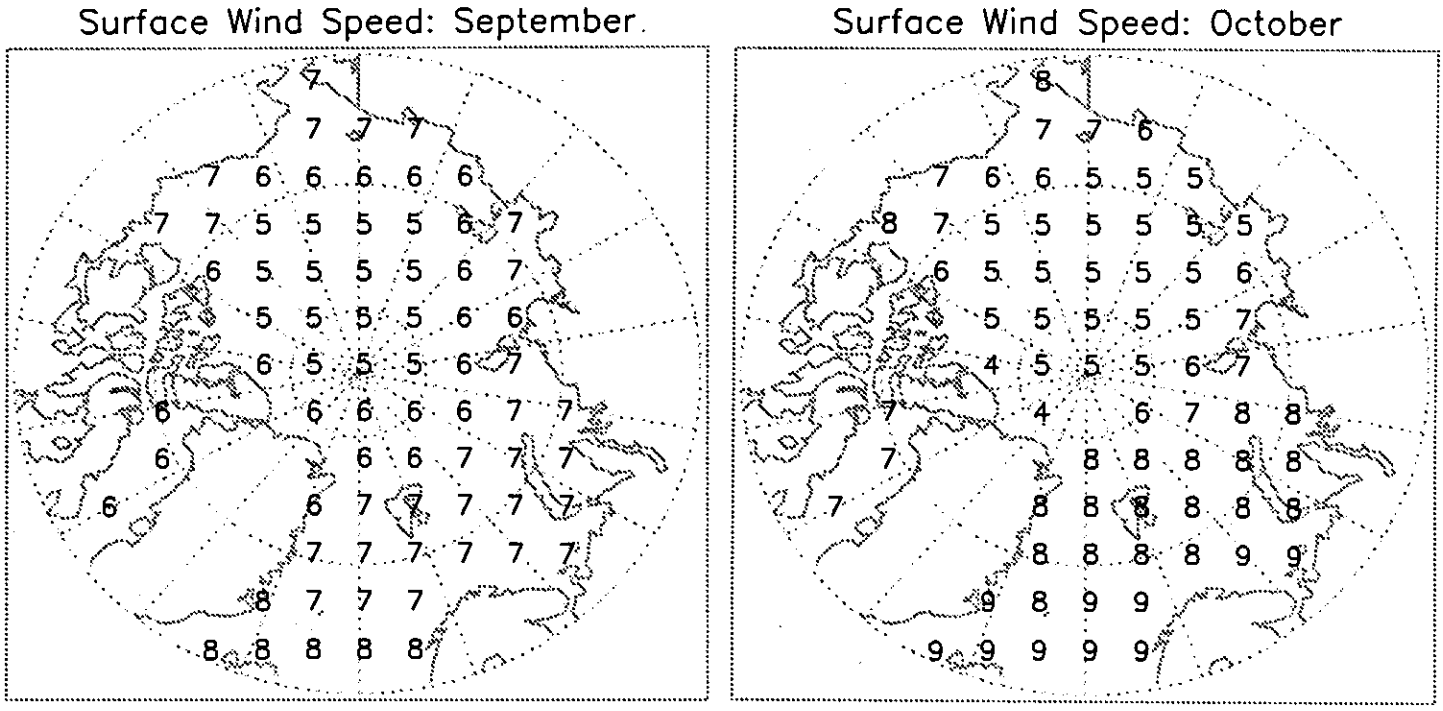

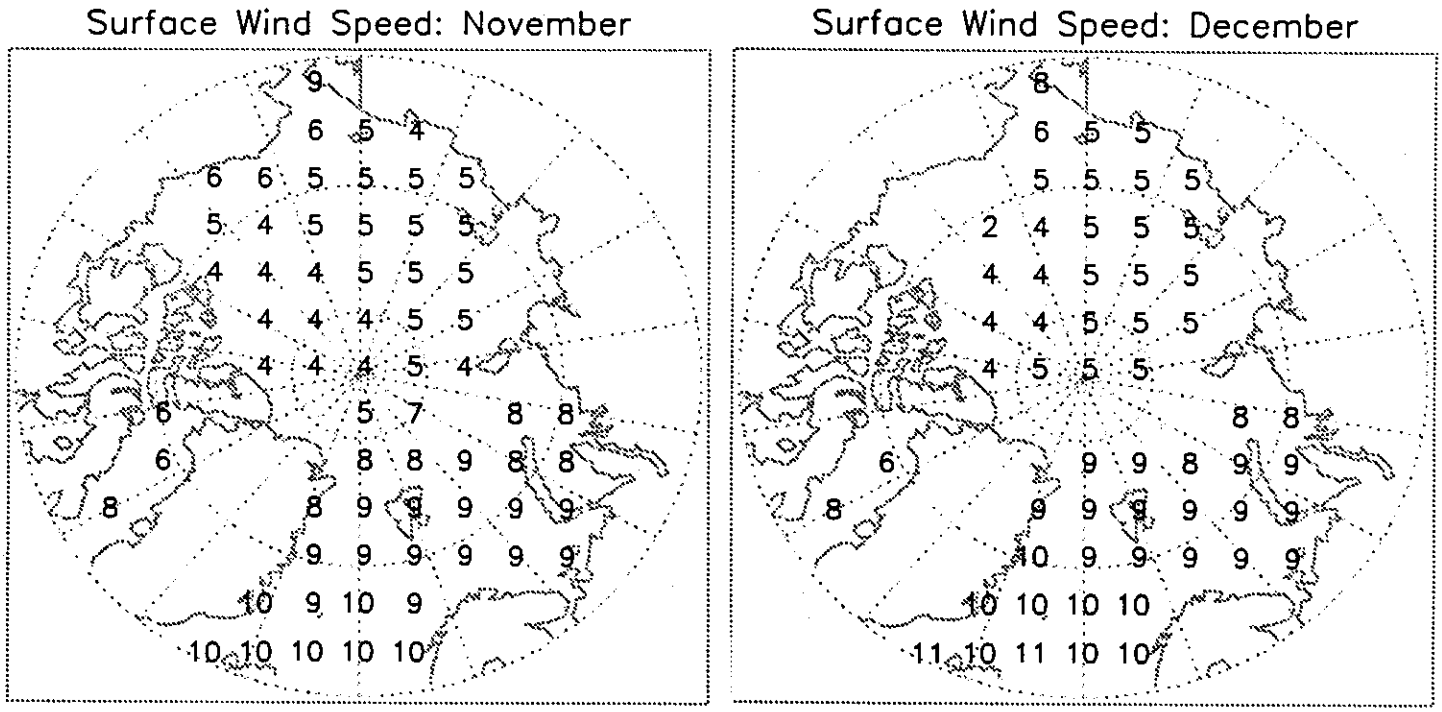

Units: m s^{-1}

Figure 2.5.2 (Continued)

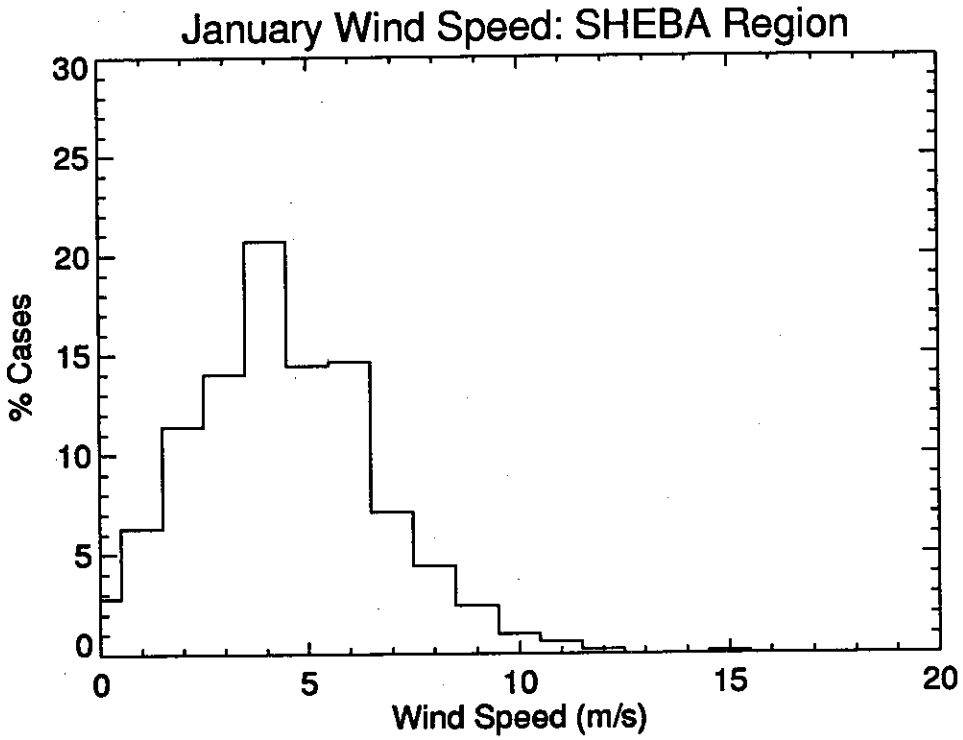

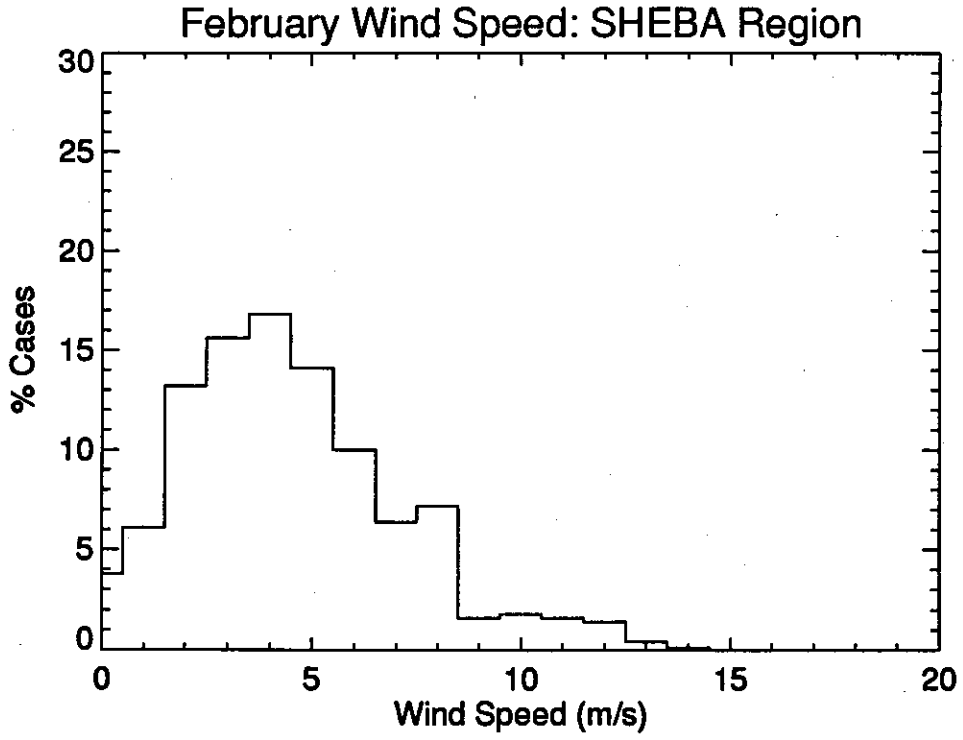

Figure 2.5.2 (Continued)

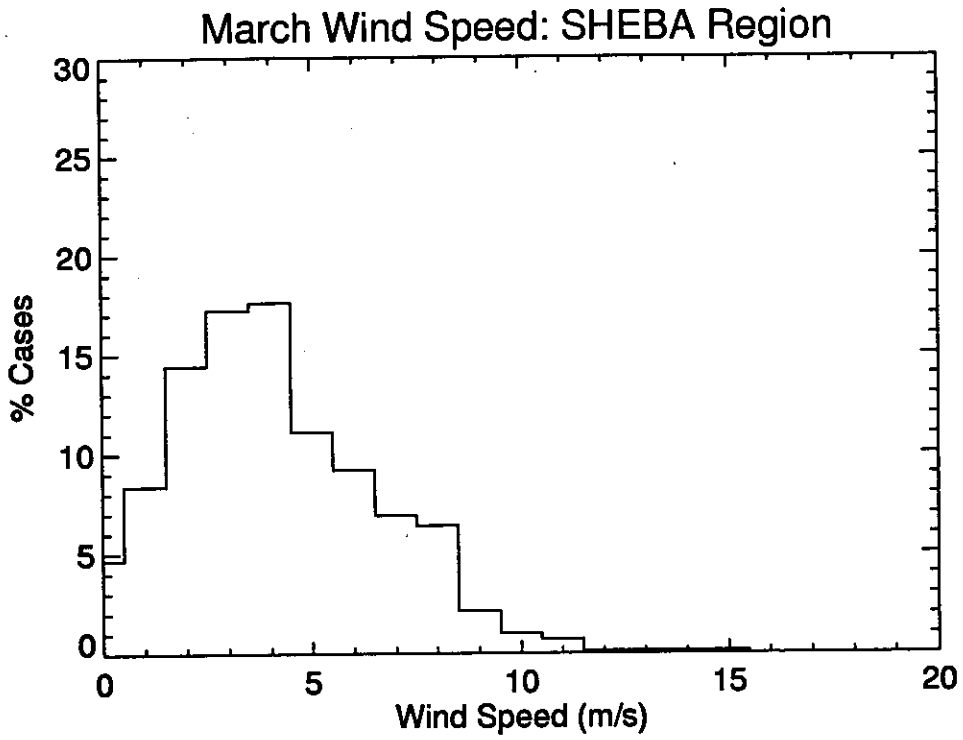

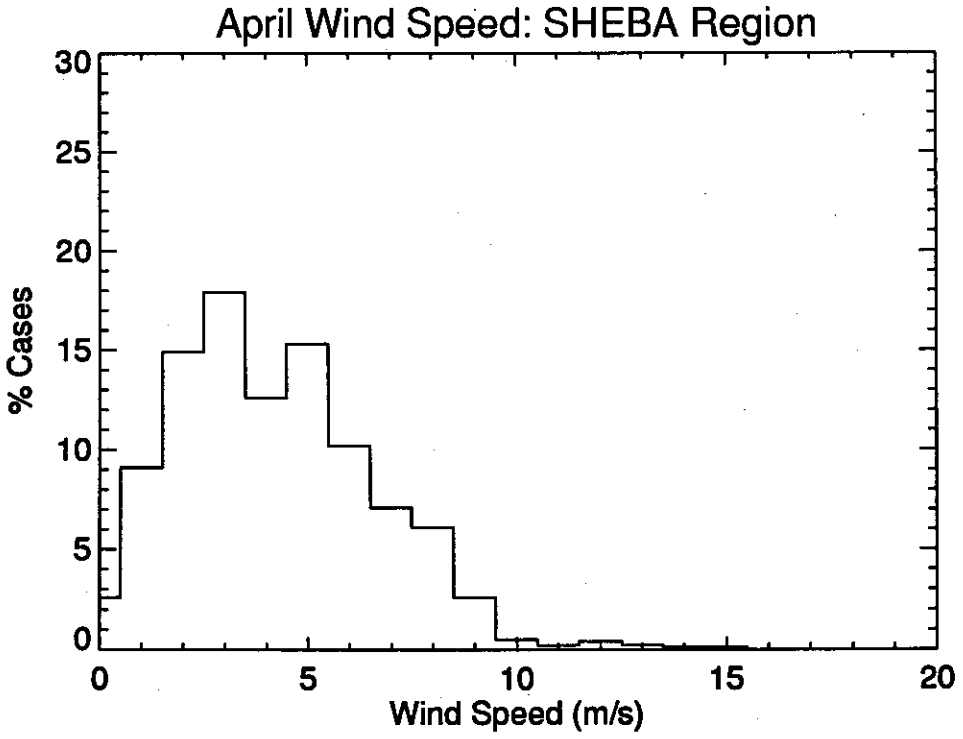

Figure 2.5.2 (Continued)

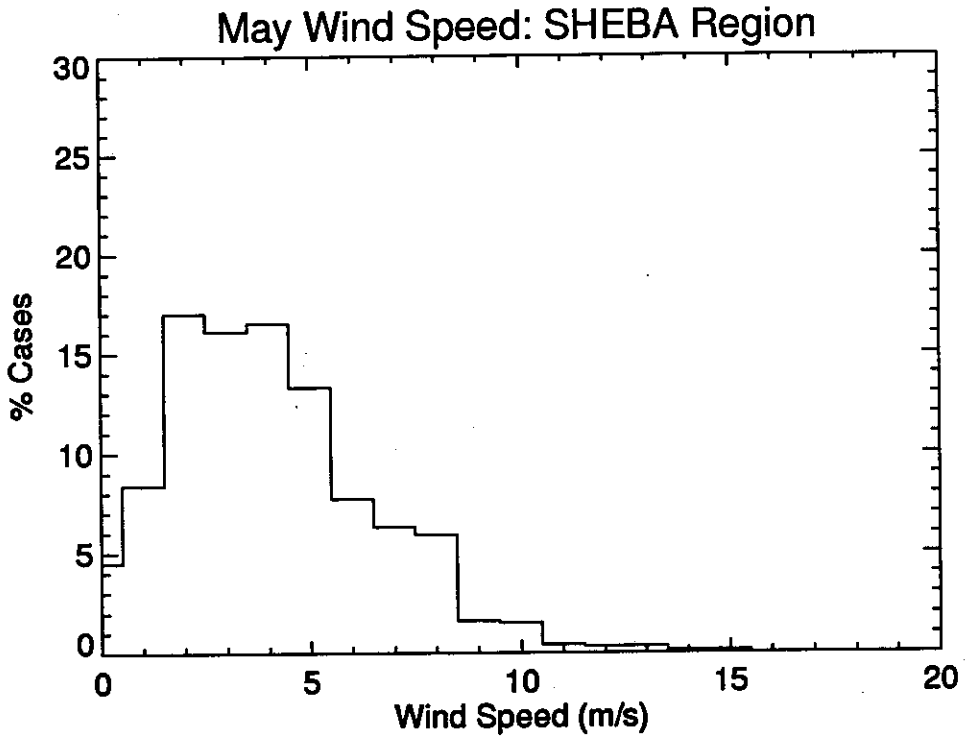

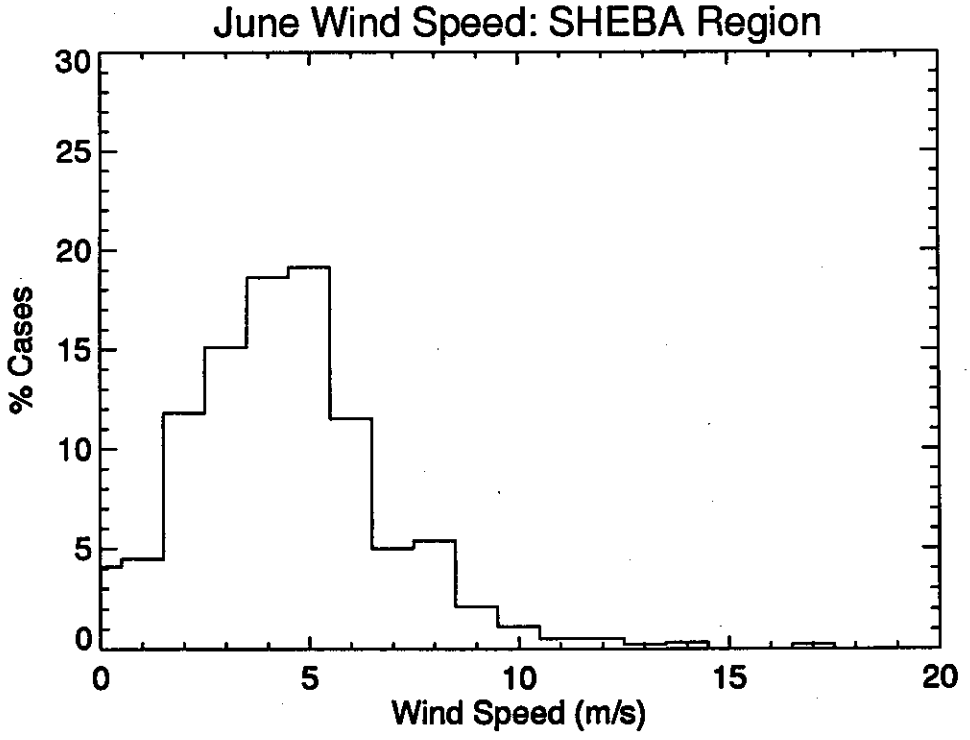

Figure 2.5.2 (Continued)

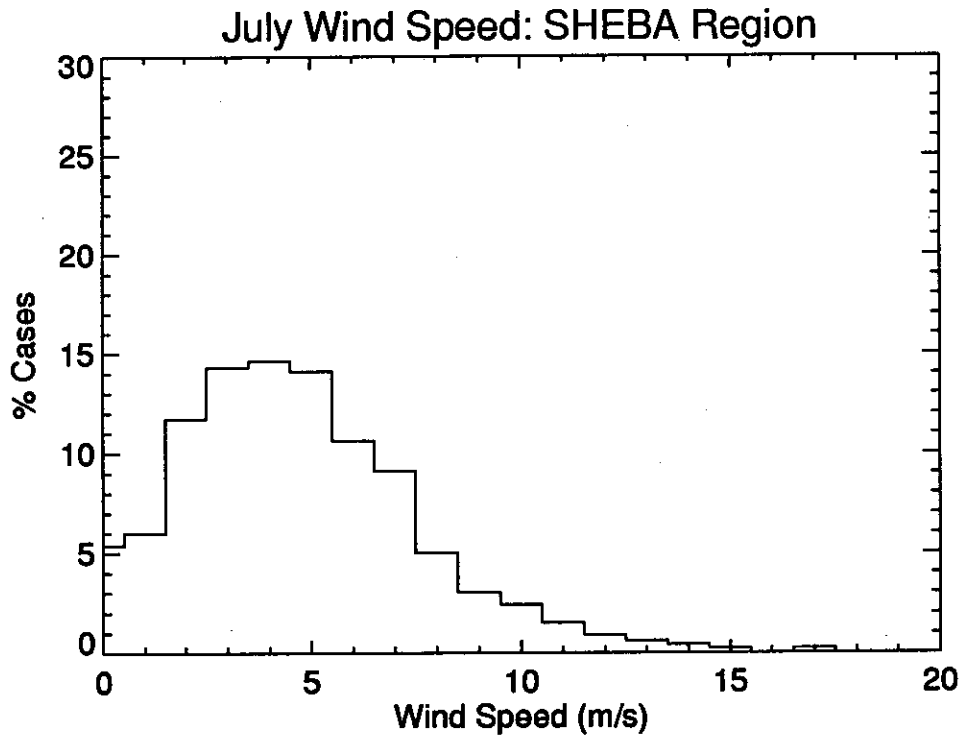

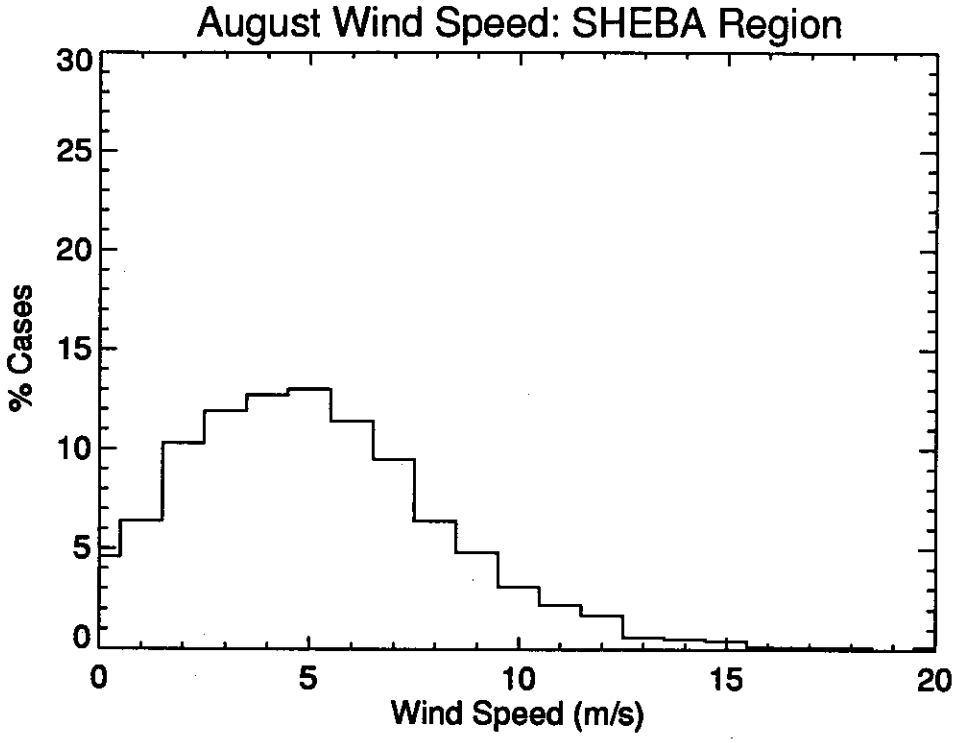

Figure 2.5.2 (Continued)

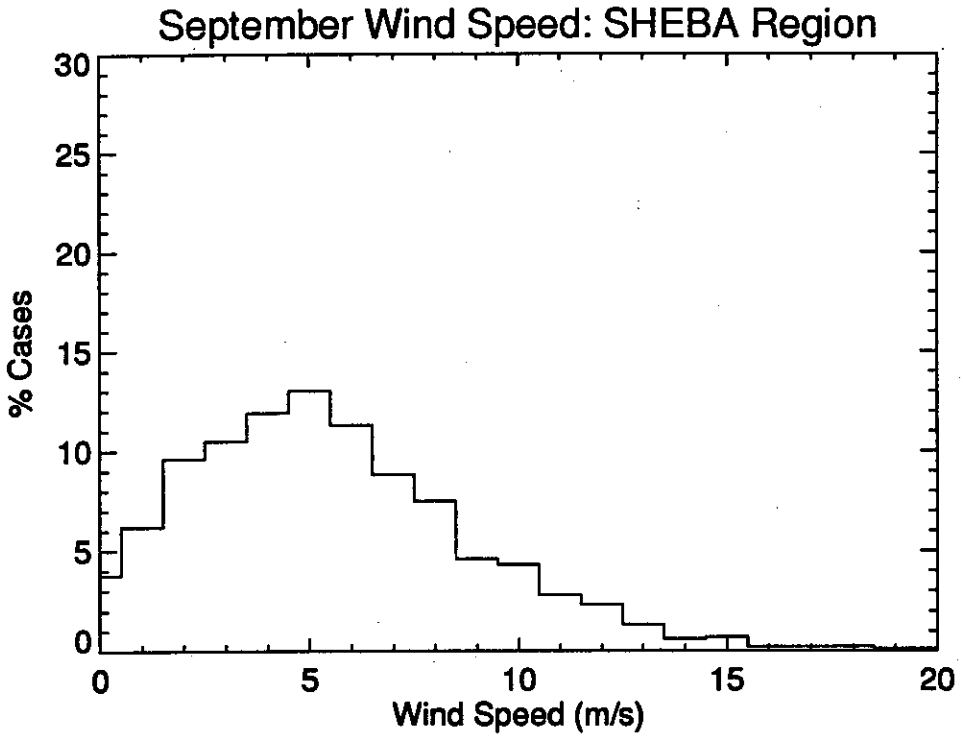

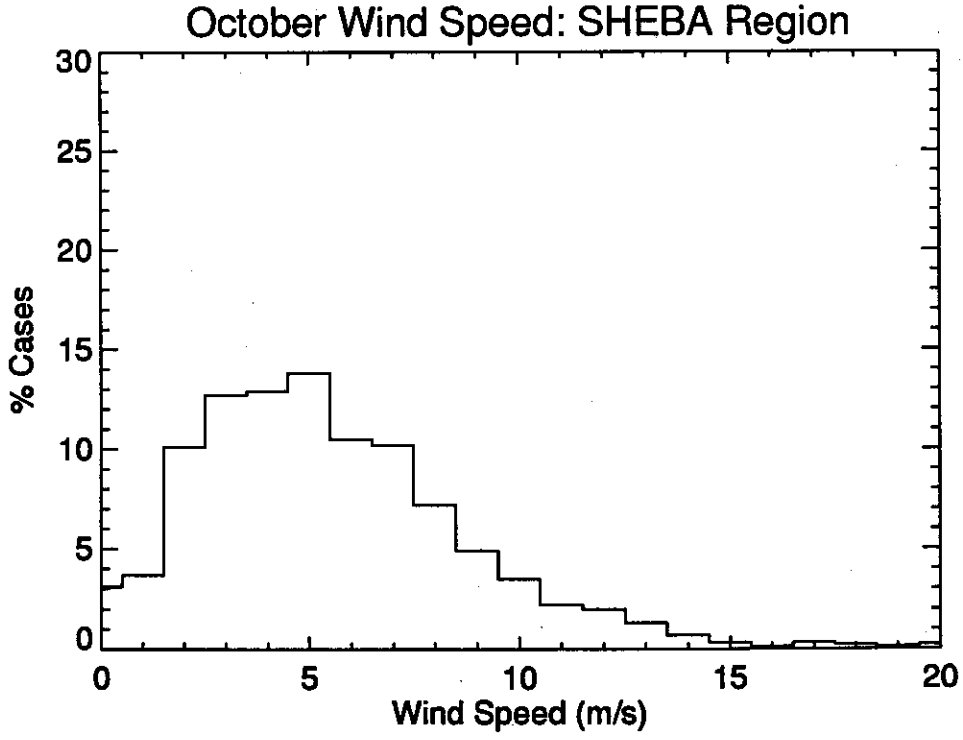

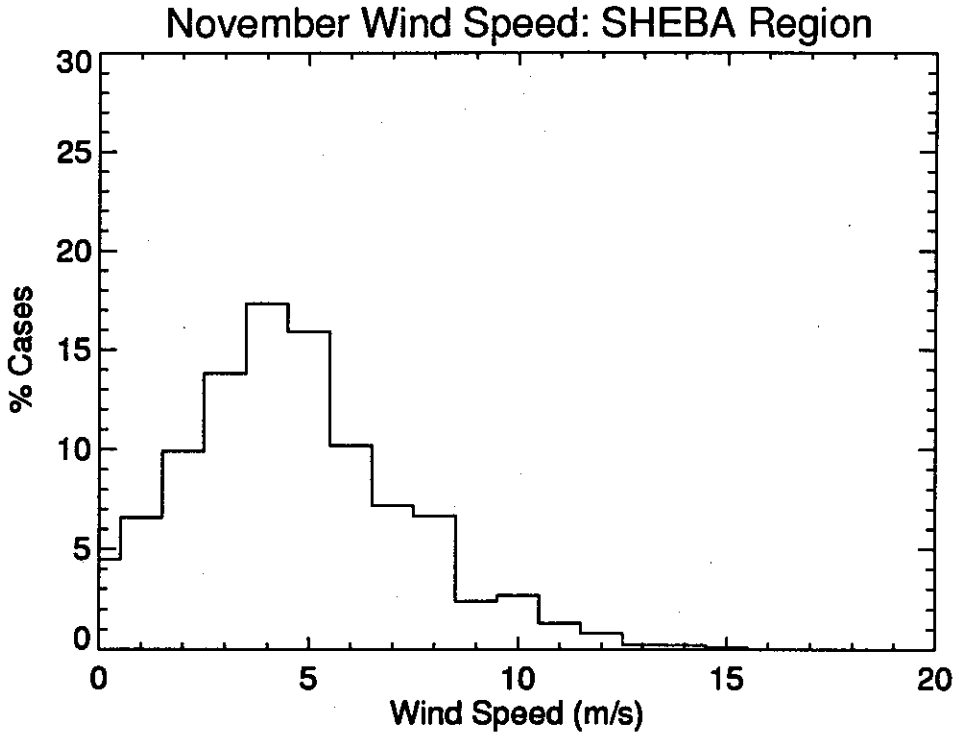
November Wind Speed: SHEBA Region
% Cases
Wind Speed (m/s)
0
5
10
15
20
25
30

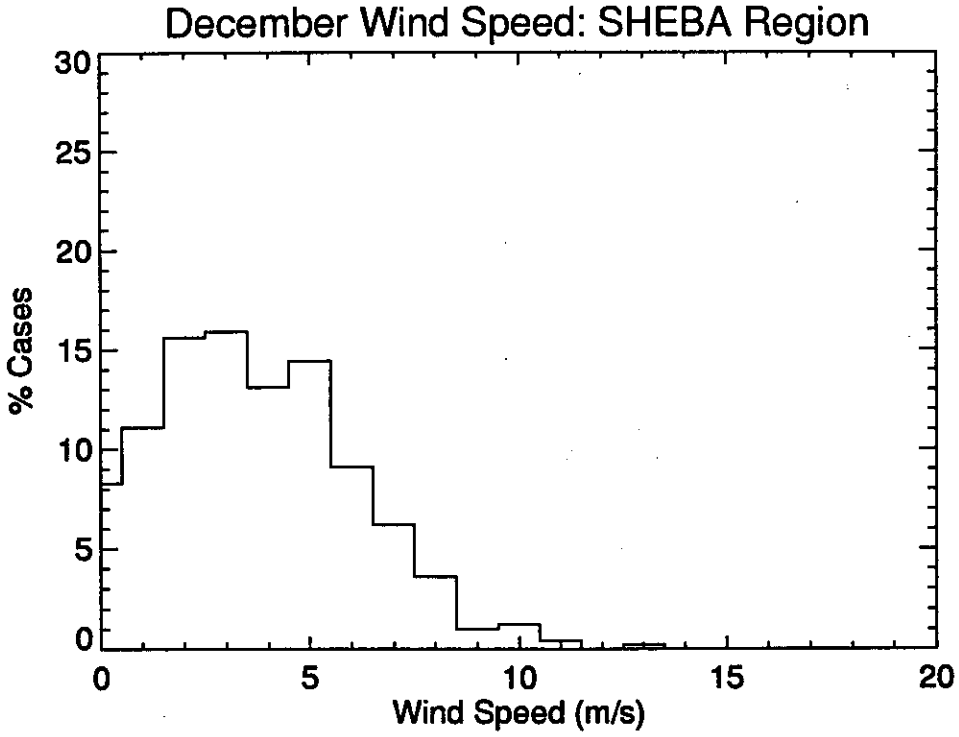
December Wind Speed: SHEBA Region
% Cases
Wind Speed (m/s)
0
5
10
15
20
25
30

3. SEA ICE

3.1 Sea Ice Extent and Concentration

Monthly fields of sea ice extent for the Arctic Ocean (Figure 3.1.1) were compiled from monthly mean sea ice concentrations estimated from Scanning Multichannel Microwave Radiometer (SMMR) and Special Sensor Microwave/Imager (SSM/I) passive microwave data for 1979-1995. The combined SMMR and SSM/I data set is described by Maslanik et al. [1996]. We display the fields in terms of the extent of ice cover of at least 50%. The different shadings indicate those areas with at least 50% ice for at least 75% of all years and for 50-75% of all years. Also shown for the Beaufort Sea, and based on the same data set, are monthly isoline maps of mean ice concentration (0-100%) and the absolute range in ice concentration between extreme years (Figure 3.1.2). For both sets of maps, concentrations represent the combination of first-year and multiyear ice. Details and references regarding the algorithm, sensors, and processing are given in NSIDC (1996) and are available at the NSIDC web site (http://www-nsidc.colorado.edu).

The Arctic Ocean maps illustrate the well-known large seasonal cycle in total ice extent, the development of extensive areas of open water or low concentration ice during summer along the Eurasian coast and north of Alaska, and the tendency for concentrations to remain high all throughout the year along the northern Canadian coast. Ice concentrations near the initial SHEBA site tend to be over 95% during winter months, falling to 80-90% during summer. However, during late summer and early autumn, the range in total ice concentration can be 20-30%. It is clear that an extended period of pronounced southward drift of the SHEBA camp could place it within marginal-ice-zone type cover.

Figure 3.1.1

Extent of Ice Cover >50%: January

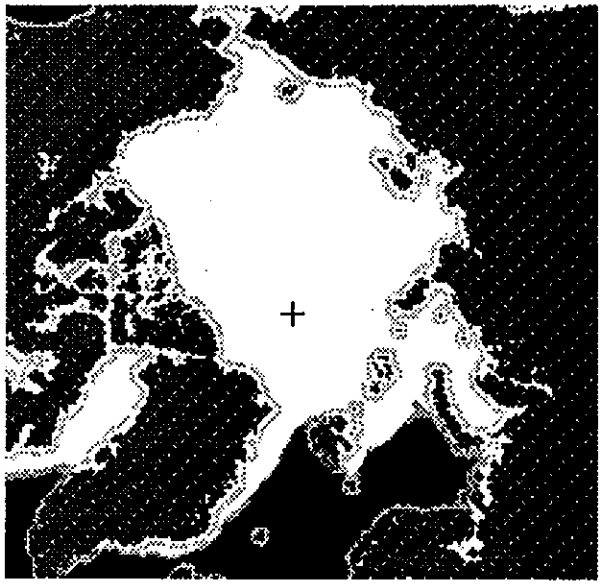

Extent of Ice Cover >50%: February

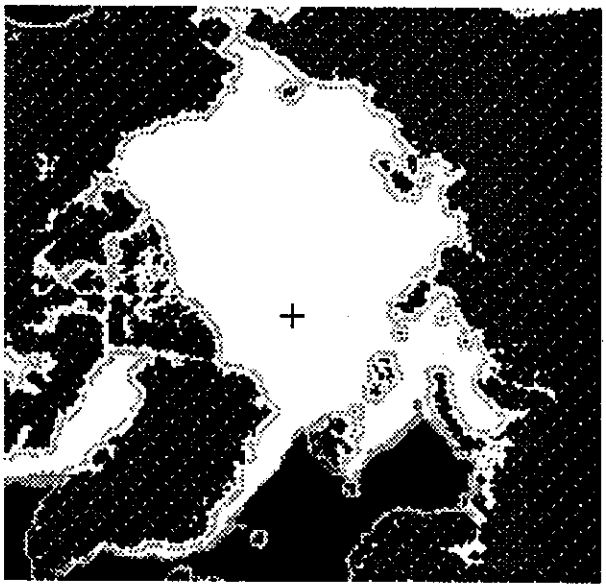

White: Ice Covered >75% of all Years
Grey: Ice Covered 50-75% of all Years

Extent of Ice Cover >50%: March

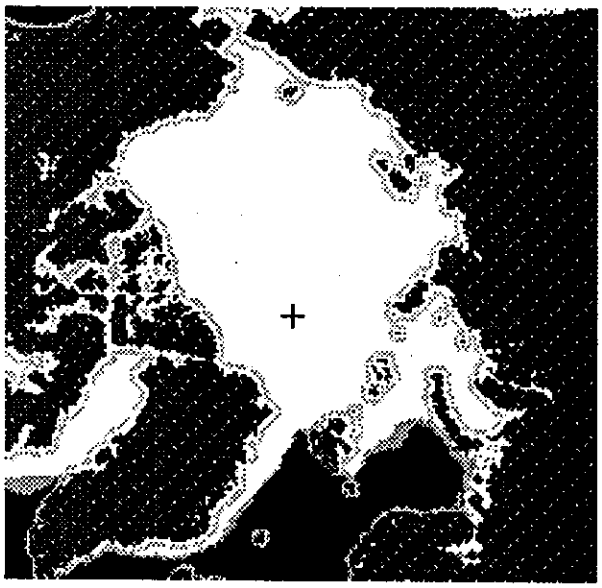

Extent of Ice Cover >50%: April

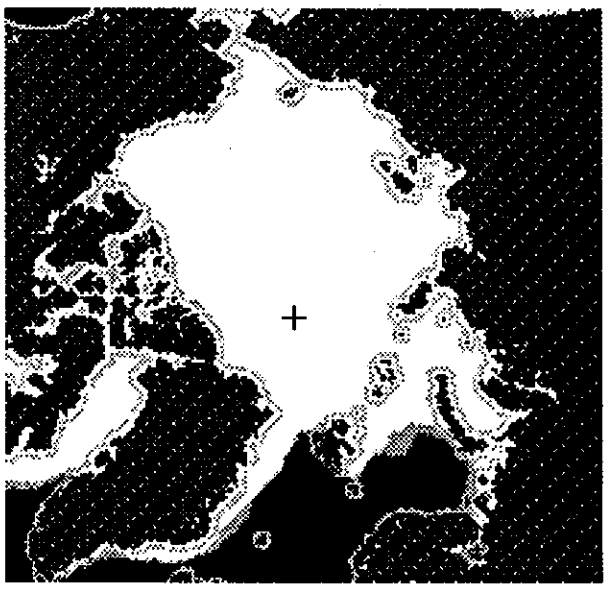

Figure 3.1.1 (Continued)

Extent of Ice Cover >50%: May

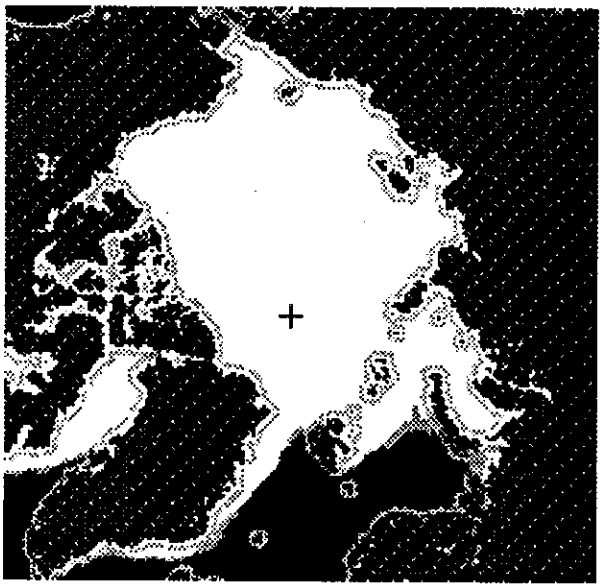

Extent of Ice Cover >50%: June

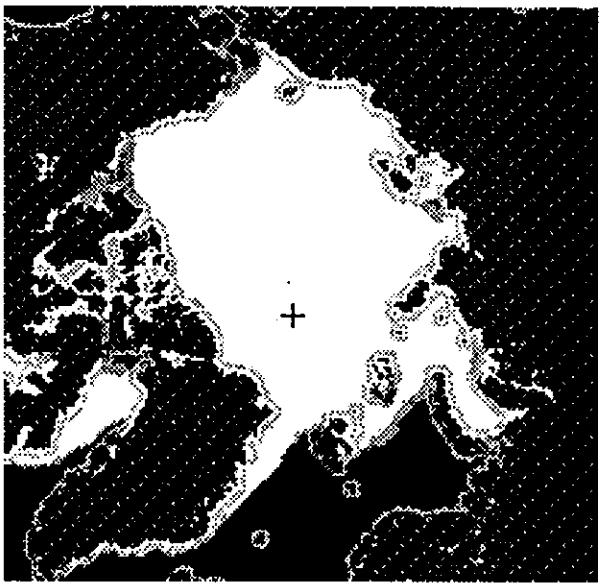

White: Ice Covered >75% of all years
Grey: Ice Covered 50-75% of all years

Extent of Ice Cover >50%: July

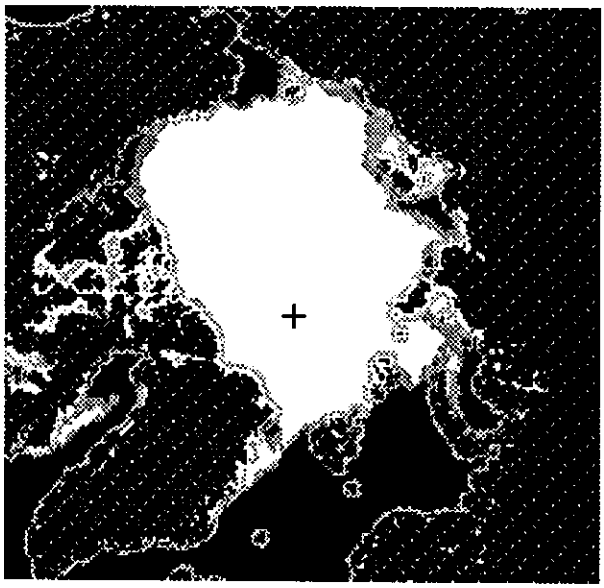

Extent of Ice Cover >50%: August

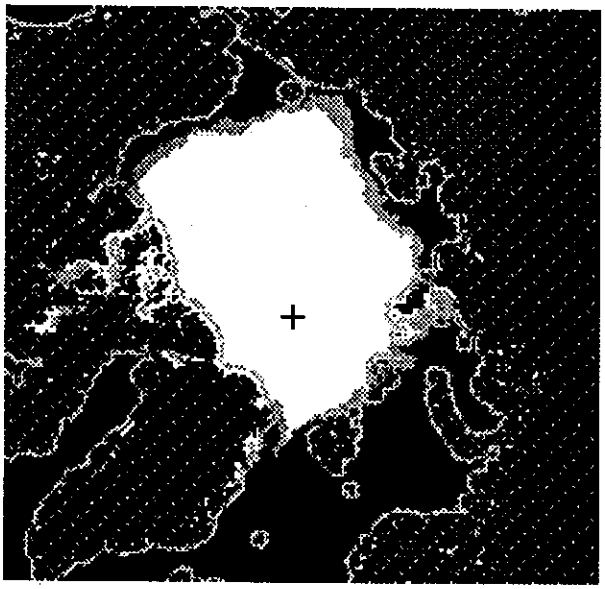

Figure 3.1.1 (Continued)

Extent of Ice Cover >50%: September

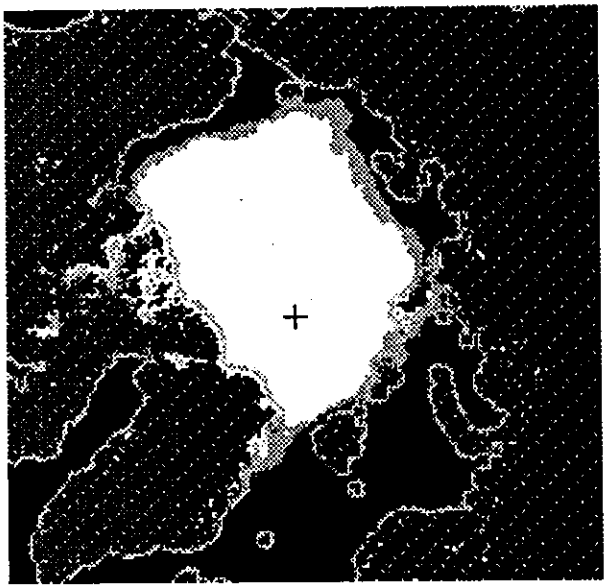

Extent of Ice Cover >50%: October

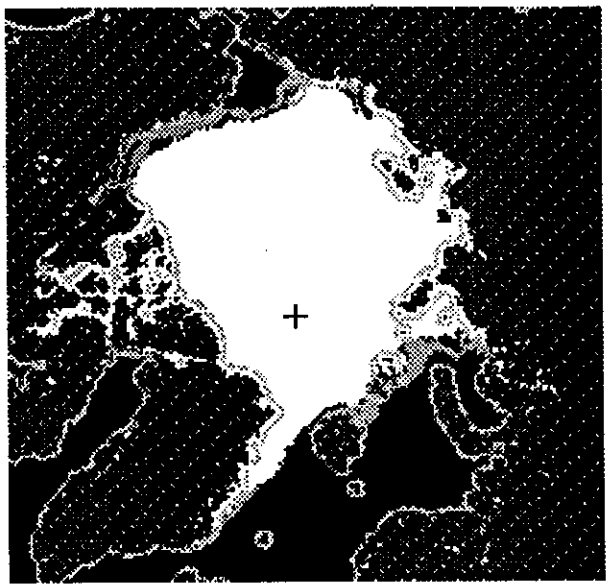

White: Ice Covered >75% of all Years
Grey: Ice Covered 50-75% of all Years

Extent of Ice Cover >50%: November

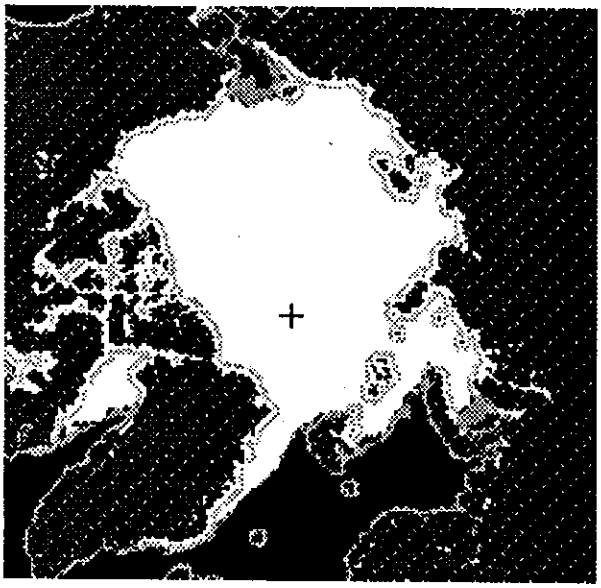

Extent of Ice Cover >50%: December

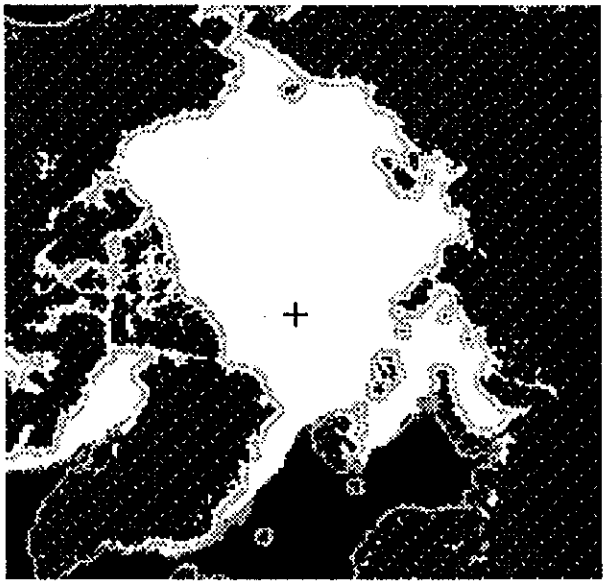

Figure 3.1.2

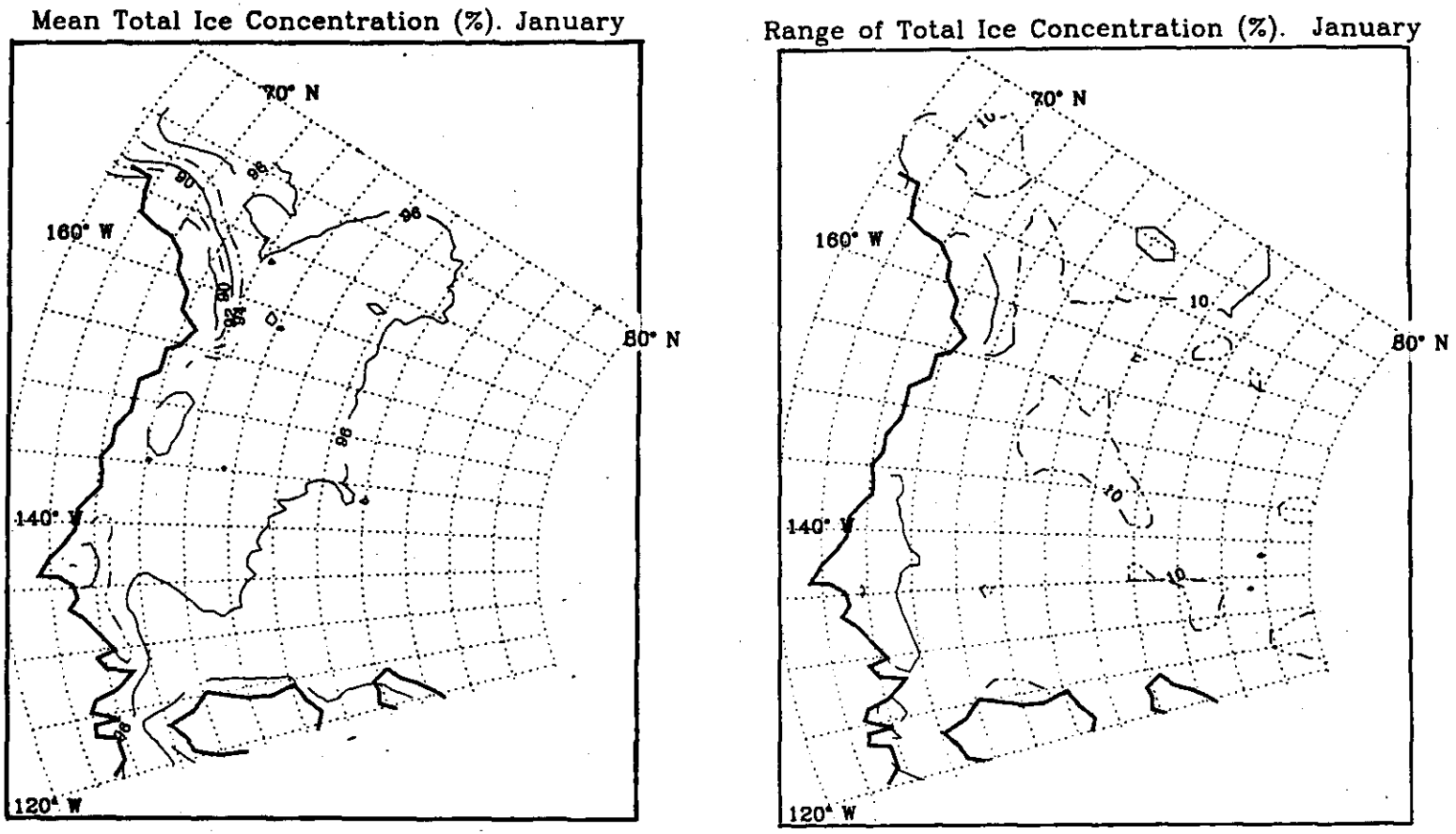
Mean Total Ice Concentration (%). January
70° N
160° W
80° N
140° W
120° W
90
96
98
Range of Total Ice Concentration (%). January
70° N
160° W
80° N
140° W
120° W
10

Figure 3.1.2 (Continued)

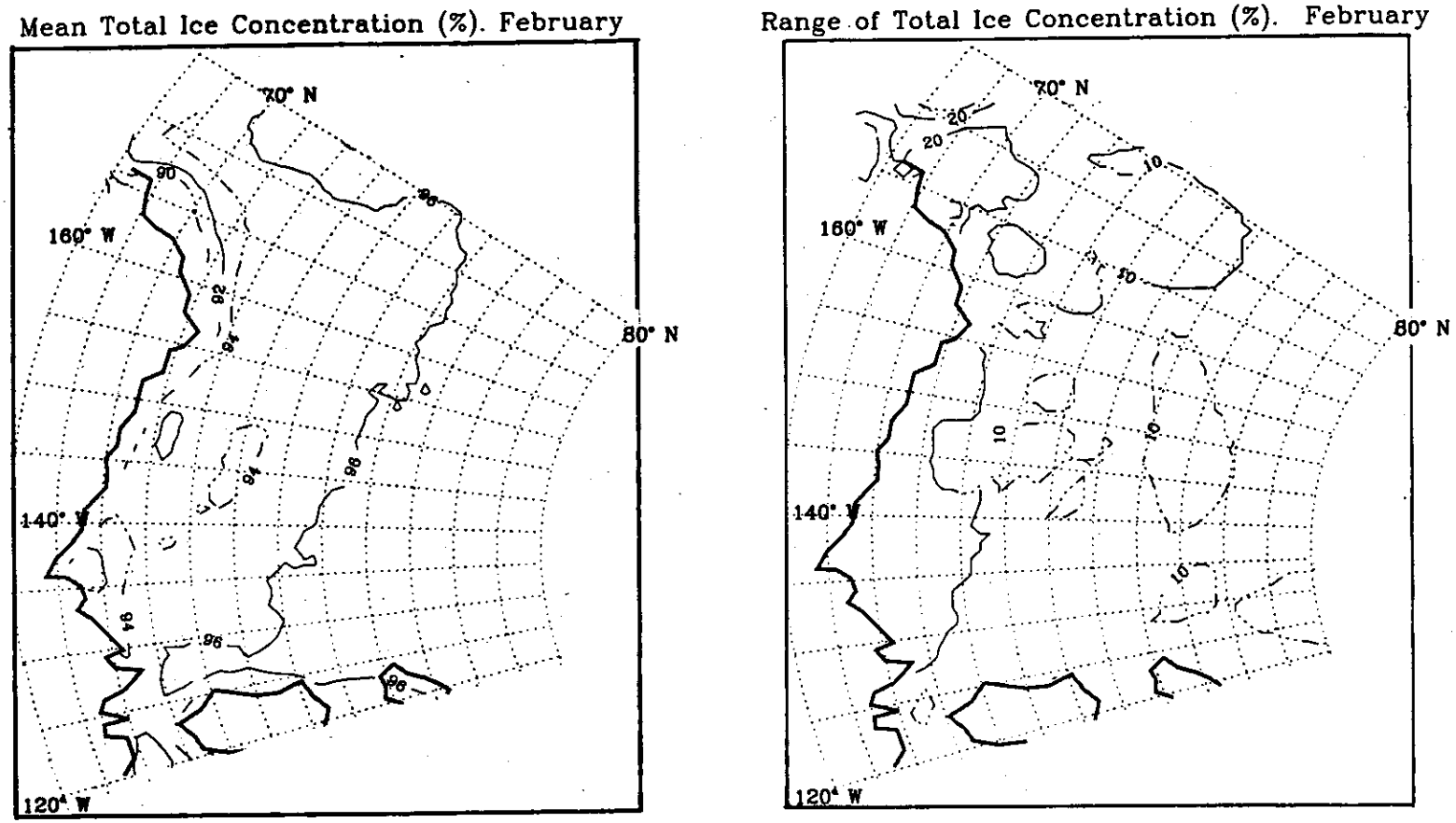

Figure 3.1.2 (Continued)

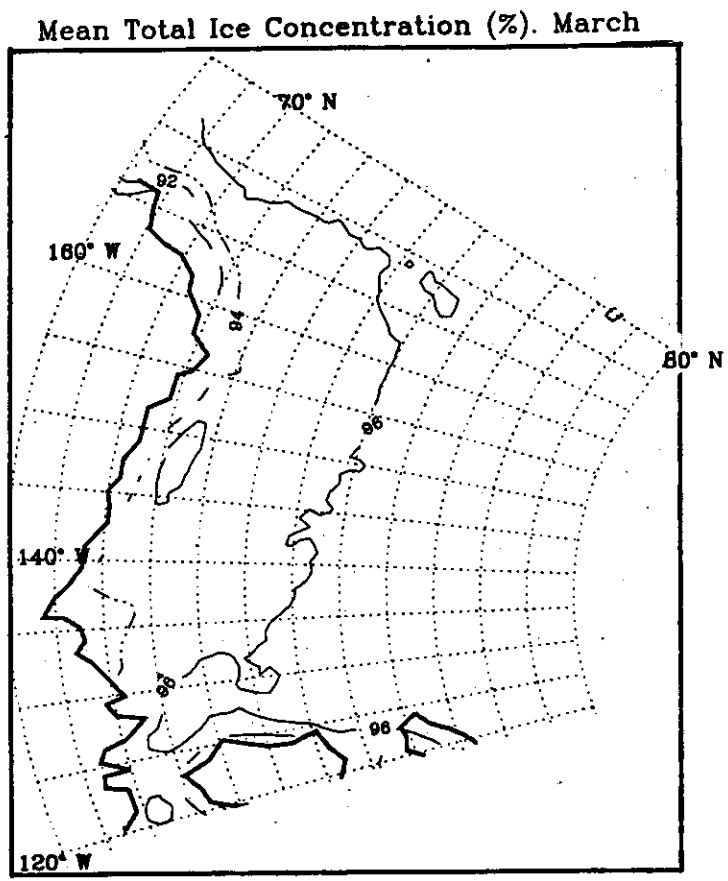

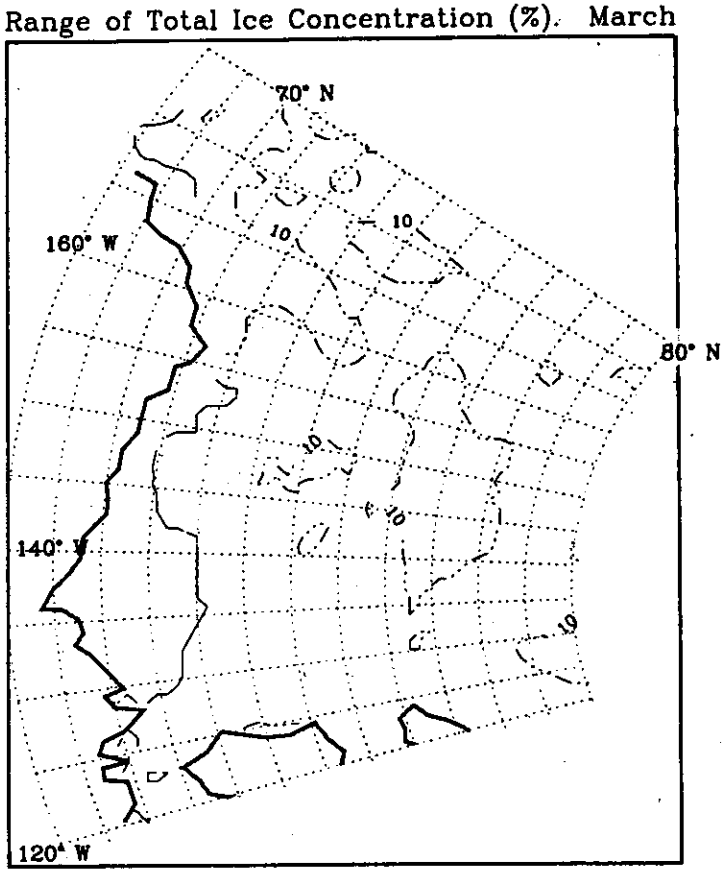

Figure 3.1.2 (Continued)

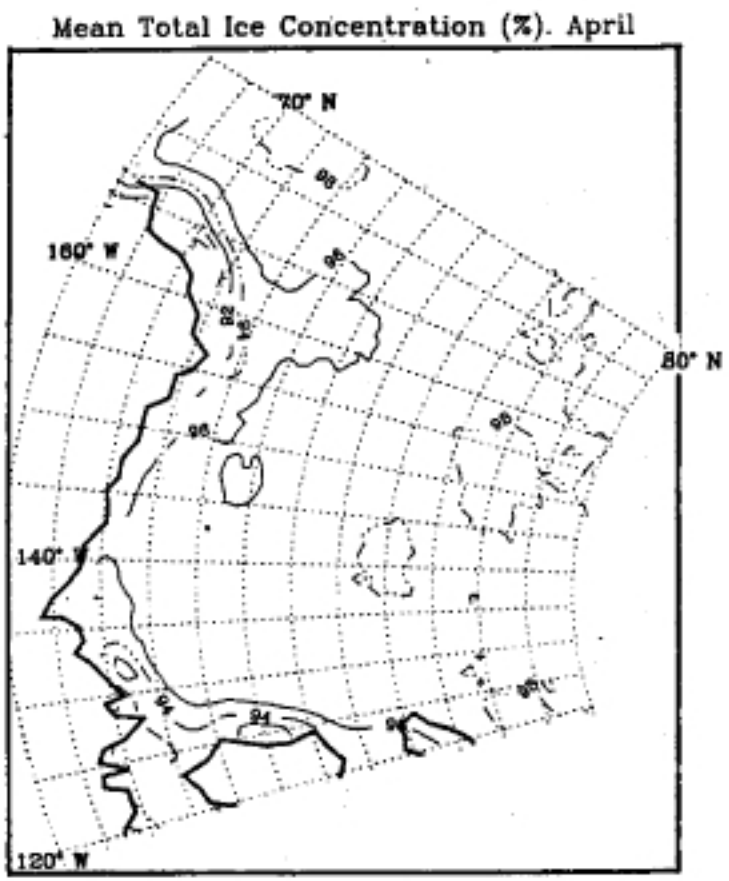

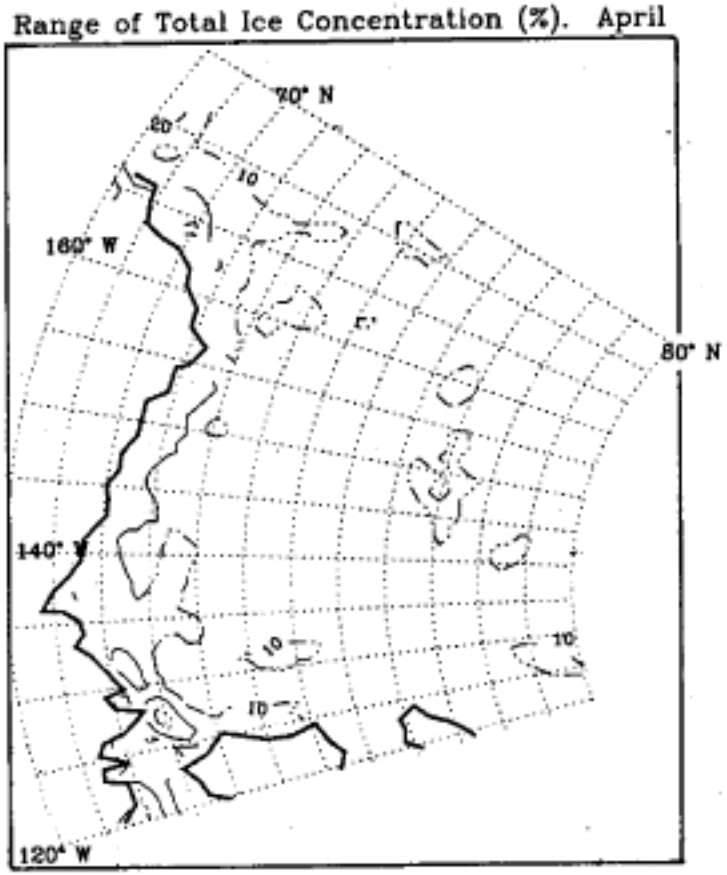

Figure 3.1.2 (Continued)

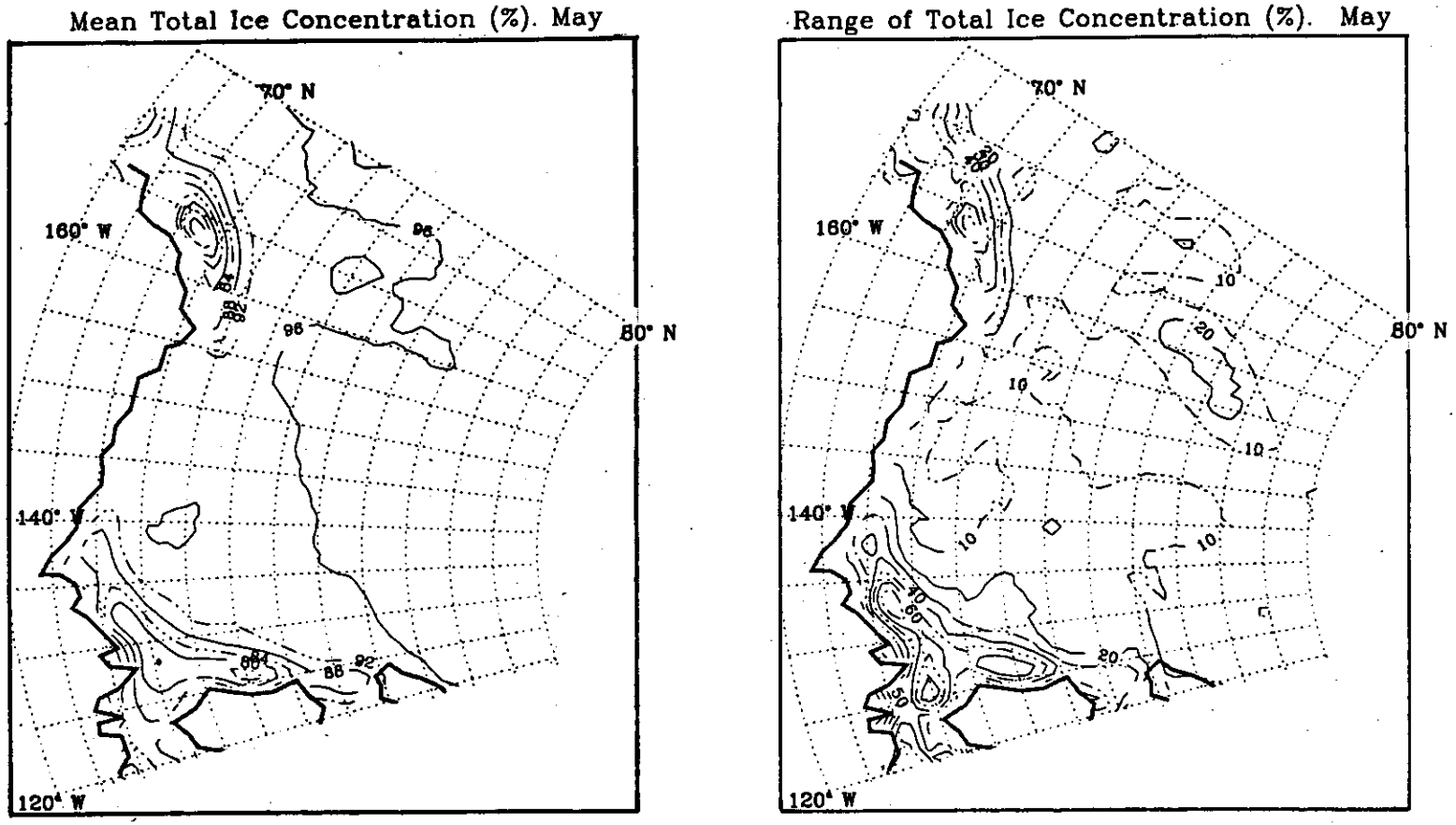

Figure 3.1.2 (Continued)

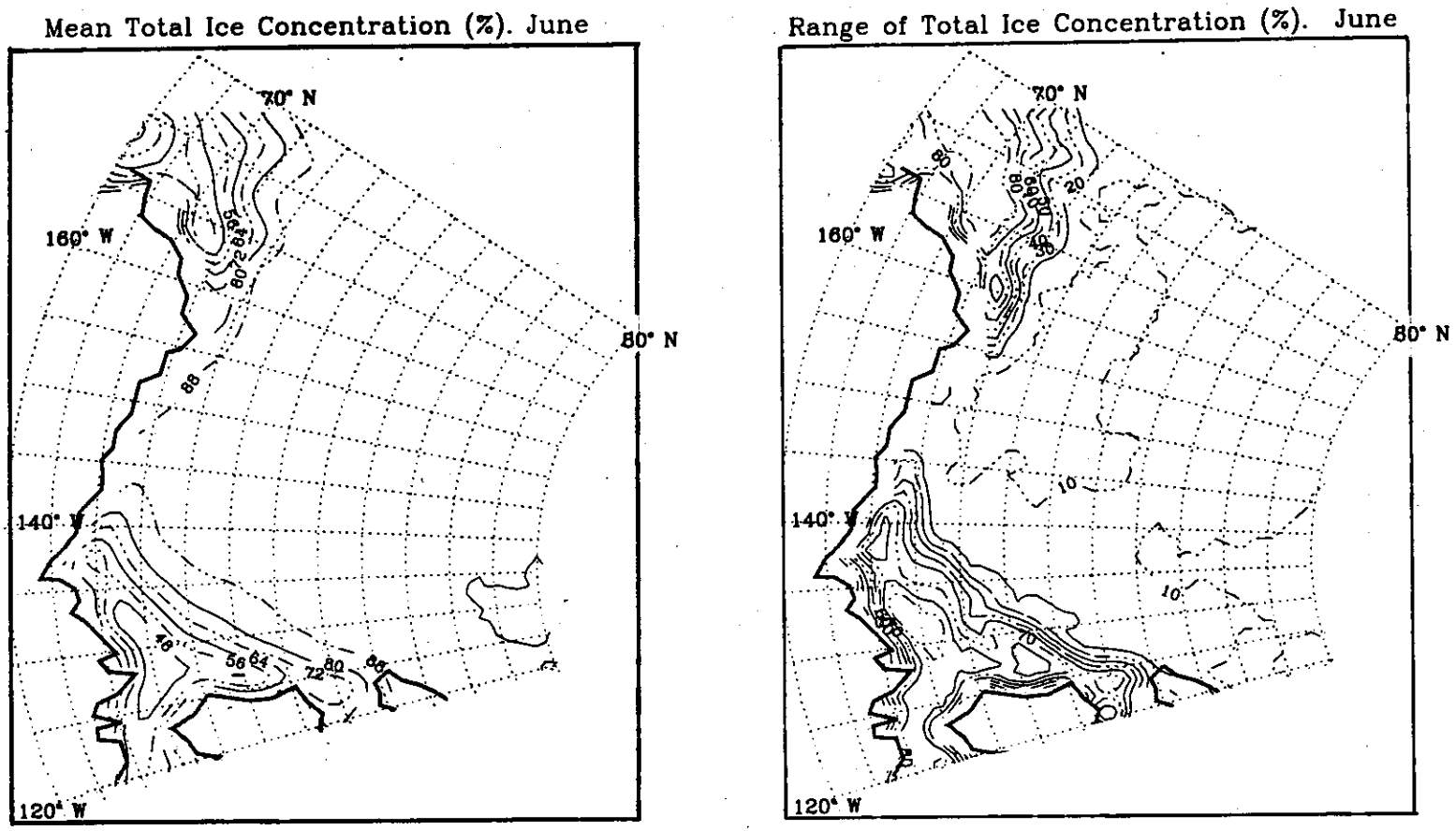

Figure 3.1.2 (Continued)

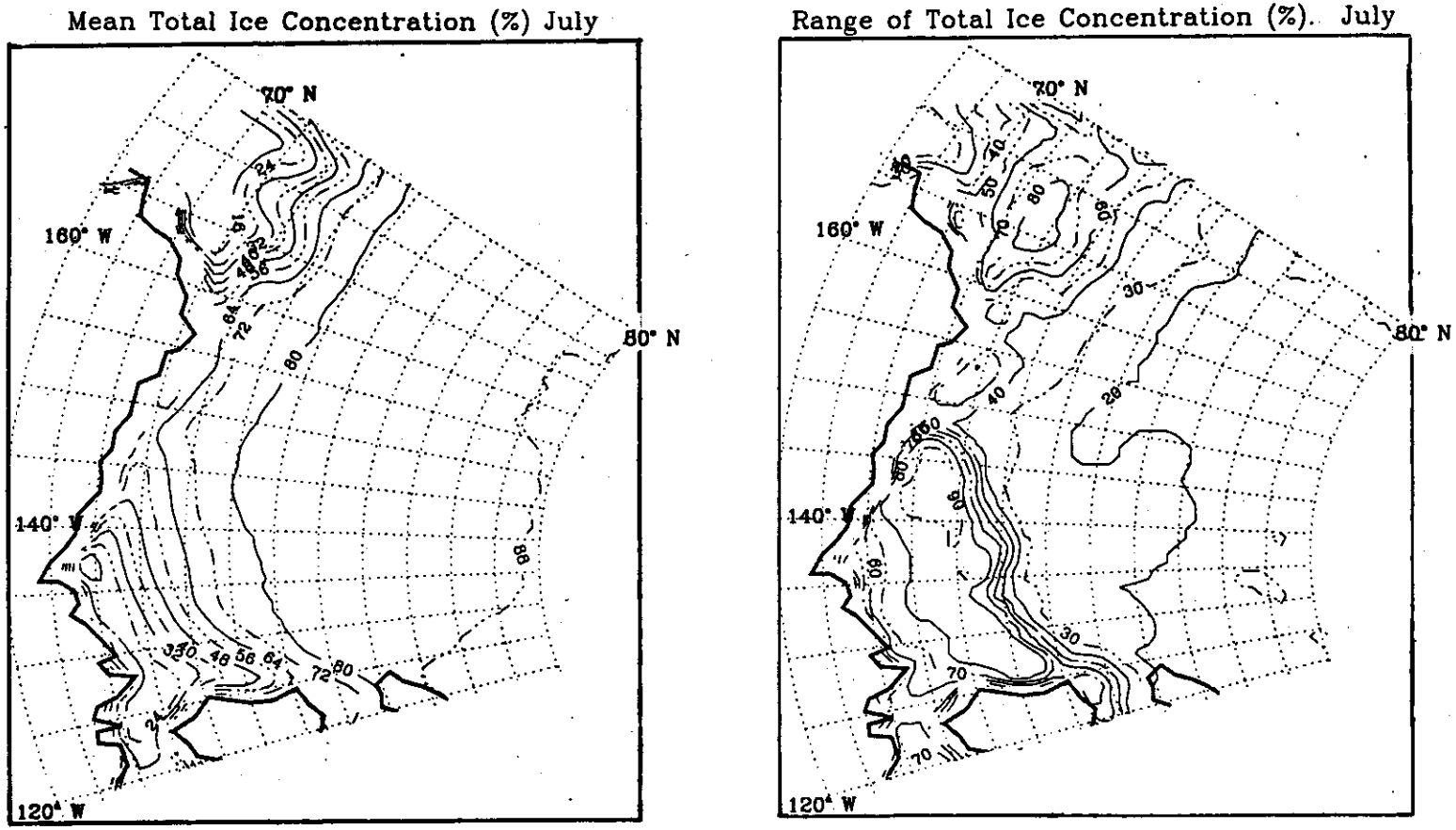

Figure 3.1.2 (Continued)

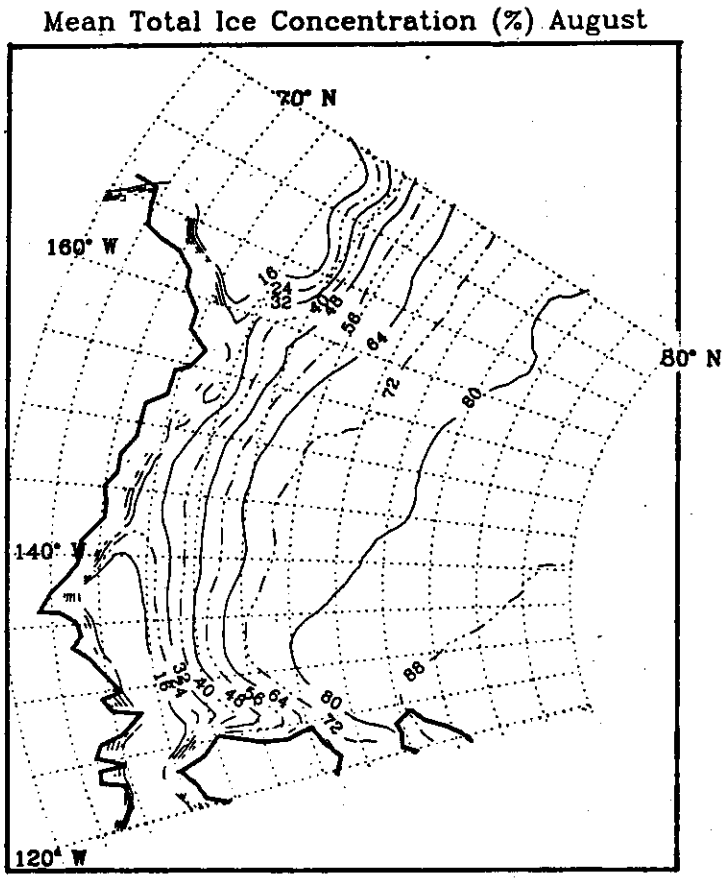

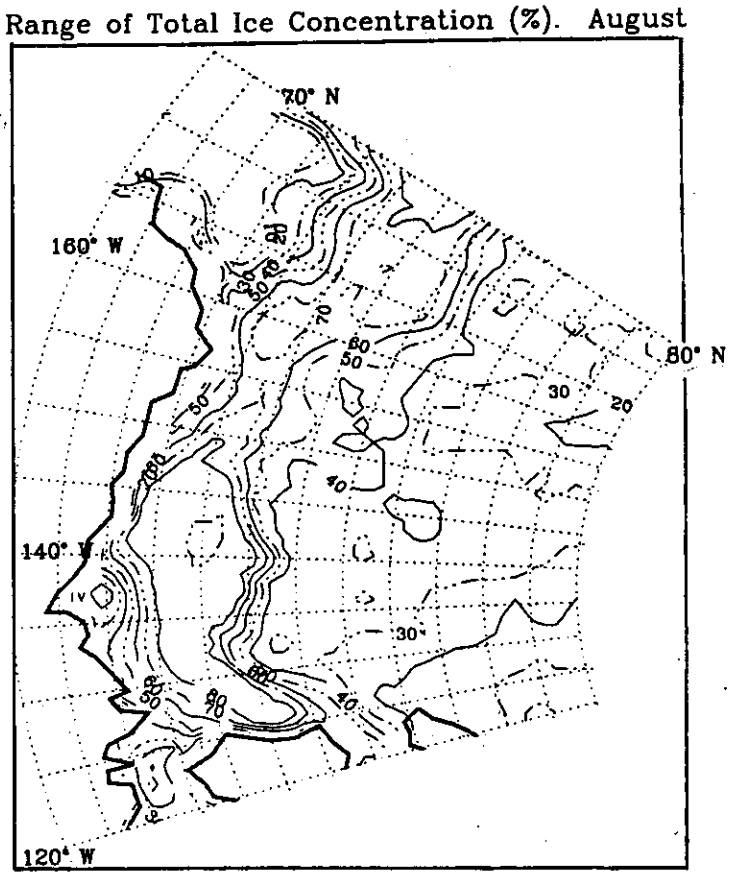

Figure 3.1.2 (Continued)

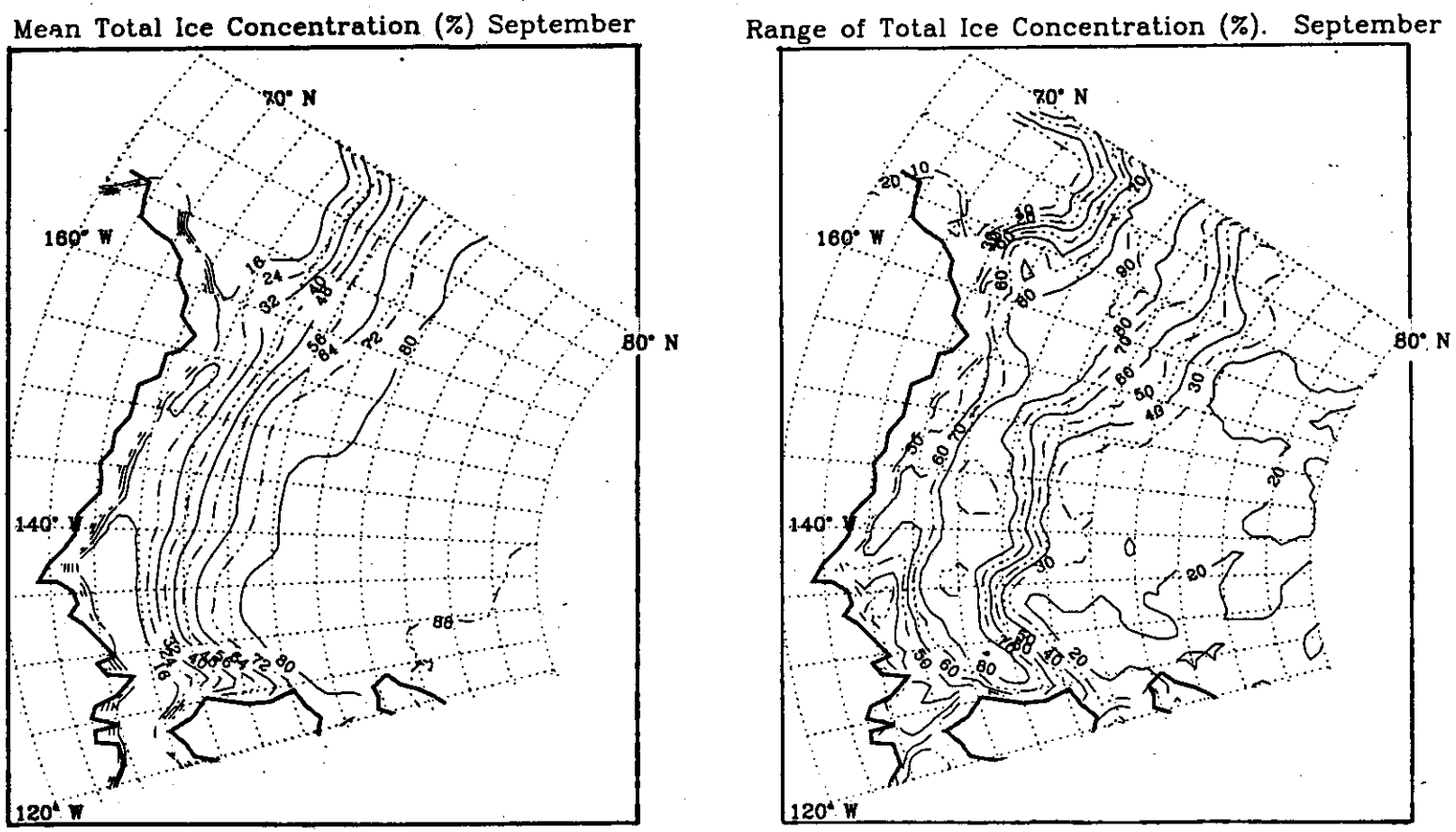

Figure 3.1.2 (Continued)

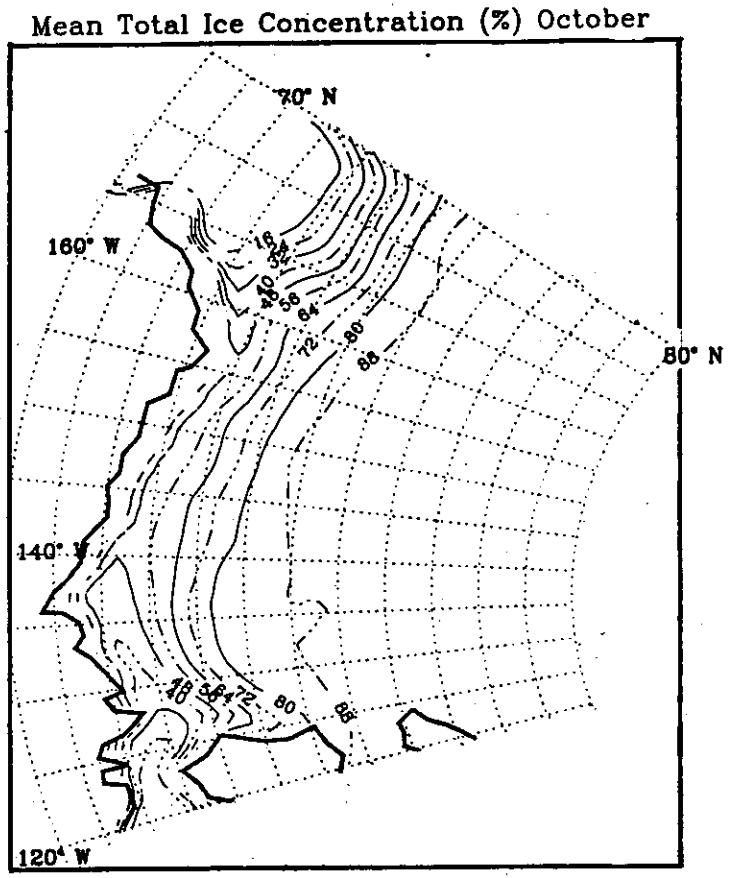

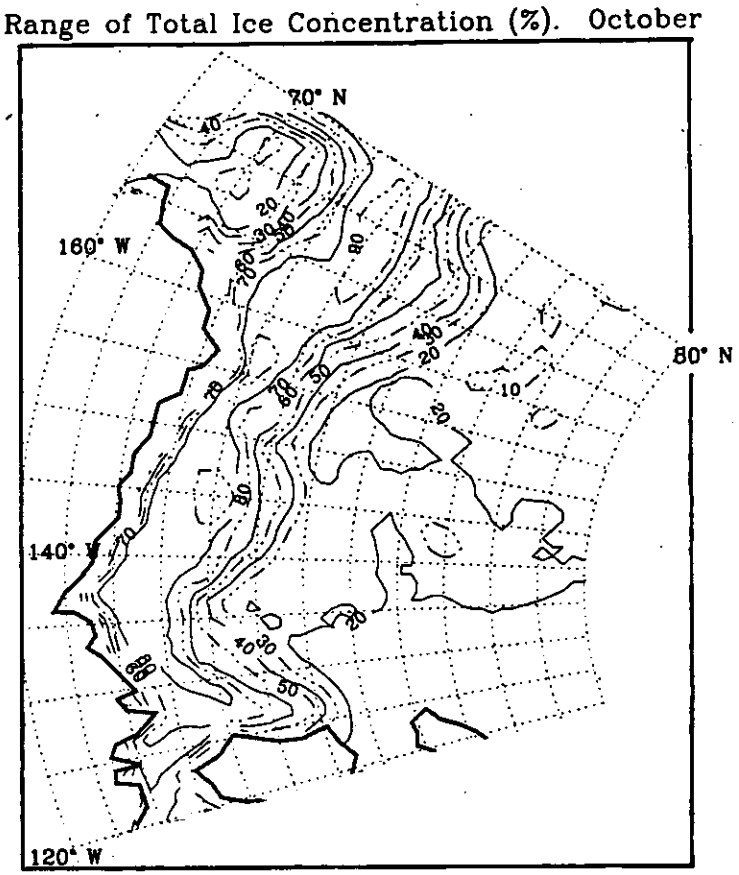

Figure 3.1.2 (Continued)

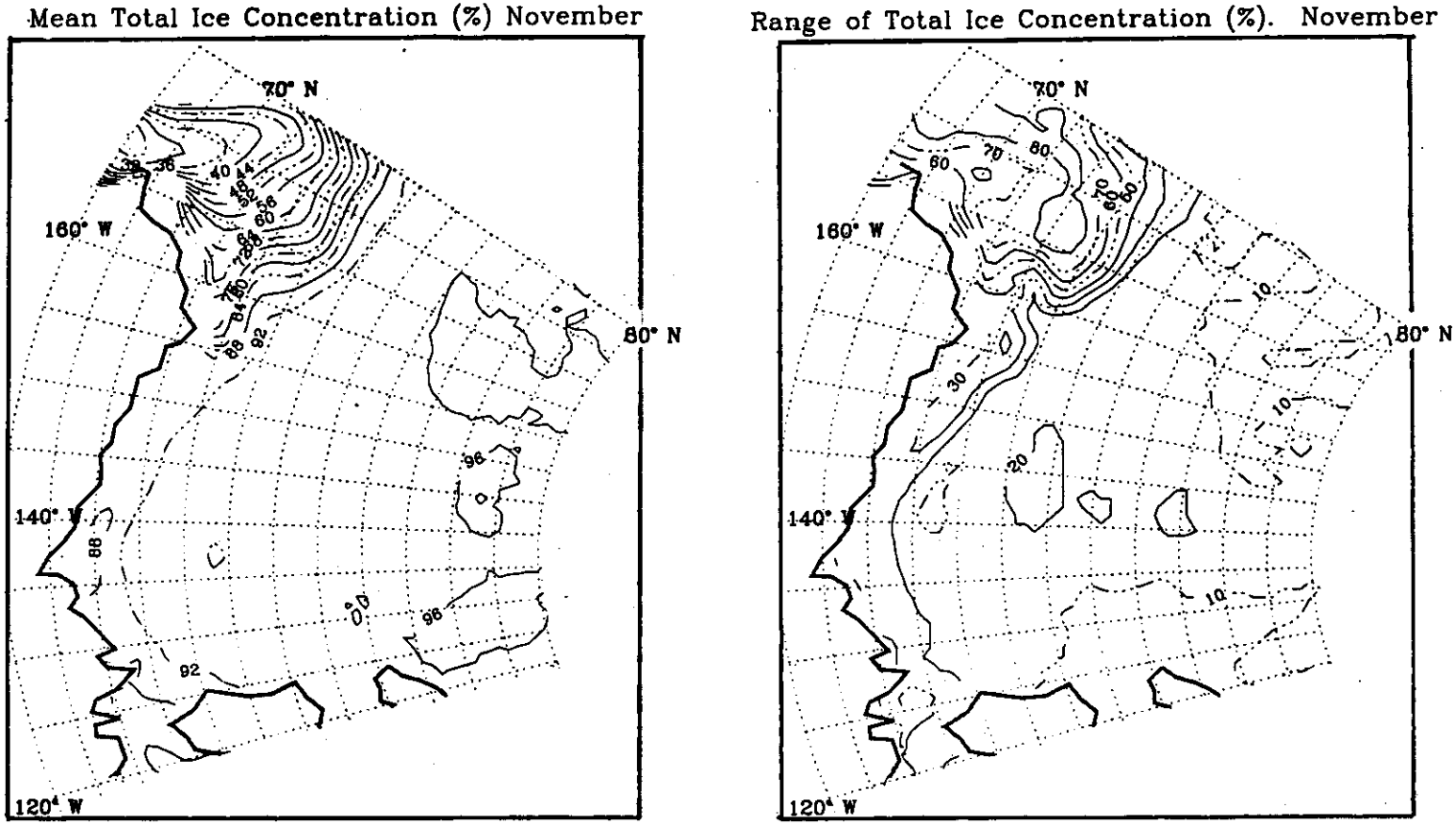

Figure 3.1.2 (Continued)

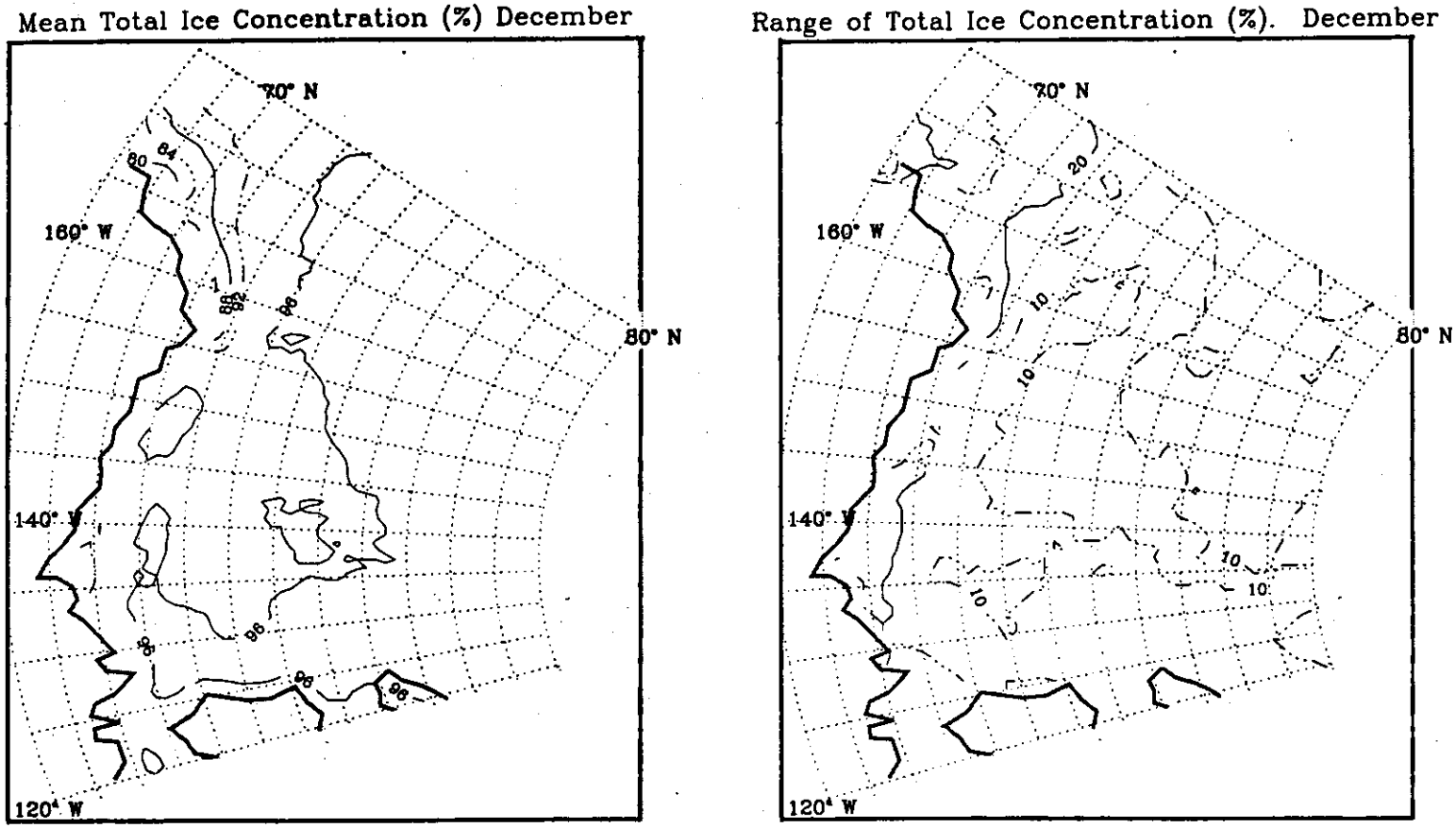

3.2 Sea Ice Velocity

Fields of monthly-mean sea ice velocity for 1988-1994 (Figure 3.2.1) are provided along with annual mean fields for individual years (Figure 3.2.2). These fields represent a combination of velocities calculated from the displacement of features observed in SSM/I 85 GHz imagery [Agnew et al., 1997; Emery et al., 1997a; 1997b], and buoy velocities provided by the IABP. Daily averages of SSM/I 85 GHz brightness temperatures were obtained from NSIDC on a 12.5-km polar grid. A maximum cross-correlation (MCC) method [Emery et al., 1991; Fowler, 1995] is applied to an 8 X 8 moving window of grid cells in the sequential, 24-hour averaged grid, with an overlap of 3 cells. The result is a 62.5 km grid of ice displacement vectors for all ice-covered areas. An oversampling method is used to improve the resolution of the MCC displacements. Analyses indicate a mean difference between IABP buoy and SSM/I-derived 24-hour motions of near zero, with a root mean-squared difference of 6 cm s^{-1} (~6 km d^{-1}). Averaging over time allows for the detection of motions slower than 6 cm s^{-1}. The SSM/I velocities are then merged via optimal interpolation with IABP buoy observations. The individual 24-hour velocities were averaged into monthly and annual means for the 1988-1994 period. Data and further details are available at http://polarbear.colorado.edu as part of the AVHRR Polar Pathfinder.

Clearly apparent is the well-known large seasonal variability in ice drift largely driven by winds; the relationship between the large-scale pattern of ice drift and geostrophic winds inferred from the mean distribution of sea level pressure is well evident (Section 1.1). Note the well-developed Beaufort Gyre and Transpolar Drift Stream circulations during April and May when the Canada Basin anticyclone is well established and the southward retreat of anticyclonic ice motion and the overlying atmospheric anticyclone into the Beaufort Sea during June and July. August also shows evidence of cyclonic motion near the pole reflecting the tendency for a mean sea-level low to develop in this area for this month. We note, however, that since the late 1980s there has been a shift in atmospheric circulation characterized by increased cyclone activity north of Siberia [Walsh et al., 1996; Serreze et al., 1997], favoring ice advection away from the Siberian coast [Maslanik et al., 1996]. From the annual mean plots, it is clear that a general southward drift of the SHEBA camp can be expected.

Figure 3.2.1

Mean Ice Drift: January

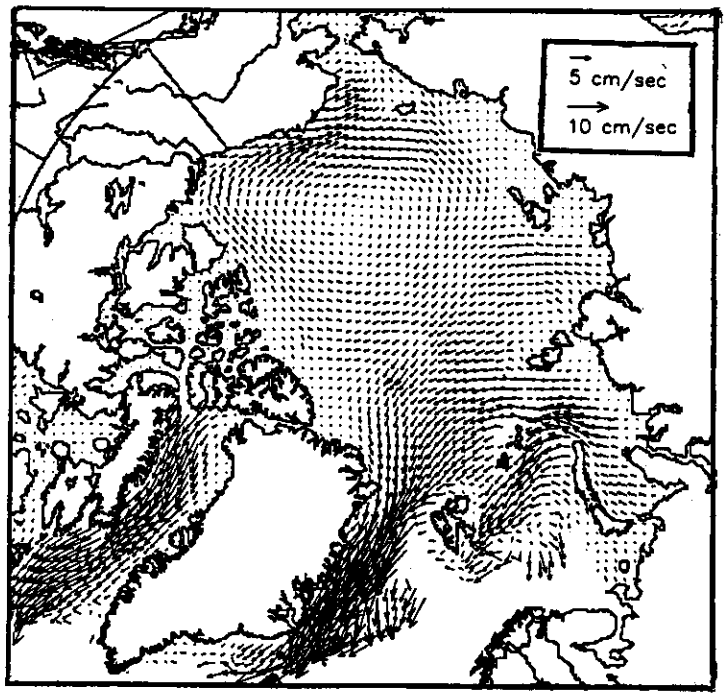

Mean Ice Drift: February

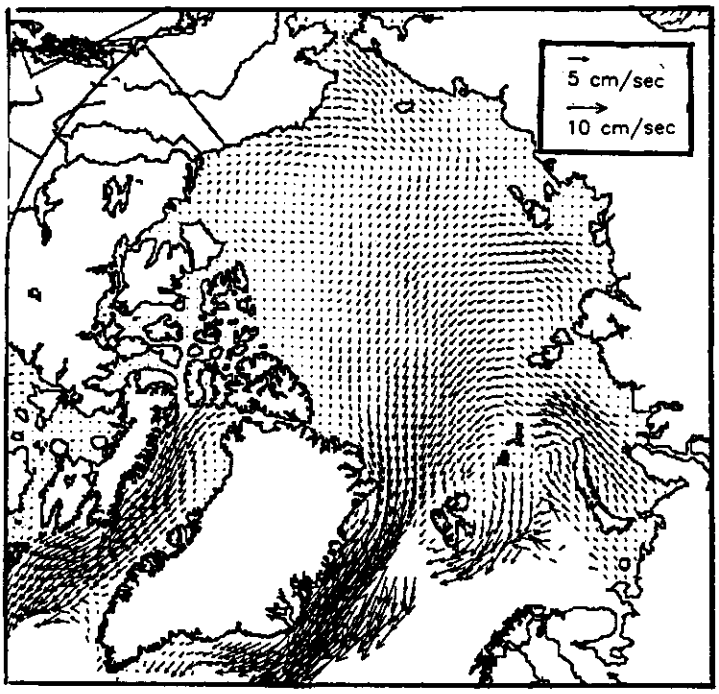

Mean Ice Drift: March

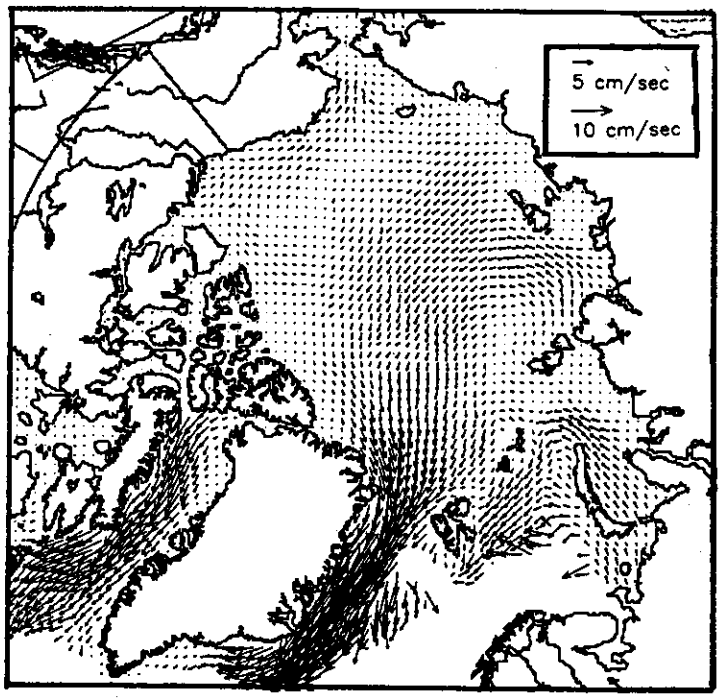

Mean Ice Drift: April

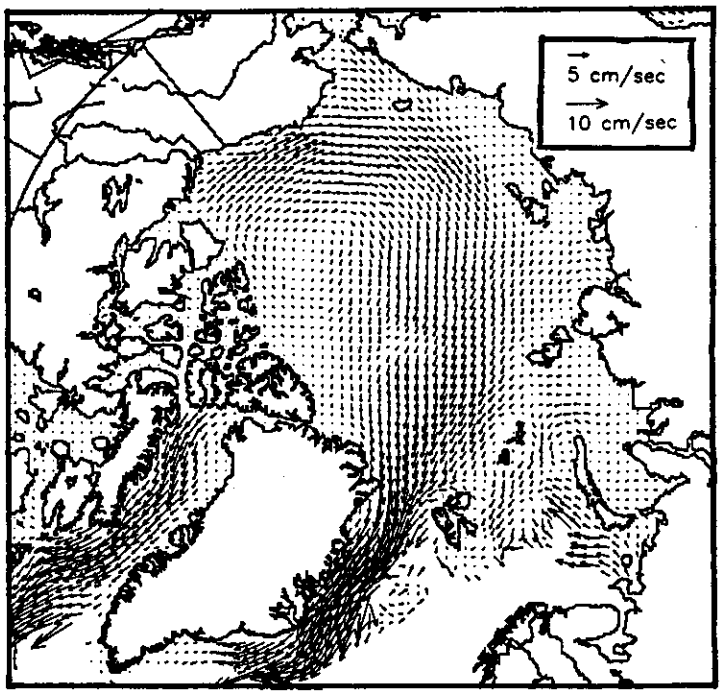

Units: cm s^{-1}

Figure 3.2.1 (Continued)

Mean Ice Drift: May

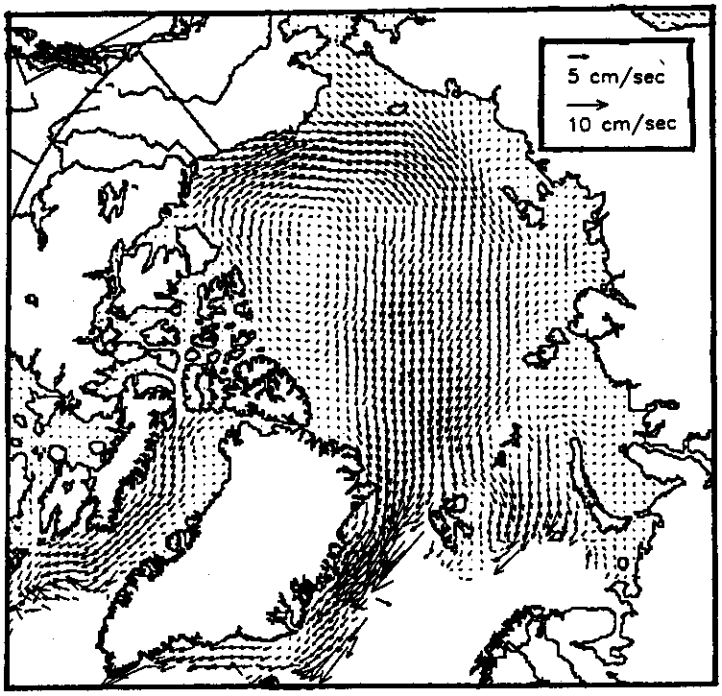

Mean Ice Drift: June

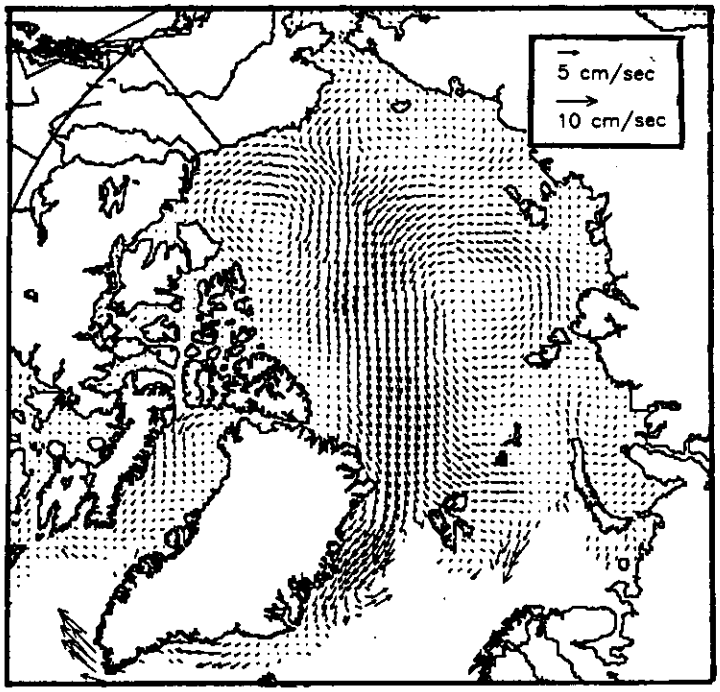

Mean Ice Drift: July

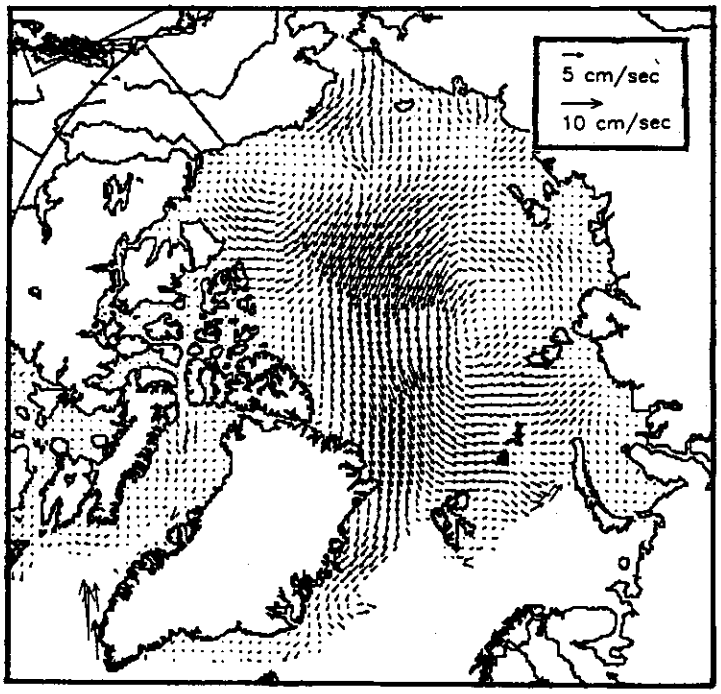

Mean Ice Drift: August

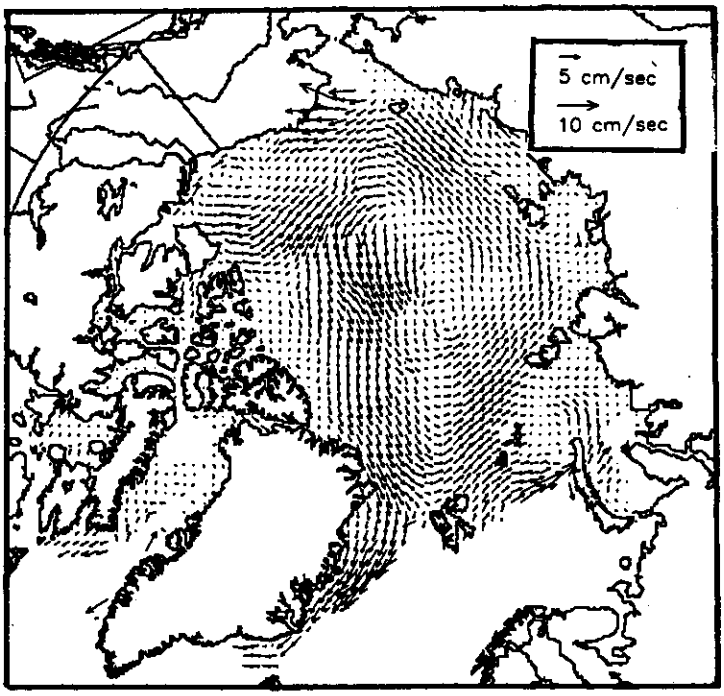

Units: cm s^{-1}

Figure 3.2.1 (Continued)

Mean Ice Drift: September

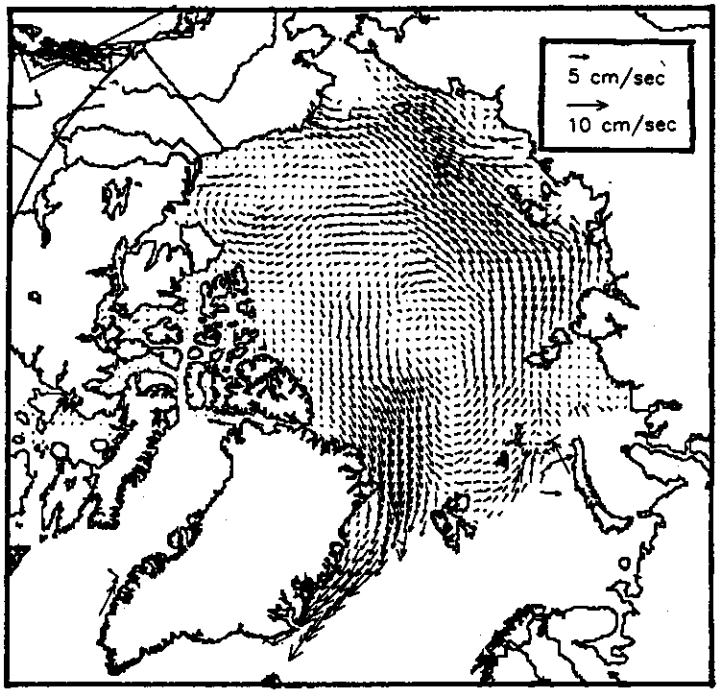

Mean Ice Drift: October

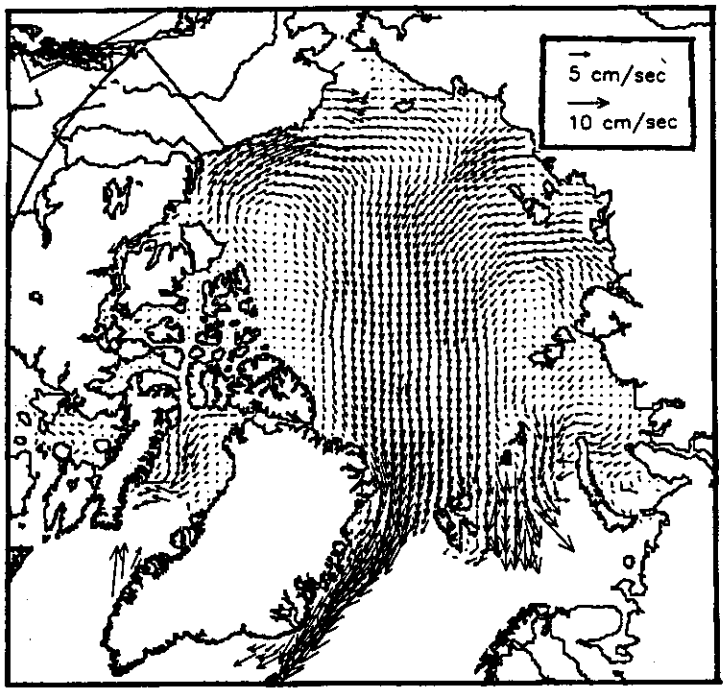

Mean Ice Drift: November

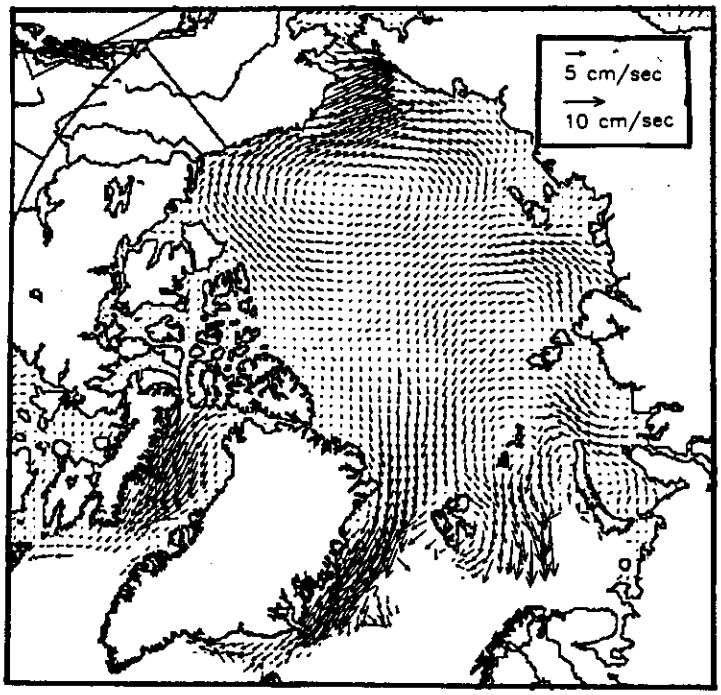

Mean Ice Drift: December

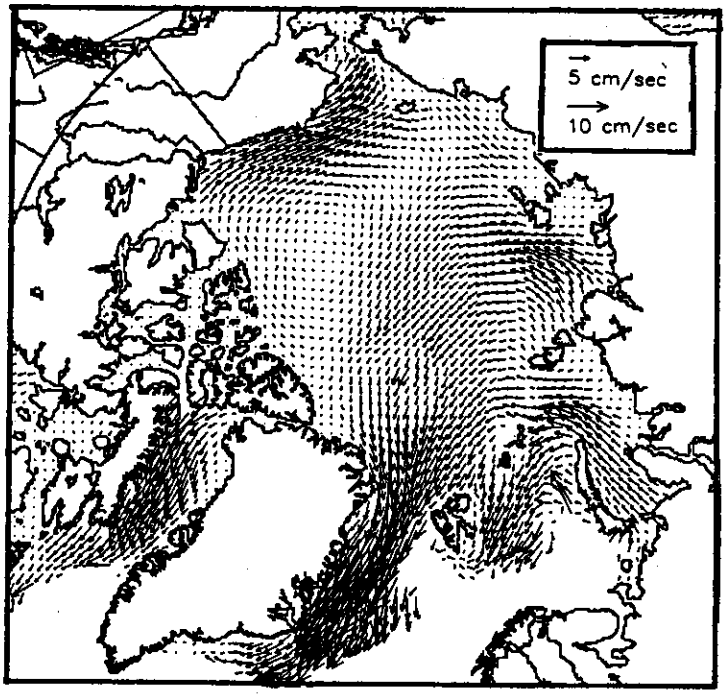

Units: cm s^{-1}

Figure 3.2.2

Mean Annual Ice Drift: 1988

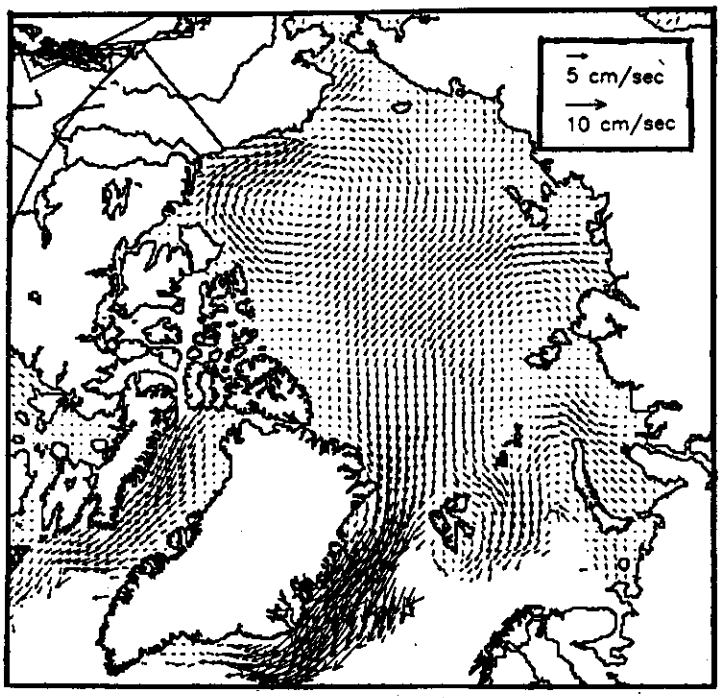

Mean Annual Ice Drift: 1989

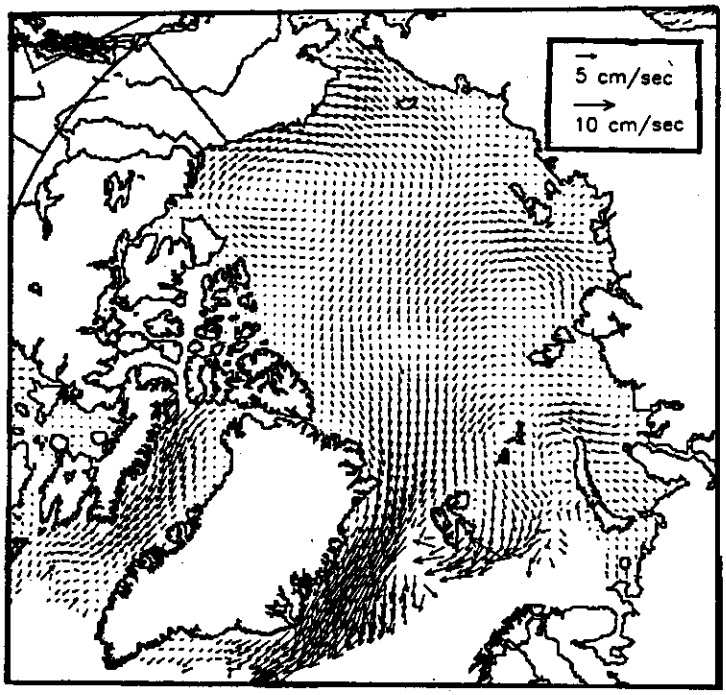

Mean Annual Ice Drift: 1990

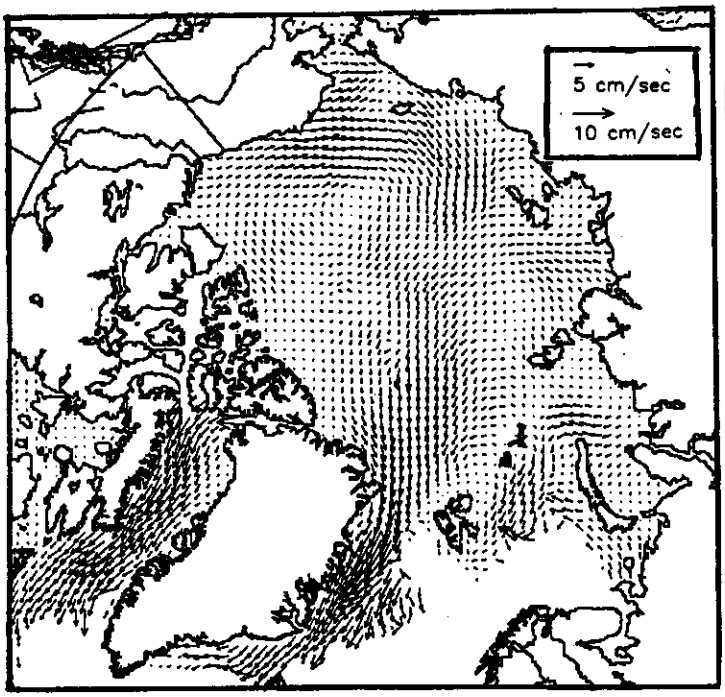

Mean Annual Ice Drift: 1991

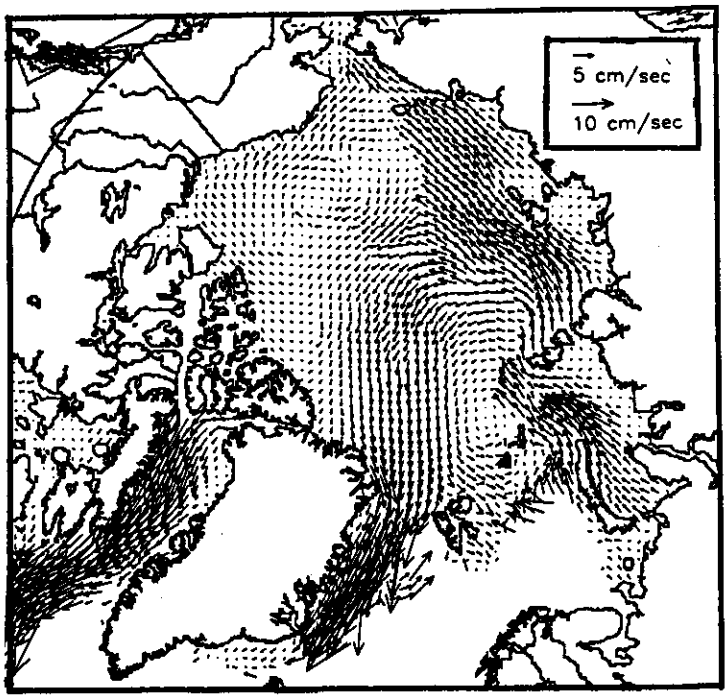

Units: cm s^{-1}

Figure 3.2.2 (Continued)

Mean Annual Ice Drift: 1992

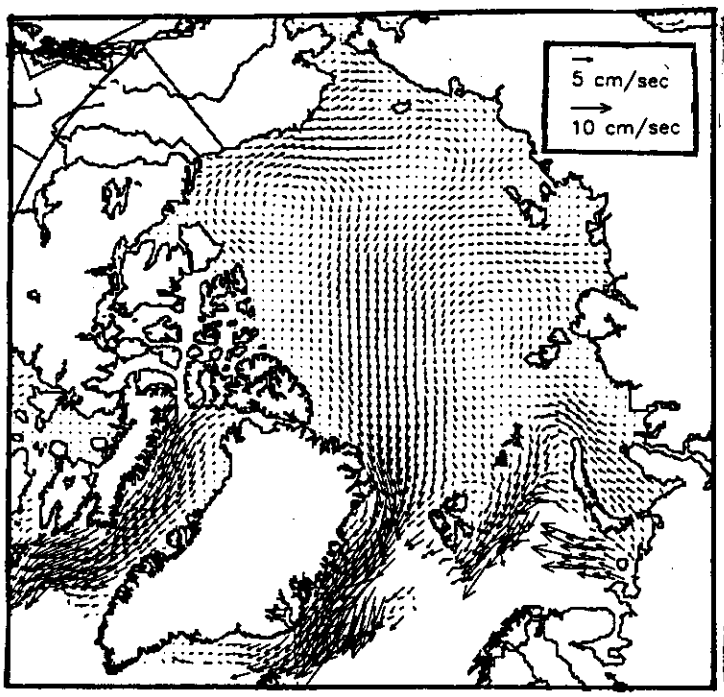

Mean Annual Ice Drift: 1993

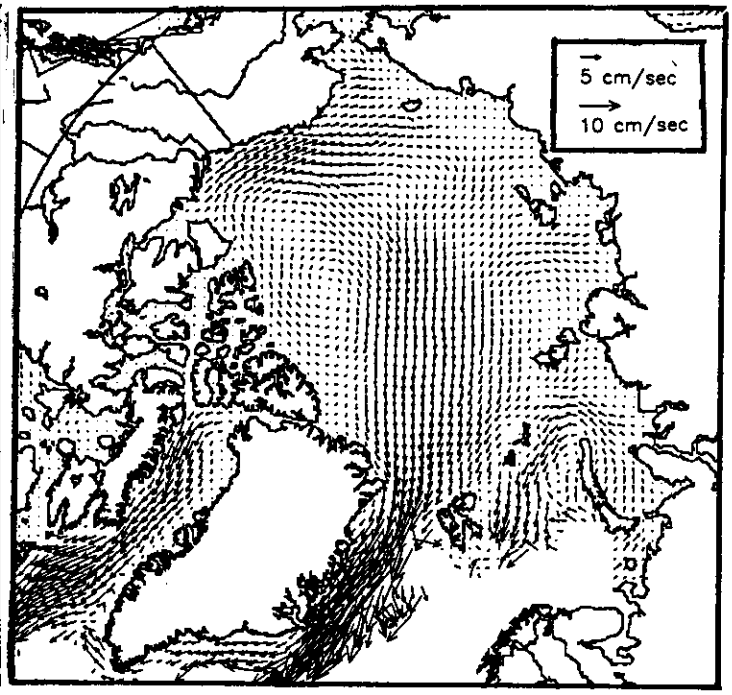

Mean Annual Ice Drift: 1994

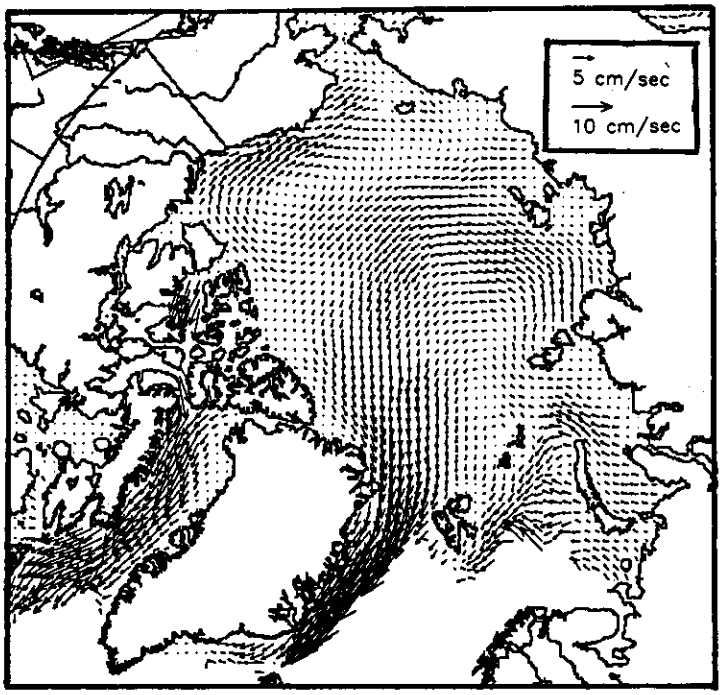

Units: cm s^{-1}

3.3 Sea Ice Divergence and Convergence

Since 1979, the IABP has provided sea ice motion fields. The ice motion fields presented in Section 3.2 use IABP drifting data for 1988-1994. University of Washington provides these data as gridded fields of ice velocity and derivatives of the ice velocity components using optimal interpolation [Thorndike and Colony, 1981]. We present maps of the grid-point frequency of daily ice divergence and daily ice convergence exceeding 0.5% per day, using the 00Z data (Figure 3.3.1). Results are also summarized for the SHEBA region as monthly means (Figure 3.3.2) and as histograms of daily divergence/convergence rates (Figure 3.3.3). Positive values in Figure 3.3.3 represent divergence and negative values represent convergence. The latter two figures are based on grouping data for two of the original IABP grid points nearest to the SHEBA region. Results were prepared using daily gridded IABP data from 1979-1994. The percent divergence/convergence is calculated by multiplying the daily divergence rate (in inverse seconds) by the number of seconds in a day. It can be interpreted in terms of percent opening or closing. For Figure 3.3.1 we transformed data from the original latitude/longitude IABP grid to a series of grid points from the EASE-Grid. We stress that the ice divergence/convergence estimates can be prone to error and should be treated with caution. Efforts have been made to minimize uncertainty by eliminating those cases for which the variance of the interpolation error at each grid point (provided with the buoy fields) is large. The values are furthermore representative of the large-scale divergence/convergence field. Local deformation rates will not be well correlated with these large-scale estimates.

As a general statement, the frequency of both large divergence and convergence episodes for the central Arctic tend to be greater during the summer months when ice concentrations are lowest. However, for winter months, large ice divergence events tends to be frequent over the Atlantic side of the Arctic. The SHEBA region shows a minimum frequency in large ice divergence events from January through June, rising to a maximum of over 25% in November, by which time rates for the central Arctic are decreasing. In contrast, the frequency of large ice convergence events displays a distinct August peak of 21% and a distinct spring minimum. These seasonal differences are apparent in the monthly histograms.

Figure 3.3.1

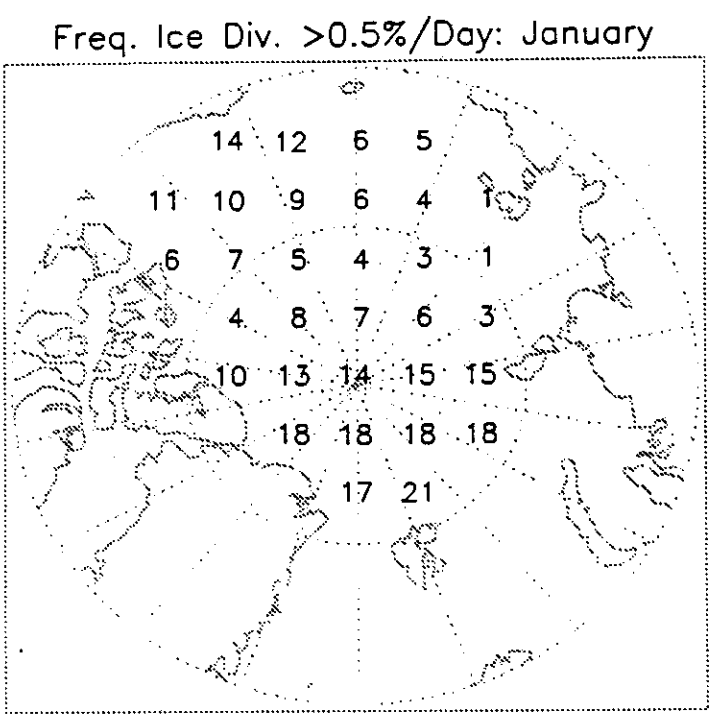

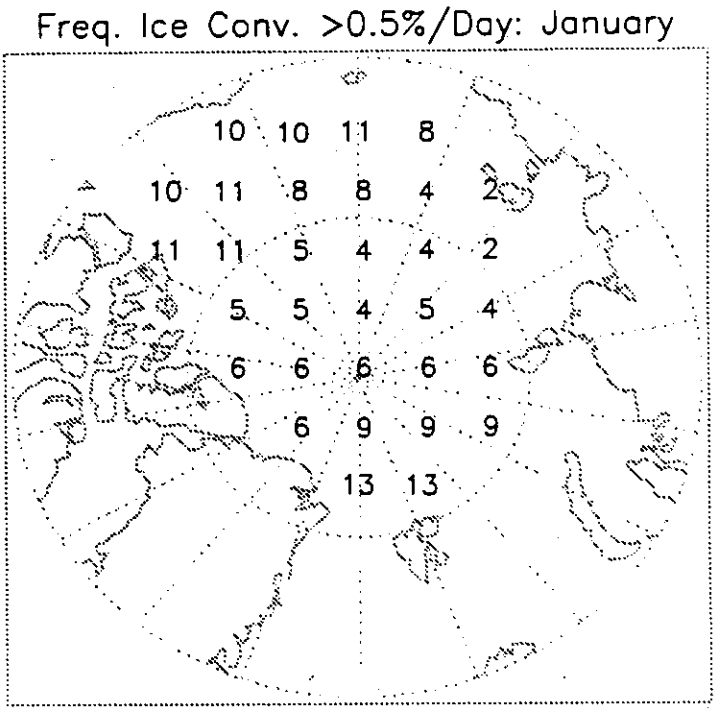

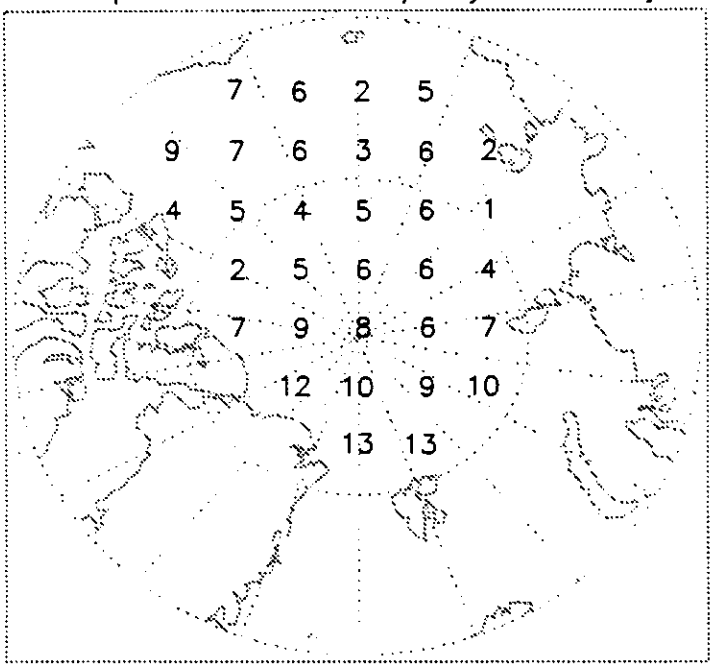

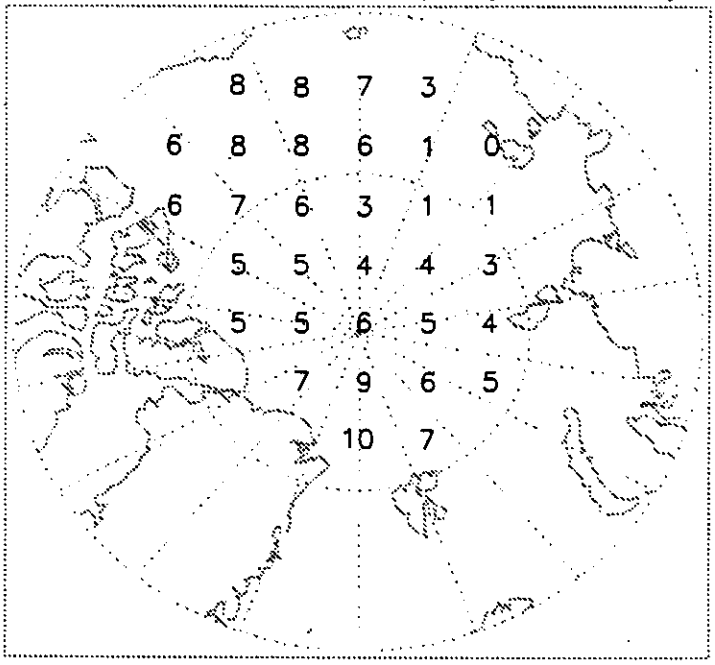

Units: % Frequency

Figure 3.3.1 (Continued)

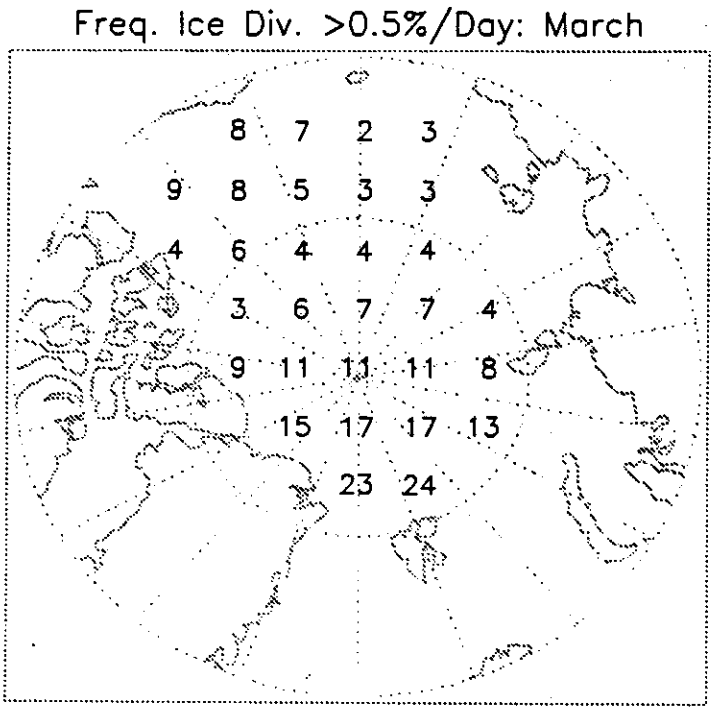

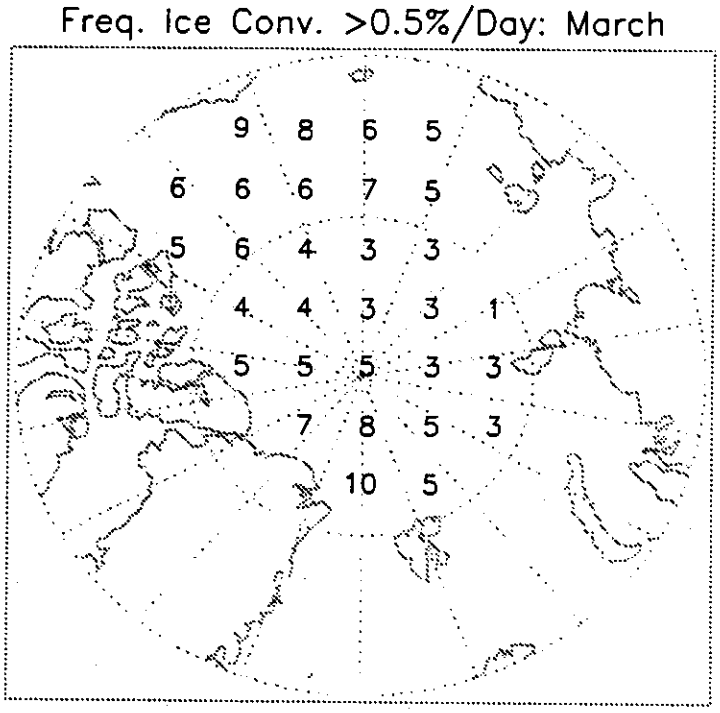

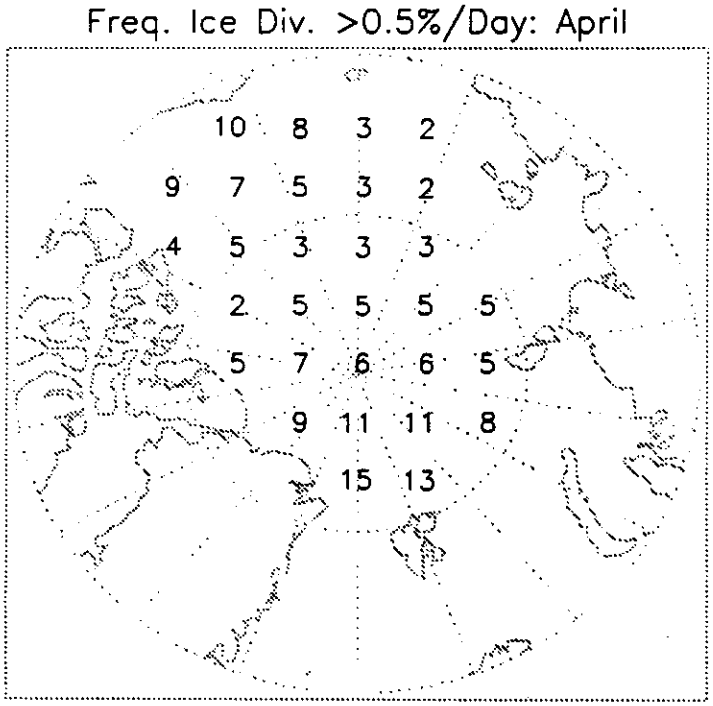

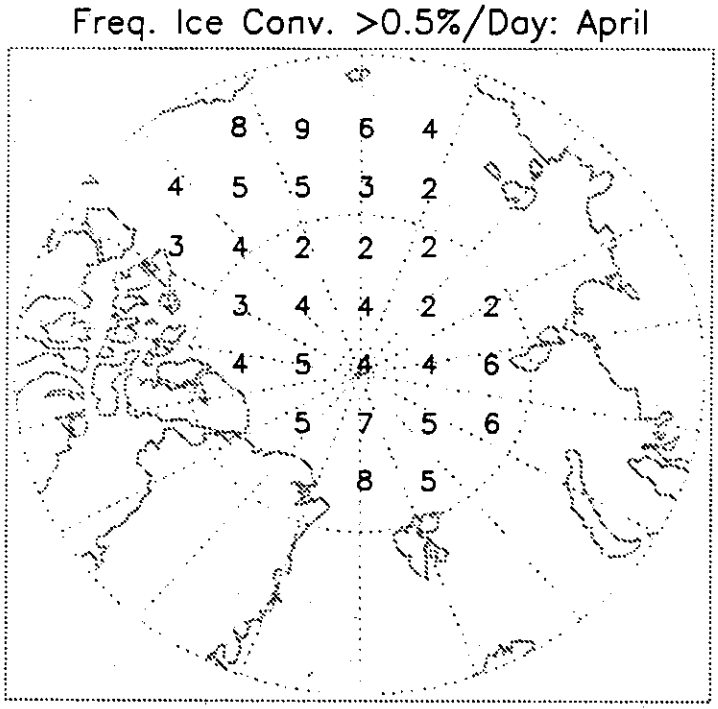

Units: % Frequency

Figure 3.3.1 (Continued)

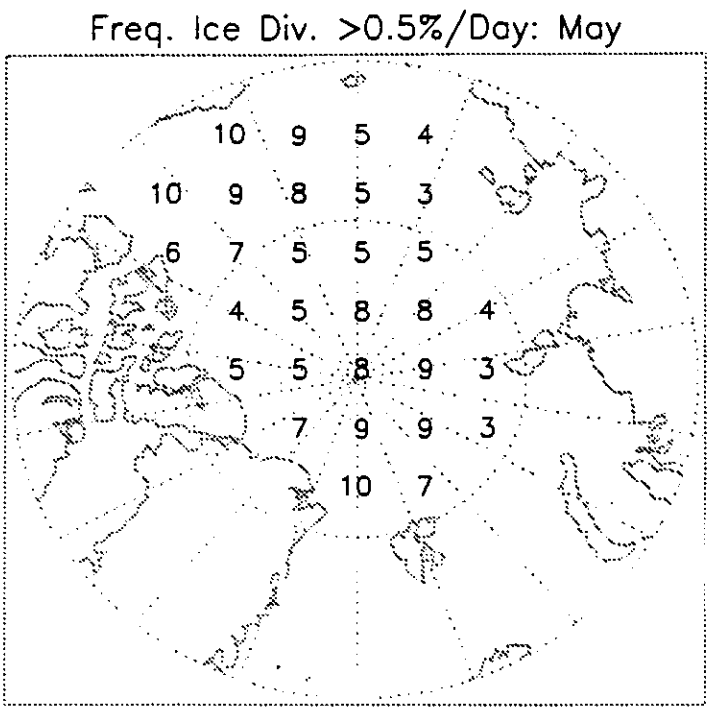

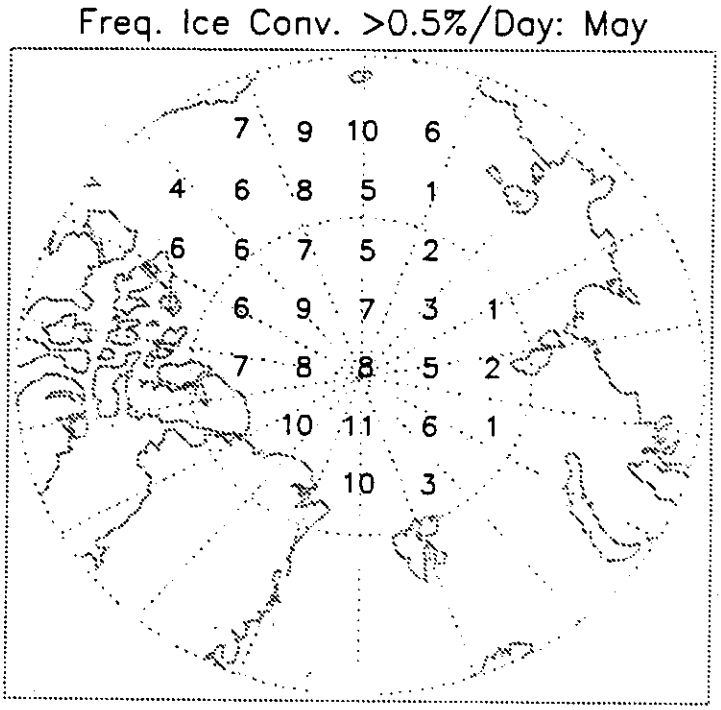

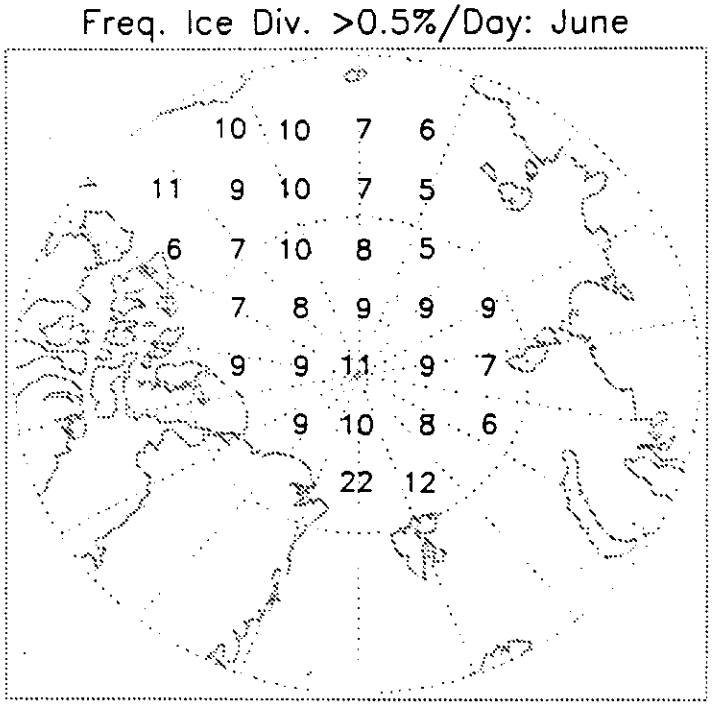

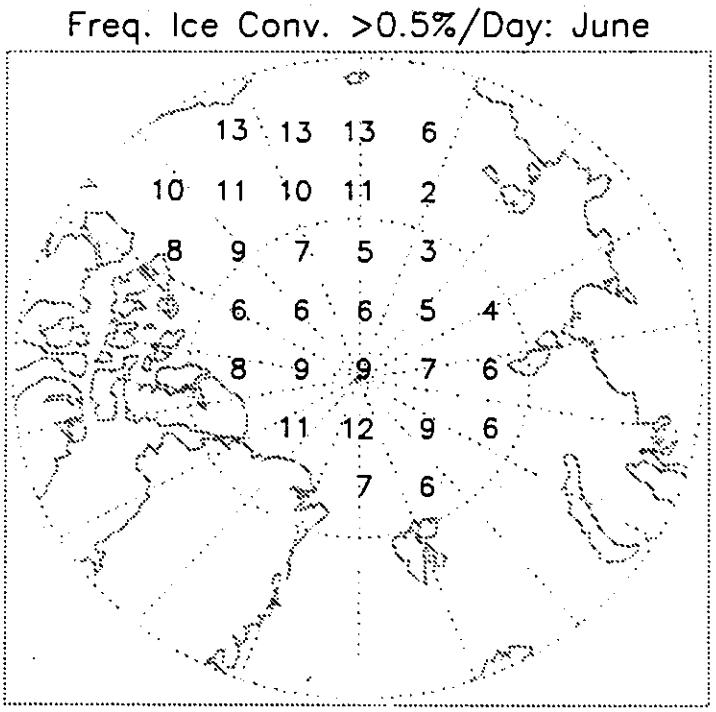

Units: % Frequency

Figure 3.3.1 (Continued)

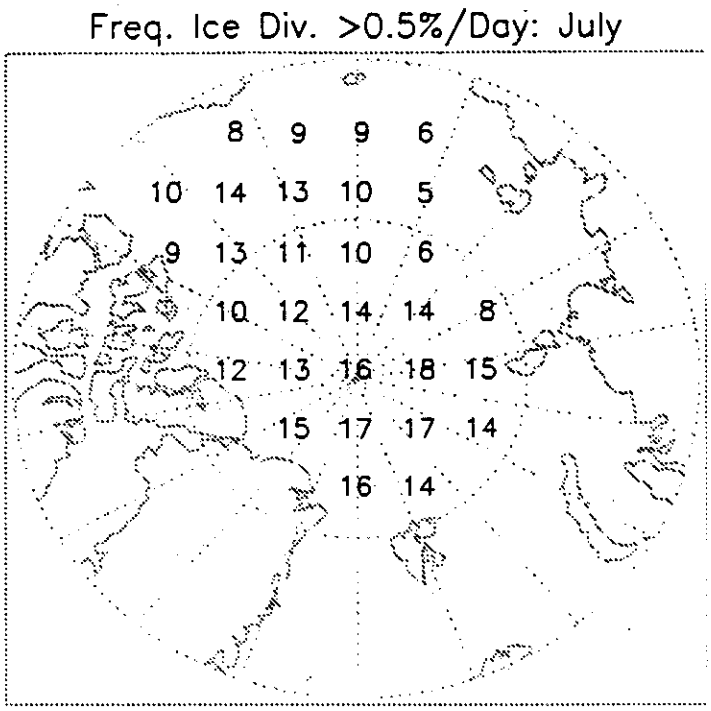

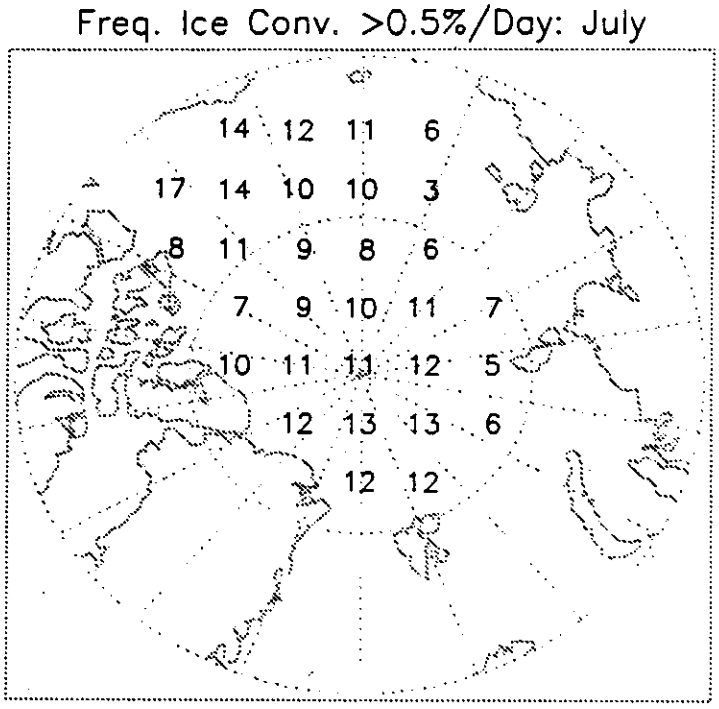

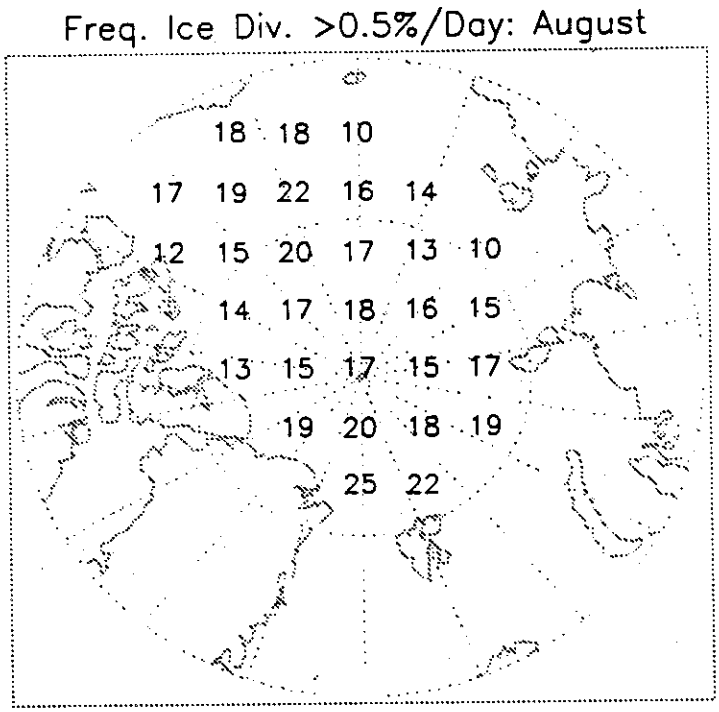

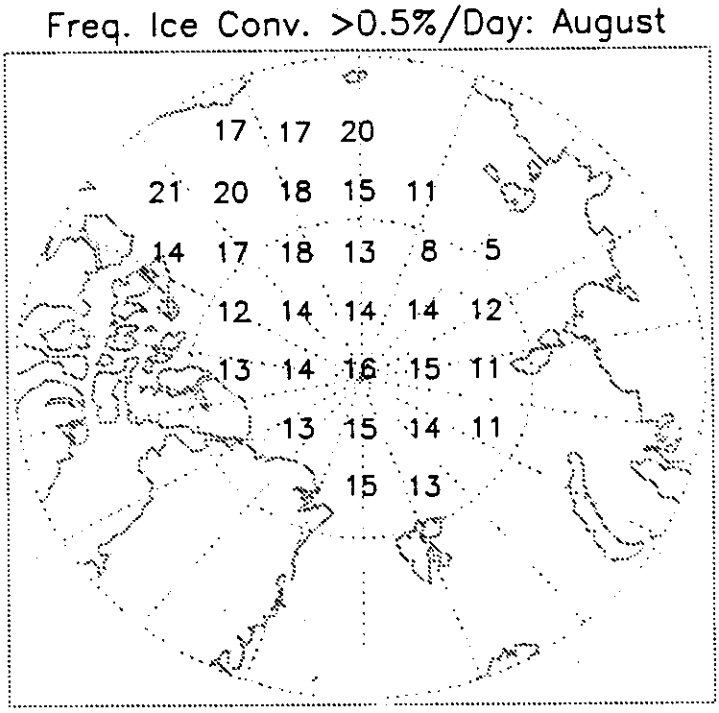

Units: % Frequency

Figure 3.3.1 (Continued)

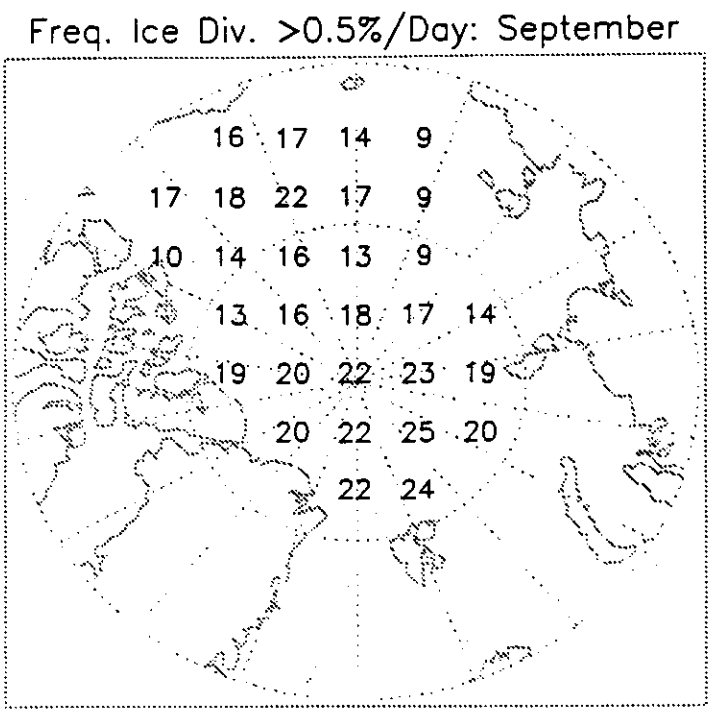

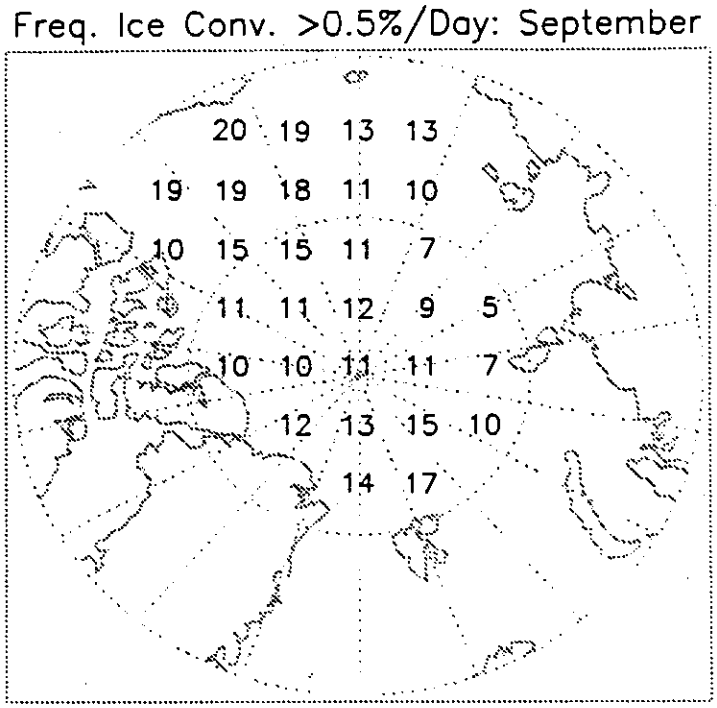

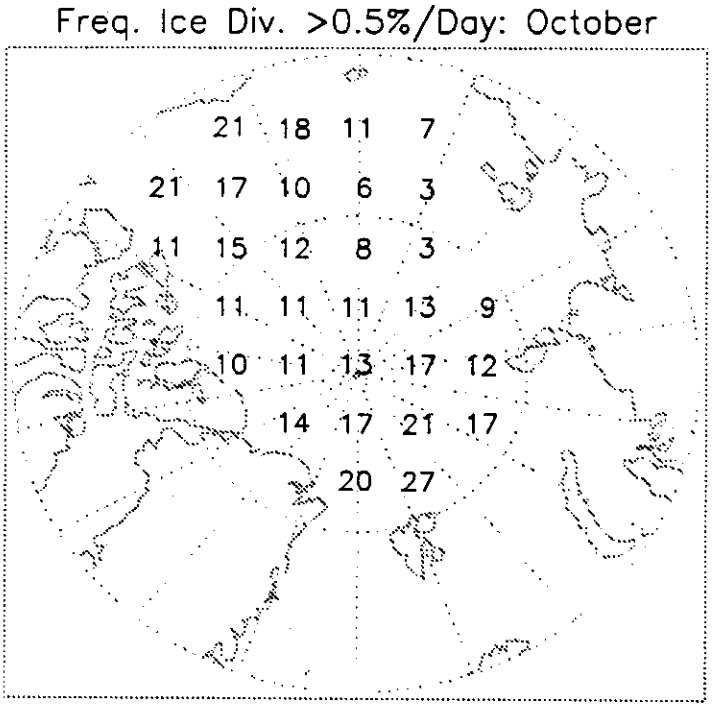

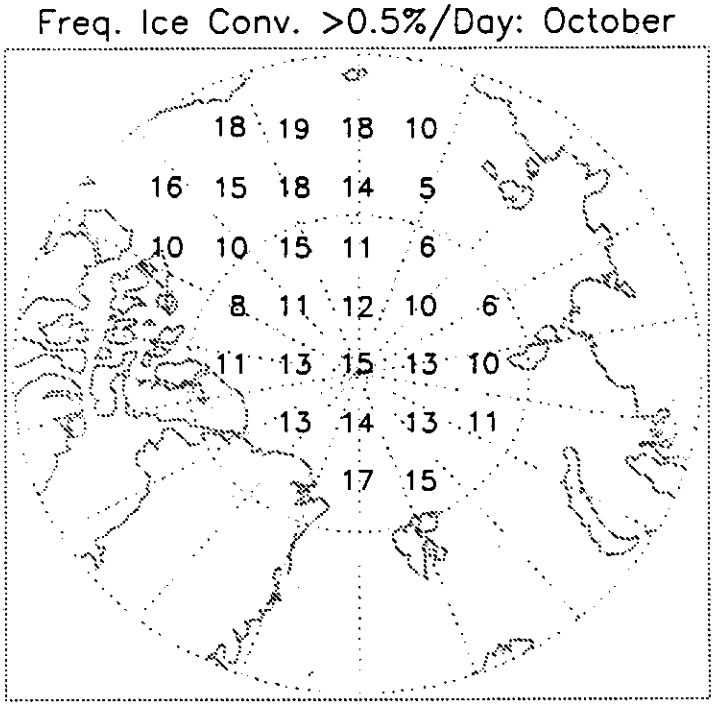

Units: % Frequency

Figure 3.3.1 (Continued)

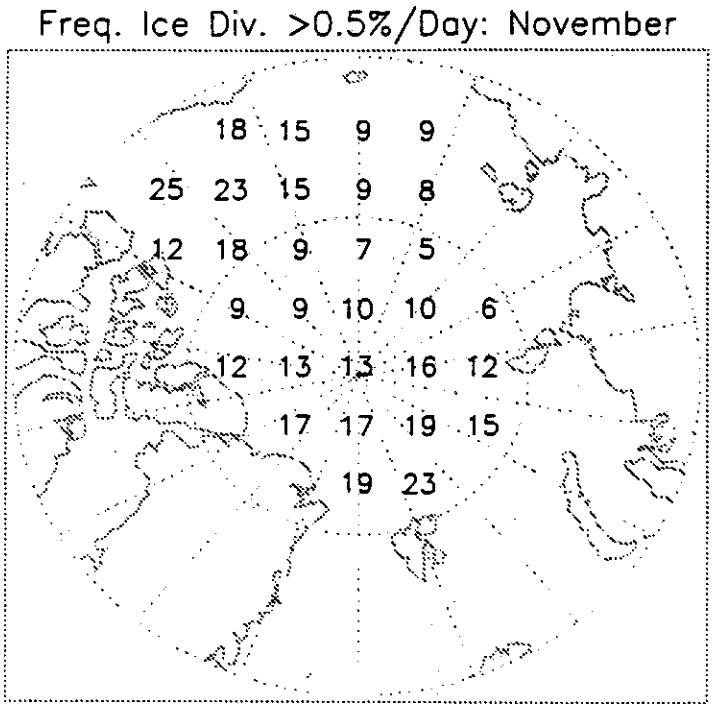

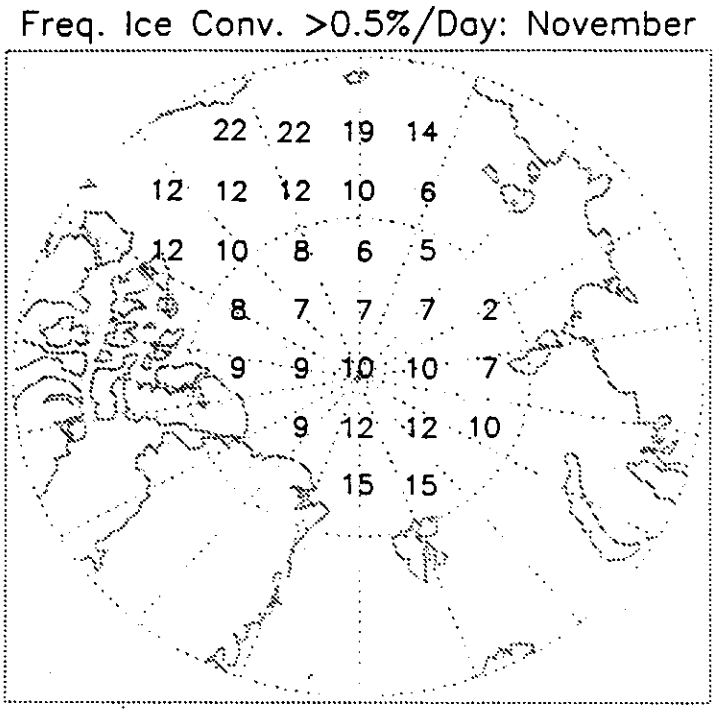

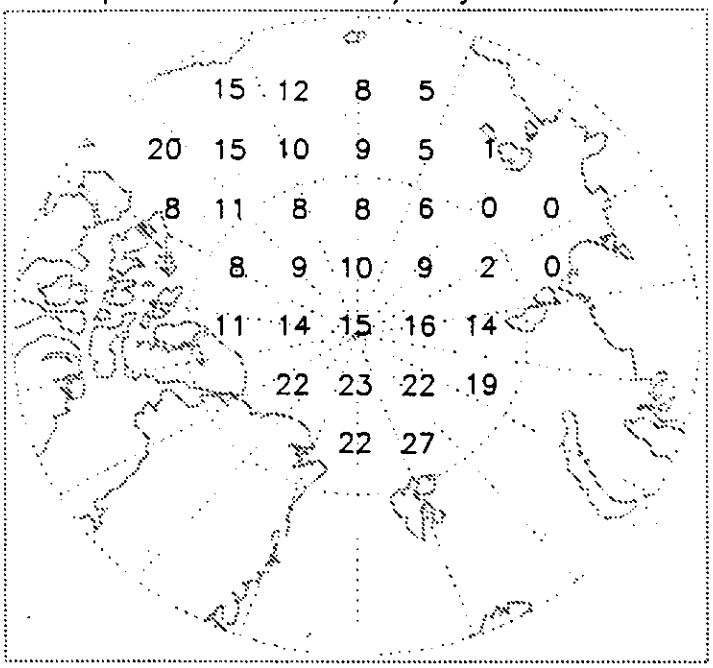

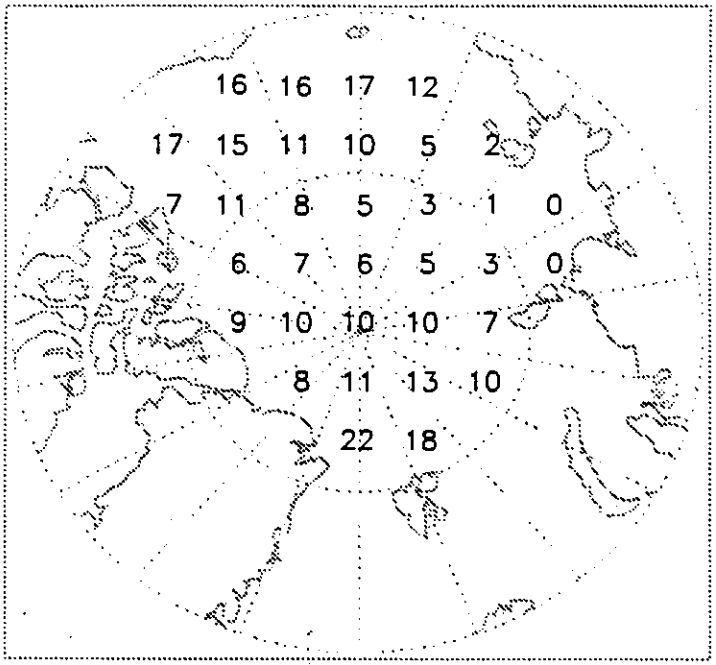

Units: % Frequency

Figure 3.3.2

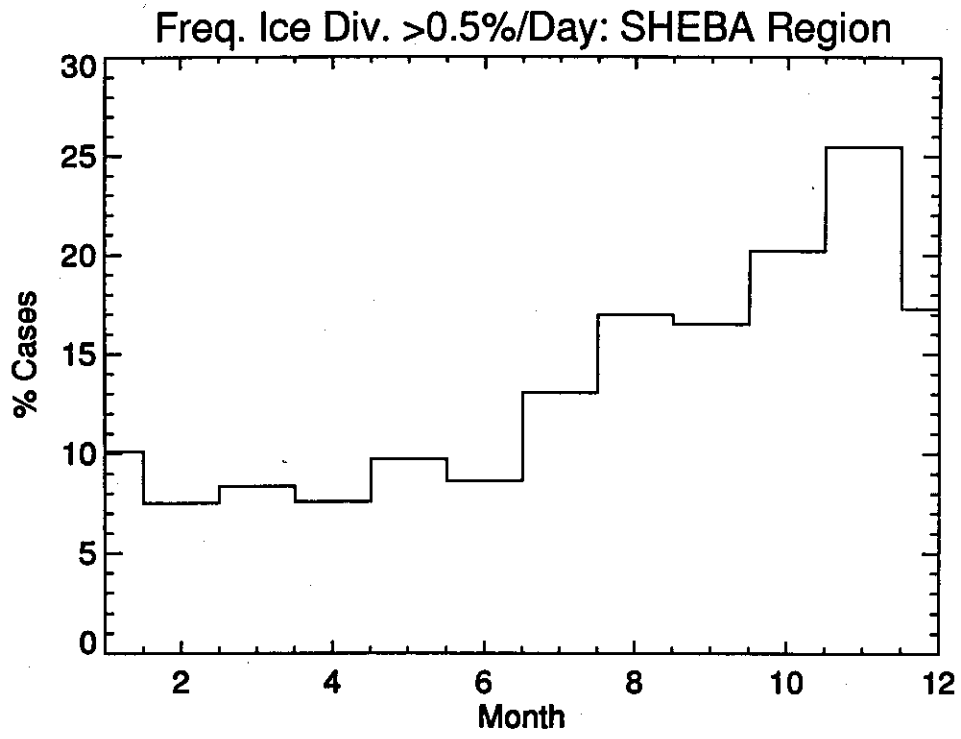
Freq. Ice Div. >0.5%/Day: SHEBA Region
% Cases
Month
0
5
10
15
20
25
30
2
4
6
8
10
12

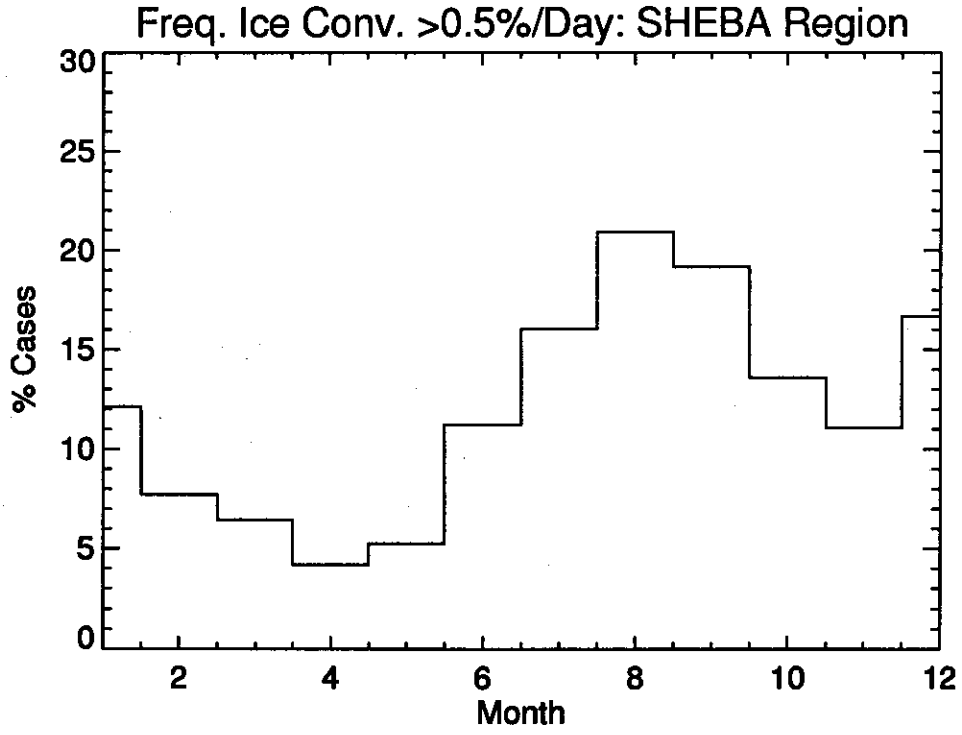
Freq. Ice Conv. >0.5%/Day: SHEBA Region
% Cases
Month
0
5
10
15
20
25
30
2
4
6
8
10
12

Figure 3.3.3

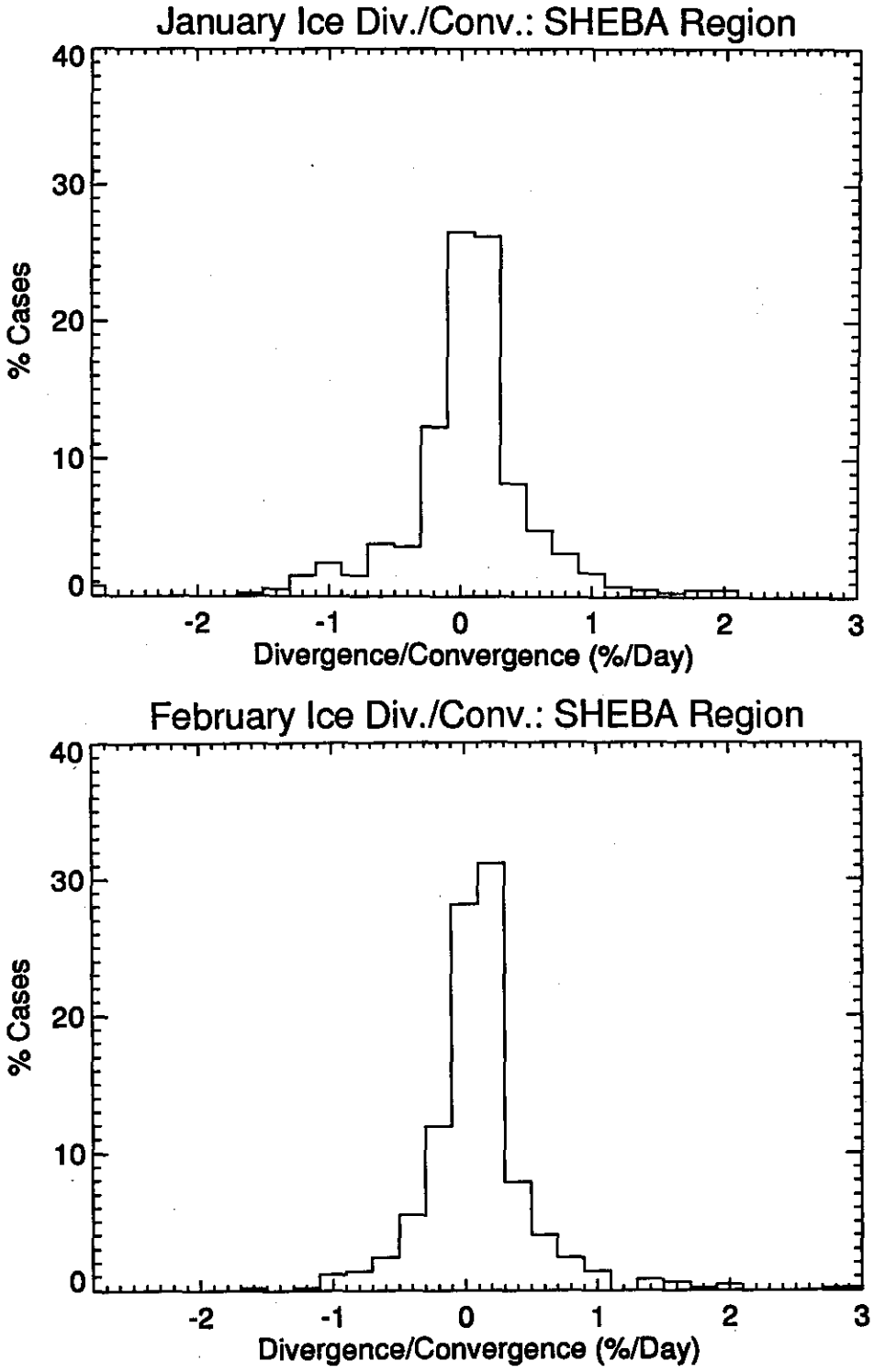
January Ice Div./Conv.: SHEBA Region
% Cases
40
30
20
10
0
-2
-1
0
1
2
3
Divergence/Convergence (%/Day)
February Ice Div./Conv.: SHEBA Region
% Cases
40
30
20
10
0
-2
-1
0
1
2
3
Divergence/Convergence (%/Day)

Figure 3.3.3 (Continued)

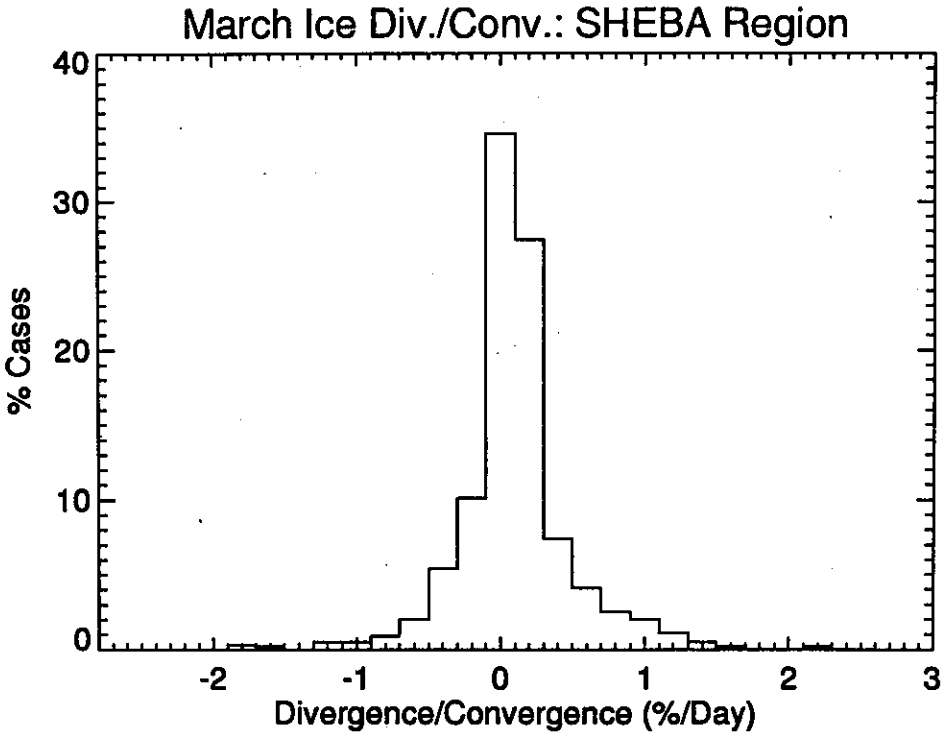

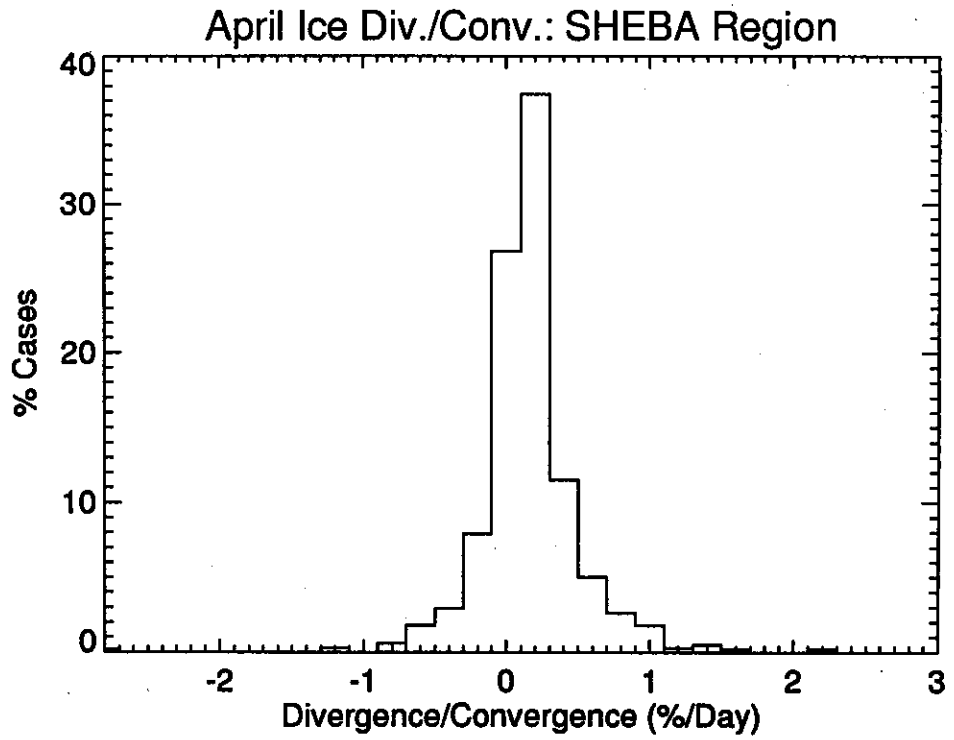

Figure 3.3.3 (Continued)

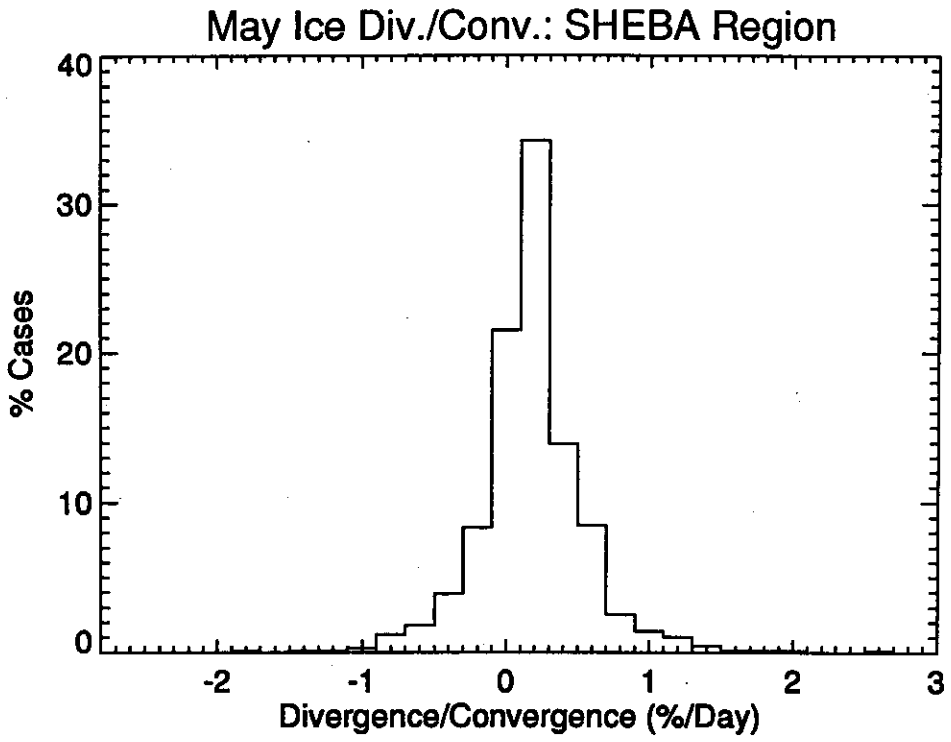

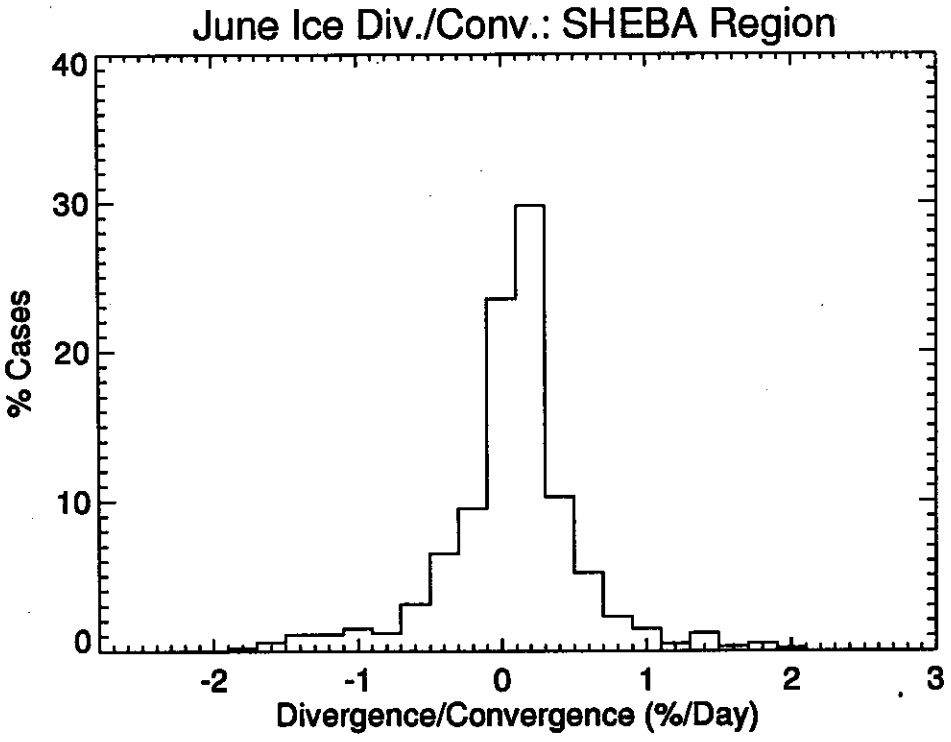

Figure 3.3.3 (Continued)

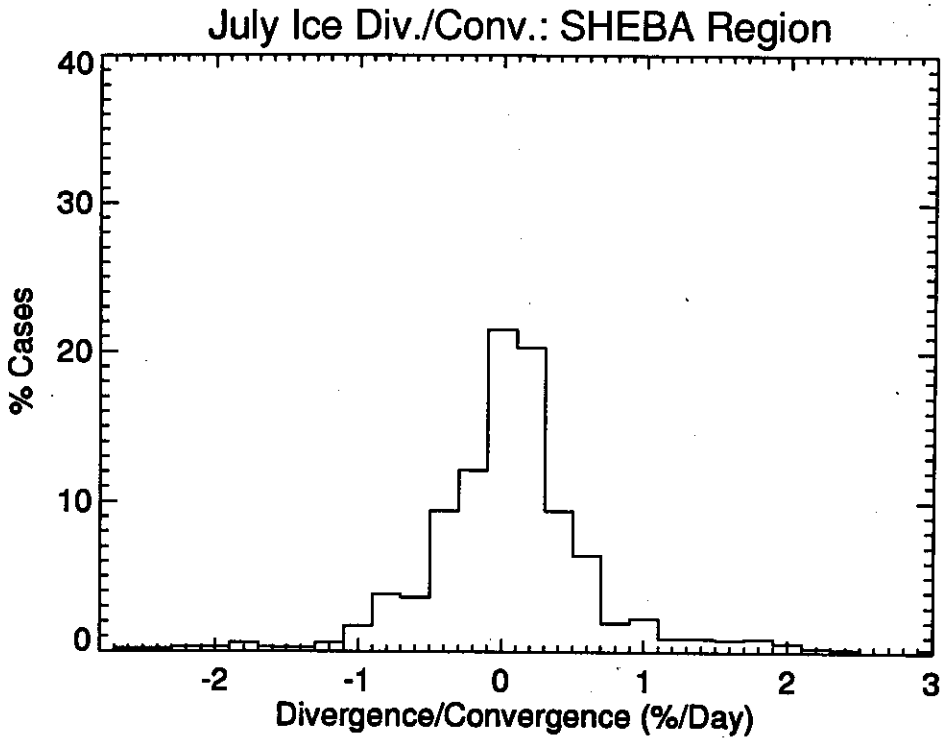

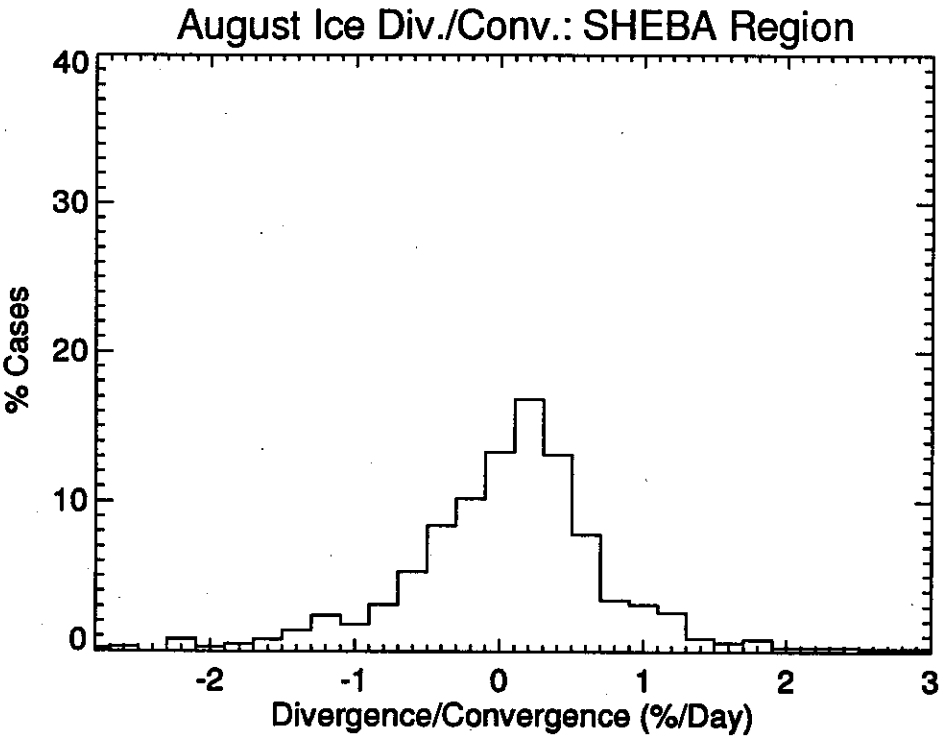

Figure 3.3.3 (Continued)

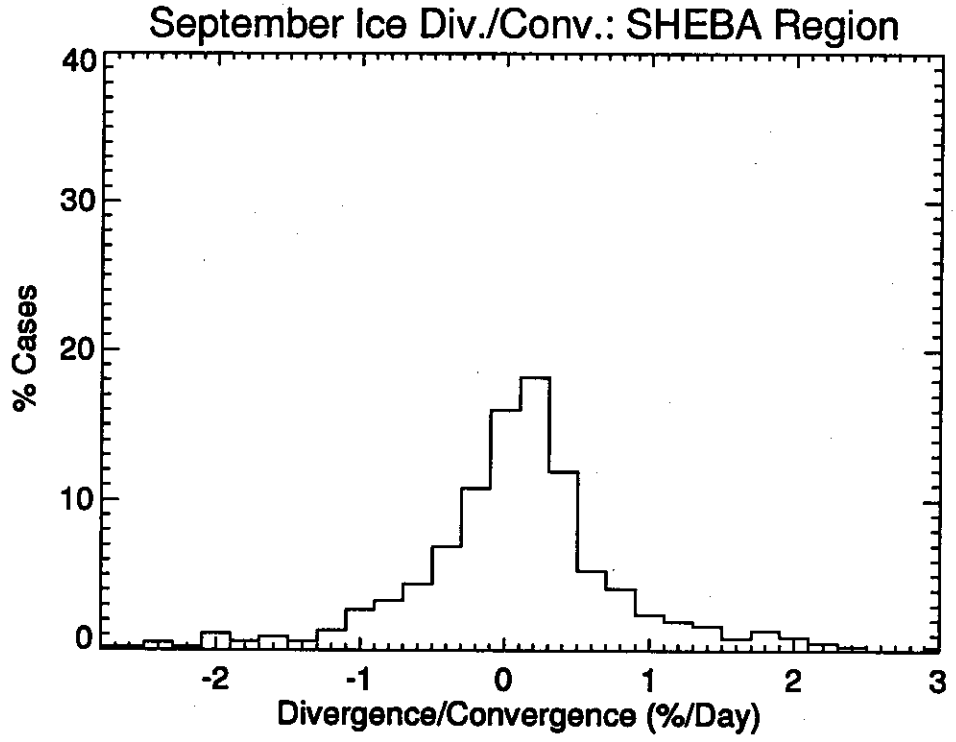

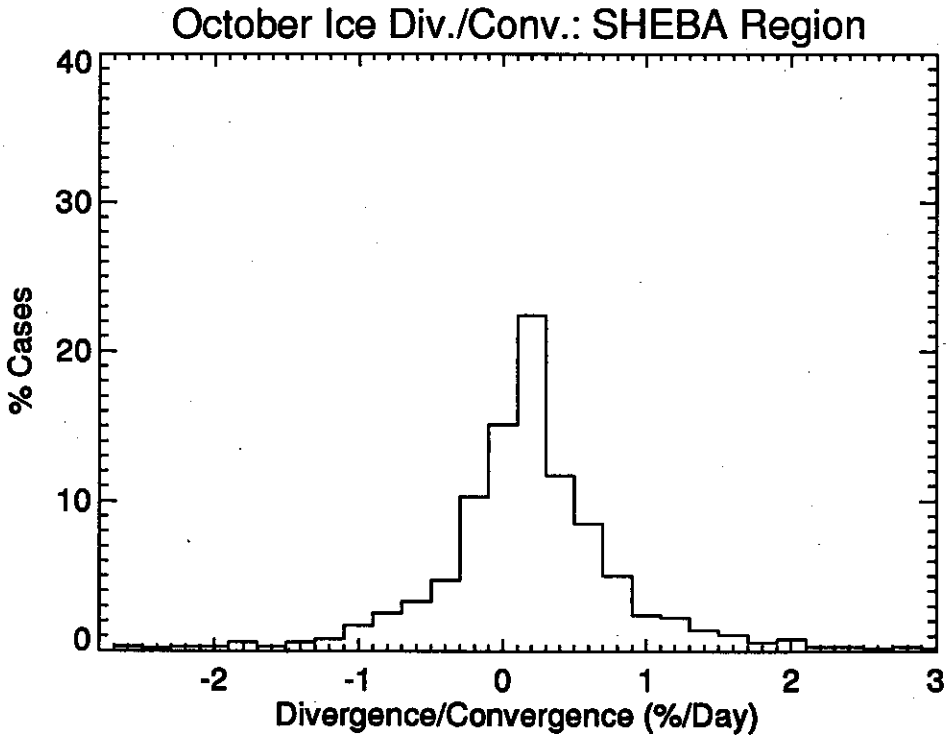

Figure 3.3.3 (Continued)

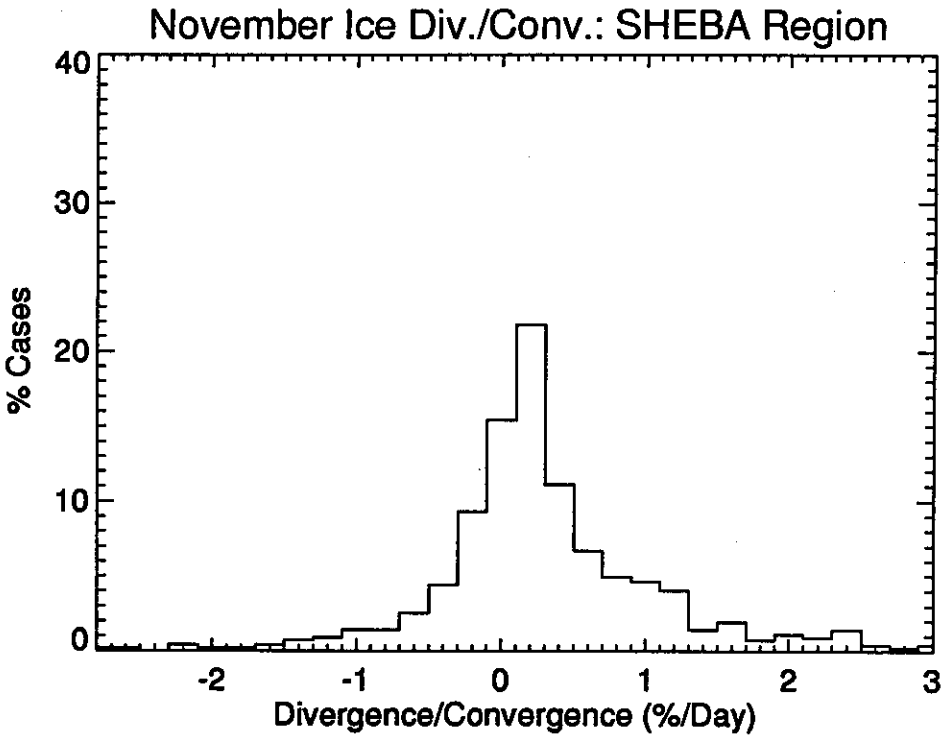

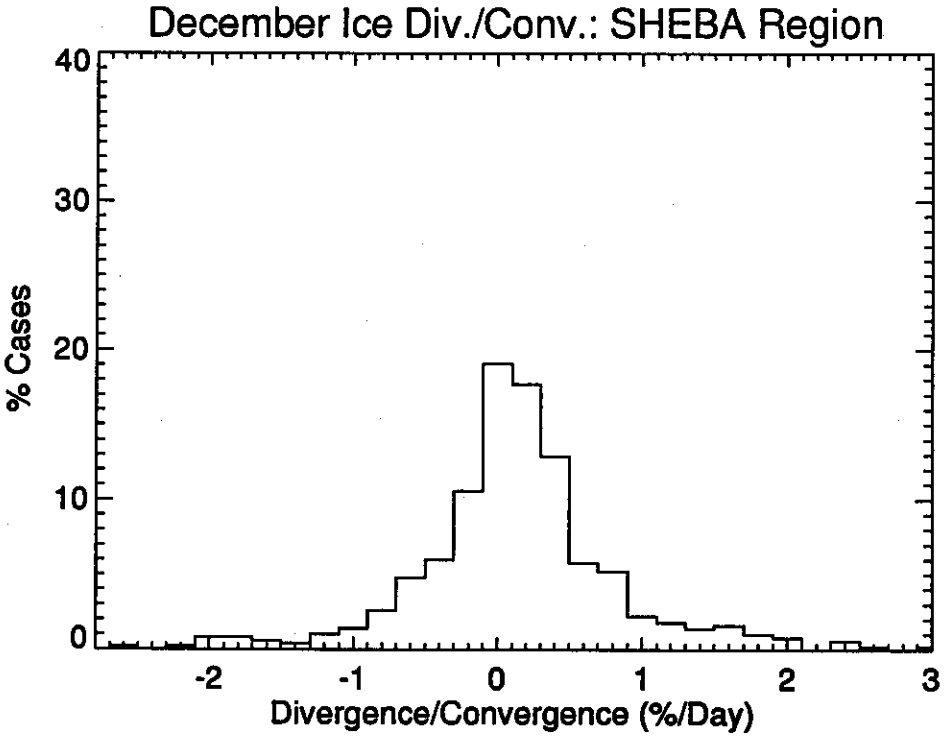

3.4 Sea Ice Melt Onset and Melting Days

The POLES 2-meter air temperatures described in Section 2.4 for 1979-1993 were used to estimate the seasonal onset and duration of surface melt. Melt onset was defined for each year and grid point as the first day (in Julian Days) of the first three-day consecutive run of temperatures of 0°C or higher. The count of melting days for each year and grid point was simply taken as the number of days for which the air temperature was 0°C or higher. The results for each year and grid point were then processed to yield the 15-year mean date of melt onset, the latest (maximum) and earliest (minimum) date of melt onset and the range between the earliest and latest dates. Similarly, we determined the 15-year mean number of melting days, as well as the minimum, maximum and range in melting days. Since these statistics are derived from air temperature measurements, they are only an approximation of the true melt statistics. Factors such as radiational heating and data accuracy will affect the relationship between the interpolated temperatures and melt onset/melting days. After all computation the results were transformed to the EASE-Grid. Results for melt onset and melting days are given in Figures 3.4.1 and 3.4.2 respectively.

Over the central Arctic Ocean, the average date of melt onset is Julian Day 170 (19 June). The SHEBA site lies between Julian Day 160 (9 June) and 170 (19 June) isolines. Although our maps indicate that melt onset for the central Arctic Ocean may range from 20 days earlier to 40 days later than the mean, several years were encountered for which the temperature time series at individual grid points near the pole indicated no melt. For computational reasons, we base our results for each grid point only on those years for which melt occurred. Hence, for a few grid points and years, a melt date is not defined. This does not present a problem for calculation of melting days, as a zero value is valid. However, these zero values were eliminated by the smoothing effect during transformation of the original POLES grid to the EASE-Grid. With this caveat in mind, the mean, maximum and minimum number of melting days for the central Arctic show largely zonal patterns. Near the pole, melt occurs for typically 30 days, but ranging from less than 10 to as high as 60-70 days, hence with a range of 50-70 days. For the SHEBA region, typically 50 melting days can be expected, bur ranging as high as 80 to as low as 30 days.

Figure 3.4.1

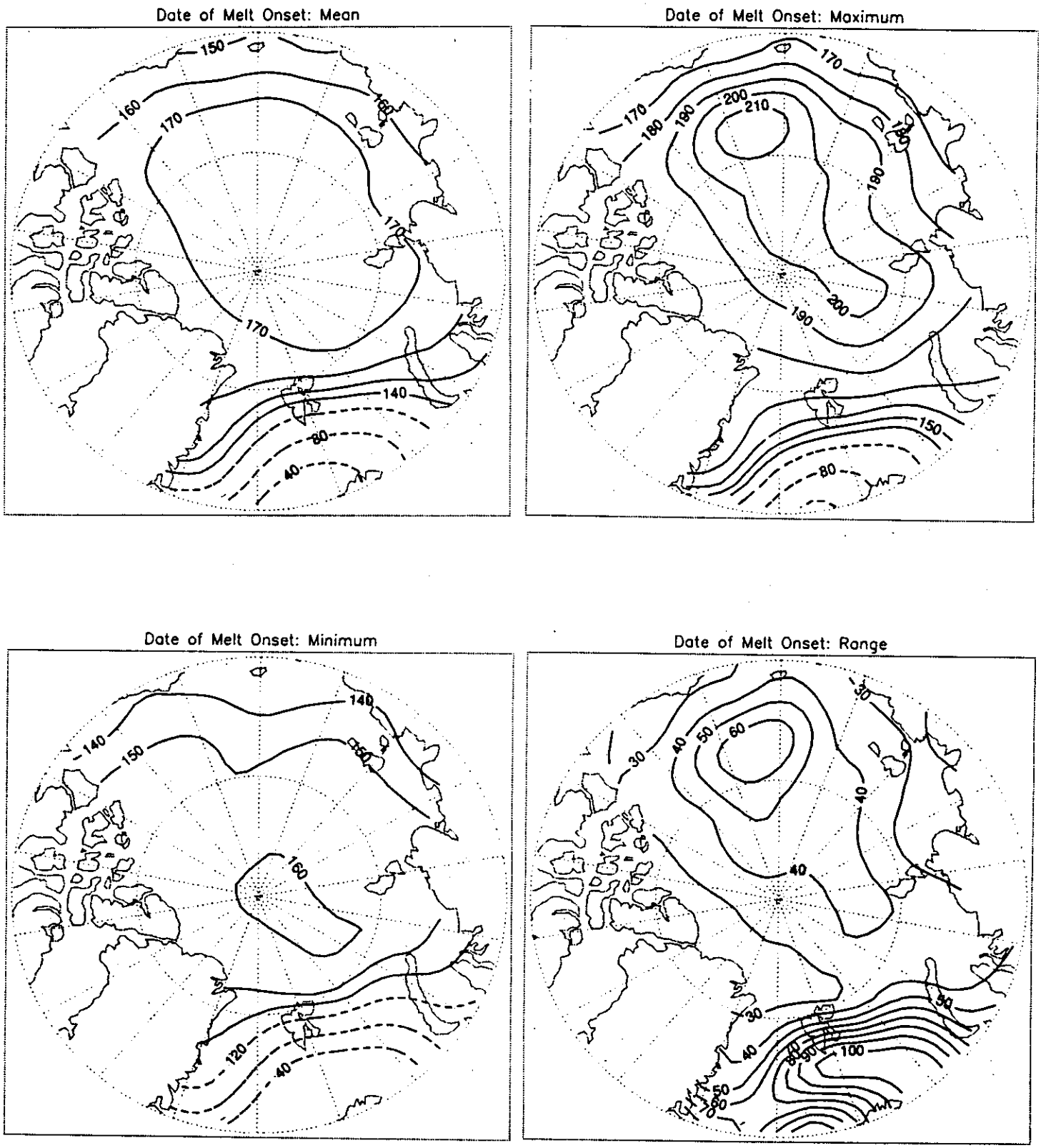

Units: Julian Days
1 May = Julian Day 121, 1 June=Julian Day 152,1 July=Julian Day 182

Figure 3.4.2

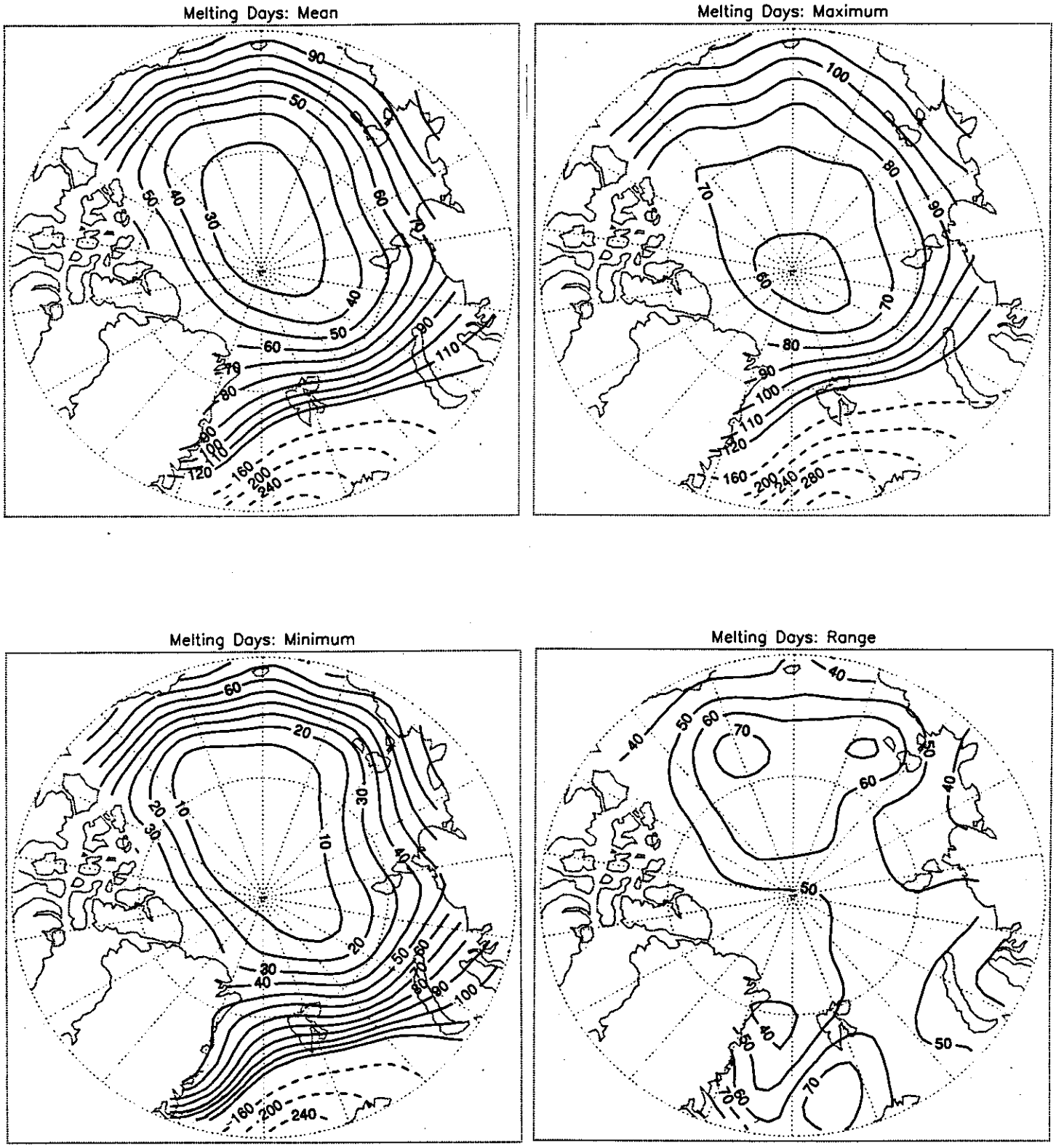

Units: Julian Days

3.5 Snow on Sea Ice

The CD-ROM containing Russian NP data discussed in Sections 2.1 and 2.3 also contains data on snow depth and density. Data represent measurements from snowlines of 1 km length as well as at snow stakes installed at the meteorological station sites. Snowline sites were chosen to be over flat ice. Measurements at each station were always taken along the same snowline. Colony et al. [1997] provide further details. Figure 3.5.1 shows the seasonal cycle in mean snow height (essentially equivalent to snow depth) and the +/- 1 standard deviation based on grouping all available snowline data. Figure 3.5.2 shows the corresponding seasonal cycle of mean snow density and the +/- 1 standard deviation. Both figures have been reproduced from Colony et al. [1997]. Although relatively few of the measurements are from the Beaufort Sea, these results nevertheless provide some estimate of conditions that can be expected at the SHEBA site. The results include both the effects of spatial sampling and interannual variability.

Snow height is maximized during May with a mean of about 35 cm, dropping to about 7 mm in August. Standard deviations tend to increase with mean snow height and are hence largest during spring and early summer. There is a general increase in snow density from August through June, which may be related to compaction of snow throughout the year. Taking the mean density and snow height, the snow water equivalent during May, when the snow depth is maximized, is about 11 cm.

Figure 3.5.1

Seasonal Cycle and Standard Deviation of Snow Height from Russian North Pole Measurements (Reproduced from Colony et al., 1997].

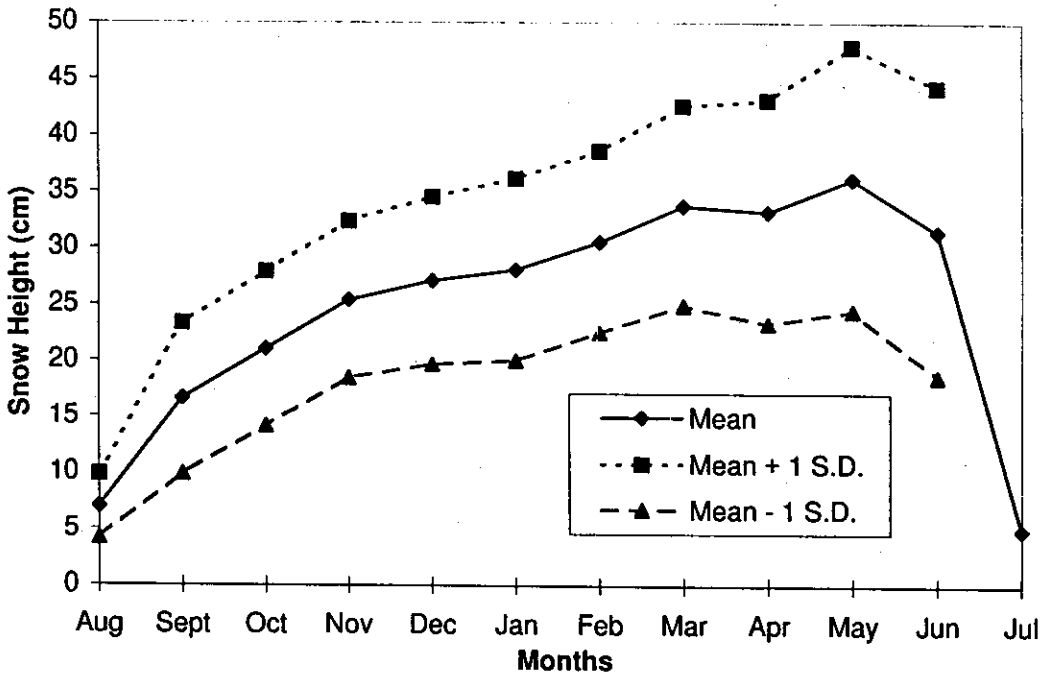

Figure 3.5.2

Seasonal Cycle and Standard Deviation of Snow Density from Russian North Pole Measurements (Reproduced from Colony et al., 1997].

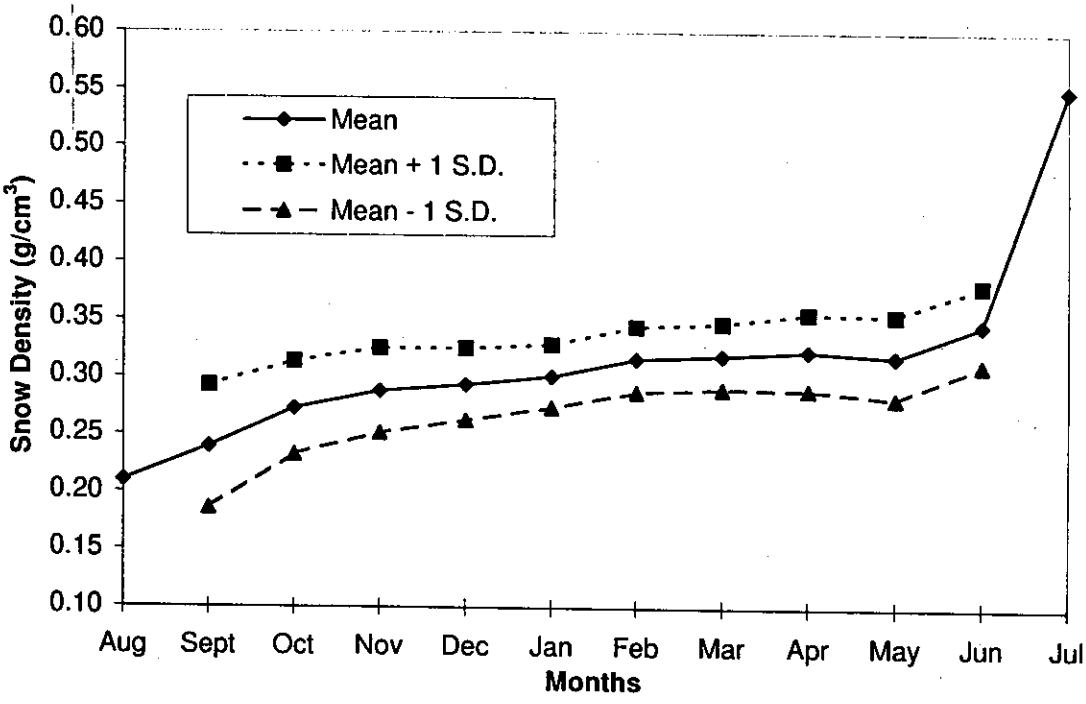

4. BIBLIOGRAPHY

Agnew, T.A., H. Le, and T. Hirose, 1997: Estimation of aggregate-scale sea ice motion from SSM/I 85 GHz imagery, *Annals of Glaciology*, 25, (in press).

Armstrong, R.L. and M.J. Brodzik, 1995: An earth-gridded SSM/I data set for cryospheric studies and global change monitoring, *Adv. Space Res.*, 16(10), 155-163.

Bryazgin, N.N. 1976: Srednegodovoe kolichestvo osadkov v Arktike s uchetom pogreshnosti osadkomerov (Mean annual precipitation in the Arctic with consideration of gauge biases), *Trudy Arkt. Antarkt. Nauch.-Issled. Inst.*, 323, 40-74.

Clark, M.P., M.C. Serreze and R.G. Barry, 1996: Characteristics of Arctic Ocean climate based on COADS data, 1980-1993, *Geophys. Res. Lett.*, 23(15), 1953-1956.

Colony, R., V. Radionov and F.L. Tanis, 1997: Measurements of precipitation and snow at the Russian North Pole drifting stations, *Polar Geography* (in press).

Cressman, G.P., 1959: An operational objective analysis system, *Mon. Wea. Rev.*, 87, 367-374.

Emery, W.J., C.W. Fowler, J. Hawkins and R.H. Preller, 1991: Fram Strait satellite image derived ice motions, *J. Geophys. Res.*, 96, 4751-4768.

Emery, W.J., C.W. Fowler, and J.A. Maslanik, 1997a: New satellite- derived sea ice motion tracks Arctic contamination, *Marine Pollution Bulletin* (in press).

Emery, W.J., C.W. Fowler, and J.A. Maslanik, 1997b: Satellite-derived maps of Arctic and Antarctic sea ice motion: A new multi-year record of ice transport, *Geophys. Res. Lett.*, 24(8), 897-900.

Fowler, C.W., 1995: Ice motion derived from satellite remote sensing with application to ice studies in the Beaufort Sea, PhD Thesis, Univ. of Colorado, 97 pp.

Gavrilova, M.K., 1963: Radiatsionnyi klimat Atktiki (Radiation Climate of the Arctic), Gidrometeorologicheskoe Izdatel'stvo, Leningrad (Translated from Russian, Israel Program for Scientific Translations, Jerusalem, 1966), 178 pp.

Hahn, C.J., S.G. Warren and J. London, 1995: The effect of moonlight on observations of cloud cover at night and application to cloud climatology, *J. Climate*, 8, 1429-1446.

Huschke, R.E., 1969: Arctic Cloud Statistics from Air Calibrated Surface Weather Observations, *Mem. RM-6173-PR*, Rand Corp., Santa Monica, CA, 79 pp.

Jacobs, J.J., R.G. Barry, R.S. Bradley and R.L. Weaver, 1974: Studies of climate and sea ice conditions in Eastern Baffin Island, 1971-1973, *Occasional Paper No. 9*, Institute for Arctic and Alpine Research, University of Colorado, Boulder Colorado, 78 pp.

Kalnay, E., M. Kanamitsu, R. Kistler, W. Collins, D. Deaven, L. Gandin, M. Iredell, S. Saha, G. White, J. Woolen, Y. Zhu, M. Chelliah, W. Ebisuzaki, W. Higgens, J. Janowiak, K.C. Mo, C. Ropelewski, J. Wang, A. Leetma, R. Reynolds, R. Jenne and D. Joseph, 1996: The NCEP/NCAR 40-year reanalysis project, *Bull. Amer. Meteorol. Soc.*, 77(3), 437-471.

Key, J., E. Amano, J. Collins, 1996: *FluxNet User's Guide*, Technical Report 96-03, Dept. of Geography, Boston University, 22 pp.

Khrol, V.P. (editor), 1996: *Atlas of the Water Balance of the Northern Polar Area*, Federal Service of Russia for Hydrometeorology and Environmental Monitoring, State Research Centre of Russian Federation Arctic and Antarctic Research Institute, St. Petersburg, Gidrometeoisdat, 12 pp. plus 82 maps.

Legates, D. and C. Willmott, 1990: Mean seasonal and spatial variability in gauge-corrected global precipitation, *Int. J. Climatol.*, 10(2), 110-127.

Marshunova, M.S., 1961: Principle Regularities of the Radiation Balance of the Underlying Surface and of the Atmosphere in the Arctic (in Russian), *Tr. Arct. Antarct. Nauchno-Issled. Inst.*, 229, 5. Transl. by Rand Corp., Memo. RM-5003-PR, 51-103.

Marshunova, M.S. and N.T. Chernigovskii, 1971: *Radiatsionnyi rezhim zarubeznhoi arktiki* (Radiation regime of the foreign Arctic), Gidrometeorologicheskoe Izdatel'stvo, Leningrad, 182 pp.

Marshunova, M.S., A.A. Mishin, 1994: *Handbook of the Radiation Regime of the Arctic Basin (Results from the Drift Stations)*, Applied Physics Laboratory, University of Washington, Seattle Washington, Technical Report APL-UW TR 9413 (V.F. Radionov and R. Colony, eds.), 52 pp. plus appendices.

Maslanik, J.A., M.C. Serreze and R.G. Barry. 1996: Recent decreases in Arctic summer ice cover and linkages to atmospheric circulation anomalies, *Geophys. Res. Lett.*, 23(13), 1677-1680.

Munoz, E.A. and S. Martin, 1995: Gridded Arctic surface temperature data sets: A comparison with Soviet ice station and land temperatures for 1987-1988, *J. Climate* (in press)

NSIDC, 1996: DMSP SSM/I Brightness Temperatures and Sea Ice Concentration Grids for the Polar Regions, National Snow and Ice Data Center Distributed Active Archive Center, CIRES, Campus Box 449, University of Colorado, Boulder, Colorado 80309-0449 USA, 110 pgs.

Ohmura, A., and H. Gilgen, 1991: Global Energy Balance Archive GEBA. Report 2: The GEBA Database, Interactive Applications, Retrieving Data. Internal Report, Department of Geography, ETH-Zürich.

Petty, G.W., 1995: Frequencies and characteristics of global oceanic precipitation from ship-board present-weather reports, *Bull. Amer. Meteorol. Soc.*, 76, 1593-1616.

Rossow, W.B. and Schiffer, R.A. 1991: ISCCP cloud data products, *Bull. Amer. Met. Soc.* 72, 2-20.

Rossow, W.B., A.W. Walker, D.E. Beuschel and M.S. Roiter, 1996: International Satellite Cloud Climatology Project (ISCCP) Documentation of New Cloud Datasets, WMO/TD-No. 737, World Meteorological Organizations, 115 pp.

Roulet, R.R., 1969: Radiation Regime of Arctic Drifting Station Arlis II, January 1964-May 1965, Department of Atmospheric Sciences, University of Washington, Scientific Report, Office of Naval Research Contract N00014-67-A-0103-0007, NR 307-252, 58 pp.

Schweiger, A. and J. Francis, 1995: Gridded daily and monthly Arctic atmospheric data from TOVS- Users Guide, Polar Science Center, Applied Physics Laboratory, University of Washington, 1013 NE 40th. St., Seattle, Washington 98105-6698 USA.

Schweiger, A.J. and J.R. Key, 1992: Arctic Cloudiness: Comparison of ISCCP-C2 and Nimbus-7 satellite-derived cloud products with a surface-based cloud climatology, *J. Climate*, 5(12), 1514-1527.

Schweiger, A.J. and J. Key, 1994: Arctic Ocean radiation fluxes and cloud forcing based on the ISCCP C2 cloud data set, 1983-90, *J. Appl. Meteorol.*, 33(8), 948-963.

Schweiger, A.J., M.C. Serreze and J.R. Key, 1993: Arctic sea ice albedo: A comparison of two satellite-derived data sets, *Geophys. Res. Lett.*, 20(1), 41-44.

Serreze, M.C., J.E. Box, R.G. Barry and J.E. Walsh. 1993: Characteristics of Arctic synoptic activity. 1952-1989, *Meteor. Atmos. Phys.*, 51, 147-164.

Serreze, M.C., J.R. Key, J.E. Box and J.A. Maslanik, 1997a: A new monthly climatology of global radiation for the Arctic and comparisons with NCEP/NCAR reanalysis and ISCCP-C2 fields, *J. Climate.* (in press)

Serreze, M.C. and M.C. Rehder, 1990: June cloud cover over the Arctic Ocean, *Geophys. Res. Lett.*, 17(12), 2397-2400.

Serreze, M.C., M.C. Rehder, R.G. Barry, J.D. Kahl and N.A. Zaitseva, 1995: The distribution and transport of atmospheric water vapour over the Arctic, *Int. J. Climatol.*, 15, 709-727.

Serreze, M.C., J.C. Rogers, F. Carse and R.G. Barry, 1997b: Icelandic Low cyclone activity: climatological features, linkages with the NAO and relationships with recent changes in the Northern Hemisphere circulation, *J. Climate*, 10(3), 453-464..

Shine, K.P., A. Henderson-Sellers and R.G. Barry, 1984: Albedo-climate feedback: the importance of cloud and cryosphere variability, Chapter 4 in: *New Perspectives in Climate Modeling, Development is Atmospheric Sciences*, 16 (A. Berger and C. Nicolis, eds., Elsevier, pp. 135-155.

Smetannikovoi, A.V., 1983: *Radiation Regime of the of the Greenland and Norwegian Seas* (in Russian), Gidrometeoizdat, Leningrad, 64 pp.

Steffen, K., 1976: North Water Project, Progress Report 1 October 1975 to 30 September 1976, ETH Zurich and McGill University, Montreal, 54 pp.

Thorndike, A.S. and R. Colony, 1981: *Arctic Ocean Buoy Program Data Report, 1 January 1980-31 December 1980*, Seattle WA, University of Washington, Polar Science Center.

Tsay, Si-Chee, K. Stamnes and K. Jayaweera, 1989: Radiative energy budget in the cloudy and hazy Arctic, *J. Atmos. Sci.*, 46, 1002-1018

Vowinkel, E. and S. Orvig, 1964: Energy Balance of the Arctic. I. Incoming and absorbed solar radiation at the ground in the Arctic, *Archiv fur Meteorologie, Geophysik und Bioklimatologie, Series B,* 13(3), 352-377.

Walsh, J.E., W.L. Chapman and T.L. Shy. 1996: Recent decreases of sea level pressure in the central Arctic, *J. Climate,* 9(2), 480-486.

Warren, S.G., C.J. Hahn, J. London, R.M. Chervin and R. Jenne, 1986: Global distribution of total cloud cover and cloud type amounts over land, NCAR Tech. Note TN-273+STR, Boulder, CO, 29 pp.

Warren, S.G., C.J. Hahn, J. London, R.M. Chervin and R. Jenne, 1988: Global distribution of total cloud cover and cloud type amounts over the ocean, NCAR Tech. Note TN-317+STR, Boulder, CO, 41 pp.

Weller, G. and B. Holmgren, 1974: Summer Global Radiation and Albedo - Data for Three Stations in the Arctic Basin, Ice Island T-3, Barrow, Prudhoe Bay, 1971-1973, Tech. Report No. 2, December 1974, Geophysical Institute, University of Alaska, Fairbanks, 31 pp.

Woodruff, S.D., R.J. Slutz, R.L. Jenne and P.M. Steurer, 1987: A comprehensive ocean-atmosphere data set, *Bull Amer. Meteor. Soc.*, 68(10), 1239-1250.

Acknowlegements

This research was supported primarily by NSF grant OPP-9504201 "Sea Ice and Atmospheric Characteristics of the SHEBA Field Area" with additional support by NSF grants OPP-9614297 "The Utility of NCEP/NCAR Reanalysis Fields for Arctic Climate Studies", OPP-9321547 "The Arctic Radiation Balance" and NASA grant NAGW-2407 (POLES) and NAG5-4119. Final data assembly and publication were supported by the National Snow and Ice Data Center DAAC under NASA contract No. NAS5-32392. Roger Colony is thanked for supplying precipitation and snow depth/density figures. Ann Brennan is thanked for technical editing.